Nanocatalysts for the Electrochemical Reduction of Carbon Dioxide to Fuels

Kalyani S. Gupta

A thesis submitted to University College London in partial fulfilment of the requirements for the degree of Doctor of Philosophy

Supervised by Professor Jawwad A. Darr

2018

Christopher Ingold Laboratories,
Department of Chemistry,
20 Gordon Street,
London
WC1H 0AJ
United Kingdom

Declaration

I, Kalyani Gupta, confirm that the work presented in this thesis is my own where information has been derived from other sources, I confirm that this has been indicated in the thesis.

Kalyani Gupta

Abstract

This thesis focuses on the synthesis of nanocatalysts for the electroreduction of CO_2 to useful fuels such as formic acid, methanol, methane and carbon monoxide. Copper-based materials were synthesised via a continuous hydrothermal flow synthesis process (CHFS). This method involved mixing pressurised precursor solutions with supercritical water to rapidly form ultra-fine nanocatalysts. CuO synthesis was investigated by varying experimental parameters, such as mixer types, temperature, pH, metal salt precursor and H_2O_2. Particle size was modulated by controlling these parameters and sub-15 nm particle sizes were possible. This has not been previously observed or reported in the literature in flow synthesis for CuO. The as-prepared CuO nanoparticles were formulated into Nafion based inks. The influence of the Nafion fraction on the Faradaic efficiencies and overpotential was explored. The highest Faradaic efficiency for formic acid production (61%) was observed with the optimum Nafion fraction. Insights into the significant increase in the Faradaic efficiency with the optimum Nafion content was elucidated with electrochemical impedance spectroscopy (EIS). Ni doped CuO synthesised via CHFS, was reported here for the first time, where higher inclusion of Ni was possible compared to co-precipitation. The Ni doped CuO samples were evaluated for their electrocatalytic properties and showed higher Faradaic efficiency at lower overpotential (<1.2 V) and below 11 at % Ni, compared to the undoped CuO. The catalysts were evaluated by EIS, Tafel analysis and structural characterisation. Rotating Ring Disk Electrode (RRDE), a hydrodynamic technique, was validated as a high-throughput tool to screen catalysts prior to bulk electrolysis. The Pt ring was successfully used to electrochemically detect formic acid, as it was formed in situ on copper-based catalysts. This was confirmed by conducting product calibration and understanding the oxidation behaviour on Pt as a function of rotation and scan rate.

Acknowledgements

This PhD would not have been completed without the support of many people and I would like to take this opportunity to thank them.

Firstly, I would like to thank my supervisor, Prof. Jawwad Darr for his encouragement and guidance during my PhD. I would also like to acknowledge the Engineering and Physical Sciences Research Council (EPSRC) for funding my PhD programme. I wish to thank the technical staff at the Department of Chemistry, especially Dr. Steve Firth, Mr. Martin Vickers and Dr. Abil Aliev for their assistance and training on various instruments mentioned in this thesis.

I am especially grateful for the support offered by Dr Marco Bersani, without whom my thesis would have taken a very different form. His constructive criticism, patience and knowledge, helped steer me in the right direction, which was helped by our many discussions over coffee, even if it was from Gordon's café!

I am grateful to the members of the Clean Materials Technology Group (CMTG) – Tom, Pete, Paul, Neel, Meggi, Marco, Liam, Ian, Dustin, Dougal, Clément, Chris, Charles, Carlos, Alistair and Adrian – without them the past four years would have been rather boring! Thank you for making my time here enjoyable; I appreciated your feedback and enthusiasm for all the baking I did. I will miss baking cakes for you all, although not so much the complaints about the cleaning rota and my 'friendly' reminders.

I am thankful to the group, particularly the post docs, for the countless hours spent maintaining the reactors and ensuring everything in the lab ran smoothly. I am also particularly grateful to Tom, Huw, Charles, Liam, Chris, Carlos and Marco for reading my thesis and for their very helpful suggestions and discussions.

I would like to thank my parents, Shreekant and Lalita, and brother Karan for their constant support, encouragement and for their enduring belief in me. I am also thankful to Kesh's parents, Rameshwar and Usha, and his brother, Vidhur, for their support during my PhD. I would like to thank my friends, in particular, Jessica, Oli, Donia and Aditi for being a constant source of laughter and joy.

Finally, I would like to thank Kesh, for his love, support and understanding. I wouldn't have been able to get to this stage without his words of encouragement and motivation. I am eternally grateful for all he has done and more.

Publications

Publications related to the work presented in this thesis:

Gupta, K, Bersani, M, Darr, J.A, Highly efficient electro-reduction of CO_2 to formic acid by nano-copper, J. Mater. Chem. A, 2016, 4, 13786-13794

Other publications:

Bersani, M*, Gupta, K*, Mishra, A.K, Lanza, R, Taylor, R.S.F, Islam, H.U, Hollingsworth, N, Hardacre, C, de Leeuw, N.H. and Darr, J.A, Combined EXAFS, XRD, DRIFTS, and DFT Study of Nano Copper-Based Catalysts for CO_2 Hydrogenation, ACS Catal., 2016, 6, 5823–5833 [*These authors contributed equally]

Wang, L, Gupta, K, Goodall, J.B.M, Darr, J.A, and Holt, K, In situ spectroscopic monitoring of CO_2 reduction at copper oxide electrode, Faraday Discuss, 2017, 197, 517-532

Zhu, X, Gupta, K, Bersani, M, Darr, J.A, Shearing, P, and Brett, D, Rotating Ring Disk Study of the Electrochemical Reduction of CO_2, *Manuscript in preparation*

Table of Contents

List of Figures

List of Tables

List of Abbreviations

Abbreviations	Description
AFM	Atomic Force Microscopy
ATR	Attenuated Total Reflectance
BET	Branaur Emmett Teller
BP	British Petroleum
BPR	Back Pressure Regulator
CCS	Carbon Capture and sequestration
CCU	Carbon Capture and utilisation
CFD	Computer Fluid Dynamics
CHFS	Continuous Hydrothermal Flow Synthesis
CJM	Confined Jet Mixer
CL	Catalyst Layer
CMTG	Clean Materials Technology Group
CTL	Coal to Liquid Fuel
CV	Cyclic Voltammetry
DFT	Density Functional Theory
DLS	Dynamic Light Scattering
DM	Dual Mixer
DMF	Dimethylformamide
DMFC	Direct Methanol Fuel Cell
DMSA	Dimercaptosuccinic acid
DRIFTS	Diffuse Reflectance Infrared Fourier Transform Spectroscopy
DSS	4,4-dimethyl-4-silapentane-1-sulfonic acid
ECR	Electrochemical CO_2 Reduction
EDTA	Ethylenediaminetetraacetic acid
EDX	Electron Dispersive X-ray
EIS	Electrochemical Impedance Spectroscopy
EXAFS	Extended X-Ray Absorption Fine Structure
FA	Formic Acid
FID	Flame Ionisation Detector
FTIR	Fourier Transform Infrared
GC	Gas Chromtography
GDE	Gas Diffusion Electrode
GTL	Natural Gas to Liquid Fuel
HER	Hydrogen Evolution Reaction
HPLC	High Pressure Liquid Chromatography
HRTEM	High Resolution Transmission Electron Microscopy
HSM	High Shear Mixer
ICP-AES	Inductively Coupled Plasma Atomic Emission Spectroscopy
ICP-MS	Inductively Coupled Plasma Mass Spectrometry
IPA	Isopropanol
IPCC	Intergovernmental Panel on Climate Change
JCPDS	Joint Committee on Powder Diffraction Standards
LSV	Linear Sweep Voltammetry
MBE	Molecular Beam Epitaxy

Abbreviations	Description
NHE	Normal Hydrogen Electrode
NMP	N-Methyl-2-pyrrolidone
NMR	Nuclear Magnetic Resonance
PBS	Phosphate-buffered Saline
PEEK	Polyether ether ketone
PEG	Polyethylene glycol
PEMFC	Proton Exchange Membrane Fuel Cell
PM	Pre-Mixer
PRV	Pressure Relief Valve
PTFE	Polytetrafluoroethylene
PVP	Polyvinylpyrrolidone
PXRD	Powder X-ray Diffraction
QMUL	Queen's Mary University London
RRDE	Rotating Ring Disk Electrode
SB	Sonic bath
SD	Size Distribution
SECM	Scanning Electrochemical Microscopy
SEM	Scanning Electron Microscopy
SG/TC	Substrate Generation/Tip Collector
SM	Single Mixer
SP	Sonic Probe
SRF	Surface Roughness Factor
STM	Scanning Tunnelling Microscopy
TCD	Thermal Conductivity Detector
TEA	Tetraethylammmonium salt
TEM	Transmission Electron Microscopy
TG/DTA	Thermal Gravimetric Analysis/Differential Thermal Analysis
UCL	University College London
UN	United Nations
UV-VIS	Ultra-violet Visible Absorption Spectroscopy
XPS	X-ray Photoelectron Spectroscopy

Chapter 1. Literature Review

1.1 Introduction

This thesis considers the use of nanomaterials, as catalysts, for the conversion of carbon dioxide (CO_2) into useful chemicals such as methanol (CH_3OH), formic acid (HCOOH), methane (CH_4) and carbon monoxide (CO). Anthropogenic activities have led to a rapid atmospheric increase of greenhouse gases such as CO_2, which has led to global warming and climate change issues. In tandem with CO_2 sequestration and storage, a possible solution to the CO_2 problem is to use it as a feedstock rather than considering it a waste product. Subsequently, this thesis evaluated the controlled synthesis of nanocatalysts, including copper-based materials via Continuous Hydrothermal Flow Synthesis, for CO_2 conversion. The nanocatalysts were tested via electroreduction of CO_2 to assess the catalyst performance.

This chapter will introduce the background on the CO_2 problem, as well as current mitigation solutions discussed in the literature, with a focus on electrochemical conversion of CO_2. The types of catalysts that have been synthesised and tested is also discussed in detail. The status of nanoparticle synthesis via conventional routes is briefly discussed followed by the use of Continuous Hydrothermal Flow processes as a novel technology for scalable synthesis of nanocatalysts.

1.2 The greenhouse gas effect and the carbon cycle

The average surface temperature of the earth is 15 °C. This is due to the surrounding atmosphere, which traps heat from the solar radiation reflected off the earth. Without this atmosphere, the surface temperature would be the −18 °C.[1] The warming of the planet, due to its atmosphere, has created

viable conditions for life to thrive. This temperature is strongly influenced by small concentration of gases in the atmosphere, in particular, by carbon dioxide (CO_2) and water vapour (H_2O). They trap heat by absorbing reflected solar radiation from the earth's surface. This is termed the greenhouse effect. The natural carbon cycle is maintained between the oceans, atmosphere and the fixation of CO_2 by plants and animals, which is balanced by emission of CO_2 from plants, animals and volcanoes.[2]

1.3 The CO_2 problem

There is overwhelming evidence that the natural equilibrium of the carbon cycle is being perturbed by the increasing concentration of CO_2 and other greenhouse gases in the atmosphere. Anthropogenic activities have led to a rapid rise of CO_2 in the atmosphere. In a recent report, the Intergovernmental Panel on Climate Change (IPCC) confirmed that the extensive combustion of fossil fuels, deforestation and agriculture were responsible for increased CO_2 concentrations in the atmosphere.[3] Worldwide industrialisation has meant that the amount of CO_2 released into the atmosphere from the combustion of fossil fuels (coal, oil or natural gas) has increased from 2 Gt/yr in the year 1850 to 40 Gt/yr in the year 2011, as shown in Figure 1-1a.[2] The level of CO_2 in the atmosphere did not vary significantly between 1850 and 1970. The majority of the increase in CO_2 concentration has happened since the beginning of the industrial revolution and over half the increase has only happened in the last 50 years or so (Figure 1-1b).[4] According to the finding of a recent investigation by BP, as part of its Energy Outlook 2030 report, estimated that 90 % of the energy produced worldwide in 2011 was obtained from fossil fuels.[5]

The issue with the CO_2 problem and its effects is made complicated by a myriad of political and socio-economic factors, such as the increasing population of the planet, projected to reach 9.7 billion by 2050,[2] a drive for strong economic growth in developing countries such as Brazil, China and

India as well as the increased reliance upon fossil fuel based technology to meet the population's growing energy needs.[6] The emission of pollutants from various sources such as automotive vehicles, airports or power plants, is not only limited to CO_2. Other harmful pollutants such as NO_2, SO_2, particulate matter as well as some greenhouse gases such as CH_4, have been increasing in concentration for the past century.[4]

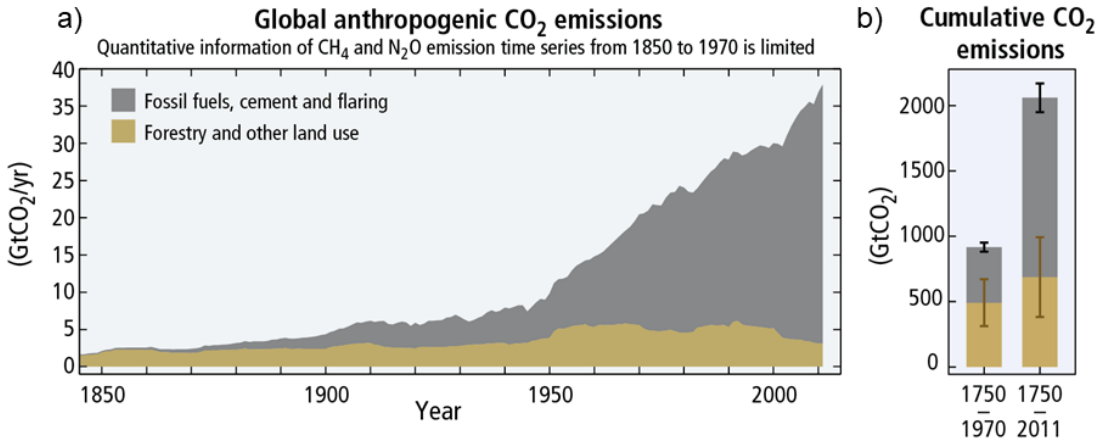

Figure 1-1 - a) Global anthropogenic CO_2 emissions from fossil fuels, cement and flaring as well as forestry and other land based use, b) Cumulative emissions of CO2 from these sources and their uncertainties are shown as bars and whiskers, respectively. Obtained from the *Climate Change 2014: Mitigation of Climate Change. Contribution of Working Group III to the Fifth Assessment Report of the Intergovernmental Panel on Climate Change*, Figure SPM.1, Page 3, Cambridge University Press, Cambridge, United Kingdom, 2014.[3]

1.4 Global warming and climate change

The effect of increasing CO_2 concentrations in the atmosphere has led to excess warming of the planet, as the radiated heat from the sun is absorbed by greenhouse gas molecules, which radiate the heat in all directions. This has led to atmospheric warming and planetary temperature rise. Since the 1900s, the temperature of the surface of the earth has already increased by 0.9 °C, with much of the increase taking place over the last 50 years.[2] As a result of this increase in temperature, the lower and upper layers of the ocean have begun to warm, as well as the outer layers of the atmosphere. Some of the consequences of this are the melting of polar ice caps and the rise of sea levels.[3]

Other possible changes that are forecast to occur are global shifts in ecosystems and species extinction, as has been observed in the past millions of the years during other major geological events before (such as ice ages). Other changes include the loss of crops and negative impacts on crop yields have been observed in some cases around the planet.[2] Major events due to global warming are thought to include climate related extreme events such as heat waves, droughts, floods, cyclones and wildfires, which can present a major threat to ecosystems, human establishments and life.

1.5 Mitigation strategies for the CO_2 problem

Due to the high global risk related to the CO_2 problem, global warming and climate change, there is a keen interest in resolving the continuing problem. A limit of 2 °C temperature rise (above pre-industrial levels) is often targeted as a way of limiting dangerous climate change. The IPCC has also identified the world's carbon budget, which is essentially the amount of CO_2, which can be emitted and still have a likely chance of limiting global temperature rise to 2 °C.[3]

There are several other solutions discussed in the literature, which aim to support reduction in CO_2 emission, which will be briefly described. Sustainable energy sources are needed to replace current fossil fuel-based energy sources and aid in the reduction of CO_2. It is imperative to consider and act on technological options available for mitigating increasing levels of CO_2 in the atmosphere. A number of responses to the problem, along with their disadvantages, are listed below and some responses are discussed in more detail in Section 1.6 and 1.7:

1. Design and develop cleaner and more efficient energy systems that do not generate pollutants such as NO_x and SO_x as opposed to post utilisation treatment, which would also minimise associated CO_2 emissions. Such examples, where cleaner and more efficient systems

have been developed include gas turbine combine cycle (GTCC), hydrogen energy and fuel cells.[4]

2. Fuel switching: from fossil fuels to renewable energy sources, such as wind, geothermal and solar.[7] Renewable energy sources present a major challenge as the sources depend on the regional distribution and seasonal availability as well as issues with energy density. Other potential sources of energy (such as CO_2 reduction to fuels) can be used to provide energy in the gaps when renewable energy sources are unavailable.
3. Carbon capture and storage: Removing and separating CO_2 from fossil fuel burning power plants and engines.[8] CO_2 can be stored in deep oceans and natural reservoirs such as geological formations. Although, the effectiveness of such an option is debatable as the long-term effects of storing carbon dioxide deep underground are unknown. One issue is ocean acidification due to carbon dioxide dissolving in the oceans, which can affect the ecosystem and aquatic organisms. Another factor to consider would be the high cost of CO_2 capture and separation.
4. Reducing the use of fossil fuels: Possible government legislation or UN frameworks can limit or cap the amount of greenhouse gas emissions countries are able to emit in the atmosphere through frameworks such as the Paris Agreement within the United Nation Framework Convention on Climate Change, which deal with the mitigation of greenhouse gases emission reduction and adaptation strategies.[9]
5. Utilisation of CO_2: CO_2 conversion to useful products such as formic acid, methanol, hydrocarbons, syn gas, etc. presents an attractive proposition in the mitigation of excess CO_2 in the atmosphere.[10] There are a number of challenges in this area as CO_2 is a thermodynamically stable molecule and it does not currently present itself as a high value product as its energy consuming conversion is viewed unfavorably.

Although a myriad of options are available and discussed as a solution, it is likely that a combination of such processes would be required in tandem to overcome the CO_2 problem.

1.6 CO_2 sequestration and storage

As mentioned in Section 1.5, carbon capture and storage (CCS), from point sources such as power plants as well as other industries reliant upon fossil fuels, such as iron, steel, cement and petroleum refining, has been discussed extensively.[10]

This process consists of three main stages: the removal of CO_2 from the exhaust stream of a plant, followed by transportation of carbon dioxide, usually in a compressed form, which is delivered to a storage site, typically geological features for long term storage (over thousands of years). Major cost considerations include the cleaning of the outflowing CO_2, and the compression or refrigeration of CO_2 to be transported either through high-pressure pipelines or by ships. As well as high costs for compression, transportation and storage, there is a high energy demand required to compress and refrigerate the CO_2.[11] It is likely that CCS would need to be employed with other alternative strategies such as nuclear and renewable energy.

1.7 Carbon capture and utilisation

CCS is an attractive mitigation technology in some sectors, however, it has significant limitations including high capital investment, uncertainty over long term storage, public resistance to CCS and it is also highly energy intensive. It is possible to consider that carbon capture and utilisation of CO_2 would play a key role in the green economy and abatement of high levels of CO_2 in the atmosphere. Instead of considering CO_2 as a waste product, it can be

considered as a carbon feedstock for the synthesis of fuels, in building materials production and use in the chemicals industry.

Processes such as natural gas to liquid (GTL) and coal to liquid fuel (CTL) via Fischer-Tropsch process are investigated extensively.[12] These processes would mean there is less dependence on imported fuels and would use coal and natural gas, which are relatively more abundant than oil. However, GTL and CTL are not sustainable as they rely on non-renewable energy sources to supply fuel. Conversion of CO_2 to useful chemicals using renewables offers a more sustainable route to solving the energy crisis and depleting levels of fossil fuels. If syn-gas can be synthesised from CO_2 conversion, then this may be a viable and sustainable option for Fischer-Tropsch catalysis.

Currently, there is a large dependency on carbon-based materials, derived from fossil fuels, in cosmetics to computers, homes to commercial buildings and drugs to plastics. Even if the energy problem is solved, our efforts should also be concentrated on finding sustainable supplies of feedstock for carbon based chemicals and organic materials.[13] Conversion of CO_2 to useful products, as mentioned above, is an appealing way to overcome this. Carbon utilisation technology can be adapted with post combustion carbon capture facilities already in place and can potentially offset the cost of compression or storage required with conventional CCS routes by converting the captured CO_2 into useful chemicals.[14]

1.7.1 CO_2 transformations

A number of different routes have been explored for the conversion of CO_2, as described in the schematic in Figure 1-2. Photochemical and chemical (hydrogenative) routes will be briefly discussed in Section 1.10 and a detailed critical review of the electrochemical route to CO_2 conversion is also discussed in Section 1.11.

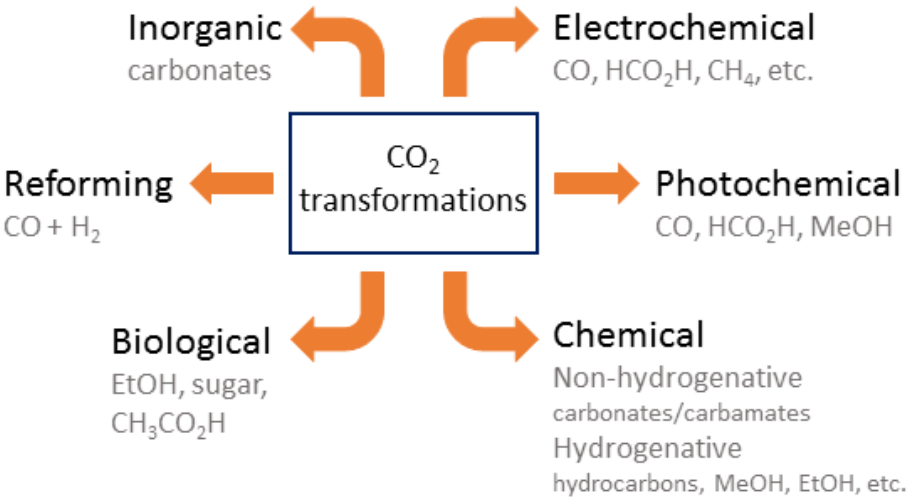

Figure 1-2 – Types of CO_2 transformations and typical products obtained in the literature. Adapted with permission from reference M. Mikkelsen, M. Jørgensen and F. C. Krebs, *Energy Environ. Sci.*, 2010, **3**, 43–81.[15]

1.8 Properties of CO_2 and the thermodynamic consideration

CO_2 is an abundant feedstock as a carbon source. Despite this, few industrial processes use it as a raw material due to its stable state, as demonstrated by its standard free energy of formation ($\Delta G° = -394.36$ kJ mol^{-1}).[13] CO_2 is in its most oxidised form and is therefore largely unreactive, requiring a large input of energy to transform it into different chemicals. This may be achieved via:

1. High energy starting materials such as hydrogen. This is currently not as feasible because of its cost but an inexpensive source of hydrogen by solar or nuclear power could alter this.
2. Achieved by choosing low energy synthetic targets
3. Altering the equilibrium of the reaction by removing the product
4. Supplying energy in the form of light or electricity

CO_2 is a linear molecule in its ground state, in the form O = C = O. The oxygen atoms are weak Lewis bases and the carbon atom is largely electrophilic due to the electronegative nature of the oxygen atoms.[16]

Nucleophilic attack on the carbon results in bending of bond angles to 120°. There is a large activation barrier to achieve this due to very different geometries of the linear and neutral CO_2 and the radical anion ($CO_2^{\bullet-}$), that is formed after the one electron reduction step. Due to the stability of the CO_2 molecule, there is a large energy input required, appropriate reaction conditions and the assistance of an effective catalyst is strongly required for the efficient conversion of CO_2.

1.8.1 Current industrial uses of CO_2

Currently, industrial processes only use 0.5 % of carbon dioxide generated from anthropogenic emissions for other applications.[4,8] CO_2 is used in the drinks industry, enhanced oil recovery and as a supercritical fluid for composite and nanomaterial production. It can also be used as a protective gas, in food perseveration and welding. It is often used as a refrigerant to substitute CFCs, which are harmful to the environment. Chemically, CO_2 is used to synthesise urea, salicylic acid, carbonates, and pigments and used as an additive for the synthesis of methanol.[17]

1.9 Uses of products from CO_2 conversion

This Section briefly discusses the applications of the products obtained from CO_2 conversion.

1.9.1 Carbon monoxide

Carbon monoxide is commonly used in mixture with hydrogen for fuel. It is also used in the manufacturing of a variety of chemicals such as acids, esters and alcohols. Carbon monoxide is also used in the biotechnology, electronics and steel industry.

1.9.2 Formic acid

Conversion of CO_2 to formic acid is considered a commercially profitable process compared to other products such as methanol, CO and long chain hydrocarbons due its many applications. Similar to methanol, formic acid can be used in a fuel cell to generate electricity. Formic acid has also been explored as an energy storage for H_2. This is ideal as formic acid is in a liquid phase at room temperature, making it ideal for storage, transportation, refuelling and handling, despite a hydrogen storage capacity of only 4.35 wt %.[18]

1.9.3 Methanol

Methanol is an excellent material to be considered as a fuel or as a precursor for other carbon-based materials, such as formaldehyde, acetic acid and methyl methacrylate. Due to its volumetric energy density relative to petrol and diesel, it can be used as a fuel on its own or blended with current fuel sources. It may also be used as a direct methanol fuel cell (DMFC), where the methanol is oxidised with air to produce CO_2 and H_2O to generate electricity. The methanol to olefin process was also discovered in the 1970s for the synthesis of light olefins (ethylene and propylene), polymers and hydrocarbon fuels.[4,17,19,20]

1.9.4 Acetic acid

Acetic acid is used as a starting feedstock for the production of esters and vinyl acetate monomers, which use an estimated one third of the acetic acid produced globally. Other examples of its uses are in acetic anhydride production, for medical purposes and in food.

1.9.5 Methane

Methane is primarily used as a fuel for domestic use and it is liquefied for ease of storage and transport. Methane is also used as a feedstock for the formation of syn-gas (CO + H_2).[6] Other examples of methane as a feedstock are for the conversion of methane into methanol and for the direct reaction of methane with sulfur trioxide.[21]

1.10 Approaches for CO_2 conversion

As mentioned in Section 1.7.1, different routes have been explored for generating products from CO_2 conversion. This Section briefly describes the heterogeneous, homogeneous and photochemical routes, as a comprehensive overview remains out of the scope of this thesis. There are a number of excellent reviews, which consider these areas in more detail.[6,15,22–25] Section 1.11 will be devoted to the electrochemical reduction of CO_2.

1.10.1 Heterogeneous conversion – hydrogenation

Catalytic hydrogenation of CO_2 to products such as methane, methanol, formic acid, and dimethyl ether have been studied intensively. For the methanation of CO_2, various supported noble metal catalysts have been considered. These include Ru/TiO_2, Ce and Ru oxides, Pd on SiO_2 and Ni based materials.[25] Of such catalysts, Ni based catalysts remain the most widely studied material. Analogously, carbon dioxide can be directly hydrogenated to other hydrocarbons by Fischer-Tropsch catalysts such as Co and Fe based catalysts. For the synthesis of methanol, although many metals have been tested, Cu remains the main catalytic component in a multi component catalyst system, which typically involves modifiers such as Zn, Zr, Ce, Si, Ti, and V. A support is used, and usually is an oxide-based material such as SiO_2, ZrO_2, Al_2O_3 and plays a role of stabilising the active catalyst. It

is also known that ZnO can play a key role in the dispersion and stabilisation of copper.[12]

The key issues with hydrogenation of CO_2 remains the source of H_2; it is typically derived from a variety of sources, including fossil fuel based sources, water or biomass.[6] From a sustainability stand point, the source of H_2 must be CO_2 emission free. The only viable option for this is water splitting to generate H_2 and O_2. However, this requires a significant energy input as well as effective catalysts that can split water without high overpotential requirements. Until such a system is available, the prospects of hydrogenation as a commercially significant process remain unviable. Other aspects of CO_2 hydrogenation that can be disadvantageous are the requirement of high temperatures and pressures (ranging from 200 to 600 °C and 50 to 100 bar pressure) depending on the synthetic target.[25]

1.10.2 Homogeneous conversion

Metal complexes with Ru, Ir, Co and Fe metals have been studied extensively in the literature.[26,27] These catalysts have shown satisfactory activities and selectivity but the recovery of the both, the catalyst and the product, remains a key issue. In addition, the regeneration of the catalyst is another key issue to be considered.

1.10.3 Photochemical conversion of CO_2

Since the advent of photocatalysis in the 1970s, much attention has been given to the use of solar energy to support catalytic reactions.[28] However, until very recently, little attention has been paid to this area in relation to CO_2 reduction. TiO_2 based materials have been used, with or without supports and often with other metals such as Cu, Ag, and Au. Other photocatalysts that have been tested include zeolites, titanates, copper promoted systems and carbon nitride.

Major issues with this process include the design of the photoreactor, which has not been agreed up on in the literature; and poor reactor design can lead to inefficiencies in the catalytic process. The quantum yield of the reaction, which determines the fraction of photon used for the conversion, has been at best only 0.01 %. Therefore, only a fraction of photons are used effectively to complete the reaction.[6]

1.11 Electrochemical reduction of CO_2

Electro-reduction of CO_2 has been considered since the 19th century but in the last 30 years, research into this area has significantly increased, mainly due to issues with global warming, climate change and the energy crisis. CO_2 has been catalytically converted at the surface of an electrode by applying a bias. This method is considered advantageous as:

1. Typically, the reactions are done in ambient conditions, especially compared to catalytic hydrogenation where temperatures in excess of 200 to 600 °C and 50 to 100 bar pressure is needed.
2. The process may be controlled with the electrode potential to target certain products.
3. Use of water as a proton source. H_2 is replaced by H^+ and e^- due to the aqueous media aided by the near equivalence of H_2 potential to proton assisted hydrogenation of CO_2 (E^0 = 0 V vs. NHE at pH 1).
4. The electricity used for the consumption of this process may be generated by renewable sources (solar, wind, geothermal and hydroelectric), which would be favourable for this process to be commercially, economically and environmentally viable.
5. Typically, the electrochemical systems can be compact and modular making them easy to scale up.

However, there are significant limitations to this process currently. These are discussed in more detail in Section 1.11.6. The electrochemical reduction

can proceed via 2, 4, 6, 8 or 12 electron reduction pathways and typically major products include carbon monoxide (CO), formic acid (HCOOH), methanol (CH_3OH), methane (CH_4), ethanol (CH_3CH_2OH) and acetic acid (CH_3COOH). The thermodynamic half reaction and their standard electrode potentials at pH 7 in an aqueous media are detailed below (Equation 1.1 – 1.8).[12]

$$CO_2 + 2H^+ + 2e^- \rightarrow CO + H_2O \qquad E^0 = -0.52\ V \qquad \text{Equation 1.1}$$

$$CO_2 + 2H^+ + 2e^- \rightarrow HCOOH \qquad E^0 = -0.61\ V \qquad \text{Equation 1.2}$$

$$CO_2 + 4H^+ + 4e^- \rightarrow HCHO + H_2O \qquad E^0 = -0.51\ V \qquad \text{Equation 1.3}$$

$$CO_2 + 8H^+ + 8e^- \rightarrow CH_4 + 2H_2O \qquad E^0 = -0.24\ V \qquad \text{Equation 1.4}$$

$$2CO_2 + 12H^+ + 12e^- \rightarrow C_2H_4 + 4H_2O \qquad E^0 = -0.34\ V \qquad \text{Equation 1.5}$$

$$CO_2 + 6H^+ + 6e^- \rightarrow CH_3OH + 2H_2O \qquad E^0 = -0.38\ V \qquad \text{Equation 1.6}$$

$$2H^+ + 2e^- \rightarrow H_2 + 2H_2O \qquad E^0 = -0.42\ V \qquad \text{Equation 1.7}$$

$$CO_2 + e^- \rightarrow CO_2^{\bullet -} \qquad E^0 = -1.90\ V \qquad \text{Equation 1.8}$$

1.11.1 Cell design

A typical electrochemical reduction reaction is undertaken in an electrolytic cell consisting of three electrodes, a working electrode (cathode in this case), a counter electrode and a reference electrode. The electrodes are submerged in an electrolyte, which transports ions between the electrodes. The working electrode is either a bulk metal or a catalyst-coated electrode. A number of set ups (Figure 1-3) have been reported in the literature, including two compartment cell with glass frits, three electrode set up separated by an H^+ conducting membrane (such as Nafion), or two compartment cells with a proton conducting membrane and a gas diffusion electrode (GDE).[6] Other examples of cell designs include the use of bench scale continuous reactor, undivided fixed bed reactor and microfluidic reactor.[29]

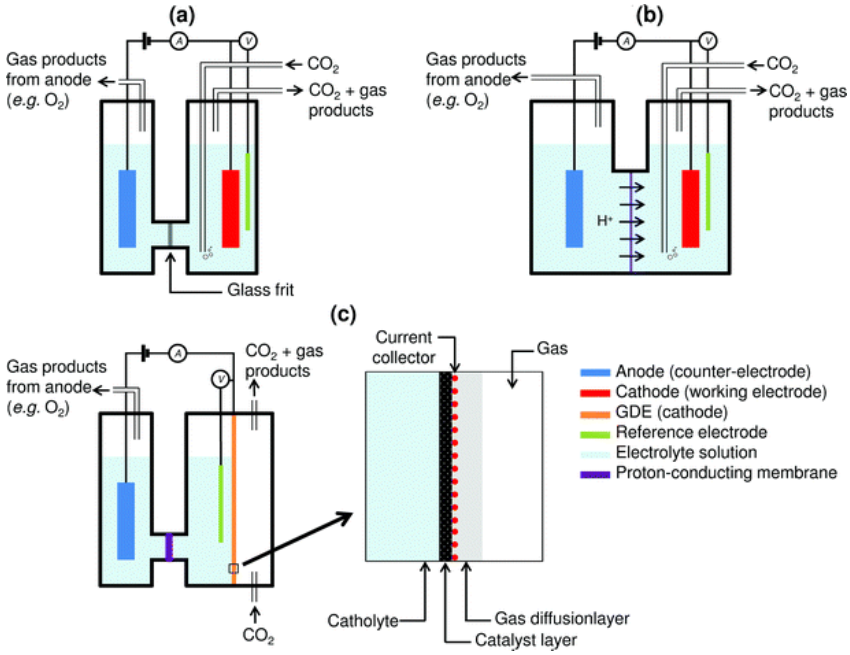

Figure 1-3 – Typical electrocatalytic set ups employed for the electrocatalytic reduction of CO_2 – a) two compartment with glass frit, b) cell with proton conducting membrane and c) with a gas diffusion electrode (GDE). Reproduced with permission from reference E. V. Kondratenko, G. Mul, J. Baltrusaitis, G. O. Larrazabal, J. Perez-Ramirez, G. O. Larrazábal and J. Pérez-Ramírez, *Energy Environ. Sci.*, 2013, **6**, 3112.[6]

1.11.2 Electrolytes

The electrolyte plays a crucial role in electrocatalysis as the medium where charge transfer takes place. If chosen appropriately, the electrolyte can be a source of hindrance or stabilisation to the catalytic process. Some research has explored the effect of the electrolyte. Electrolytes are typically divided into two areas; aqueous and non-aqueous.

When CO_2 is dissolved in aqueous electrolytes, a number of complex reversible reactions take place. These can be adjusted by varying the pH, as shown in the scheme and Figure 1-4 below.[30]

$$CO_{2(g)} \overset{H_2O}{\rightleftharpoons} CO_{2(aq)} \overset{H_2O}{\rightleftharpoons} H_2CO_{3(aq)} \overset{H_2O}{\rightleftharpoons} HCO_3^- + H_3O^+ \qquad p\textit{K}a = 6.4 \qquad \text{Equation 1.9}$$

$$HCO_{3(aq)}^- \overset{H_2O}{\rightleftharpoons} CO_{3(aq)}^{2-} + H_3O^+ \qquad p\textit{K}a = 10.3 \qquad \text{Equation 1.10}$$

The pH of the electrolyte is a crucial parameter that affects CO_2 electroreduction. In acidic media, the hydrogen evolution reaction (HER) is dominant and thermodynamically more favourable than the CO_2 electroreduction. The reduction of CO_2 generates hydroxide ions; the local pH at the electrode surface is therefore more basic than the bulk, which is likely to adversely affect the CO_2 electroreduction.[31] From the reversible reactions in Scheme and Figure 1-4, the formation of carbonate at high pH is more favourable, but evidence from a number of papers in the literature suggests that potentially only dissolved CO_2 or HCO_3^- species can be reduced and not the carbonate species. As the pH is increased near the electrode surface, the presence of dissolved CO_2 decreases, which would decrease the formation of products such as formic acid and CO.

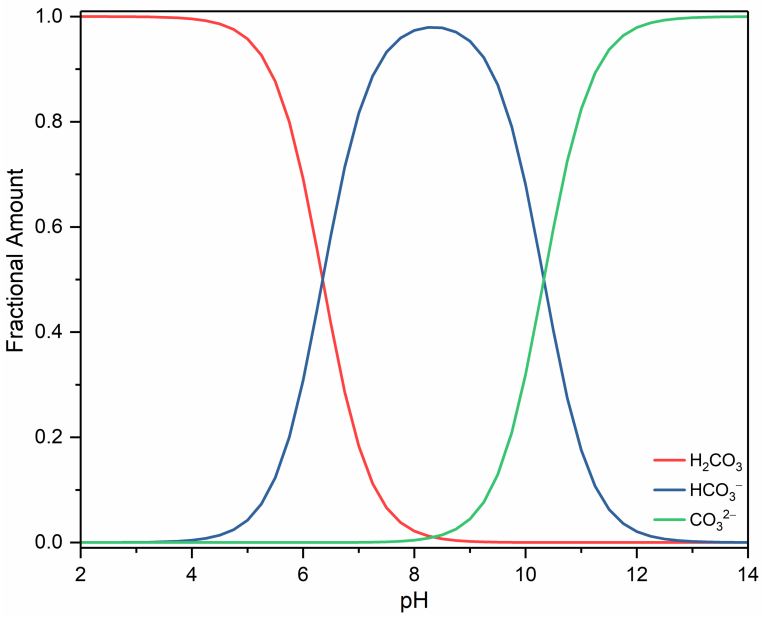

Figure 1-4 – Carbonate equilibrium in water as a function of pH.

To avoid this issue, electrolytes with a buffering capacity, such as $KHCO_3$ or K_3HPO_4 are commonly used. As HER is prevalent in acidic medium, most reactions in the literature are reported at around a neutral to slightly acidic pH (around pH 6.8).[32]

Non-aqueous electrolytes have also been investigated, due to the higher solubility of CO_2 in non-aqueous compared to aqueous electrolytes. The solubility of CO_2 in aqueous electrolytes is only 0.08 M. Commonly, KOH/CH_3OH mixtures are used as the solubility of CO_2 in methanol is five times higher than in water. Other organic electrolytes also used are dimethylformamide (DMF), MeCN, dimercaptosuccinic acid (DMSA) and tetraethylammmonium salt (TEA).[29]

Another type of non-aqueous electrolyte increasingly being used are ionic liquids, which are molten inorganic salts with large cation or anions. Ionic liquids have been used due to their stability, large potential window, high solubility and their ability to bind CO_2, which can aid in bending the CO_2, resulting in low overpotentials for CO_2 reduction.[29] However, ionic liquids remain expensive and time consuming to synthesise. In addition, reports of ionic liquids reacting with reactants have also been documented, so care is needed when using ionic liquids, as they might not be considered as inert solvents.[33]

1.11.3 Product Analysis

The quantitative analysis of products from electroreduction is an important aspect of the electrocatalytic process to evaluate and optimise the reaction conditions and the catalyst performance. The typical products obtained are CH_4, CO, H_2, O_2, CH_3OH, CH_3COOH, HCOOH and the products can be divided into gas or liquid phases. This Section will discuss the main techniques used to detect products.

Gas chromatography (GC) is commonly used to detect both gas and liquid phase products. Gas chromatography is an analytical technique, which involves the injection of a sample into a column. The sample is carried in the column using a carrier gas (typically He or N_2), which is used to separate the components within the sample. The components in the sample will be

adsorbed differently and at different points of the column and as the components exit the column, they are detected. The elution order and retention time are key parameters considered when analysing products. A number of different types of columns have been used and the usual detectors used are thermal conductivity detectors (TCD) and flame ionisation detectors (FID). Both are sensitive to the range of nano to picogram. TCDs work by measuring the difference of thermal conductivity between the compound and the carrier gas. The signal to noise ratio is higher if this difference is larger. FIDs are a sample destructive detector and employ a hydrogen/air flame, which oxidises the organic molecules; the ions produced are detected as an electrical signal. Usually, alcohols, permanent gases (CO_2, CO, CH_4, N_2, O_2) and hydrocarbons are analysed by GC. For carbonate/bicarbonate and carboxylic acids such as formic acid and acetic acid, the characterisation via GC is not straightforward. This is due to difficulty in vaporising such compounds easily after injection, decomposition upon heating and their adherence to the column walls. Therefore, other techniques are used for analysis of carbonate/bicarbonate and carboxylic acids instead.

Nuclear magnetic resonance (NMR) spectroscopy is a powerful technique for the structural analysis of compounds. It is commonly used for electrocatalytic reduction of CO_2 products in conjunction with GC. This technique is useful for use in the analysis of liquid phase products, especially carboxylic acids as they are difficult to analyse by GC. For the quantification of products, a calibration of known concentrations of each analyte should be conducted. This is the case for both GC and NMR. With NMR, an internal standard such as 4,4-dimethyl-4-silapentane-1-sulfonic acid (DSS) may be used.

Another technique that has been used includes mass spectrometry. This is often accompanied by a GC where the separated compounds are eluted into the mass spectrometer, where the products are then ionised and detected

based on their molecular weight. The quantification of products is not straightforward with a GC-MS; however, this technique is commonly used due to its high sensitivity and unique identification abilities. Infrared spectroscopy (IR) and Diffuse Reflectance Infrared Fourier Transform Spectroscopy (DRIFTS) have also been used to follow the consumption of CO_2 and the presence of CO and HCOOH.[34] IR spectroscopy can highlight particular functional groups but this technique is mainly used qualitatively. Other examples of analytical methods include ion chromatography, high-pressure liquid chromatography, UV and visible spectrophotometry.

A powerful electrochemical technique, known as Rotating Ring Disk Electrode (RRDE) may be used for in-situ product detection.[35] This comprises of a disk electrode, which typically has a catalyst coated on its surface surrounded by a ring electrode in a cylindrical PTFE holder. As the products and/or intermediates are formed on the disk electrodes, they are swept outwards to the ring electrode and can be electrochemically detected and thus the reaction mechanism may be elucidated, and the kinetics understood. The theory of this particular technique is discussed in more detail in Chapter 6.

1.11.4 Electrode structure

Initial studies concerning electrocatalytic reduction of CO_2 have largely been conducted on planar metal and mesh electrodes for ease of testing.[6,36] The focus has remained on understanding the effect of different transition metals on the product speciation. However, the use of bulk metal electrodes has continuously resulted in unsatisfactory Faradaic efficiencies and high overpotentials. Recently, the focus has moved on to use of gas diffusion electrodes (GDE), adapted from fuel cells, to overcome some of the issues that have emerged from planar or mesh electrodes.[37]

The key issue that remains for the electrocatalytic reduction of CO_2, is the low solubility of CO_2 in aqueous solvents (0.08 M) and therefore the low CO_2 transfer rate to the electrode. This issue may be overcome by using GDEs, which operate by providing a three-phase interface for gaseous reactants and products, the electrode and the electrolyte.[29] The gas diffusion layer comprises of a catalyst layer, typically a catalyst coated on carbon black, pressed with a porous layer, comprising of a carbon paper or cloth with a dense array of carbon fibres. The role of the GDE is to allow a pathway for the reactant, in this case CO_2, as well as electrolyte diffusion; acting as an intermediate for proton or electron transfer. The GDE also provides a clear pathway for product removal and controls heat and water transfer. A significant emphasis is placed on the catalyst layer (CLs), which usually has a catalyst ink cast onto a substrate. The catalyst may be an expensive noble metal, which is finely dispersed across the substrate. This is particularly the case when Pt is used for PEMFC, where platinum is the active catalyst.[38]

A key consideration in using the GDE is optimisation of each layer of the composite electrode to allow for high operational performance. This has to be conducted for each application and in the context of the operational conditions. The catalyst layer requires particular attention in order to optimise the catalyst surface area to improve catalytic performance. In the case of ECR of CO_2, in a number of reports the catalyst suspension is cast on to inert support electrodes, such as glassy carbon or stainless steel as opposed to using GDEs, and their performance has been subsequently evaluated. The optimisation of the catalyst layer is discussed in more detail in Chapter 4.

1.11.5 Electrocatalysts used for CO_2 electroreduction

A number of different metals and metal oxides, both in the bulk, nanostructured and metal complexes have been employed as catalysts for the electroreduction of CO_2. This Section discusses typical elements and compounds used, as well as, the final products obtained. Seminal work by

Hori et al. in the 1980s, was conducted where different metal electrodes were considered, such as Pb, Ni, Cu, In, Au, Fe, and Ag. The product speciation obtained on these electrodes was also discussed.[36,39,40] Table 1-1 summarises the metals tested and the products obtained.

Table 1-1 Summary of the major products obtained on simple metal electrodes.[36,39,40]

Metals	Major products
Au, Ag, Zn, Pd and Ga	Carbon monoxide
Pb, Hg, In, Sn, Cd, Th	Formic acid with small amounts of H_2
Ni, Fe, Pt and Ti	H_2
Cu	Hydrocarbons and formic acid

The pathways by which such products are obtained on different metal electrodes has been researched and can be summarised in Figure 1-5. The rate limiting step can be described as the formation of a high-energy $CO_2^{\bullet-}$ radical anion intermediate by the following reaction:

$$CO_2 + e^-_{aq} \rightarrow CO_2^{\bullet-} \ (E^o = -1.9 \text{ V}) \qquad \text{Equation. 1.11}$$

This particular step is highly energy intensive, due to the requirement of the linear CO_2 molecule to accommodate the electron by changing the configuration to a bent molecule, with a bending angle of 120°.[12] Furthermore, stabilisation of this particular intermediate is important in order to ensure further reaction of $CO_2^{\bullet-}$ to higher order products (CH_3OH, CH_4 and HCOOH). Otherwise, products such as CO can form, as $CO_2^{\bullet-}$ is not reduced further, particularly seen in the example of metals such as Au and Ag.

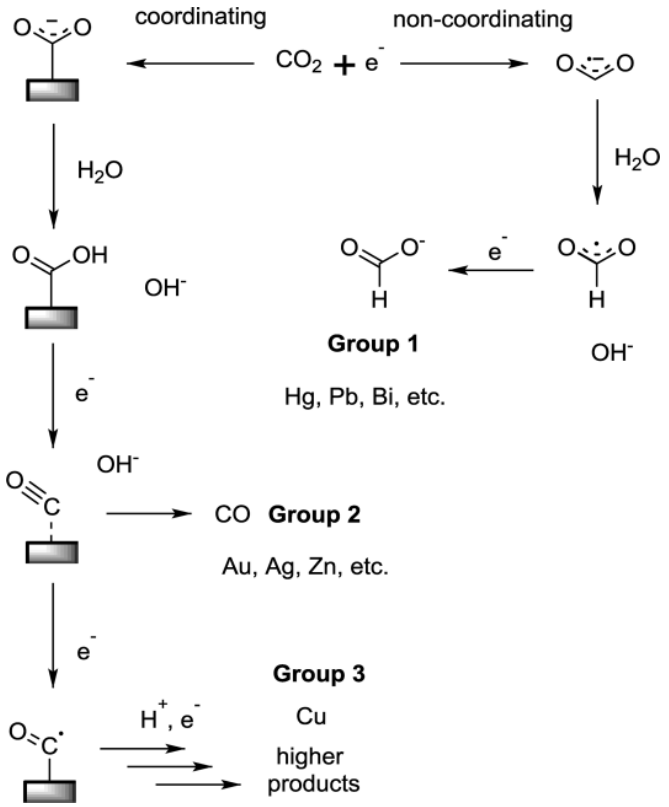

Figure 1-5 – Simplified mechanism of electroreduction of CO_2 in water on different metal surfaces. Reproduced with permission from reference J. P. Jones, G. K. Prakash and G. A. Olah, *Isr. J. Chem.*, 2014, **54**, 1451–1466.[31]

1.11.5.1 Pb, Hg, In and Sn metals

This group of metals predominantly produce HCOOH. They have a significantly high overpotential for hydrogen, which can be advantageous, as CO_2 reduction competes with water splitting. It is common to achieve significantly high Faradaic efficiencies for formic acid with these metals (in excess of 70 %, sometimes at 90 %).[41]

1.11.5.2 Au and Ag metals

Also, observed in Figure 1-5, these metals mainly produce CO and H_2, however in this particular area, much of the focus is not on targeting the highest Faradaic efficiency but instead specific ratios of CO and H_2, as this can be fed into a Fischer-Tropsch heterogeneous reactor for the production of higher order hydrocarbons.[42] Typically, syn-gas mixtures are derived from fossil fuel based sources so this would be an environmental friendly process to obtain the reactant gases. If the ratio of CO and H_2 can be controlled by

altering the reaction conditions, potential applied, electrolyte, then this can be an attractive way of recycling CO_2 to commercially valuable products. For example, a ratio of 2:1 H_2:CO can be used for the synthesis of methanol.

1.11.5.3 Copper-based materials

Copper was the only metal found to be an effective catalyst in converting CO_2 to hydrocarbons such as methane and ethane and alcohols, with high Faradaic efficiency. A range of experiments involving Cu based catalysts including Cu single crystals,[43] pure Cu electrodes[44] and Cu alloy electrodes[45] have been studied. Despite the effectiveness of Cu to reduce CO_2 to hydrocarbons, it can be inefficient with a large overpotential requirement.

The initial discovery by Hori et al. reported the production of CH_4 at high Faradaic efficiencies (average 38.5 %) with some formic acid and minor amounts of CO and H_2 on copper.[46] Another report by the same authors showed the temperature dependency on the formation of hydrocarbons such as ethylene and methylene at copper cathodes.[39] In both cases, bulk copper sheets were utilised to conduct the experiments. A potential dependence on the products was observed by Ito, Frese and Hori, where typically at lower negative potentials, CO and CH_4 were predominant and at higher negative potentials, higher hydrocarbons such as methylene were favoured.

Single crystal work on copper indicated a significant dependence of the product distribution based on which copper crystal face was investigated. The Cu (111) showed a predominance over methane, whereas Cu (100) favoured ethylene formation. Cu (110) favoured the formation of C2 and C3 hydrocarbons such as acetic acid. Results from studies on single crystal work indicated the importance of electrode preparation in order to expose the desired crystal faces for particular products.[30,47,48]

Other factors investigated that affect the performance of copper electrodes was the electrolyte, temperature and pressure. The purity of the electrolyte is

a key concern, as evidenced by Gupta et al. and Le et al. in the literature.[30,49] Due to the high negative potentials needed for CO_2 reduction, any trace level impurities, such as iron, zinc or other metals in the electrolyte can change the electrode surface, which adversely affects the performance of the electrode.[30] Murata et al. investigated the effect of cations on the electrochemical reduction of CO_2 on Cu electrodes. Hydrogen carbonate solutions were investigated where the cations were varied from Li^+, Na^+, K^+ and Cs^+. CO_2 reduction was found to be favourable with Na^+, K^+ and Cs^+, whereas H_2 evolution was dominant with a Li^+ cation. The concentration of the HCO_3^- was also changed, where the product selectivity varied with the concentration. This was rationalised by the local pH rising at low HCO_3^- concentrations as the ^-OH ions were not neutralised by the lack of HCO_3^- ions.[46]

The temperature of the electrolyte has also been investigated, where the formation of formic acid does not vary with temperature on copper electrode. However, the H_2 and ethylene Faradaic efficiencies decrease with a reduction of temperature and the Faradaic efficiency of methane increases to 65 % from 5 % at 40 °C. The decrease of reaction temperatures would also affect the adsorption equilibria and CO_2 solubility, resulting in higher reaction rates.[39] If the CO_2 pressure has been increased, the CO_2 solubility can also be increased.[30]

Frese et al. reported that surface modification resulted in the improvement of Faradaic efficiency and overpotential of CO_2 reduction.[50] Deliberate oxidation of copper sheets was performed by thermal oxidation for different time periods. The Faradaic efficiency for methane formation decreased on a partially oxidised copper surface and further decreased with thicker oxidised films that were thermally treated for 72 h. In the electrolysis conditions used, copper oxide (Cu_2O or CuO) reduced in situ but this form of Cu was not ideal for methane formation.

Electrochemical reduction of CO_2 to methanol was shown on various intentionally oxidised Cu films, prepared by a range of methods. Oxidised Cu films on Ti substrate were found to give the highest current density for the formation of methanol, rationalised by the high surface area and dispersion of Cu_2O/Cu on Ti substrate. At heavily oxidised surfaces, very small amounts of methane and ethene were formed. This demonstrated that there is a weak binding of linear CO on Cu_m single crystals, whereas there is stronger binding of CO_2/CO molecules on Cu_2O and CuO compared to Cu_m.[51]

Following such reports, extensive work has been conducted on understanding the role of Cu (I) or Cu (II) species for the electrochemical reduction of CO_2. It is generally agreed that although long term stabilisation of CuO/Cu_2O is not feasible and the oxidised species would be reduced in situ to copper, the presence of the oxide layer is significant enough and present for a long enough time to see the change in product selectivity. Theoretical modelling work has shown that methane formation is favoured on fully metallic copper surfaces (Cu (111)), whereas methanol formation is favoured over fully oxidised Cu (Cu_2O) surfaces and partially oxidised Cu surfaces.[52]

Other influential factors affecting CO_2 electroreduction include the Cu metal overlayer. For example, the deposition of copper metal on Pt surface has been investigated, where it is thought that due to substrate metal and copper lattice misfit and strain, the binding energy of the products and intermediates from CO_2 reduction are altered. This was investigated by Reske et al. where Cu metal layers were deposited on Pt substrate. The HER reaction was significantly suppressed as well as the thickness of the copper layer was found to affect the product selectivity and distribution. The amount of methane and ethylene formed at the catalyst increased with increasing copper layers.[53]

The surface morphology of the Cu electrode has also been found to play a key role in the electroreduction of CO_2. The roughening of the electrode was found to improve the performance of the catalyst over smooth Cu foil type electrodes. The roughening of the electrode increases the availability of active sites for CO_2 reduction and HER. The presence of dendritic Cu has been shown to change the product selectivity compared to 3D and honeycomb type structures. Higher order hydrocarbons were formed on 3D structures and CO and methane was favourably formed on dendritic Cu.[54]

1.11.5.4 Nanostructured copper and copper oxide electrodes

Recently, nanostructured catalysts have been utilised for electroreduction of CO_2 due to their unique physical, chemical and electronic properties. Bulk polycrystalline copper is able to produce hydrocarbons and alcohols, however it can suffer from high overpotentials, low Faradaic efficiencies and poisoning issues, from adsorbed CO or the formation of graphitic carbon.[55] The use of nano copper is thought to overcome these challenges posed by bulk copper.

Cu nanoparticles, ranging in different sizes (2 to 15 nm), were compared for their activity. It was shown that the current density was increased significantly compared to bulk copper electrodes, however, the product selectivity was altered. Products such as methane and ethylene were suppressed and HER was significantly increased.[56]

However, in a similar size distribution electrocatalysis study conducted by Manthiram et al, the opposite trend was observed.[57] Small size (7 nm) copper nanoparticles on glassy carbon electrodes were used for electroreduction of CO_2. The selectivity for methane increased when compared to bulk foil electrodes and the current density was comparable to foil electrodes at low overpotentials. It was twice as high when more reducing overpotentials were applied. This clearly demonstrates the need for more than singular changes in reactor designs and highlights the key role the

electrolyte also plays in the electroreduction of CO_2. This is further supported by the studies conducted on Pt substrates, as mentioned in Section 1.11.5.3.

Different electrode preparation methods have also been explored, where a sputtered copper surface, copper nanoparticle covered surface and electropolished copper surface were compared by Tang et al. The nanoparticle covered surface and sputtered copper surface showed higher selectivity towards hydrocarbon, whereas the electropolished copper surface favoured H_2 formation.[58]

Electrochemically deposited copper nanofoams have also been investigated, which were synthesised at high negative potentials. Bubble formation from water splitting was the cause for the formation of porous copper electrodes, which significantly increased the Faradaic efficiency of HCOOH to 37 %.[59]

Recently, deposited copper oxide nanoparticles have also been explored. For example, as prepared Cu_2O particles were deposited on a carbon cloth electrode, and the predominant product was shown to be CH_3OH.[60] Ohya et al. explored composite electrodes of CuO-Zn by pressing Zn particles and CuO or Cu_2O powders together.[61] The composite used showed that some product control could be achieved by altering catalyst composite structure. The products obtained with the composite electrode included CH_4 and C_2H_4 with the composite electrode. Without copper oxide, the products were limited to CO and HCOOH.

Nanostructured copper/copper oxide electrodes with distinct morpoholgies have also recently been investigated. Work carried out by Li et al. involved preparation of 3 μm thick Cu_2O nanorods films on copper by electropolishing and subsequent annealing in air for varying periods of time.[62] The overpotential was significantly reduced for CO production, where a Faradaic efficiency of 45 % was achieved in the range –0.3 to –0.5 V vs. RHE and 33 % for HCOOH in the range –0.45 to –0.65 V vs. RHE. After electroreduction,

formation of smaller particles, roughly 20 nm in size, embedded in the rod structure was also observed. The change in catalyst morphology is an important parameter that needs to be assessed, especially when considering long term use of the catalyst. There is little evaluation of this in the literature with most catalysts that are tested for the conversion of CO_2.

CuO derived copper nanoflowers synthesised hydrothermally were also investigated. They exhibited a particularly high Faradaic efficiency for HCOOH of 40 % at onset potentials more positive than compared to bulk polycrystalline Cu electrodes, whilst also suppressing H_2 evolution. It was argued that the formation of amorphous carbon was key in the formation of CH_4 and C_2H_4 with this particular electrode system. The thickness of the carbon film was key where build-up of thick carbon film resulted in catalyst deactivation and the blocking of active sites.[63]

1.11.6 Limitations in the electrocatalytic reduction of CO_2

The advantages of CCU via electrocatalysis have been presented; however, some significant challenges remain to make this process industrially viable. One key challenge that remains is the energetic efficiency of the reaction. The energetic efficiency (EE) is a crucial parameter as it signifies the energy cost of obtaining the product. High EE is possible through high Faradaic efficiency for a specific product at low overpotentials. The overpotential is defined, as the potential difference between the thermodynamic and the applied potential. The Faradaic efficiency can be described as the selectivity of a particular product, based on how much charge is passed to obtain the product. Reasons for low energy efficiency are particularly high overpotentials or low selectivity, where energy is wasted on undesired products. The catalysts that are employed are not active enough and/or the final products (HCOOH, CH_3OH, CH_4 and CO) are usually produced as a mixture, which creates an additional step to the process. Ideally, catalysts with high selectivity for a specific product is required.

Another key factor to consider when ensuring that this process is industrially viable, is the stability of the catalyst over a significant period of time (excess of 100 hours). Other electrocatalytic processes such as chloro-alkali or water-splitting electrolysers and PEMFC show outstanding durability lifetimes as high as 40,000 h. In comparison, the CO_2 electroreduction process would require catalysts to have a stability target of 5000 h at least.[64] This is typically the least reported area in the literature, and when it is, the catalyst usually fails to remain stable over 100 hours. This may be due to poisoning effects from CO or the formation of carbon. Therefore, the stability of the catalyst remains a key obstacle to overcome.[64]

1.12 Nanomaterials as catalysts

Nanoparticles are defined as materials with at least one dimension between 1 and 100 nm ($1 – 100 \times 10^{-9}$ m). At such a scale, nanomaterials are known to display interesting optical, electronic and catalytic properties compared to their bulk counterparts (at a micro or macroscopic dimension). Nano materials have been used for centuries, however, in recent years, the area of nanomaterials has rapidly expanded. Nanomaterial metal oxides remain a key focus in novel functional and smart materials applications, due to their unique physical and chemical properties (increase in surface area to volume ratio, quantum confinement effects and changes in surface energy).[65] They are commonly used for a number of applications such as catalysis, gas sensing and energy storage.[66] The properties of nanomaterials are dependent on the size, shape, composition and structure, which may be controlled by the synthesis method employed. Quantum confinement and surface properties dictate the unique optical, electronic, mechanical and magnetic properties the materials possess. For example, bulk gold is chemically inert but nanosized gold is catalytically active for the oxidation of CO. Similarly, iron and cobalt oxide nanoparticles have been used in Fischer-Tropsch catalysis, where size effects have found to be crucial in stabilising and improving the catalytic process. Due to the high surface area of

nanomaterials, and therefore, access to available catalytic sites, they can act as excellent catalysts, in increasing the reaction rates compared to their bulk counterparts, which often show little or no catalytic activity. Specifically, nanomaterials are being used extensively in the energy sector, for fuel cells, hydrogen storage, batteries, thin films for electronics, lighting LED, sensors, and as catalysts for CO_2 capture and utilisation (Figure 1-6).

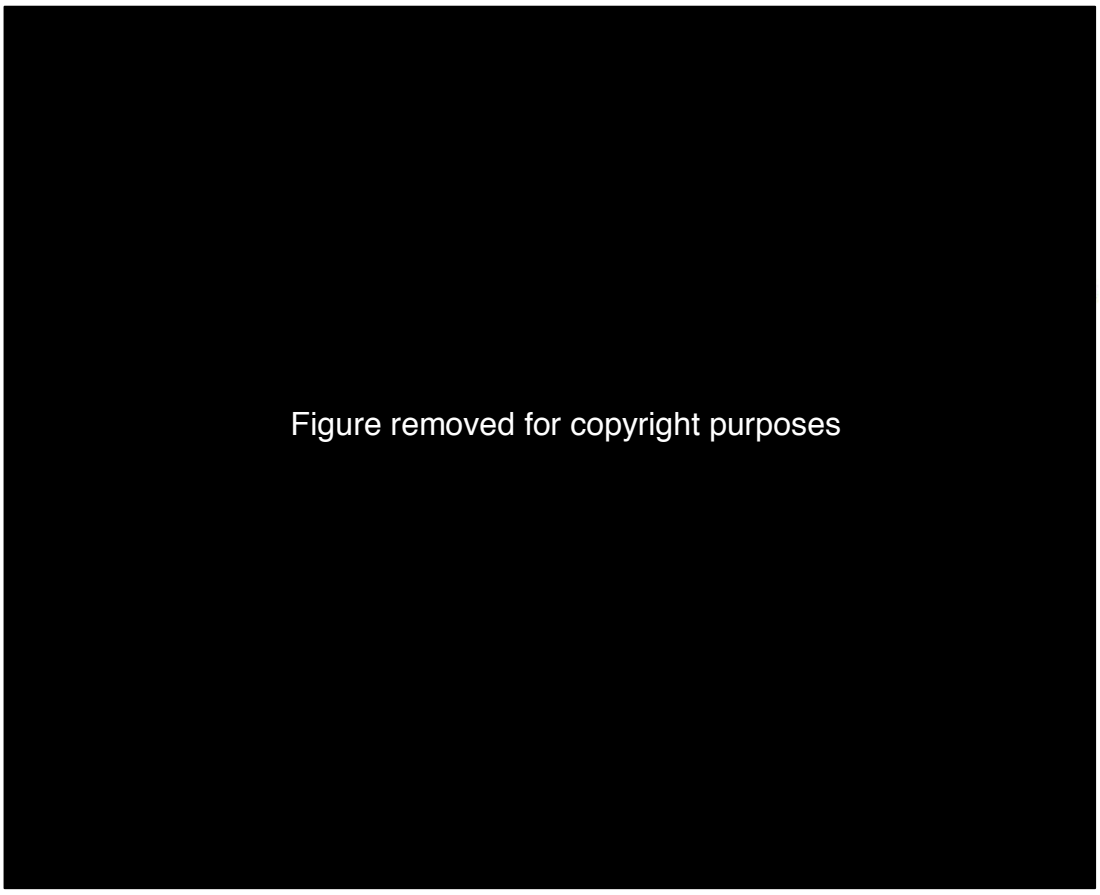

Figure 1-6 – Illustration of applications of nanomaterials in the energy sector. Adapted from reference M. H. Van de Voorde and H. Dosch, *Grand European initiative on nanoscience and nanotechnology using neutron and synchrotron radiation sources*, Max-Planck-Institut Fur Metallforschung, Stuttgart, 2009.[66]

As the properties of the nanoparticle are highly reliant on their size and shape, controlling the nucleation and growth is imperative in determining the crystal structure, shape, size and size distribution of the nanoparticles. The ability to control these aspects of nanoparticles properties is crucial in the success of industrial applications of nanotechnology as well as successful use of nanoparticles for specific applications, such as catalysis for CO_2

conversion. Therefore, in the following Section, the typical nanomaterial synthesis approaches are presented before discussing in detail the use of continuous hydrothermal flow techniques to synthesise nanoparticles.

1.12.1 Synthesis approaches

Top down synthesis involves the breaking down of an initial macroscopic structure by, grinding and milling, to obtain nanoparticles. Examples include ball milling,[67] lithography[68] and etching.[69] Top down methods are typically slow to use, difficult to scale up and more importantly, control of how nanostructures grow is inconsistent and difficult. Lithography based processes may introduce surface defects and imperfections during the processing, which can alter the surface chemistry and properties of the nanoparticles. Ball milling can produce particles with larger size and broad size distribution. Moreover, there is a significant issue of contamination during the process. Although, lithography is used in the manufacturing of circuits, quantum dots, and gratings, the use of top down methods is not as widespread as bottom up approaches.[67]

Bottom up synthesis method involves the building of nanoparticles from atoms and molecules. This approach directs the growth of nanoparticles in a more controlled manner, where a variety of reaction parameters can be used to control the nucleation and growth of nanoparticles. Precursors, used as the building blocks, may be delivered in a variety of forms (liquid, solid, gas) to form a range of nanostructures (nanorods, wires, spheres and cubes). Examples of bottom up approaches include chemical vapour deposition, flame-based synthesis or plasma synthesis. Liquid phase methods range from simple precipitation reactions to polyol synthesis and sol-gel synthesis. These methods allow for synthesis of nanoparticles with fewer defects, homogeneous chemical composition, and better control over size and shape.

The nucleation and growth of the nanoparticles plays a key role in determining the final crystal structure, size and shape of the particles. Therefore, it is important to firstly understand the theoretical mechanism of particle nucleation and growth in a bottom up approach. This will allow to fine tune the synthesis and reaction parameter to form nanoparticles with the desired physical and chemical properties. The following Section will discuss the mechanism of how nanoparticles form and grow.

1.12.2 Mechanism of nanoparticle formation and growth

The formation of nanoparticles can be divided into four key stages: i) precursor formation, ii) nucleation, iii) growth and iv) termination. The widely accepted La Mer model describes the classical nucleation and growth mechanism of nanoparticles and has been pictorially represented in Figure 1-7 below. This model also is the foundation of other mechanisms and has been extended.

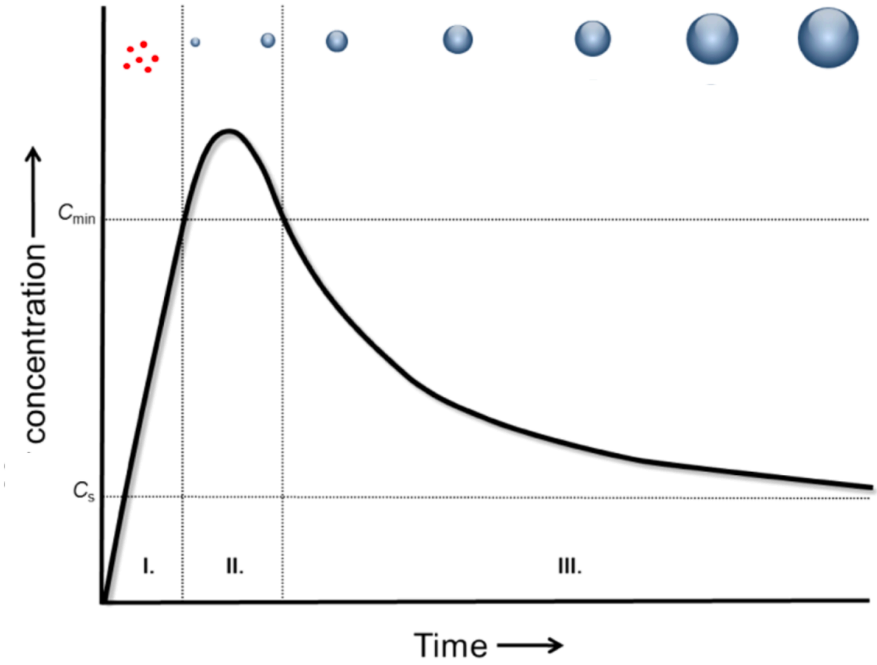

Figure 1-7 – Illustration of the widely accepted La Mer model of nucleation and growth of nanoparticles. Reproduced with permission under an ACS AuthorChoice License from reference E. C. Vreeland, J. Watt, G. B. Schober, B. G. Hance, M. J. Austin, A. D. Price, B. D. Fellows, T. C. Monson, N. S. Hudak, L. Maldonado-Camargo, A. C. Bohorquez, C. Rinaldi and D. L. Huber, *Chem. Mater.*, 2015, **27**, 6059–6066.[70]

The initial stage consists of the formation of zero-charge precursor molecules after the mixing of the reactants that react in acid-base type reactions (typically involving metal salt or alkoxides with an acid or base), denoted as I in the graph. As the concentration increases, a supersaturation condition is reached.[71] Supersaturation can be described as a point where there is more dissolved solute than that would be possible at equilibrium and is considered to be the driving force for nucleation or crystallisation (II in the graph).[72] As nucleation begins, the precursor molecules are consumed, which leads to a decline in the concentration of the precursor. Following nucleation, growth from solution may occur followed by some aging processes, leading to a termination point where the formation of nanoparticles has ceased (III in graph). Changing reaction parameter (temperature, pressure, pH, precursors) can allow control of the supersaturation, nucleation and growth of the particles, affording some control over nanoparticle synthesis.

The main stages of the formation of nanoparticles is discussed in more detail in the following Sections.

1.12.2.1 Nucleation

The formation of crystals in solution begins with nucleation, where small nuclei or molecular clusters form. The driving force of nucleation and growth is the supersaturation, which can be described by the chemical potentials of the chemicals in solution:

$$\Delta\mu = \mu_s - \mu_c \qquad \text{Equation 1.12}$$

Where, μ_s and μ_c are the chemical potential of a molecule in the solution and the bulk of the crystal phase, respectively. When the $\Delta\mu > 0$, the solution is supersaturated, which is when the nucleation and growth of nuclei will be possible. If $\Delta\mu = 0$ or < 0, then the nuclei will not be able to form. The driving force for nuclei formation may also be written as:

$$\Delta\mu = kT \ln S \qquad \text{Equation 1.13}$$

Where k is the Boltzmann distribution, T is the absolute temperature and the S is the supersaturation ratio, which can be defined in terms of the activity of the ions in solution:

$$S = a_1^{n1} a_2^{n2} \dots a_j^{nj} / a_{1e}^{n1} a_{2e}^{n2} \dots a_{je}^{nj} \qquad \text{Equation 1.14}$$

The work done to form a cluster can be described as follows:

$$W(n) = -n\Delta\mu + \varphi(n) \qquad \text{Equation 1.15}$$

Where φ (in Joules) describes the effective excess energy of the cluster. The chemical potential is derived from Equation 1.13. However, one of the most difficult problems with nucleation theory is the process of experimentally determining the excess energy of the cluster. The nucleation theorem, as described below, allows for the nucleus size, nucleus work and supersaturation to be related without considering the φ term and the type of nucleation (heterogeneous or homogeneous), shape of the cluster or the interface of the solid/liquid as the nuclei form in the solution.

$$dW^*/d\Delta\mu = -n^* \qquad \text{Equation 1.16}$$

The above equation can be related to supersaturation as follows:

$$dW^*/d(\ln S) = -n^* kT \qquad \text{Equation 1.17}$$

For the formation of a spherical cluster, with an assumption that the surface tension and the interface energy is isotropic, the process of nuclei formation can be summarised thermodynamically by considering the total free energy of the nanoparticle in solution. This is a sum of the surface free energy and the bulk free energy:

$$\Delta G = -\frac{4}{3}\pi r^3 \Delta G_v + 4\pi r^2 \gamma$$ Equation 1.18

Differentiating the above equation results in the critical free energy term and critical radius term and can be represented graphically in Figure 1-8. The graph shows the maximum free energy the nucleus will pass through to form a stable nucleus. The critical radius, r_c, can be described as the minimum nucleus size that is possible without re-dissolving. If the radius of the cluster is below r_c ($r < r_c$) then the nuclei will redissolve and if the radius of the cluster is larger than r_c ($r > r_c$) then the particles will begin to grow.

$$r_c = -\frac{2\gamma}{\Delta G_v} \qquad \Delta G^* = \frac{4}{3}\pi\gamma r^{2*}$$ Equation 1.19

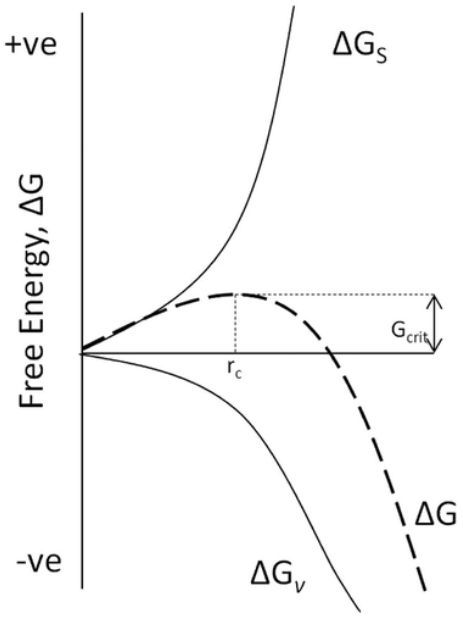

Figure 1-8 – Illustration of the critical free energy and the critical radius term. Reproduced with permission under an ACS AuthorChoice License from reference N. T. K. Thanh, N. Maclean and S. Mahiddine, *Chem. Rev.*, 2014, **114**, 7610–7630.[73]

1.12.2.2 Growth

As the precursor concentration decreases below the nucleation threshold (Figure 1-8), the growth of the nuclei begins. The growth is dependent on the available nuclei and the precursor concentration, so the growth of the particles can be controlled by tuning the supersaturation and other reaction

parameters. The growth stage can occur via two different pathways i) diffusion limited or ii) reaction limited pathway. If the growth rate is fast, then growth will occur via a diffusion limited pathway. However, if the transfer of reagent to the nuclei is slow, then growth will occur via a reaction limited pathway. The role of concentration gradient and temperature becomes crucial when considering the rate at which the growth will occur and what path might be taken. The growth rate in a diffusion limited pathway can be described as:

$$\frac{dr}{dt} = \frac{Dv}{r}(C_b - C_s) \qquad \text{Equation 1.20}$$

Here, r is the radius of the particle, D is the diffusion coefficient, v is the molar volume, C_b is the concentration of the reagent and C_s is the solubility of the solid. This equation shows that the growth rate is faster for smaller particles. The opposite is true for reaction limited growth where the rate of growth is favoured for larger particles and determined by the rate of the surface reaction.

Following nucleation and growth processes, some coarsening or Ostwald ripening may occur. This is a phenomenon where smaller nanoparticles dissolve and redeposit on larger particles, which is thermodynamically more favourable as this reduces the surface energy. Small particles are more susceptible to dissolving, as they have a greater solubility than larger particles. This has been described in the Gibbs-Thomson equation, where the solubility C is given as a function of r:

$$C_r = C_b \exp\left(\frac{2\gamma v}{r k_B T}\right) \qquad \text{Equation 1.21}$$

Coalescence and orientated attachment are other examples of particle growth mechanisms where the two particles get attached to each other. Coalescence is the random attachments of particles where

crystallographically, there is a mismatch of lattice planes. Oriented attachment, however, occurs where there is a perfect match of particles with the same lattice plane.

Termination of the nanoparticle nucleation and growth occurs as the reactants are consumed and where the nanoparticle has adopted the most stable conformation possible. This in turn minimises the surface energy. Two approaches are typically used to stabilise nanoparticles: i) steric hindrance caused by capping agents (organic, polymers, surfactants) or ii) by electrostatic repulsion from charged species adsorbed onto the nanoparticle surface.

This Section covered the nucleation and growth mechanism of nanoparticles. The nucleation and growth are controlled by the specific synthesis method that is employed. Temperature, changes in the surface energy and precursor concentration can alter the nucleation and growth parameters. The typical bottom up methods used in the literature are covered in the following Section.

1.13 Synthesis methods for nanoparticles

This Section describes the typical synthesis methods adopted in the literature for the synthesis of copper-based materials. The focus remains on copper-based materials as they are frequently identified as an excellent catalyst for CO_2 conversion to fuels.

1.13.1 Synthesis of copper-based nanomaterials

Copper-based nanomaterials have been investigated extensively for a range of applications (Figure 1-9), especially due to copper's high natural abundance, low cost as well as relatively straightforward and simple preparation methods. This Section will briefly discuss typical bottom up

synthesis methods used in the literature. Top down methods have been used but due to the advantages of bottom up approaches, as well as their relevance to this thesis, examples of top down methods are not discussed further.

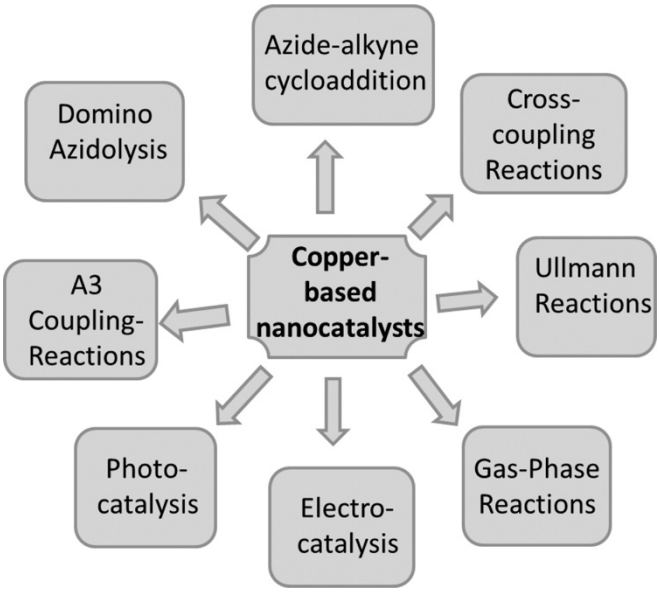

Figure 1-9 – General applications of Cu based nanocatalysts. Reproduced with permission under an ACS AuthorChoice License from reference M. B. Gawande, A. Goswami, F.-X. Felpin, T. Asefa, X. Huang, R. Silva, X. Zou, R. Zboril and R. S. Varma, *Chem. Rev.*, 2016, **116**, 3722–3811.[74]

Copper oxide, CuO, a *p*-type semiconductor with a narrow band gap, 1.2 to 1.5 eV, has been extensively researched for its catalytic, optical, electrical and thermal properties with applications in lithium ion batteries as anode materials,[75] catalysis for the reduction of CO_2,[76] gas sensing either reducing gases such as NH_3 and oxidising gases such as NO_2,[77] and use as a supercapacitor.[78] A number of methods have been explored to synthesise CuO, including decomposition of copper substrates, solid-state synthesis,[79] sol-gel[80] and simple chemical precipitation method[81] and electrochemical routes.[82] Hydrothermally CuO has been extensively synthesised in batch processes. The effect of temperature, in the range 100 to 300 °C, has been explored.[83] 200 °C was found to be the optimum temperature as CuO was formed, as at 100 °C $Cu(OH)_2$ was still present as an impurity and at 300 °C copper was formed. Different precursors have also been investigated. Copper

acetylacetonate and $Cu(NO_3)_2$ were tested at different concentrations at 180 °C.[84] The size of CuO nanoparticles was reported to increase with the concentration of the metal salt. Similar work with copper nitrate salt at different concentrations and a range of temperatures, 350 to 500 °C, indicated the reaction time was an important feature. Shorter reaction time lead to $Cu(OH)_3NO_3$ impurities.[85] Shape control has also been achieved with varying temperatures, without the addition of any surfactants.[86]

Cu_2O is also a *p*-type semiconductor with a direct band gap of 2.17 eV.[87] A number of methods have been used to synthesise Cu_2O. It typically requires higher temperatures or higher concentration of reducing agents. Morphological control was explored, by tuning the length of the cube depending on the addition of NaOH to ascorbic acid and copper acetate solutions at room temperature.[88] Reverse micelle microemulsion has been explored as well where $CuCl_2$ is used as the copper precursor along with n-heptane and a non-ionic surfactant to form the microemulsion.[89] Sodium borohydride is used as reducing agent and acetone is used to break the micelles to begin precipitation. Hydrazine has also been used as a reducing agent with PEG acting as a capping agent to form nano-whiskers.[90]

1.13.2 Nanomaterial synthesis in water

As more emphasis is placed on sustainability of chemical processes, the environmental and health impact of using organic solvents becomes a significant cause for concern, especially considering the loss of solvents to rivers, oceans and soil. Solvent usage is a key part of manufacturing process and nanomaterial synthesis, whether it is at lab scale or in an industrial process. With a strong drive towards greener solvent usage, various clean solvents have been evaluated. An ideal green solvent should be cheap, non-toxic, and readily available. It should also aid in the specific reaction it is used in and be recyclable. Water is the only known naturally abundantly available

solvent, which is also environmentally benign and inexpensive and fulfils this criteria.[91]

Water is commonly considered as the universal solvent as it is able to dissolve a number of substances, not usually possible with many other solvents. Its polar nature (due to the electronegativity of the oxygen) and the ability to form H-bonds allows for ionic compounds to dissolve easily due to ion solvation, complexation and hydration of the ion. Some challenges with water usage as a solvent remain; many organic compounds are insoluble in water and even with purification small impurities remain; new ultra-purification technologies are needed to resolve these issues.

1.13.2.1 Supercritical water as a solvent

Supercritical fluid technology has been proposed to solve many environmental problems in nanomaterials synthesis with respect to the principles of the green chemistry. Supercritical fluids exhibit interesting properties, which allow the reaction environment, like density, viscosity, diffusivity and surface tension, to be controlled by changing the temperature and pressure.[92] Supercritical fluids such as CO_2, water and methanol have been used for numerous applications and are not limited to nanomaterial synthesis. For example, supercritical water has been used in applications such as treatment of hazardous water, non-catalytic chemical reactions as well as a medium for nanoparticle synthesis.[93]

From the phase diagram of water, the critical point can be observed at Tc = 373.95 °C and Pc = 22.06 MPa, denoted as B, in Figure 1-10. Below this point, the vapour pressure curve separates the gaseous and liquid phases. At the critical point, the properties of both phases become increasingly similar and above the critical point, the properties of water change dramatically, and the density of supercritical water can be altered between liquid and gas phase in a continuous manner.

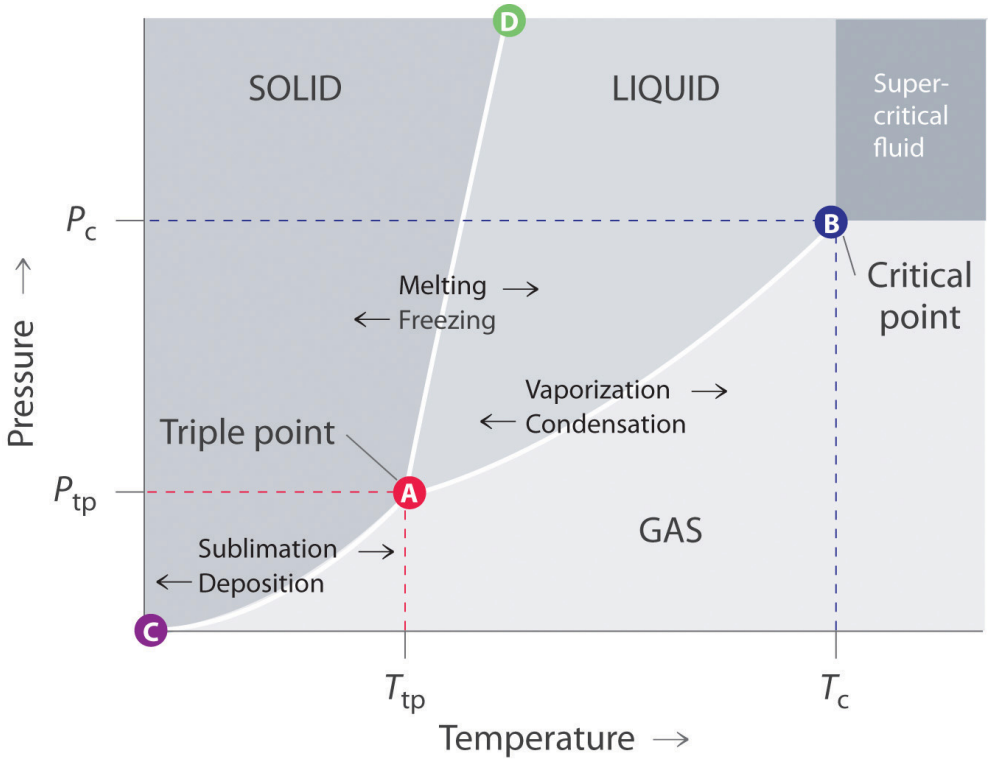

Figure 1-10 – Illustration of the water phase diagram, showing the triple point and the critical point. Reproduced with permission under a creative commons licence (CC BY-NC-SA 3.0 US) from reference D. Larsen, 'Phase Diagrams' Chem Wiki: The Dynamic Chemistry Textbook.[94]

This phenomenon may be observed in a high-pressure view cell, as shown in Figure 1-11. As the temperature and pressure is increased from figures a) to d), the density of the liquid decreases and the density of the vapour increases, the meniscus or the phase boundary begins to disappear and at the critical point, it disappears altogether leading to a homogeneous phase.[95]

Figure removed for copyright purposes

Figure 1-11 – Images showing the phase boundary change as temperature and pressure is increased (a – d), where the liquid and gaseous phase boundary disappears at the critical temperature and pressure.

As a consequence of the elevation of the temperature and pressure of water, the density of water changes dramatically. At ambient conditions, the density is 1000 kg m^{-3} and it decreases to 322 kg m^{-3} at the critical or supercritical point (Figure 1-12). With the rapid change of density beyond the critical point, the solubility of a substance can be altered, since solubility and density are related.[96] This occurs as the hydrogen bond network breaks down and results in polar inorganic salts becoming significantly insoluble whilst polar organic solvents become soluble in supercritical water.

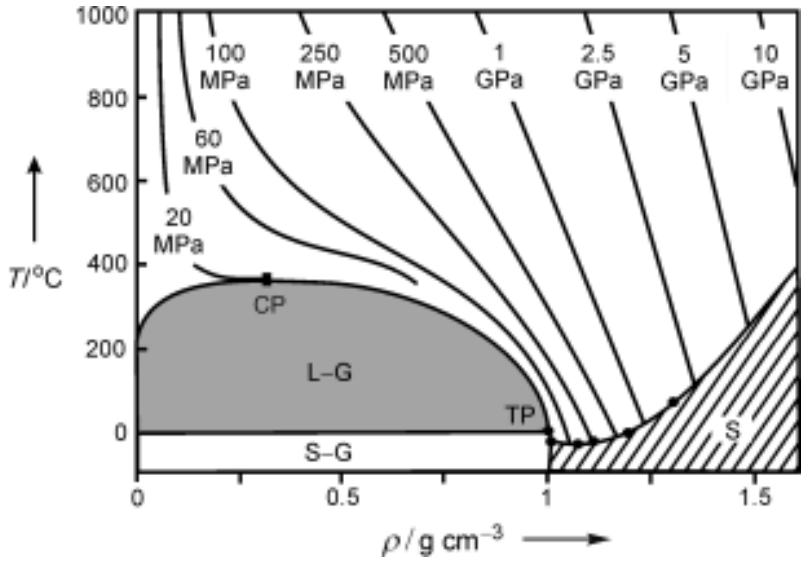

Figure 1-12 – Variation of the density of water as the temperature and pressure increases. Reproduced with permission from reference H. Weingärtner and E. U. Franck, *Angew. Chemie - Int. Ed.*, 2005, **44**, 2672–2692.[95]

Similarly, the dielectric constant changes significantly with elevated temperatures and pressures; the dielectric constant decreases from 80 (ambient) to 33 (at 185 °C) to around 5 at the critical temperature (Tc = 373.95 °C) as seen from the saturation curve (Figure 1-13). This is partially due to extensive degradation of hydrogen bonding at supercritical temperatures and pressures. In such conditions, organic, non-polar solvents are soluble in water whereas inorganic salts are highly insoluble, leading to their rapid precipitation.

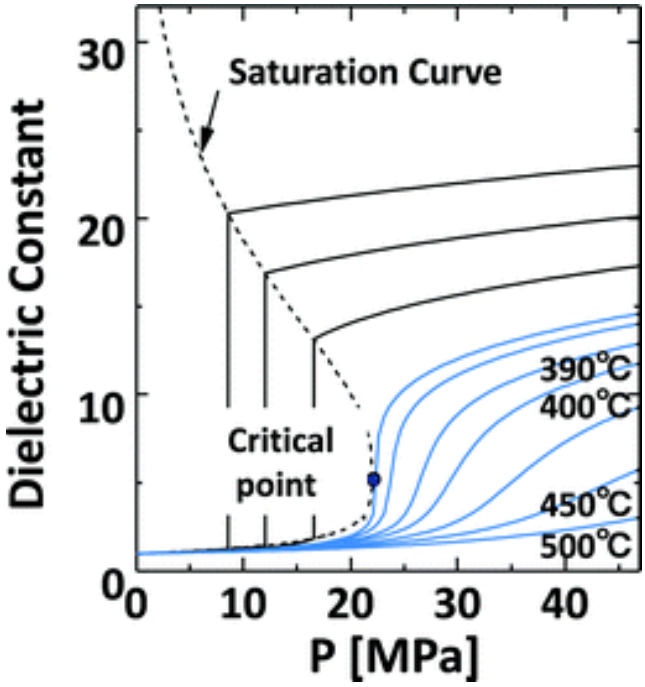

Figure 1-13 – Variation in the dielectric constant as temperature and pressure change, showing the dielectric constant at the critical point. Reproduced with permission from reference G. Brunner, *Annu. Rev. Chem. Biomol. Eng.*, 2010, **1**, 321–342.[97]

Another property that is changed dramatically is the equilibrium constant of water, K_w, which can be defined as:

$$K_w = [H^+][^-OH] \qquad \text{Equation 1.22}$$

At supercritical conditions, the concentrations of H^+ and ^-OH increases as the equilibrium constant increases compared to the ambient conditions. The K_w at ambient conditions is ca. 10^{-14} mol^2 dm^{-3}, which rises to a maximum of 10^{-11} mol^2 dm^{-6} at 350 °C (Figure 1-14). Above the critical point, the ion product varies significantly (10^{-11} and 10^{-20} mol^2 dm^{-6}) depending on the temperature and pressure. This means that at these temperature and pressures, the concentration of H^+ and OH^- increases significantly creating a very hydrolysing environment for metal salts.

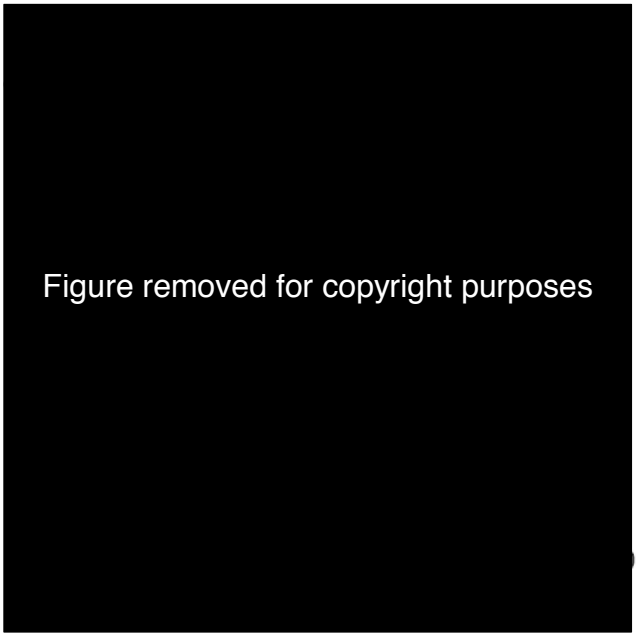

Figure 1-14 – Graph of the equilibrium constant variation with temperature. Obtained from reference J. W. Tester and J. Cline, *Corrosion*, 1999, **55**, 1088–1100[98].

Significant changes to the anions and cations of metal salts take place in critical conditions. In ambient conditions, the cation is surrounded by water molecules in the first solvation shell with little presence of the anion. However, near the critical point, cations can become surrounded by the anions instead. Subsequently, solvation shells are disrupted, whereby, acids become much weaker under supercritical conditions. As an example, Ni^{+2}, ($NiBr_{2(aq)}$) is surrounded by six water molecules in ambient conditions, which are replaced by four anions in supercritical conditions.[99]

The combination of such unique properties of supercritical water mean that when metal salts are suddenly mixed with supercritical water, the metal salt is rapidly hydrolysed to metal hydroxides and subsequently dehydrated to metal oxide nanoparticles. Rapid nucleation of nanoparticles in this medium, yields well defined nanoparticles with a relatively narrow size distribution. As discussed in Section 1.12.2, the key to nanoparticle synthesis is the supersaturation, which increases the nucleation rate. Use of supercritical water in an engineered reactor allows for the synthesis of small size

nanoparticles. The following Section will discuss the practical application of supercritical water to synthesise nanoparticles.

1.14 Hydrothermal Synthesis

The word 'hydrothermal' has its origins in geology, but in materials chemistry it can be defined as a heterogeneous reaction in the presence of aqueous solvents under elevated temperatures and pressures to dissolve and precipitate particles that would otherwise not be able to nucleate at ambient conditions.[100] Hydrothermal synthesis methods may be advantageous over conventional synthesis methods due to its 'green' nature, as it uses water, as opposed to organic solvents (which are expensive, toxic and environmentally unfriendly). It also allows for high diffusivity in a solution media in a closed system. This is also advantageous for producing particles with high crystallinity, uniformity, homogeneity as well as a narrow size distribution with a controlled morphology. Generally, hydrothermal synthesis is undertaken in batch reactors, in stainless steel autoclaves. The reactants are premixed, placed in the autoclave and the reactor is heated to the desired temperature, for a number of hours or days. There are inherent issues with batch process such as batch-to-batch variations, being a slow process (hours to day timescales), difficult to scale up and there is poor control of parameters. Continuous flow methods can overcome such issues and with this in mind, continuous hydrothermal flow synthesis (CHFS) was developed. The Section below discusses this process and its evolution to the current stage.

1.14.1 Continuous Hydrothermal Flow Synthesis

Initially developed by Arai et al. in the early 1990s in Japan, this process involved a feed of supercritical water that met with a feed of metal salt (and auxiliary reagents) in an engineered mixer. The mixing results in the formation of metal oxides in a continuous manner. A number of other groups have adopted this technology and engineered different variations of the

CHFS system from the original design by altering a range of different parameters.

This Section will review the brief history of initial CHFS systems, specifically mixer designs and the development of the patented mixer at the Clean Materials Technology Group (CMTG) at UCL.

Hydrothermal synthesis occurs via a hydrolysis and dehydration reaction of metal salt precursors via the following reactions. An example is shown with metal nitrate ions.

$$M(NO_3)_{x(aq)} + xH_2O \rightarrow M(OH)_{x(s)} + xHNO_3 \qquad \text{Equation 1.23}$$

$$M(OH)_{x(s)} \rightarrow MO_{(\frac{x}{2})(s)} + \frac{x}{2}H_2O \qquad \text{Equation 1.24}$$

Initial reactor design developed by the Adschiri and Arai group, included passing the water feed through a heater (465 °C), which met with a cold feed of metal salt at the mixing point (Figure 1-15). The mixture was then fed through a heated reactor (763 K) and cooled. The pressure was maintained between 30 and 35 MPa.[101] Another CHFS type system developed in USA, used a single heated tube (in a furnace) to feed metal salt solution through. Due to the nature of this simple process, a quench was used to hinder the growth of the rapidly nucleating particles. Despite this simple design, the inflexibility of this process meant other designs were more favoured.

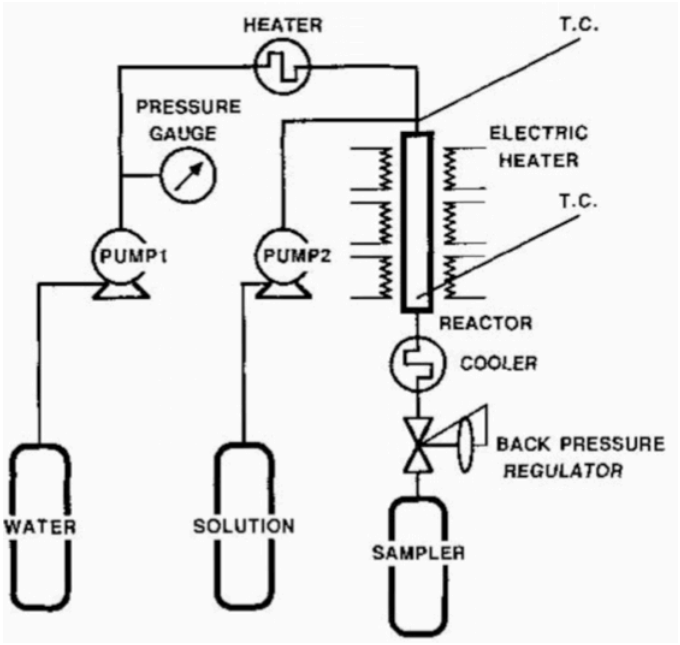

Figure 1-15 – Initial design of the Continuous Hydrothermal Flow Synthesis (CHFS) developed by Adschiri and Arai. Reproduced with permission obtained from reference T. Adschiri, K. Kanazawa and K. Arai, *J. Am. Ceram. Soc.*, 1992, **75**, 1019–1022.[101]

Since then, a number of design modifications to the original Adschri reactor design, have been employed by the group of Adschiri and other groups around the world.[102] Additional pumps were added and the reactor configurations were altered. The new design included a change that meant the metal salt and base feeds met in a tee piece before mixing with supercritical water. This was created to prevent undesirable precipitation of metal hydroxides or oxides upon mixing of metal salt and base reactants before pumping. The addition of mineralisers such as base was found to be crucial for nanoparticles precipitation.

The widely-adopted design uses an engineered mixer to control precipitation of metal ions, therefore, much emphasis has been given to studying and improving its design to further control how nanoparticles nucleate and grow. A number of different materials have been synthesised by using the CHFS processes, such as Fe_3O_4, CuO, NiO, ZrO_2, ZnO, Co_3O_4, CeO_2, AlO(OH). The Section below briefly discusses some prominent designs and their benefits and limitations.

1.14.1.1 Mixing point designs

The design criteria for an ideal mixer have been highlighted by Lester et al., based on Computational Fluid Dynamics (CFD) modelling; the optimisation of the reactor design relies on the density difference of two fluids mixing. The authors stated that ideal mixing should involve:[103]

1. 'Instantaneous and uniform mixing' of the two fluids to produce small nuclei.
2. Short residence times to minimise growth of the nanoparticles.
3. Little to no pre-heating of the metal salt solutions to avoid precipitation of metal salts prior to meeting the supercritical water feed.
4. Strong eddies for the transport of precipitated particles – to avoid accumulation of any particles in the reactor, which could lead to blockages or particle growth.

Ideal mixing regimes would involve homogeneous mixing of both the supercritical and metal salt feeds. Poor mixing can lead to local hotspots, which would affect supersaturation and therefore size and size distribution of particles. A good mixing regime allows for the rapid nucleation of nanoparticles but also prevents occurrences of blockages, which would lead to reactor downtime. Several different designs have been evaluated in the literature, such as, tee-mixers, swirling mixers, counter current and co-current mixers. In order to understand the mixer designs, it is imperative to understand reaction parameters, which would affect mixing regimes such as, flow rates, temperatures and buoyancy.

An important parameter that is often discussed when comparing mixing point designs is the Reynold's number, R_e. This can be evaluated to:

$$R_e = \frac{\rho v d}{\mu}$$ Equation 1.25

Where ρ = density of the fluid, v = mean velocity, d = inner diameter of the pipe and μ = viscosity of the fluid. This parameter describes the flow of the fluid, whether it is ordered or not. This can be defined into three fluid movement regions. Laminar flow occurs when R_e is < 2000 and turbulent flow occurs when R_e is > 4000. The region in between, 2000 < R_e < 4000, can be defined as transitional. As R_e is dependent on pipe diameter, density and viscosity, the flow regime can be altered by changing the pipe size, temperature and flow rates. Figure 1-16 represents the natural flow of the fluid.

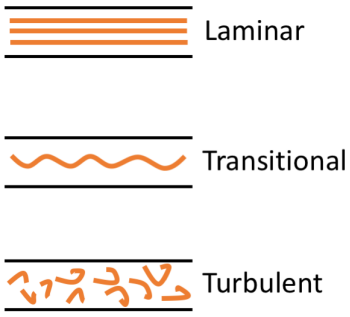

Figure 1-16 – Schematic of the mixing regimes which describes the flow of fluid in a pipe, showing laminar, turbulent and transitional flow.

To evaluate and optimise good mixing of supercritical water and precursors, tee mixers with different internal diameter pipe sizes, flow rates and concentration have been investigated by Kawasaki et al, using NiO as a test sample. The mixing direction of each fluid was also altered. It was reported that inner diameter of the pipe sizes made a significant difference in decreasing the NiO particles size and with increasing flow rate. However, not much difference was observed when introducing the individual feeds from different directions.[104]

Tee-mixers are widely used but they can suffer from a number of issues. They are particularly prone to blockage issues, inhomogeneous back mixing and the presence of stagnant zones.[104] Due to such mixing regimes, the particles are likely to have a wide particle distribution as differing reaction environments are present.[103] Tee-mixers were compared with swirling mixer

designs, with the latter resulting in better mixing regimes with smaller particle size than tee mixers. This was due to considerably higher Reynold's numbers and faster heating rates. Supercritical water was fed through at an angle of 60° and met the precursor feed from both sides, resulting in a swirling supercritical water feed.[105] However, such designs cannot be made with off the shelf parts and instead require custom made parts (Figure 1-17).

Figure 1-17 – Schematic design of the swirling mixer developed by Kawasaki et al. Image obtained from reference S. ichiro Kawasaki, K. Sue, R. Ookawara, Y. Wakashima and A. Suzuki, *J. Oleo Sci.*, 2010, **59**, 557–562.[105]

Recently, central collision type mixers have also been developed to avoid heterogeneous nucleation of metal oxides on the walls of reactor pipes as well as homogeneous nucleation, which leads to wider size distributions (Figure 1-18). Fe_2O_3 was used as a model reaction by Sue et al.; here the supercritical water was split before entering the central collision mixer. The precursor met the supercritical water from a horizontal axis as they travelled downstream to avoid contact with any inner walls during nucleation.[106]

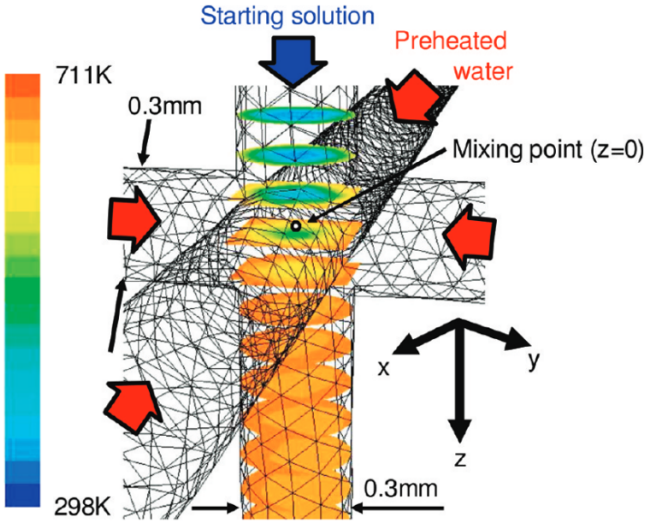

Figure 1-18 – Example of a central collision type mixer. Reproduced with permission from reference K. Sue, T. Sato, S. Kawasaki, Y. Takebayashi, S. Yoda, T. Furuya and T. Hiaki, *Ind. Eng. Chem. Res.*, 2010, **49**, 8841–8846[106].

To overcome issues with tee-mixers, Lester et al. developed a counter current mixer, where opposing flows of supercritical water and precursor feed met. It was argued by the authors that the buoyancy driven mixing of the supercritical water and cold precursor led to a naturally turbulent flow, arising from the density difference of the two solutions. This was previously hampered by the tee-mixer, as it was inefficient at tolerating such mixing regimes.

A pipe in pipe arrangement was used, where the supercritical water was fed downstream through a nozzle type pipe and the metal salt fed through counter current, upwards towards the water (Figure 1-19). The authors argued, based on CFD modelling, that instantaneous and uniform mixing took place in this reactor and the eddies that formed due to the mixing were fed downstream to the outlet.[103]

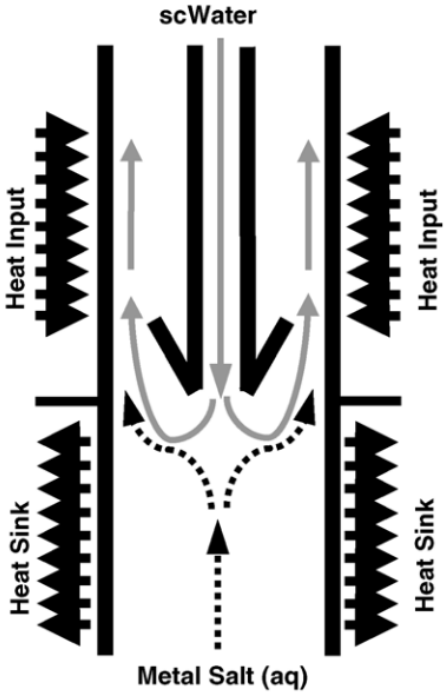

Figure 1-19 – Counter current mixer developed by Lester et al. for homogeneous and uniform mixing to maximise supersaturation. Reproduced with permission from reference E. Lester, P. Blood, J. Denyer, D. Giddings, B. Azzopardi and M. Poliakoff, *J. Supercrit. Fluids*, 2006, **37**, 209–214[103].

Recent studies conducted by Tighe et al. to gain deeper understanding of counter current mixer found supercritical water penetrated the metal salt feeds, which led to pre-heating of metal salt solutions and this is undesirable for the controlled synthesis of nanoparticles.[107] The temperature of the supercritical water was also found to be cooler than expected when it met with the metal salt. To overcome these challenges with counter-current mixers, a new type of mixer was developed at UCL by Gruar et al., called a co-current mixer (confined jet mixer (CJM)).[108,109] Here, the supercritical water and cold temperature precursor met in a co-axial arrangement (Figure 1-20). The mixer involved a pipe in pipe configuration, where the inlet of the supercritical water flow was confined within the exit of the outlet pipe. This was found to be an important placement to avoid blockages within the mixer and also promote uniform and homogeneous mixing of the two feeds.[109,110]

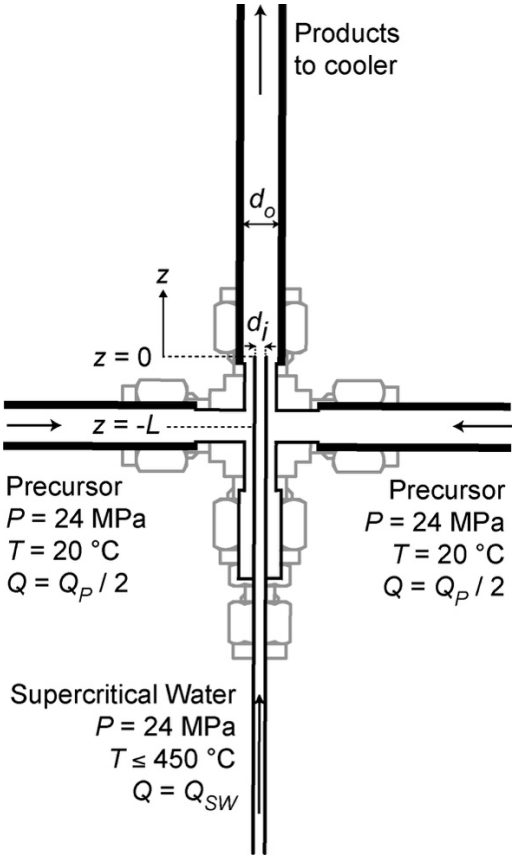

Figure 1-20 – Co-current mixer developed by Gruar et al. to overcome mixing issues from the counter current mixer. Reproduced with permission from reference R. I. Gruar, C. J. Tighe and J. A. Darr, *Ind. Eng. Chem. Res.*, 2013, **52**, 5270–5281[109].

The mixer was shown to be effective in synthesising ZnO at both lab scale and pilot scale. Despite an increase in pipe sizes, the particles were found to be similar at both scales and could be successfully operated for extended durations. The in-situ temperature measurements showed instantaneous mixing at the mixing point (exit of the inner pipe).

A modification of this mixer was also investigated by Gruar et al. to functionalise the surface of nanoparticles. In numerous applications, nanoparticles are used as dispersions. Surface functionalisation is the most common route for dispersions and can be conducted by using surface agents; either through steric hindrance or electrostatic repulsion. Gruar et al. reported the synthesis and functionalisation of iron oxides by using a co-current mixer (CJM) to synthesise iron oxides. A counter current mixer upstream of the CJM was used to introduce the capping agent feed (citric

acid) to the nascent nanoparticle stream. The turbulent mixing of the capping agent and nanoparticle stream was cited as the reason for stable dispersion of iron oxides.[111]

1.15 Thesis outline and hypotheses

This chapter highlighted the current status of the CO_2 problem and possible mitigation solutions, with a particular emphasis on the electrochemical reduction of carbon dioxide. The status of this method was also discussed in detail, with attention paid to the types of catalysts previously used in the literature. The synthesis of nanomaterials, particularly, copper-based systems was presented, and the mechanism of nanoparticle growth was discussed in detail. The benefits of using a continuous hydrothermal flow technique was also presented and the evolution of this technique was briefly discussed.

The overall hypothesis of this thesis is whether the controlled synthesis of ultra-fine copper-based nanoparticles using a continuous hydrothermal flow process can be used to enhance the electrochemical performance of CO_2 reduction. CHFS can be used to generate large sample numbers and therefore a secondary hypothesis is whether a high-throughput electrochemical testing system may be devised through a Rotating Ring Disk Electrode system. Thus, the main objectives of this thesis are as follows:

1. Synthesis of copper-based systems - To use CHFS as a method to control the size and shape of CuO nanoparticles. To investigate how experimental parameters can affect the nanocatalyst properties. How the mixer design can affect the properties exhibited by CuO nanoparticles? Is it possible to synthesise Cu_2O and Cu nanoparticles in flow, using the CHFS reactor at UCL?
2. Understanding the role of ionomers in the electrochemical reduction of CO_2 – Ionomers, particularly Nafion, are commonly used in catalyst

inks but the effect of an ionomer is not well known. How do they affect the electrochemical reduction of CO_2? Is there an optimum ionomer content that should be considered? Can the catalyst ink and its processing be optimised to obtain favourable electrochemical activity, in terms of reducing the overpotential and/or increasing the Faradaic efficiency?

3. Synthesis of doped CuO and its effect on CO_2 electroreduction – Can CHFS be used to synthesise doped CuO, with transition metals such as Ni? If the synthesis of Ni doped CuO is possible, how does this compare to Ni doped CuO previously synthesised in the literature? What is the limit of Ni inclusion within the CuO host structure? Moreover, how does this affect the electrocatalytic behaviour? Is it possible to improve the Faradaic efficiency, change the product selectivity and reduce the overpotential required to drive CO_2 conversion?
4. Products such as, CH_4, CH_3OH, CO, HCOO, derived from CO_2 reduction are usually detected and quantified by ex-situ analytical techniques such as gas chromatography, ^1H NMR, HPLC and mass spectrometry. Is it possible to use the catalysts developed via CHFS for in situ product detection via a rotating ring disk electrode? Can mass transport issues related to CO_2 solubility be overcome by using a rotating electrode? Can this method be used as a future high throughput screening technique for catalysts developed at scale via CHFS?

In summary, this thesis will investigate the synthesis of copper-based systems via continuous hydrothermal flow synthesis for the electrochemical reduction of carbon dioxide to products such as HCOOH, CO, CH_3OH and CH_4. The materials will be characterised by a range of structural techniques such as PXRD, TEM, SEM, XPS and developed into inks to be used as electrocatalysts. The electrochemical activity will be evaluated by a range of

electrochemical techniques such as cyclic voltammetry, constant potential electrolysis, electrochemical impedance spectroscopy as well as post catalysis structural characterisation. It is anticipated that the use of ultra-fine copper-based catalysts developed via CHFS will be able to improve the Faradaic efficiency and the overpotential of the electrochemical reduction of CO_2 and aid the development of a solution to the CO_2 problem.

Chapter 2. Experimental Methods

2.1 Introduction

This chapter discusses the methodology and experimental techniques used in this thesis. Continuous Hydrothermal Flow Synthesis (CHFS) process is described initially, including an overview of the process and the mixer types used. Following this, sample processing and the structural characterisation techniques for nanopowders used in the thesis are described. Ink formulation methodology and common electrochemical techniques used for the electrochemical reduction of CO_2 is also presented. A general overview of each technique is given; however, each chapter will also include a description of specific material synthesis and electrochemical testing as necessary.

2.2 Continuous Hydrothermal Flow Synthesis

Prof. Jawwad Darr (JD) initially developed the continuous hydrothermal flow synthesis process at Nottingham with Dr Paul Hamley and further improved the design with Dr Paul Boldrin at Queen's Mary University (QMUL),[112] which was further modified and developed by Drs. Rob Gruar (RG), Neel Makwana, Chris Tighe (CT) and Clément Denis at University College London.[107–109,113–115] This included the development of a lab scale plant (by JD, CT and RG) for high throughput production of nanomaterials at a kg day^{-1} rate and a pilot plant to produce nanomaterials at a kg h^{-1} rate. This section details which CHFS configurations were used for the production of nanomaterials for the electroreduction of CO_2.

2.2.1 Lab scale CHFS reactor

For the production of nanocatalysts for the electrochemical reduction (ECR) of CO_2, the lab scale reactor was used for the entirety of this thesis. This was developed and modified from an older version, initially developed at QMUL, to increase the output of the nanomaterials produced by using pumps that would allow the flow of higher volumes, using Swagelok™ stainless pipes and mixers with larger diameters.

The process typically uses three to four pumps, depending on the configuration used (discussed further in Section 2.2.2). Each pump (Milton Roy model PrimeRoyal K) is configured to allow an independent feed of either deionised (D.I.) water, metal salt precursors or chemical additives to feed into the mixing point. Due to the independent nature of each pump, this allowed each feed to be modified (concentration, flow rates, precursors) independently of each other, allowing the high throughput production of nanomaterials with different reaction conditions at kg day^{-1} rate. The CHFS set up is shown in Figure 2-1.

Each pump was connected to a 100 L water tank as a supply of D.I. water, which could be used as a feed at various stages. The pumps feeding precursors into the reactor were also supplied with a 1 L conical flask, which were connected to the pumps with 1/2" tubing. Each feed line was then connected to a pressure relief valve (PRV) (Parker HPRV, Buckinghamshire, UK), pressure gauge and a non-return assembly prior to being fed in to the reactor system. The PRVs (set at 276 bar) were present to ensure the system pressure did not exceed this limit, in case of any blockages caused by production of nanomaterials. Pressure gauges were used to monitor the pressure throughout the experimental run. The non-return valve assembly was used to prevent the back flow of any precursor or nanomaterials, in case of pump failures.

Pump 1 was used to feed D.I. water only (resistivity ~ 15 MΩ), which fed through the custom made electrical heaters (to heat it up to 450 °C) prior to entering the confined jet mixer (CJM), whereupon it met the precursors feed. Pump 2 and 3 were used for the precursors feeds mainly; Pump 2 was used to feed metal salts into the reactor and Pump 3 was used to pump auxiliary reagents such as KOH. The feeds from Pump 2 and Pump 3 initially met in tee-piece mixer before the combined feed reacted with the supercritical water, in the temperature range 305 to 375 °C. The premixed precursors from Pump 2 and 3 then met with the superheated water from Pump 1 in a confined jet mixer (CJM) (discussed further in 2.2.2). The newly formed nanoparticles slurry was cooled by a pipe in pipe heat exchanger to approximately 50 °C. The products were then continuously collected from the exit of the back-pressure regulator (BPR), which maintained the system pressure at 24 MPa. For Chapter 3, a Tescom BPR was used (Tescom model 26-1762-24-194, Emerson Process Management Regulator Technologies, South Lanarkshire, UK). For work in Chapter 4 onwards, this was changed to an Equilibar BPR (model EB1HP2 HF, with a 1 mm thick PEEK diaphragm, Equilibar, Fletcher, North Carolina, U.S.), due to design issues.

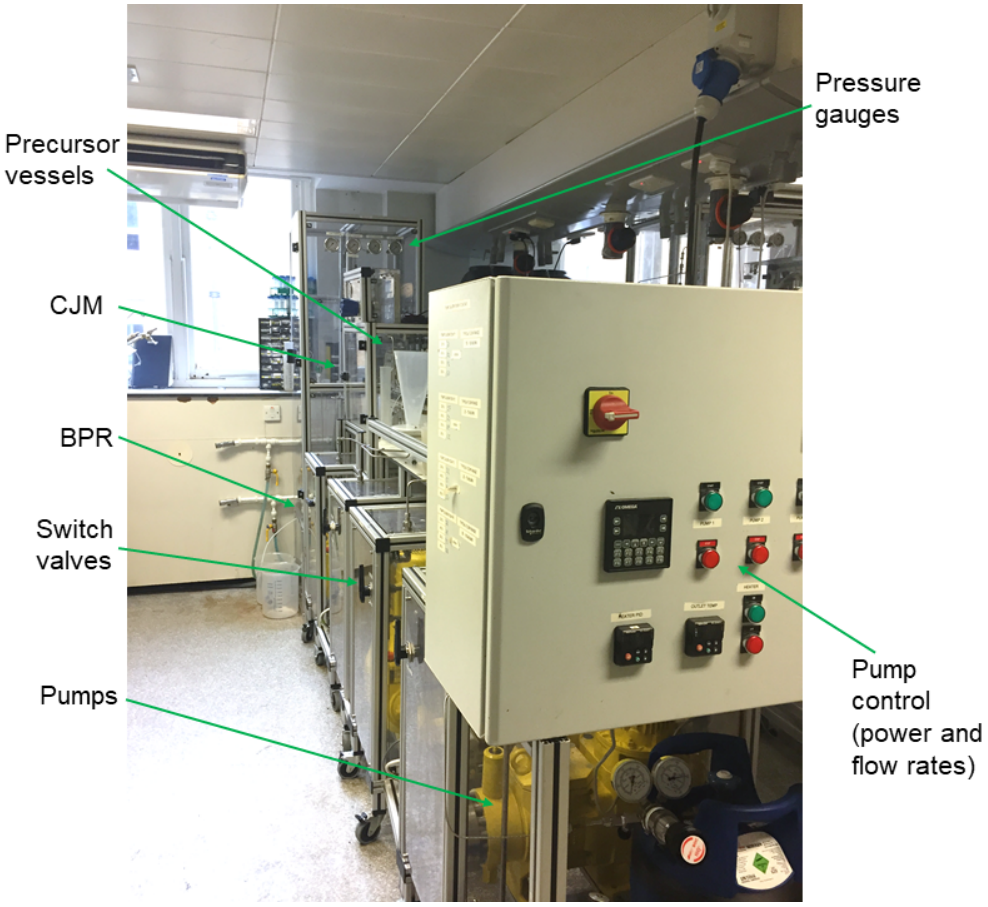

Figure 2-1 - Photograph of the lab scale CHFS reactor from the side on.

Modified heaters (with improved thermal stability) were used for the synthesis of nanoparticles in this thesis.[114] The custom-made heater design included an aluminum core with a bored through hole. A 6-meter length of 1/2" Swagelok stainless steel coil was tightly wound around the aluminum core to allow good contact. A 5/8" diameter, 2000 W heater cartridge (Firerod, L8A80–L10J48T, Watlow) was inserted in the aluminium core. 3 x 500 W band heaters (Mineral Insulated Band Heater MB2J1JN1–E60, Watlow) were placed on the coiled pipe. For each specific experiment conducted using the CHFS process, the flow rates and mixing temperatures are stated in the relevant Chapters.

2.2.2 Confined Jet Mixer (CJM)

The point where the supercritical water and pre-mixed precursors meet is defined as the mixing point, and from herein, referred to as the confined jet

mixer (CJM). This was developed and patented by Prof. Darr, Drs. Robert Gruar and Chris Tighe at UCL, to allow the effective mixing of both streams in a turbulent manner whilst also avoiding preheating of precursors or particle accumulation or blockage in the pipes.[110] A co-current mixing design was adopted for the mixing of the two streams (see Figure 2-2 for the schematic of the mixer). This type of mixer was used to conduct all experiments relating to nanomaterial synthesis in this thesis. In this mixer, the supercritical water travelled upwards towards a cross union (size 3/8”), referred to as the mixer. The pre-mixed precursors were entrained in a jet of superheated water in a co-axial geometry and travelled upwards towards the pipe-in-pipe heat exchanger.

2.2.2.1 Single mixer CJM arrangement

In this arrangement of CHFS, a single CJM was used for the synthesis of nanomaterials. A 3-pump configuration was used, where Pump 1 supplied the D.I. water and Pump 2 and 3 fed in the precursor solutions. A schematic is given in Figure 2-3, which shows the how the configuration was arranged. Typical flow rates and temperature conditions are given in the schematic. The general schematic of the entire reactor design in shown in Figure 2-3.

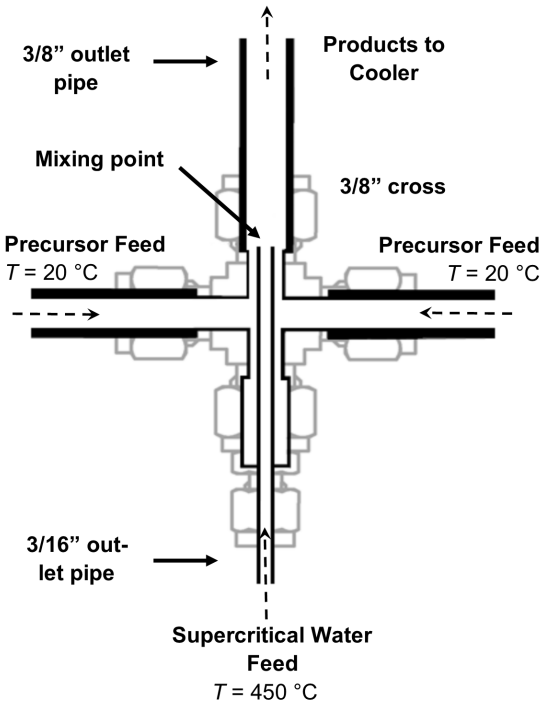

Figure 2-2 – Detailed schematic of the confined jet mixer (CJM) showing the 3/8" union cross with an inlet pipe size (O.D.) of 3/16" and and an outlet pipe size (O.D.) of 3/8". The precrusor feeds are shown.

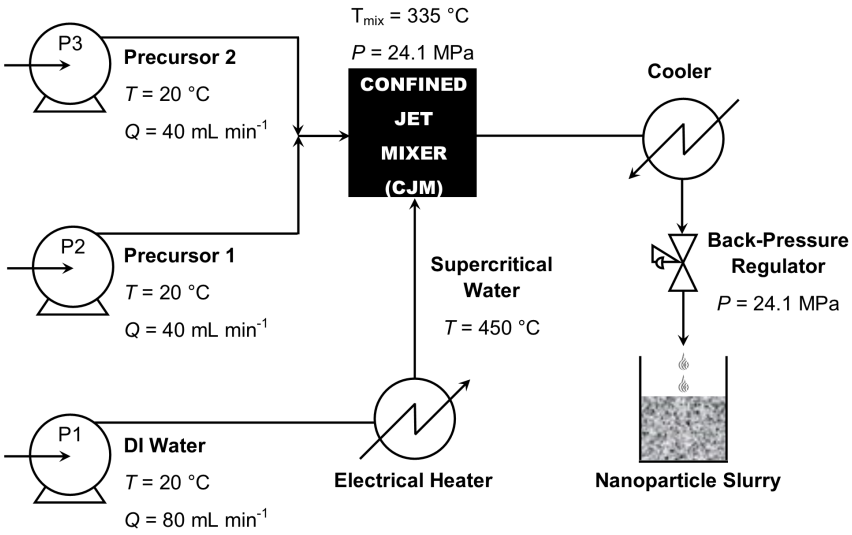

Figure 2-3 – Schematic of the CHFS process using a single CJM mixer set up for the synthesis of ultrafine nanocatalysts in flow using supercritical water. Pumps are denoted by P. Water at room temperature is drawn from P1 and is heated in flow before it enters the first confined jet mixer in the supercritical state. The metal salt feed is drawn from P2 and the base feed from P3. The metal and base feed first meet in a tee piece, then travel to meet the supercritical water feed in a confined jet mixer (denoted as CJM1).

2.2.2.2 Dual mixer CJM arrangement

In this arrangement, dual CJMs were used for the synthesis of nanomaterials. A modification was added by Drs. Neel Makwana and Clément Denis to include a fourth pump into the standard pump configuration. This feed was introduced via a second CJM (3/4" union cross) placed directly above (10 cm) the first CJM to allow for the introduction of cold D.I. water or chemical additives such as capping agents to the nascent nanoparticles, to hinder their growth, as shown in Figure 2-4 and the schematic in Figure 2-5.

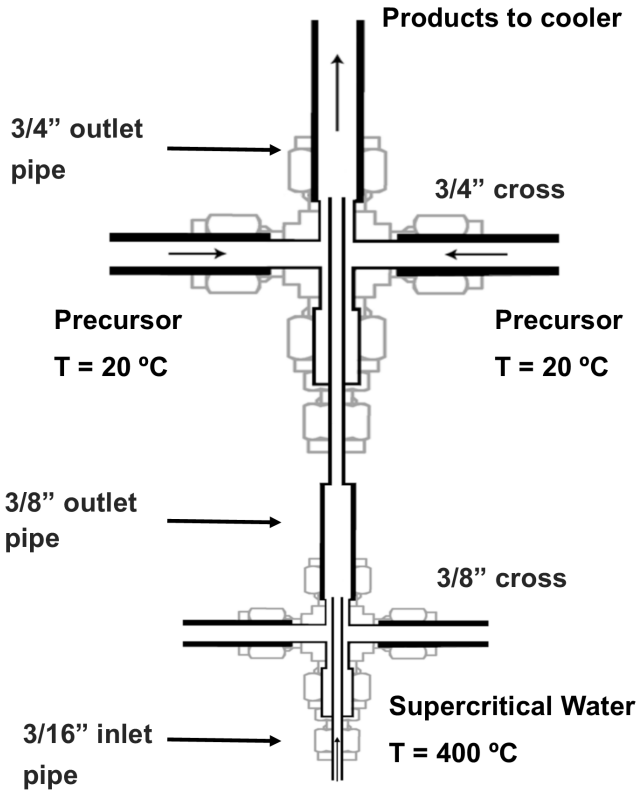

Figure 2-4 - Detailed schematic of the dual confined jet mixer (CJM) set-up, showing the 3/8" union cross with an inlet pipe size (O.D.) of 3/16" and and an outlet pipe size (O.D.) of 3/8" for CJM 1 and and 3/4" cross for the quench feed. The precrusor feeds are shown for each mixer.

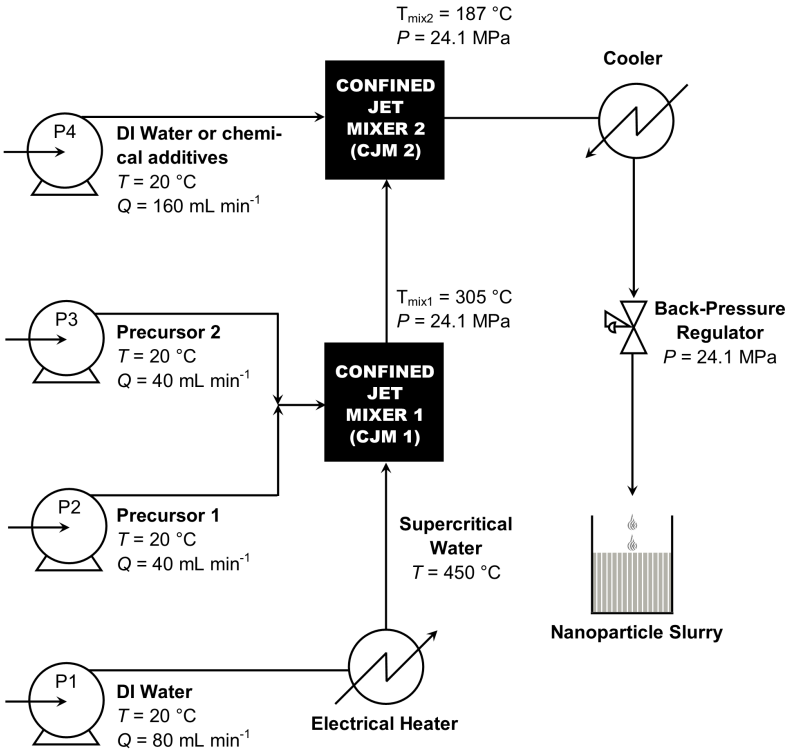

Figure 2-5 – Schematic of the CHFS process using a dual CJM mixer set up for the synthesis of ultrafine nanocatalysts in flow using supercritical water. The nanoparticles form instantaneously in CJM1 and travel to meet the quench feed inside CJM2.

As the nascent nanoparticles met with an incoming feed of cold D.I. water or chemical additives, the temperature rapidly decreased. A temperature profile was also evaluated to monitor how the temperature regime changed with the incorporation of a second CJM (Figure 2-6).[115] Due to this decreased temperature, organic agents could be introduced. This was particularly important as higher mixing temperatures were achieved in the first CJM (range of 300 to 375 °C) and the organic capping agents typically used in this process would likely have decomposed. The mixing temperature in the second mixer, based on the heater temperature of 450 °C, was *ca*. 180 °C, with a Reynolds number of *ca*. 3300. The quench feed was run at 160 mL min^{-1} for all reactions to achieve the maximum quenching effect and rapidly cool the nanoparticle slurry.

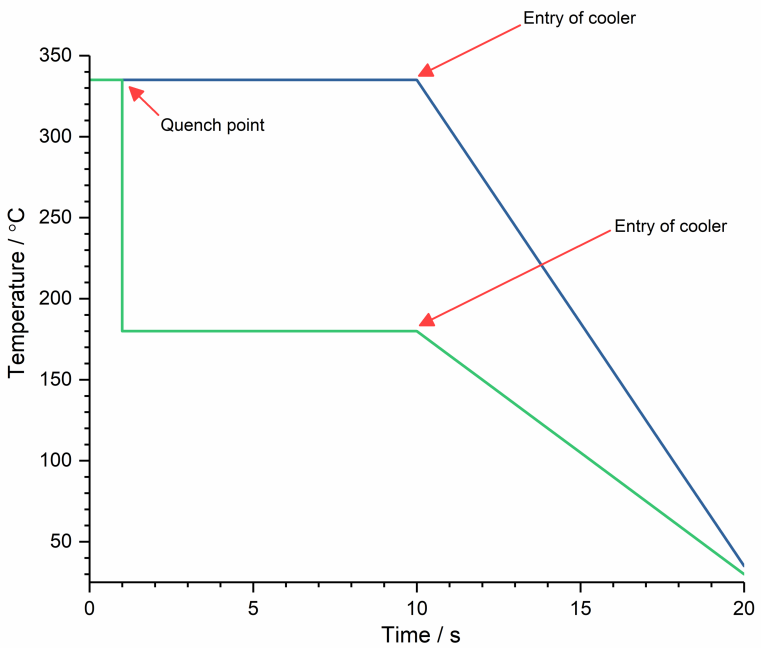

Figure 2-6 – Temperature profile of the nanoparticle slurry when a single mixer is used versus a dual mixer with a quench feed (adapted from ref[115]).

2.2.3 Cooling process

The newly formed nanoparticle stream was cooled via a pipe-in-pipe heat exchanger with a total pipe length of 60 cm. The cooling mixture (50 % ethylene glycol in water) was fed through the pipe-in-pipe cooler by an external chiller (Thermoflex 5000, Thermo Fisher Scientific, Hertfordshire, UK) in a circulating closed system, which maintained the temperature in the range 10 and 20 °C during the experimental run.

2.3 Sample processing

This section details how the nanoparticle laden slurry obtained from the CHFS reactor was processed and cleaned. For samples that were not air or moisture sensitive and easily settled, the nanoparticles were left to sediment under gravity over a 12-hour period. Following this, the excess supernatant was decanted and the slurry was centrifuged (Sigma 4-15 10730, Sigma Laboratory Centrifuges, Gottingen, Germany) at 4500 rpm for up to 15 mins. This process was repeated a minimum of three times, with each cycle repeated with fresh D.I. water and the slurry mixed well with the aid of a

vortex mixer, until the conductivity of the supernatant was below 50 μS as measured by a conductivity probe (Hanna HI 98311).

For samples that did not settle over a 12-hour period, NaCl was added to flocculate the particles. The slurry was centrifuged to remove excess supernatant and the samples were dialysed in D.I. water. Samples were dialysed in cellulose based membranes with an appropriate molecular weight cut off. A wet paste containing the nanoparticles was obtained following an initial centrifugation, and was transferred into the dialysis membranes, which were sealed from both ends and placed in D.I. water to allow the transfer of unreacted precursors, by-products and salt from the sample. The D.I. water was replaced up to 5 times until the conductivity was below 50 μS.

For air and moisture-sensitive samples that could not be left to settle, the nanoparticle laden slurry was centrifuged immediately after synthesis and the same process was followed as described above. If the nanoparticles failed to settle after a prolonged centrifugation cycle, an organic solvent (acetone/ethanol) was added to promote solvent precipitation and subsequently, the acetone was left to evaporate in air. The solvent also provided a protection from air and moisture, which would promote oxidation of air-sensitive materials.

After cleaning, the samples were freeze dried using a VirTis Genesis 35 XL freeze drier. The samples, in the form of a wet paste, were placed in centrifuge tubes; the caps were perforated for water removal during the drying process. The samples and condenser chamber were frozen to below –40 °C and the samples were slowly heated from –40 to 25 °C over a 24 h period under vacuum (*ca.* 10 to 15 Pa).

2.4 Materials Characterisation Techniques

This section details the materials characterisation techniques used to identify and analyse each material synthesised by Continuous Hydrothermal Flow process. If more than one instrument is used for a particular technique, the chapter where the technique is used is also mentioned.

2.4.1 Powder X-Ray Diffraction (PXRD)

Powder X-ray diffraction was used to identify the phase composition of each sample synthesised. PXRD patterns were obtained from a Bruker D4 endeavour diffractometer with a 64-position automated sample changer to enable high throughput data collection. The diffractometer was equipped with a Cu $K_{\alpha 1}$ radiation source (λ = 1.541 Å) and the patterns were collected between a 2θ range of 10 to 80°, step size of 0.05° and a count time of 4 s per step. The powders were ground prior to mounting onto a PMMA flat-plate holder.

Diffraction patterns were also collected on a STOE STADI P diffractometer, equipped with a Mo $K_{\alpha 1}$ radiation source (λ = 0.709 Å). The samples were prepared and mounted in transparent foils for analysis. The patterns were collected in the 2θ range of 2 to 40°, step size of 0.5° and the count time was varied from 5 s to 20 s per step, depending on the sample.

The patterns were identified by comparing with standard reference patterns available on Joint Committee on Powder Diffraction Standards (JCPDS) database website through the Royal Society of Chemistry (RSC). The standard patterns are given in each chapter when discussing PXRD patterns of synthesised materials for ease of reference. Further characterisation of the sample included estimating the size of the crystallites. For this, the Scherrer equation was applied to selected peaks in the diffraction pattern (Equation 2.1):

$$d = \frac{K\lambda}{\beta \cos\theta} \qquad \text{Equation 2.1}$$

where d is the crystallite size (given in nm), K is the Scherrer constant (taken as 0.9), λ is the radiation source, β is the full width peak at half maximum (FWHM) of the peak and θ is the Bragg angle of the peak.

2.4.2 High Resolution Transmission Electron Microscopy (HRTEM)

High-resolution transmission electron microscopy (HRTEM) was conducted to examine the morphology and size of the nanopowders synthesised via CHFS. In a TEM, an electron source emits electrons that travel through the microscope and electromagnetic lenses focus the beam. The beam travels through the sample and electrons are scattered. The unscattered electrons interact with a fluorescent screen resulting in an image, which can be studied to understand the morphology and size.

Typically, the HRTEM samples were prepared by dispersing the nanoparticles in methanol (99.9 % purity) by ultra-sonication before dropping the resulting dispersion onto 300 mesh Holey copper film grids. Images were obtained on a JEOL JEM 2100 TEM with 200 keV accelerating voltage and a $LaBF_6$ filament equipped with a GATAN CCD camera for digital imaging. Energy dispersive X-ray spectroscopy (EDX) was conducted on the JEOL JEM-2100 TEM fitted with an Oxford Instruments X-MaxN 80 T Silicon Drift Detector (SDD). Analysis was conducted using the Aztec TEM software.

2.4.3 Scanning Electron Microscopy (SEM)

Field Emission Scanning Electron Microscopy (FE-SEM) was used to characterise electrodes pre- and post- electrochemical testing. SEM uses a focused beam of high-energy electron, scanned in a rectangular raster to

generate signals based on sample-electron interaction and give information on the morphology, composition and crystalline structure. Images were obtained by using a JEOL JSM-6700F microscope. Electrodes were mounted on 0.5 cm circular aluminium stub using a double-sided adhesive carbon tape. Copper tape was attached to the side of the electrode and the stub to assist with electrical conductivity during imaging and prevent particle charging. For imaging purposes, a working distance of 8 mm was typically used and an accelerating voltage of 10 kV.

Energy dispersive X-ray spectroscopy (EDX) on the JEOL JSM-6700F microscope was conducted equipped with an Oxfords Instrument Inca 400 EDX unit operating at 10 kV accelerating voltage and a working distance of 15 mm, optimum for EDX measurements to ensure high resolution images and maximum counts are achieved.

2.4.4 X-ray Photoelectron Spectroscopy (XPS)

XPS spectra are obtained by irradiating a sample with X-rays and measuring the kinetic energy and photoelectrons emitted as a subsequence. XPS can provide surface chemical information, such as oxidation states and band gap. Surface chemical analysis was carried out using a Thermo Scientific™ K-Alpha™ X-ray photoelectron spectrometer with a two chamber vacuum system, using Al-K_α radiation. Survey scans were conducted at a pass energy of 150 eV and high-resolution region scans were conducted at 50 eV (using a 128-channel position sensitive detector). The XPS spectra were processed using CasaXPS™ software. The samples were prepared by placing nanopowders on double-sided adhesive carbon tape whereas electrodes were directly placed on the carbon tape to analyse pre- and post-electrochemical testing.

2.4.5 Dynamic Light Scattering (DLS)

The particle size distribution was measured using Dynamic Light Scattering (DLS). DLS is used to measure particle size and size distribution in suspensions and solutions. The measurements are conducted by irradiating a sample with light. The molecules in the solution scatter light and this fluctuates with time due to molecules undergoing Brownian motion. The scattered light leads to constructive and destructive interference, which contain information of the time-scale movement of the particles. This provides size information as larger molecules move slowly compared to smaller molecules.

The measurements were conducted using Malvern Zetasizer nano (ZEN3600). The particles were measured as suspensions either directly from the dilute particle suspensions (*ca.* 1 mM) or as catalyst inks. Each sample was sonicated prior to measurement and the dispersion was then placed in 3 mL disposable PMMA cuvettes with a nominal path length of *ca.* 1 cm. Each measurement was conducted using the backscatter geometry and the intensity of the scattered light of the sample was measured at 173°. Measurements were typically carried out over 25 measurements for 10 s each and size parameters are given as the Z-average diameter (harmonic intensity averaged particle diameter) and the polydispersity index (PDI).

2.4.6 Brunauer-Emmett-Teller (BET) surface area analysis

BET surface area analysis was conducted to determine the surface area of the nanopowders as synthesised by CHFS. This method relies upon the multilayer adsorption of non-corrosive gases, such as nitrogen, to determine the specific surface area by calculating the amount of gas corresponding to a monolayer on the surface.

For Chapter 3, BET measurements were conducted using Micromeritics ASAP 2420 instrument. Samples were degassed under vacuum at 150° C for 12 h, weighed, and then the adsorption isotherms were measured. BET measurements were also conducted using Micromeritics TriStar II instrument for some samples in Chapter 3 and Chapter 4 onwards. The samples were degassed under the flow of N2 in the range 110 to 150° C for 12 h before measurements were taken.

2.5 Electrode preparation

2.5.1 Optimised ink formulation

Approximately 50 mg of as-prepared dried nanopowder was suspended in a mixture of isopropanol (IPA), methanol and DI water in a volume ratio of 1:6:6, respectively. This particular solvent system was optimised to this ratio and particular solvents to achieve a homogeneous consistent dispersion. Different solvents and ratios were tested and are discussed further in Chapter 4. The Nafion content was varied at values of 1, 10, 25 and 66 wt% (vs. total solid fraction) in Chapter 4.

The suspension was sonicated using a high-power dispersion sonic tip (Branson Sonifiers 250D, Geneva Switzerland) for 30 mins at 20 % amplitude with a pulse sequence, where the pulse was on for 0.2 s and off for 0.5 s. The ink suspension was immersed in an ice bath to avoid solvent evaporation and conversion of CuO to copper carbonates, as well as prevent any degradation of the Nafion polymer. Various methods were used to disperse the inks and this is also discussed further in Chapter 4.

2.5.2 Ink deposition

A glassy carbon sheet (1 x 1 cm) (Alfa Aesar, Lancashire UK) was used as an inert electrode support for the deposition of the catalyst ink. The electrode was cleaned by polishing using a 0.05 μm alumina slurry (Buehler, Stuttgart

Germany) prior to drop casting. The electrode was polished in a figure of 8 on both sides. The alumina was rinsed with D.I. water and the electrodes were further cleaned by sonication in D.I. water to remove any remaining alumina. The electrodes were dried in a vacuum oven (Heraeus Instruments VT6025 Vacutherm) at 40 °C prior to drop casting. Electrodes were prepared by casting CuO inks on a glassy carbon sheet to have a loading of approximately 0.3 mg cm^{-2}. The glassy carbon was dried overnight in a vacuum oven at 40 °C to give a homogeneous catalyst film. This was evaluated as best practice due to contamination from the solvents used in the ink (confirmed by ^{1}H NMR).

2.6 Electrochemical testing

This section discusses the various electrochemical techniques used to evaluate the electrocatalytic behaviour of the nano-catalysts prepared by CHFS. The catalysts were tested in a conventional three-electrode set up; where a (0.5 mm OD) platinum coil (Alfa Aesar, Lancashire UK) was used as a counter electrode, a Ag/AgCl electrode (BASi, Indiana USA) was used as a reference electrode and the working electrode was a catalyst coated glassy carbon sheet. A Gamry 1000 potentiostat (Gamry, Pennsylvania USA) was used for all electrochemical experiments. All experiments were conducted at ambient temperature. All potentials quoted in this thesis are reported against Ag/AgCl. Any literature values referenced are converted to Ag/AgCl from their respective potentials for ease of reference. A schematic of the electrochemical cell set up is given in Figure 2-7a and the side on photo of the cell as used (Figure 2-7b)

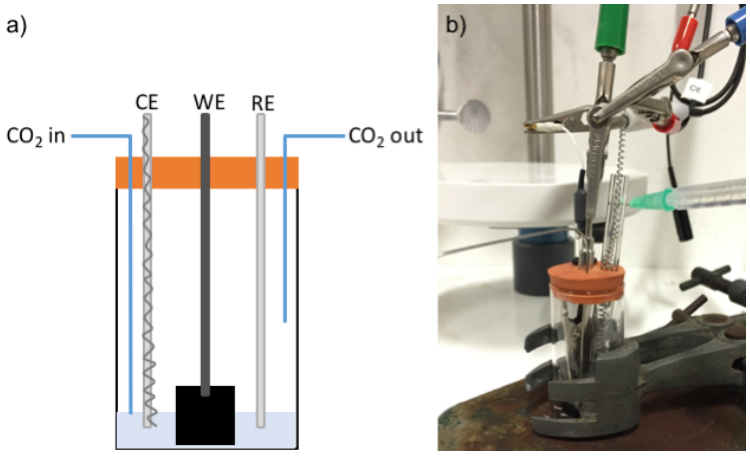

Figure 2-7 – a) Schematic of a three-electrode cell used for the electrochemical reduction of CO_2, where the counter electrode is a platinum coil, the working electrode is the catalyst coated glassy carbon electrode and the reference electrode is a Ag/AgCl electrode. Two injection ports are also annotated for CO_2 in and out. 3 mL of electrolyte was used in all experiments and b) shows the side on photo of the cell as used during experiments.

2.6.1 Cyclic voltammetry

Cyclic voltammetry is used to study the electrochemical properties of an analyte and provides information about its redox behaviour. In a typical scan, the working electrode is ramped linearly with time between two set potentials and this may be repeated over a number of cycles. The current response to the potential change over time is measured and plotted versus the potential of the working electrode.

The inks were characterised by cyclic voltammetry prior to any other electrochemical testing. The cell was set up as described in Section 2.6. This technique was used to evaluate how the catalyst phase changed in the chosen electrolyte environment. 0.5 M $KHCO_3$ electrolyte was saturated with CO_2 for 30 mins before cycling. The electrode was cycled in the range 0.7 to –0.8 V vs. Ag/AgCl at 100, 50, 20 and 5 mV s^{-1} in the case of copper oxide catalyst.

2.6.2 Surface area measurements by capacitance

For surface area measurements, all catalyst coated electrodes were held at a constant potential of –1 V vs. Ag/AgCl for 1 hour in a CO_2 saturated 0.5 M

$KHCO_3$ electrolyte. Surface area measurements were conducted by cycling in the range –0.25 to –0.45 V in 0.1 M H_2SO_4. The electrodes were rinsed with D.I. water before being placed in the electrolyte.

2.6.3 Constant potential electrolysis

Constant potential electrolysis is a bulk electrolysis technique, which employs a three-electrode system; the working electrode is held at a fixed potential over time and the current response is measured. At the set potential, in the case of CO_2 electroreduction, CO_2 is reduced to products such as HCOOH, CH_3OH, CH_4 and CO. From the integral of this plot, the charge passed to generate the products can be obtained, which can be used to calculate the Faradaic efficiency (FE) for a certain product, following Equation 2.2 to 2.4, where Q is charge, I is current, t is time, n is the number of electrons involved in the process and F is Faraday's constant.

$$Q_{theo} = I\,t \qquad \text{Equation 2.2}$$

$$Q_{exp} = nFmol[product] \qquad \text{Equation 2.3}$$

$$FE = Q_{exp}/Q_{theo} \qquad \text{Equation 2.4}$$

To evaluate the electrochemical reduction of CO_2, each electrode was held at a constant potential in the range –0.6 to –1.4 V vs. Ag/AgCl for 3 h. In each case, 3 mL of 0.5 M $KHCO_3$ was used, which was saturated with CO_2 for 30 mins. Where a different electrolyte was used, this has been specified at the relevant point in each chapter. Headspace analysis of the cell was conducted by extracting aliquots (10 μL) with a gas tight syringe and analysed via a Shimadzu GC 2014 equipped with TCD and FID detectors and a packed CTR-1 column. Liquid phase products were analysed post electrolysis using a 600 MHz Bruker ^{1}H NMR using DSS in H_2O/D_2O as a reference control.

2.6.3.1 ^{1}H NMR

^{1}H NMR was used to determine liquid products from the electro-reduction of CO_2. A co-axial insert (5 mm O.D) was used to hold the external locking solvent and reference material, which was D_2O and 4,4-dimethyl-4-silapentane-1-sulfonic acid (DSS), respectively. The insert was prepared with 100 μM DSS in D_2O, which was diluted from a stock solution of 4.5 mM DSS in H_2O.

NMR experiments were conducted on Bruker Avance III 600 spectrometer equipped with a DCH cryoprobe for ^{13}C and ^{1}H NMR measurements. The instrument was also equipped with a BACS 60 sample changer for high throughput measurement of samples. 400 μL of sample was taken for each NMR sample. Each measurement was undertaken for a minimum of 64 scans to improve the signal to noise ratio of the data.

The NMR was calibrated with known concentrations of expected products (such as formic acid, methanol and acetic acid) in different concentration ranges. The product peaks were calibrated against the known amount of DSS in the insert. Table 2-1 details the concentration ranges calibrated for each product.

Table 2-1 - The chosen concentration range for products, formic acid, methanol and acetic acid.

Product	Concentration range
Formic acid	100 μM to 15 mM
Methanol	50 to 200 μM
Acetic acid	50 μM to 200 μM

The calibration curve for formic acid is shown in Figure 2-8. Formic acid was calibrated over a wide range of concentrations, as the product range from the catalysis was quite broad, depending on the potential applied. A straight-line fit was obtained with a R-square value of 0.994, which suggested a reasonable linear fit. This calibration fit was used to calculate the concentration of formic acid formed.

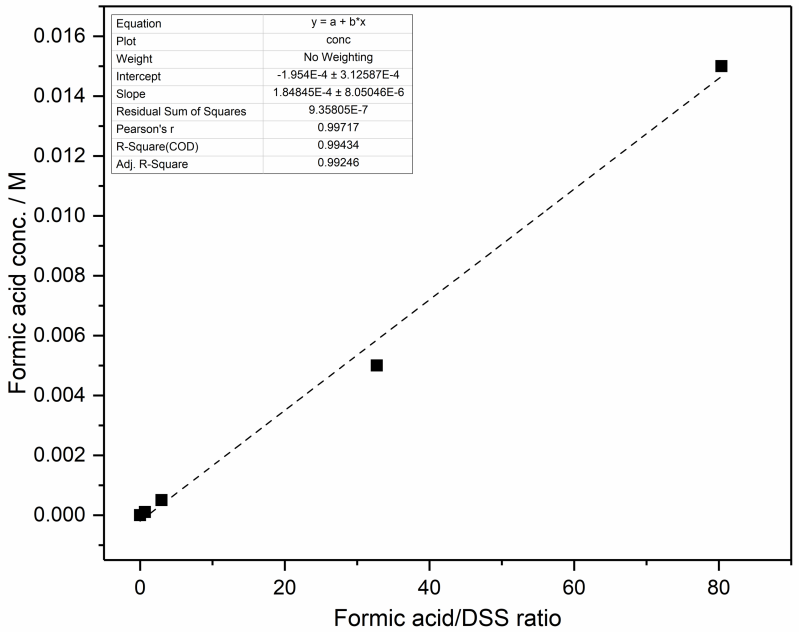

Figure 2-8 – Calibration curve of formic acid (0 to 15 mM concentration range) given

2.6.3.2 Gas Chromatography

Gas chromatography (GC) was used to determine the gaseous products observed from the electrochemical reduction of CO_2. Shimadzu 2014 equipped with a CTR1 dual column was used for this analysis. This column allowed for the separation and analysis of permanent gases, such as, N_2, CO_2, CH_4, CO, O_2. A TCD and FID detectors were used. Liquid samples were not analysed by the GC due to the presence of formic acid in each sample. Formic acid is known to be a problematic product to detect by the GC as it often adheres to the column walls and is not detected by the FID detector. As the column is also not suitable for water containing samples, aqueous liquid samples were not directly injected into the GC.

2.6.4 Control experiments

Control experiments were conducted to confirm that the products observed in the NMR or GC were present due to the electroreduction of CO_2 and not due to any other contamination or the glassy carbon acting as the catalyst.

Following the experiments, NMR and GC measurements were taken as per standard procedure.

2.6.4.1 Control 1 – no CO_2 bubbled in the electrolyte

A control experiment was conducted where no CO_2 was bubbled through the cell prior to conducting a constant potential electrolysis experiment. The electrode was cleaned as per standard procedure and subsequently the catalyst was drop coated on to the glassy carbon sheet. A potential of –1.4 V vs. Ag/AgCl was applied across the electrode for 3 h and samples taken from the electrolyte and cell headspace, as described above.

2.6.4.2 Control 2 – no catalyst deposited on the glassy carbon

A control experiment was conducted where no catalyst was used on the glassy carbon electrode. The cell was set up as described previously and the electrolyte was saturated with CO_2 for 30 mins. The electrode was cleaned as per standard procedure and a potential of –1.4 V vs. Ag/AgCl was applied across the electrode for 3 h and samples taken from the electrolyte and cell headspace.

2.6.5 Electrochemical Impedance Spectroscopy (EIS)

For EIS measurements, a normal three-electrode set up was employed (as described in Section 2.6) The 0.5 M $KHCO_3$ electrolyte was saturated with CO_2 for 30 mins. The measurement was performed over a frequency range of 10 kHz to 0.1 Hz with an AC perturbation of 5 mV at the same applied potentials as used in the constant potential electrolysis (Section 2.6.3). The EIS data was analysed by Gamry EChem Analyst software by developing an equivalent model circuit for the chemical processes occurring in the cell during the measurements. The model was fitted to the raw data and simulated values of charge transfer and mass transport resistances were obtained. The equivalent model circuit and simulated values are given in the relevant Chapters.

2.6.6 Rotating Ring Disk Experiments

Rotating Ring Disk Electrode is a powerful technique for analysing products, side products and short-lived intermediates. The RRDE set up comprises of a disk electrode, in this case made of glassy carbon, surrounded by a concentric platinum ring electrode in a cylindrical PTFE shroud (RRDE AFE7R9GCPT, PINE Research Instrumentation, North Carolina, USA). An insulating material separates the disk and ring electrode. Using RRDE allows for higher throughput screening of products from CO_2 electroreduction. A photo of a blank RRDE is shown in Figure 2-9, which shows the glassy carbon electrode, Pt ring electrode and the Teflon encasing.

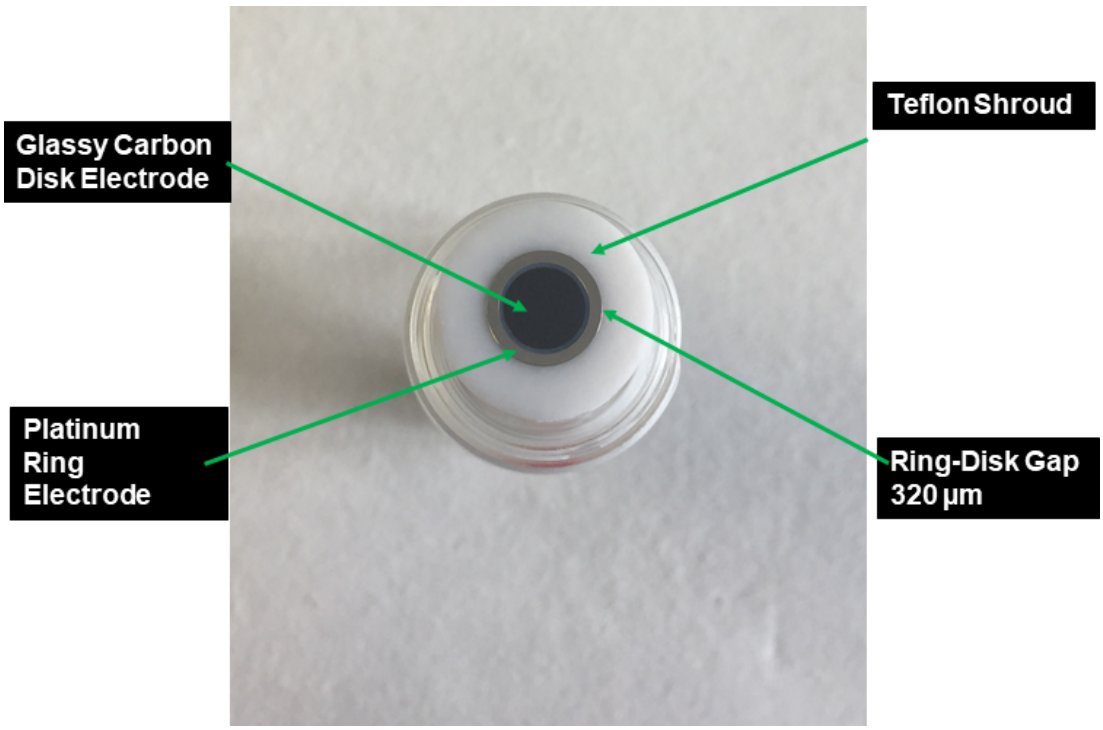

Figure 2-9 – Photo of the rotating ring disk electrode (RRDE) used in the electrochemical reduction of CO_2.

2.6.6.1 Electrode preparation

The RRDE was cleaned as described above for the glassy carbon sheet (Section 2.5.2). The inks were sonicated prior to drop coating (see Section 2.5.1) on to the electrode, to ensure the inks were completely homogenous. Typically, 3 x 10 µL of ink was drop coated on the glassy carbon surface,

ensuring the ink did not flow on to the ring or the gap between the disk and ring, to have a loading of 0.3 mg cm^{-2}, the same as on the glassy carbon sheet. In the case of this eventuality, it is possible there would be some short-circuiting or noise in the data collection. Therefore, it is important to prevent the ink dispersing on to the ring.

2.6.6.2 Cell set up

A RRDE cell was used (Adams & Chittenden, model no. 946088), to conduct all RRDE experiments (see Figure 2-10 for the set-up). A platinum mesh (woven from 0.1 mm Pt wire) connected to a Pt wire (0.5 mm O.D) was used as a counter electrode, a Ag/AgCl electrode was used as a reference and the working electrode was the RRDE with the catalyst ink drop-coated on the electrode. Approximately 150 mL of electrolyte was used for every experiment.

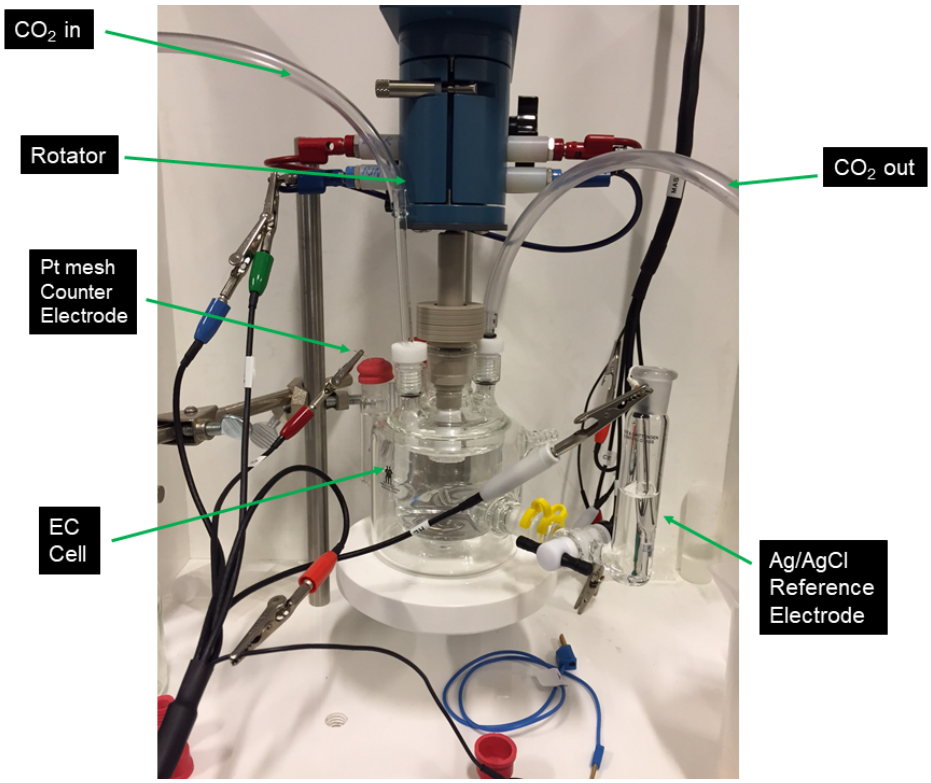

Figure 2-10 - Photograph of the rotating ring disk electrode set up showing the RRDE immersed in the electrolyte, with the Pt mesh, Ag/AgCl electrodes and the ports for the CO_2 gas inlet and outlet.

The chosen electrolyte (0.5 M $KHCO_3$ or K_2HPO_4) was saturated with CO_2 for 30 mins. A bearing assembly (PINE Research Instrumentation, AC01TPA6M) was used to create a gas tight cell. The RRDE was screwed into the MSR precision shaft (PINE Research Instrumentation, AFE6MB) and a pine modulated speed rotator (PINE Research Instrumentation, AFMSRCE) was used to rotate the shaft and RRDE.

2.6.6.3 Collection efficiency tests

The axial flow pattern of solution towards the electrode brings molecules and ions towards the disk surface. The outward flow pattern from the disk towards the ring, which remains downstream, means products and intermediates evolving from the disk, can be detected by the ring. The collection efficiency describes the fraction of material that can be detected at the ring surface. This is the function of disk and ring dimensions and the gap between the disk and ring. Although, the collection efficiency may be calculated theoretically using the disk outer diameter and the ring outer and inner diameter, experimentally some minor deviation may be observed. This may be due to polishing and cleaning leading to scratches on the ring surface or temperature cycling as well as any uncertainties in the machining process during the manufacturing of the RRDE. Therefore, the collection efficiency is always tested empirically by using a well-known one-electron reaction such as the reversible reaction of ferro/ferricyanide.

2.6.6.4 Product calibration tests

As the ring is used as a tool to detect products from CO_2 reduction on the disk, a calibration was required in order to evaluate at what potential the products from electroreduction reaction oxidised at the Pt ring surface in the chosen electrolyte. In order to do this, known concentrations of the products were added into the electrolyte. For each calibration, fresh electrolyte was used and the RRDE was cleaned and polished between each run. Prior to

the addition of any calibrants, the electrolyte was saturated with CO_2 for 30 mins.

Chapter 3. Continuous Hydrothermal Flow Synthesis of CuO, Cu_2O and Cu Nanoparticles

3.1 Introduction

Copper is cheap, abundant and copper systems present interesting properties for applications in nanoscience. Nano copper is used in methanol synthesis[116] and hydrogen production in the water-gas shift reaction.[117] Its optical properties, arising from the localised surface plasmon resonance occurring in the visible region, allow for it to be used for diagnostics applications. Copper's high electrical conductivity is also of interest for applications in transparent and flexible conducting films. Similarly, copper oxides (CuO and Cu_2O) are both *p*-type semiconductors with a narrow band gap of 1.2 eV and 2 eV for CuO and Cu_2O, respectively.[118] These materials are of interest for applications in photovoltaics, catalytic and gas sensing applications due to their high optical absorption coefficient. Copper and its oxides are also key catalysts for the electroreduction of CO_2 to products such as methanol, acetic acid, CO, formic acid and methane.[30]

Numerous methods have been employed to synthesise copper-based materials including solution methods (hydrothermal and chemical precipitation), thermal conversion, electrochemical methods and microwave synthesis. The synthesis of nanomaterials in batch processes can present inherent issues with reproducibility and scalability. There are also additional cost and processing steps that should be considered in the synthesis of nanomaterials via batch methods. Continuous hydrothermal flow synthesis (CHFS) offers a scalable and controllable way of large scale synthesis of nanomaterials. CuO has been synthesised via continuous flow techniques.

Sue et al. successfully synthesised CuO at 375 °C and 30 MPa using $Cu(NO_3)_2$, yielding an average particle size of 30 nm.[119] In another study, the same authors studied the effect of residence time in a T-type micro mixer, where appreciable CuO nucleation did not occur at 0.002 s but with increasing residence time to 0.157 s, CuO nucleation, growth rate and conversion increased.[120] Zhou et al. recently investigated the impact of mixing (using tee-mixers, side angle tee-mixers and symmetric multiple tee-mixers) for the production of CuO nanoparticles using copper sulfate and identified and optimised the mixer configuration for the production of small sized CuO nanoparticles.[121] The formation of smaller CuO nanoparticles was observed for mixers with small diameters and shorter residence times and therefore, higher Reynolds number. The use of tee-mixer can result in blockages, back-mixing and inhomogeneous mixing zones, which lead to a wide particle size distribution. This may be avoided by using a confined jet mixer, which limits particle growth and maximises high nucleation rates, as discussed in more detail in this Chapter.

For the synthesis of CuO via continuous flow techniques, the focus has largely been on optimising mixer types to favour a more turbulent mixing regime, reducing residence time or understanding the impact of CuO solubility by varying temperature (and occasionally pH). There have been few reports where the effect of the metal salt precursor, temperature or the use of KOH have been collectively considered. H_2O_2 has been extensively used in continuous supercritical water oxidation,[122] however, its use in metal oxide synthesis has been limited to a few reports. Boldrin et al. used H_2O_2 in the synthesis of Co_3O_4 and NiO compounds and showed it may be used to control the particle size.[122] Similarly, Shi et al. used H_2O_2 in the synthesis of ZnO and showed that the presence of H_2O_2 altered the solubility of ZnO, promoting growth of certain facets.[123] For the synthesis of Co_3O_4, H_2O_2 has been used to enhance the oxidation of cobalt as well as reduce particle size.[113] H_2O_2 is an oxidising agent and can lead to higher oxidation states

(dependent on the element), as it decomposes to oxygen and hydrogen in supercritical conditions.[124] In the case of CuO, this chapter will consider a systematic approach in optimising the synthesis of small sized CuO by investigating the effect of copper salt, use of a quench feed, temperature and base concentrations and the influence of H_2O_2.

The synthesis of Cu_2O and Cu nanoparticles via hydrothermal flow techniques has been limited and has not been previously attempted on the CHFS reactor at UCL.[125–127] Previously, copper nanoparticles have been synthesised in supercritical conditions with H_2 derived from the decomposition of formic acid, acetic acid (from copper acetate), or formaldehyde.[125–127] Capping agents such as PVP, 1-hexanethiol and EDTA have been used to protect and hinder the growth of Cu nanoparticles. A key issue is the stability of Cu_2O and Cu phases, as they rapidly oxidise to CuO. The synthesis of pure phase copper nanoparticles has been targeted due to its promising applications as mentioned above, however, both Cu_2O and Cu phases will be targeted in this study, particularly as Cu_2O is a promising photoelectrocatalyst for CO_2 reduction. The aim is to synthesise pure phase Cu_2O and Cu nanoparticles via CHFS and to assess the feasibility of surface modification in flow for the synthesis of Cu_2O and Cu.

3.2 Materials and Methods

3.2.1 Materials

Copper(II) nitrate trihydrate [$Cu(NO_3)_2{\cdot}3H_2O$, technical grade, >98 %], copper(II) sulfate pentahydrate [$Cu(SO_4)_2{\cdot}5H_2O$, technical grade, >99 %], polyvinylpyrrolidone [PVP, average molecular weight 10,000], H_2O_2 solution [30 % (w/w)] and formic acid were supplied by Sigma Aldrich, (Dorset, UK). Copper(II) acetate monohydrate [$Cu(COOCH_3)_2{\cdot}H_2O$, technical grade, >98 %], sodium pyrophosphate ($Na_4P_2O_7$) and D-fructose were supplied by Alfa Aesar (Lancashire, UK). Potassium hydroxide pellets (KOH) was supplied by

Fischer Scientific. All reactions were conducted in deionised water (>10 MΩ). All chemicals were used as purchased.

3.2.2 CHFS mixer design and set up

For the synthesis of copper-based products, single (three-pump arrangement) and dual mixers (four-pump arrangement) were used, as detailed in Chapter 2. Pump 1 (P1) was used to feed the water feed through the heaters. Pump 2 (P2) and Pump 3 (P3) were used to feed the metal salt and base solutions, respectively. When the dual mixer was used, Pump 4 (P4) was used to feed either D.I. water or a capping agent. This will be highlighted for specific reactions. Table 3-1 and Figure 3-1 below detail the mixer set up, dimensions, flow rates, residence times and the Reynolds number in the respective mixers used for the synthesis of copper-based materials in this chapter. The detailed schematic of the pre-mixer used in the synthesis of Cu_2O and Cu nanoparticles is shown below (Figure 3-1), with the single and dual mixer for ease of reference.

Table 3-1 - Mixer set up information detailing flow rates (represented by Qsw, Qp, Qq for supercritical water, precursors and quench feed, respectively), heater set temperature, mixing temperature for CJM1 and CJM2, residence time (represented by τ) and Reynolds number (Re) in the respective mixers.

Mixer type	Q_{sw} / mL min^{-1}	Q_p (total) / mL min^{-1}	Q_q / mL min^{-1}	Heater Temp. /°C	T_{mix1} / °C	T_{mix2} / °C	τ / s	Re_{mix1}	Re_{mix2}
SM	80	80	-	400	305	-	4.35*	6079	-
DM	80	80	160	400	305	168	0.84	6079	2989
DM	80	80	160	450	335	187	0.76	6939	3354
DM	80	50	160	450	375	204	0.69	7782	3323
PM	80	80	20†	450	330†	305‡	4.35*	4620	7713

Note: CJM1 is represented by mix1 and CJM2 by mix2. *The residence time referred here is from the single mixer to the heat exchanger ~ 60 cm. †refers to the mixing temperature in the pre-mixer, where the supercritical water meets the feed of formic acid and ‡refers to the mixing temperature of the CJM1 when the precursor feed meets the formic acid and supercritical combined feed. Single mixer is denoted by SM, dual mixer by DM and pre-mixer by PM.

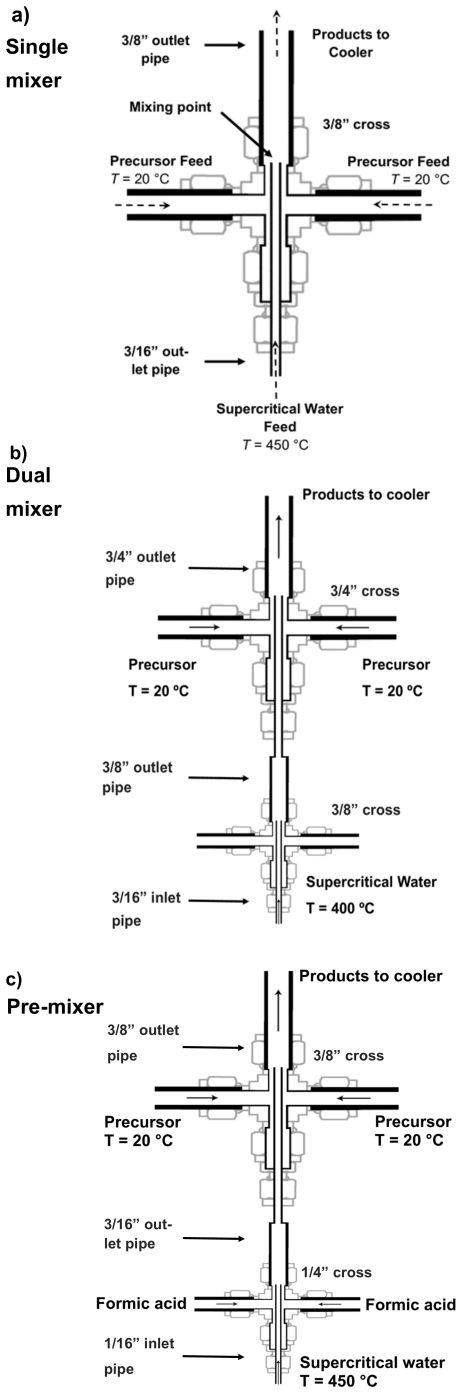

Figure 3-1 - Detailed schematic of the mixer set ups used in this chapter showing a) single mixer with 3/8" union cross with an inlet pipe size (O.D.) of 3/16", b) dual mixer with 3/8" cross (as in the single mixer) and 3/4" cross for the quench and c) pre-mixer set up (used for the synthesis of Cu_2O and Cu only) to introduce formic acid to meet with the supercritical feed. The pre-mixer was a 1/4" union cross with an inlet pipe size (O.D.) of 1/16" and and an outlet pipe size (O.D.) of 3/16" for the decomposition of formic acid. The precrusor feeds are shown as they meet the supercritical water feed in a 3/8" cross with an inlet pipe size (O.D.) of 3/16" and an outlet pipe size (O.D.) of 3/8".

3.2.3 Experimental conditions

3.2.3.1 Synthesis of CuO

Table 3-2 highlights the experimental parameters for the synthesis of CuO. Only D.I. water was used in the quench feed.

Table 3-2 - Experimental parameters for the synthesis of CuO.

Sample	Cu^{2+} conc./ M	KOH conc./M	H_2O_2 / v/v%	Mixing temp./° C	Mixer Type	Product
CuO-SO_4/SM	0.1[1]	0.2	-	305	SM	CuO*
CuO-NO_3/SM	0.1[2]	0.2	-	305	SM	CuO
CuO-OAc/SM	0.1[3]	0.2	-	305	SM	CuO
CuO-SO_4/DM	0.1[1]	0.2	-	305	DM	CuO
CuO-NO_3/DM	0.1[2]	0.2	-	305	DM	CuO
CuO-OAc/DM	0.1[3]	0.2	-	305	DM	CuO
CuO-1:1/305	0.1[1]	0.1	-	305	DM	$Cu_4SO4(OH)_6$
CuO-1:2/305	0.1[1]	0.2	-	305	DM	CuO
CuO-1:4/305	0.1[1]	0.4	-	305	DM	CuO
CuO-1:1/335	0.1[1]	0.1	-	335	DM	CuO*
CuO-1:2/335	0.1[1]	0.2	-	335	DM	CuO
CuO-1:4/335	0.1[1]	0.4	-	335	DM	CuO
CuO-1:1/375	0.1[1]	0.1	-	375	DM	CuO
CuO-1:2/375	0.1[1]	0.2	-	375	DM	CuO
CuO-1:4/375	0.1[1]	0.4	-	375	DM	CuO
CuO[0.1]	0.1[1]	-		305	DM	-
CuO[0.1]	0.1[2]	-		305	DM	-
CuO[0.05]	0.05[3]	-	-	305	DM	CuO
CuO[0.1]	0.1[3]	-	-	305	DM	CuO
CuO[0.2]	0.2[3]	-	-	305	DM	CuO
CuO[0.3]	0.3[3]	-	-	305	DM	CuO
CuO[0.05]-H_2O_2[1]	0.05[3]	-	1	305	DM	CuO
CuO[0.1] -H_2O_2[1]	0.1[3]	-	1	305	DM	CuO
CuO[0.2] -H_2O_2[1]	0.2[3]	-	1	305	DM	CuO
CuO[0.3] -H_2O_2[1]	0.3[3]	-	1	305	DM	CuO
CuO[0.1]-H_2O_2[0.5]	0.1[3]	-	0.5	305	DM	CuO
CuO[0.1]-H_2O_2[2]	0.1[3]	-	2	305	DM	CuO
CuO[0.1]-H_2O_2[4]	0.1[3]	-	4	305	DM	CuO
CuO[0.1]-H_2O_2[0]/SM	0.1[3]	-	-	305	SM	CuO
CuO[0.1]-H_2O_2[0.5]/SM	0.1[3]	-	0.5	305	SM	CuO
CuO[0.1]-H_2O_2[1]/SM	0.1[3]	-	1	305	SM	CuO
CuO[0.1]-H_2O_2[2]/SM	0.1[3]	-	2	305	SM	CuO

Key: In reference to copper salt, 1 = $(SO_4)_2$, 2 = $(NO_3)_2$ and 3 = OAc_2. SM refers to the single mixer set up and DM refers to dual mixer (utilising a quench). For all samples that used a DM, the flow rate was 160 mL min^{-1} and only D.I. water was used. The * refers to contaminated CuO (containing brochantite). The metal salt was fed through P2 whilst KOH and H_2O_2 were fed through P3. For the flow rates for each specific mixing temperature, the reader is referred to Table 3-1 H_2O_2 mentioned in [ ] refers to vol%.

3.2.3.2 Synthesis of Cu_2O and Cu

Table 3-3 details the experimental parameters for the synthesis of Cu_2O and Cu nanoparticles. For all samples, the metal salt concentration was kept at 0.1 M, where the reducing agent concentration is altered, this is highlighted in the Cu:RA column. PVP was used as capping agent and added through the quench feed at 160 mL min^{-1}. For Cu_2O and Cu synthesis, degassing the precursor feeds with N_2 was necessary otherwise CuO impurities formed regardless of reducing agent concentration tested.

Table 3-3 - Experimental parameters for the synthesis of Cu_2O and Cu.

Sample	Cu^{2+} conc./M	Cu:RA	PVP	Mixer type	Product
Cu_2O/Cu-PM-1:5	0.1[1]	1:5	-	PM	Cu_2O/Cu
Cu-PM-1:50	0.01[1]	1:50	-	PM	Cu_2O/Cu
CuO-FA-1:1	0.1[1]	1:1	-	DM	CuO
Cu_2O-FA-1:3	0.1[1]	1:3	-	DM	Cu_2O
Cu_2O/Cu-FA-1:5	0.1[1]	1:5	-	DM	Cu_2O/Cu
Cu_2O-PVP0	0.1[1]	1:3	-	DM	CuO
Cu_2O-PVP1	0.1[1]	1:3	1 wt%	DM	Cu_2O
Cu_2O-PVP2	0.1[1]	1:3	2 wt%	DM	Cu_2O
Cu_2O-PVP3	0.1[1]	1:3	3 wt%	DM	CuO
Cu_2O-PVP4	0.1[1]	1:3	5 wt%	DM	Cu_2O
Cu_2O-SO_4/1:3C	0.1[1]	1:3†	-	DM	Cu_2O
Cu_2O-SO_4/1:5C	0.1[1]	1:5†	-	DM	Cu
Cu_2O-SO_4/1:3C/P	0.1[1]	1:3†	-	DM	Cu_2O
Cu_2O-SO_4/1:5C/P	0.1[1]	1:5†	-	DM	Cu
Cu_2O-OAc	0.1[3]	-	-	DM	CuO
Cu_2O-OAc/1:3C/P	0.1[3]	1:3†	-	DM	Cu_2O
Cu_2O-OAc/1:5C/P	0.1[3]	1:5†	-	DM	Cu

Key: In reference to copper salt, superscript 1 = $(SO_4)_2$, 2 = $(NO_3)_2$ and 3 = OAc_2. PM refers to a pre-mixer, SM refers to the single mixer, DM refers to dual mixer (utilising a quench). For all samples that used a DM, the flow rate was 160 mL min^{-1} D.I. water was used, unless PVP is utilised. The metal salt and reducing agent was fed through P2 whilst KOH was fed through P3. The KOH concentration was 0.2 M for all runs. PVP was fed through P4. The mixing temperature was kept at 335 °C for all samples. The reader is directed to Table 3-1 for details on the flow rates.

3.2.4 Materials Characterisation

The as-prepared samples were characterised by PXRD, XPS and TEM as described in Chapter 2. For size measurements, 100 particles were used as a sample size.

3.3 Results and Discussion

3.3.1 Synthesis of CuO

3.3.1.1 Effect of metal salt and mixer types

The effect of the mixer design and the metal precursor was investigated by synthesising CuO in a single and dual mixer set up. Copper sulfate, nitrate and acetate salts were used at a concentration of 0.1 M with 0.2 M KOH and the slurry was collected at the output of the BPR. For all samples, the products were a dark brown colour. The yield was generally >80% for all samples except for CuO-SO_4/SM and CuO-OAc/DM, where the yield was <65% (Table 3-4). This may be due to sample processing issues or due to the short residence time of the synthesis process, where the copper ions have not had sufficient time to nucleate and grow. It is unlikely to be related to the precursor, as this was not observed for samples synthesised with the same precursor but in a different mixer. The PXRD patterns for the as-prepared dried CuO nanopowder are given in Figure 3-2a for the single mixer and Figure 3-2b for the dual mixer. Pure phase CuO was formed in all cases and matched well with the standard CuO reference pattern, JCPDS 01-089-2529, except, when copper sulfate was used in the dual mixer (Figure 3-2b). Impurity peaks were identified being similar to the mineral brochantite, $Cu_4SO_4(OH)_6$ that has a standard reference pattern JCPDS 01-087-0454 and are marked by an asterisk in the XRD pattern.

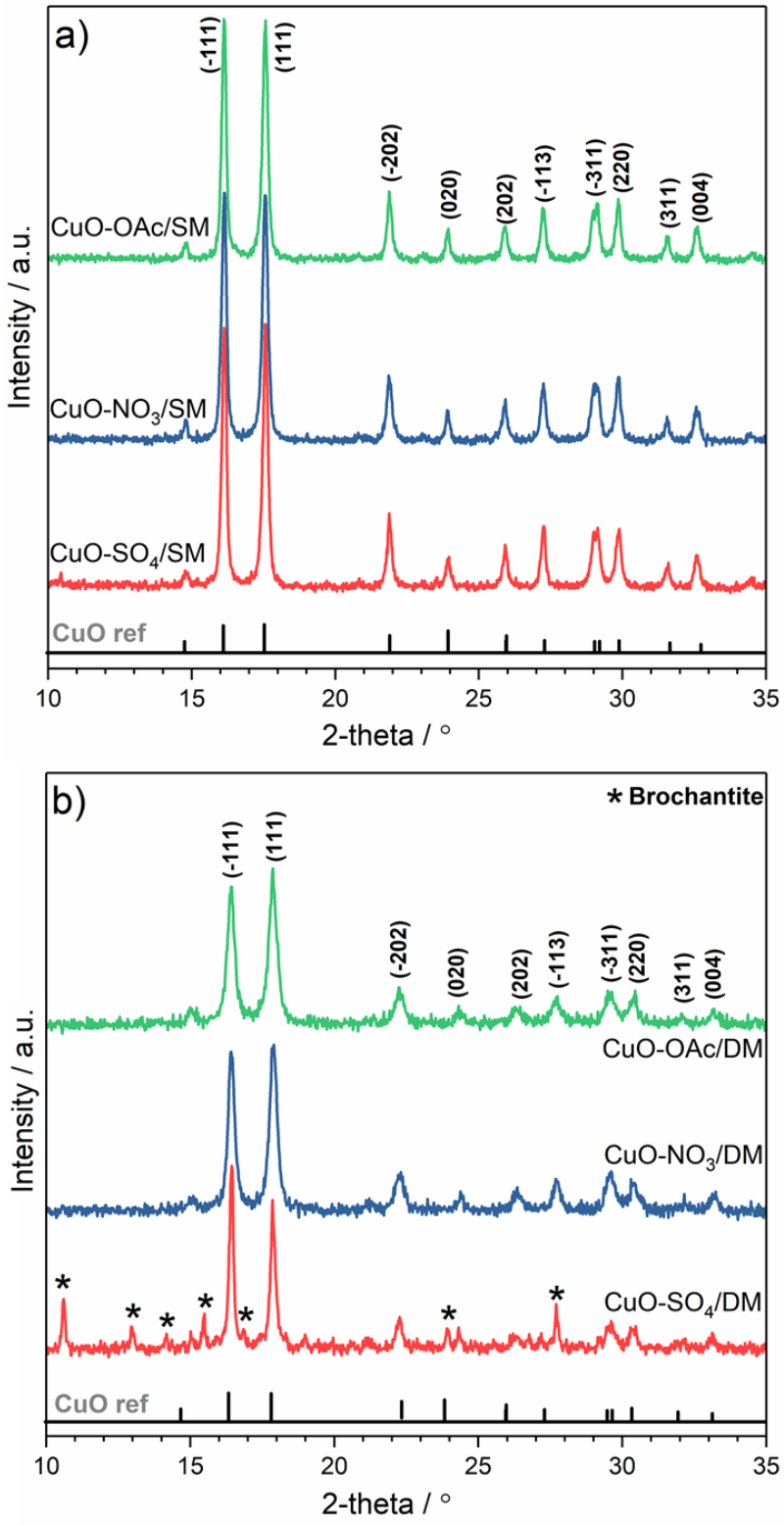

Figure 3-2 – a) PXRD patterns for CuO synthesised via the single mixer and b) PXRD patterns for CuO synthesised via a dual mixer set up. Samples were synthesised using copper sulfate, nitrate and acetate metal salts (0.1 M) and KOH (0.2 M) at a mixing temperature of 305 °C at 24.1 MPa. The asterisk in Figure 3-2b shows an impurity phase brochantite $Cu_4SO_4(OH)_6$.

The crystallite size, as measured by the Scherrer equation, showed the crystallite size was smallest for samples prepared using the copper nitrate precursor (with the single mixer, CuO nitrate was 11.8 nm and CuO-acetate was 16.6 nm). However, there was not a significant difference between the samples and the crystallite size was slightly larger for samples prepared by the quench, in the case of CuO-sulfate and CuO-nitrate and for CuO-acetate the crystallite size decreased ca. 6 nm when the quench was used (Table 3-4).

During the formation of metal oxides via hydrothermal synthesis, it is commonly reported and assumed that the formation of metal oxides proceeds via the formation of metal hydroxide, which is subsequently dehydrated to form the metal oxide. Early experimental studies considering the titration of sodium hydroxide and copper sulfate solution indicated that the mixing of these species does not result in copper hydroxide, however, it forms copper sulfate hydroxide.[128] Brochantite is only stable at a certain pH, as indicated by the Pourbaix diagram (Figure 3-3). According to the Pourbaix diagram, the formation of brochantite is possible in slightly acidic conditions (pH range 5 to 7), whereas the synthesis of CuO is favoured at higher pH. The stability field of copper sulfate hydroxide phases is also affected by the activity of aqueous copper species, where antlerite is possible at low Cu activities, in a more acidic region.[129]

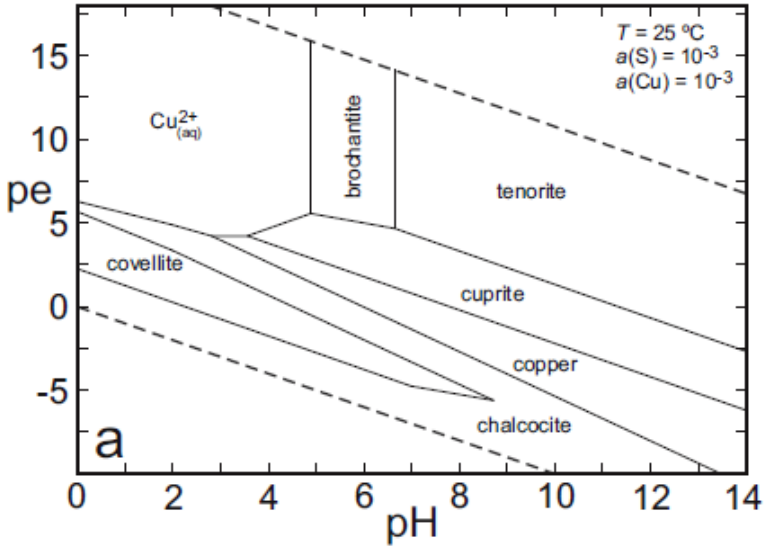

Figure 3-3 – Pourbaix diagram for Cu-S-H system at 25 °C for specified activities (Reproduced with permission from ref[129]).

During the synthesis of metal oxides via the CHFS reactor, the metal salt and KOH precursors met in a tee-piece at room temperature before meeting the supercritical water feed. This is an approach designed to avoid blockages and ensure homogeneous mixing of the precursors prior to meeting the supercritical water, as mentioned in Chapter 1. The pH of the copper sulfate and KOH at room temperature was tested at the metal to base ratio of 1:2 (as used in the synthesis in the CHFS reactor) and was found to be pH 7.1. If a lower metal to base ratio was used (1:1), the pH at room temperature upon mixing was pH 5.2. It is evident that the synthesis of CuO via copper sulfate is sensitive to pH changes upon the initial mixing. Although the selected metal to base ratio was favourable for the formation of copper oxide, herein, this was not observed. It is possible that during this run, the flow rates were not optimised, resulting in the formation of brochantite impurities with CuO formation. To further understand the effect of the metal to base ratio, different concentrations of KOH were tested with a constant copper sulfate concentration. The effect of temperature was also investigated using a dual mixer and is discussed in more detail in Section 3.3.1.2.

XPS survey analysis revealed the presence of Cu and O as well as adventitious carbon (Figure 3-4a) and the high-resolution scans confirmed

the presence of Cu^{2+} due to the position of the Cu $2p_{3/2}$ (934.3 eV) and Cu $2p_{1/2}$ (954.2 eV) peaks as well as the presence of satellite peaks, which are only present for Cu^{2+} (Figure 3-4b). The oxygen high resolution scan (Figure 3-4c) revealed the presence of some surface carbonate, which is likely present due to the copper oxide exposure to the atmosphere post synthesis as carbonate species tend to bind strongly to copper. When a depth profile was conducted, carbonate species were not observed in the Cu high resolution scan, which confirmed that the carbonate was only present as a surface species.

The particle size and morphology of CuO nanoparticles synthesised via the single mixer and dual mixer were compared by TEM (Figure 3-5). The particles were generally cuboid in morphology and changes to the morphology were not observed for CuO samples when a single mixer was used versus a double mixer. However, the average particle size was, in general, larger for the particle synthesised when no quench was used (Figure 3-5). Table 3-4 details the average particle size, size distribution and crystallite size as obtained from the Scherrer equation. The particle size distribution was significantly broader for samples synthesised via a single mixer. The particle size did not vary significantly between each of the precursors, indicative that the anion had no significant impact on the solubility and supersaturation behaviour of CuO. A number of changes occur to the interaction between cation and anions in the supercritical conditions. In the case of Co_3O_4 for example, the nature of the anion was found to change the particle morphology, during batch hydrothermal synthesis, however any anion dependence was not observed for CuO.[122] This is further corroborated by studies in the literature, where the solubility enhancing effects of complexing ligands (chlorides and acetates) were found to be insignificant for CuO at elevated temperatures in both oxidising and reducing conditions.[130–133]

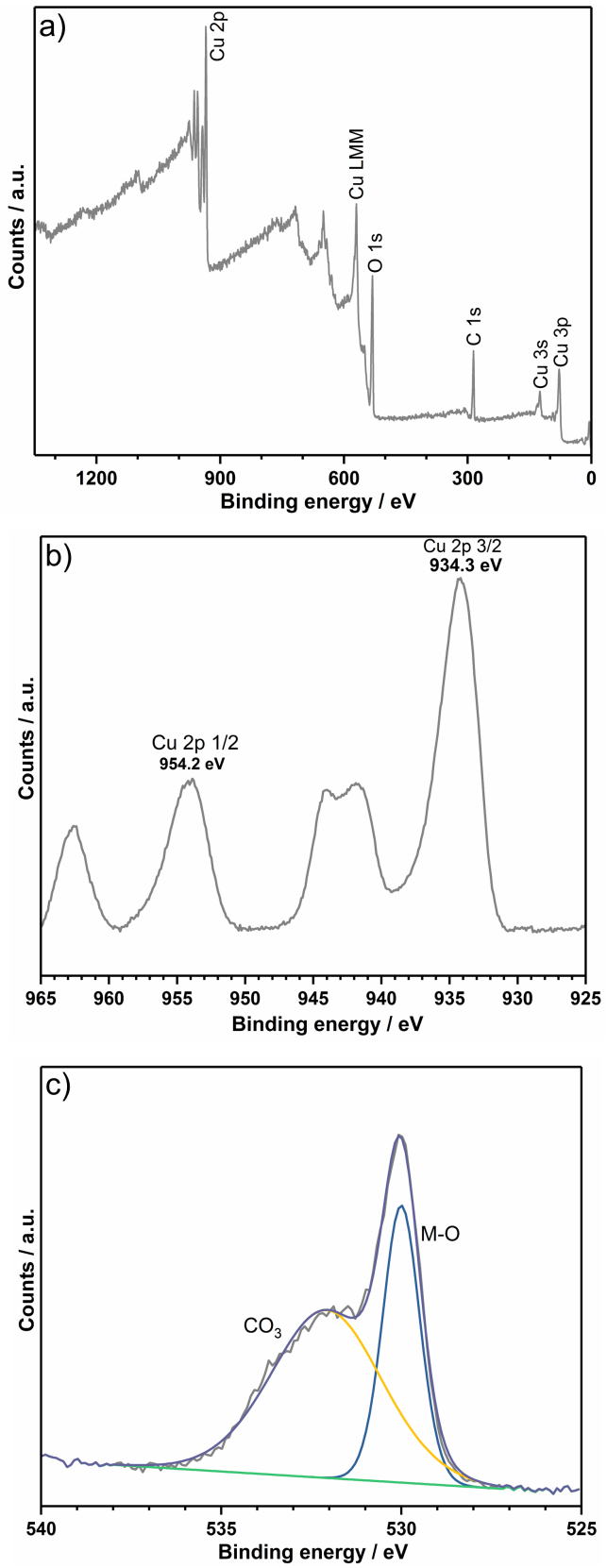

Figure 3-4 – XPS spectrum for sample CuO-NO_3/DM synthesised using copper nitrate (0.1 M) and KOH (0.2 M) at a mixing temperature of 305 °C, using a dual mixer set up – a) survey spectrum, b) Cu^{2+} high resolution 2p scan and c) O^{2-} high resolution 1s scan.

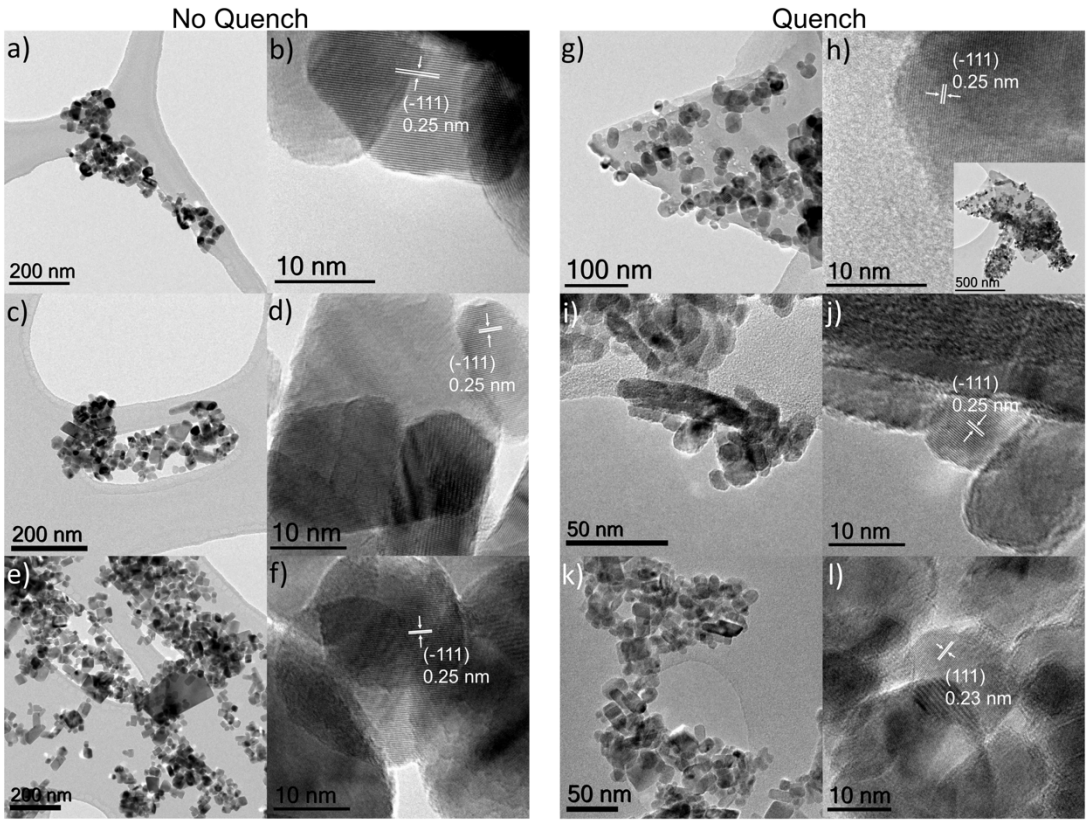

Figure 3-5 – TEM image of CuO synthesised using different copper precursors a) sulfate, c) nitrate and e) acetate precursors using the single mixer (no quench) with the corresponding high resolution TEM image from b, d and f. CuO synthesied via the dual mixer are shown using copper g) sulfate, i) nitrate and k) acetate with the corresponding high resolution TEM image from h, j and l. For Figure 3-5h, the inset shows the low magnification image to show the brochantite sheets.

The formation of large sheets (>500 nm) was observed in the case of CuO-SO_4/DM (Figure 3-5g), with CuO particles embedded in the sheets. It was not possible to obtain high resolution lattice plane images for the sheet structures, however, based on the observations from the PXRD pattern that a secondary phase was present, the sheets were deemed to be brochantite with CuO forming on the brochantite sheet. The high resolution TEM images of the particles within the sheet structure confirmed to be CuO (d-spacing 0.25 nm corresponding to the (–111) plane).[134]

A significant particle size reduction was observed when the quench was used (for all precursors). For example, in the case of CuO-acetate, the particle size decreased from 37.8 to 13.5 nm when the quench was used, which was the largest particle size reduction. For copper sulfate, the particle size reduction

was only 5.6 nm and for the CuO-nitrate, the particle size reduction with a quench, was more significant at 15.3 nm. Similarly, the surface area was lower for samples prepared via the single mixer. The quench was successful in reducing the particle size of CuO and hindering particle growth, that continued to occur via the single mixer. Commonly in the literature, the synthesis of CuO via CHFS type processes has been limited to >30 nm.

Table 3-4 - Data summary for CuO synthesis via sulfate, nitrate and acetate synthesised with and without a quench including yield, crystallite size, surface area (measured by BET) and particle size.

Sample		Yield / %	Crystallite size / nm (PXRD)	Surface area / $m^2\ g^{-1}$	Avg. particle size / nm (TEM)	SD for particle size / nm
No quench	CuO-sulfate	53	17.5	28.8	35.1	14.1
	CuO-nitrate	89	11.8	35.2	31.3	12.7
	CuO-acetate	97	16.6	25.3	37.8	15.5
Quench	CuO-sulfate	92	19.1	28.2	29.5	16.5
	CuO-nitrate	83	12.2	45.4	16.0	5.4
	CuO-acetate	63	10.5	51.4	13.5	6.1

The particle size could be controlled by utilising different CJM mixer set ups. The effectiveness of the dual mixer has also been shown in the synthesis of Co_3O_4, where sub-10 nm particles could be synthesised when the quench was in place downstream of the initial CJM mixing point. To verify the effect of the quench, the particle size distribution was approached through D90, D50 and D10 values, which show the particle size below the 90^{th}, 50^{th} and 10^{th} percentile, respectively (Figure 3-6). This analysis was carried out for the CuO samples synthesised with and without quench and showed the impact the presence of the quench has on limiting particle growth as well as the size distribution. This indicated that when CuO was synthesised with no quench, CuO nuclei were generated in the first mixer which continue to grow through coalescence. As the yields of the samples prepared by the quench were still high, it did not suggest that CuO particles were growing from ions in solution. The particle growth was limited when the quench was used, as the residence time was significantly shortened (from 4.35 to 0.76 s) by introducing an

ambient temperature D.I. water feed post CuO synthesis. The high resolution TEM images for most samples (except sample CuO-OAc/DM) indicated the formation of CuO (d-spacing of 0.25 nm, (–111)) as shown in Figure 3-5. For sample CuO-OAc/DM, d-spacing of 0.23 nm corresponding to the CuO (111) plane was observed.[134,135]

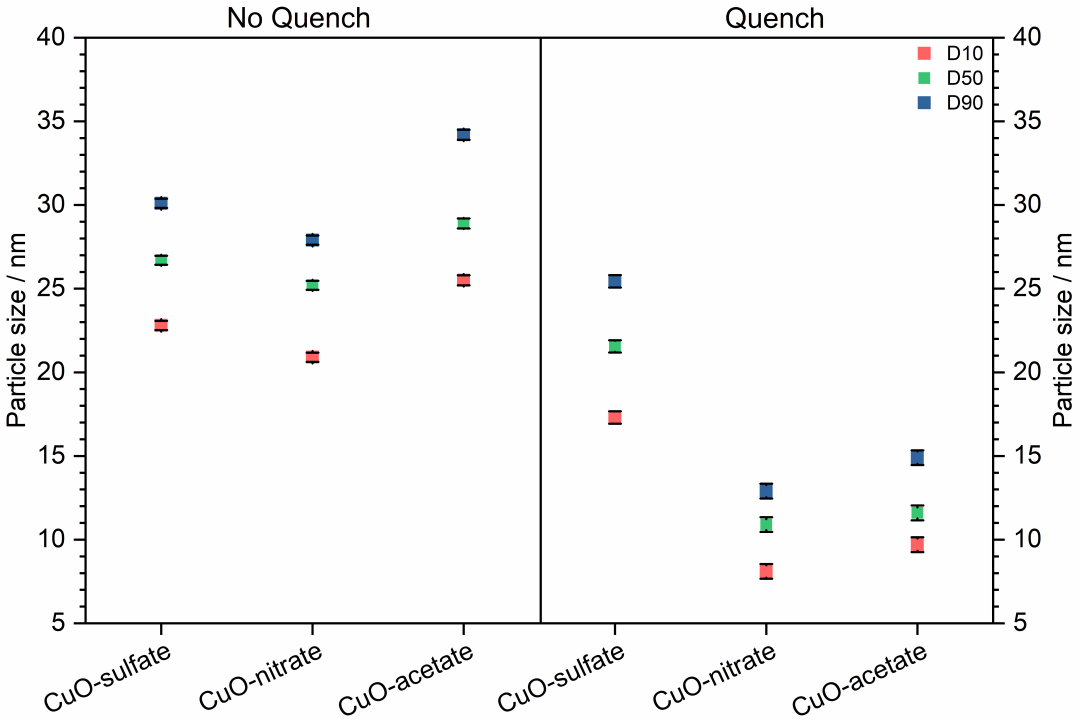

Figure 3-6 – Parameters of the size distribution (D90, D50 and D10 values) for CuO synthesised via copper sulfate, nitrate, acetate precursors, comparing use of no quench versus quench mixers

3.3.1.2 KOH concentration and temperature effects

The synthesis of CuO from copper sulfate presented with an impurity brochantite phase and CuO, so the effect of KOH and temperature on the synthesis of CuO was studied to gain a better understanding of how the pH and temperature altered the nucleation and growth dynamics. The copper sulfate concentration was kept at 0.1 M and the KOH concentration was varied in the range 0.1 to 0.4 M at mixing temperatures of 305, 335 and 375 °C. The formation of pure phase brochantite was evident from the PXRD pattern at a metal to base ratio of 1:1 (Figure 3-7) at mixing temperatures of 305 °C, similar to the reference pattern JCPDS 01-087-0454. At 335 °C

brochantite was formed in conjunction with CuO, which indicated there was some temperature dependency, as CuO was also formed. The formation of brochantite was not observed at a mixing temperature of 375 °C. At metal to base ratio of 1:2 and above, the formation of brochantite was also not observed. CuO was formed directly at this KOH concentration and above, regardless of the mixing temperature. The impurity peaks (marked by asterisks in Figure 3-7c) observed in the case of higher temperatures (T_{mix} = 375 °C) at higher base concentrations (Figure 3-7c) was due to the presence of $CaCO_3$, possibly arising from the clean-up stage. The mixing temperature clearly played a role in the formation of brochantite at low metal to base ratio. The thermal stability and decomposition of brochantite has been studied previously via thermogravimetric/differential thermal analysis (TG/DTA), where conversion of brochantite to CuO and Cu_2OSO_4 was observed at around 400 °C (Equation 3.1) and then the decomposition of the sulfate occured at 700 °C according to Equation 3.2.[136]

$$Cu_4(OH)_6SO_4 \rightarrow Cu_2OSO_4 + 2CuO + 3H_2O \qquad \text{Equation 3.1}$$

$$Cu_2OSO_4 \rightarrow 2CuO + SO_3 \qquad \text{Equation 3.2}$$

Novikova et al., synthesised CuO nanoparticles from brochantite and observed the formation of CuO from 400 °C.[137] It was evident from these experiments that the synthesis of CuO from copper sulfate was highly dependent on the mixing temperature and the reaction pH. Therefore, it is sensitive to any error in the flow rates of the initial mixing of the precursors in the tee-piece mixer prior to meeting the supercritical water feed.

The temperature and the base concentration were found to affect the crystallite size and surface area (Figure 3-8). The crystallite size for the sample at 0.1 M KOH at low mixing temperatures was taken for brochantite. For other samples, the crystallite size was calculated for the CuO peaks. At low base concentrations (0.1 M KOH), the crystallite size was the smallest

(14.1 nm) for high mixing temperatures and at mixing temperatures <350 °C, the crystallite size was ca. 28 nm. The general trend was that the crystallite size increased with increasing base concentration and mixing temperatures. Similarly, the surface area decreased with increasing base concentrations and mixing temperatures. An optimum base concentration (0.2 M) and mixing temperature (305 °C) was found where the smallest crystallite size (sub-10 nm) was obtained. The synthesis of CuO using supercritical water has been investigated previously but the focus has remained on understanding the effect of mixing or comparing the synthesis of different metal oxides in the context of varying residence times. Specifically, the addition of KOH and temperature has not been studied for the synthesis of CuO. Sue et al., reported that the particle size of NiO nanoparticles decreased from 17 to 3 nm upon the addition of KOH.[119]

The results can be explained by considering the solubility of CuO in water at elevated temperatures and pressures. The solubility of CuO is strongly coupled with the pH and temperature. Below neutral pH, the CuO solubility decreased with increasing temperature, however, above neutral pH, the solubility of CuO increased up to 250 °C then decreased rapidly, according to Palmer et al.[138] This was also investigated by Sue et al.[139] who stated that solubility of CuO was at a maximum around 320 °C and then decreased with increasing temperature. However, the authors did not consider the effect of pH in this case. Nucleation theory dictates that the degree of supersaturation determines the formation of small particle sizes as small nuclei are formed at high supersaturation rates. When the solubility of CuO is high in water, the supersaturation rates are lower, resulting in the formation of few nuclei and hence, leading to the formation of larger particles as CuO continues to grow from solution.

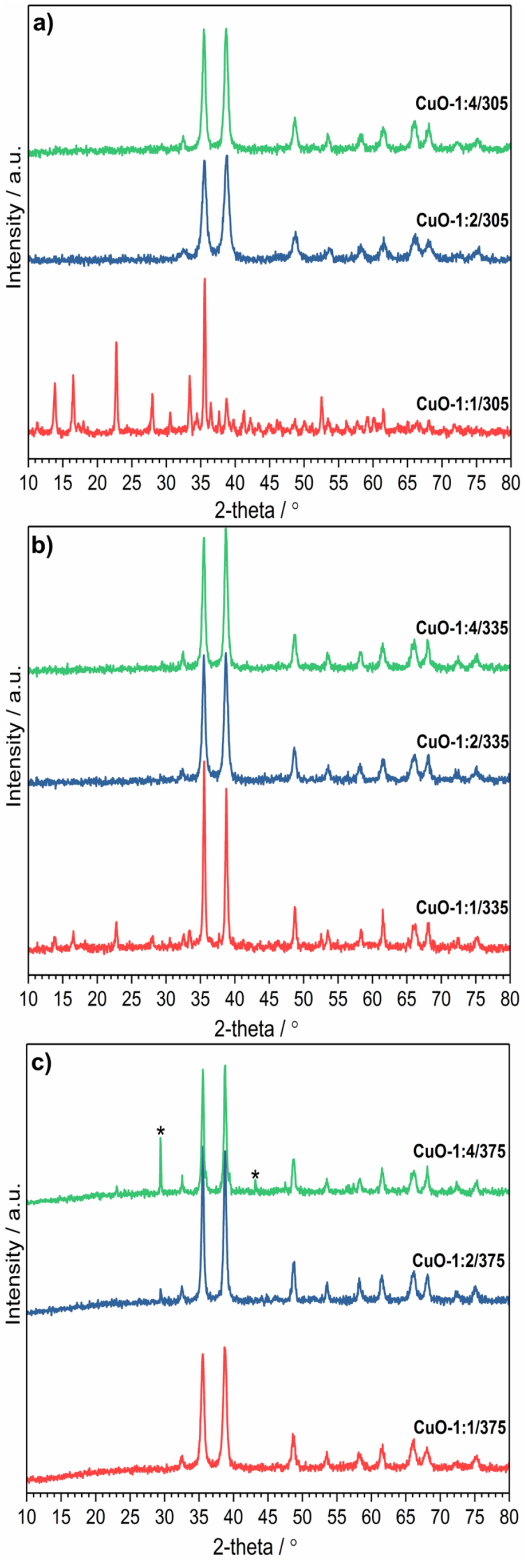

Figure 3-7– PXRD patterns for the synthesis of CuO from copper sulfate (0.1 M) with increasing KOH concentration (0.1, 0.2 and 0.4 M) at mixing temperatures of a) 305 °C, b) 335 °C and c) 375 °C using a dual mixer CHFS set up. Asterisk marked in Figure 3-7c shows an impurity phase $CaCO_3$ arising from the clean-up stage.

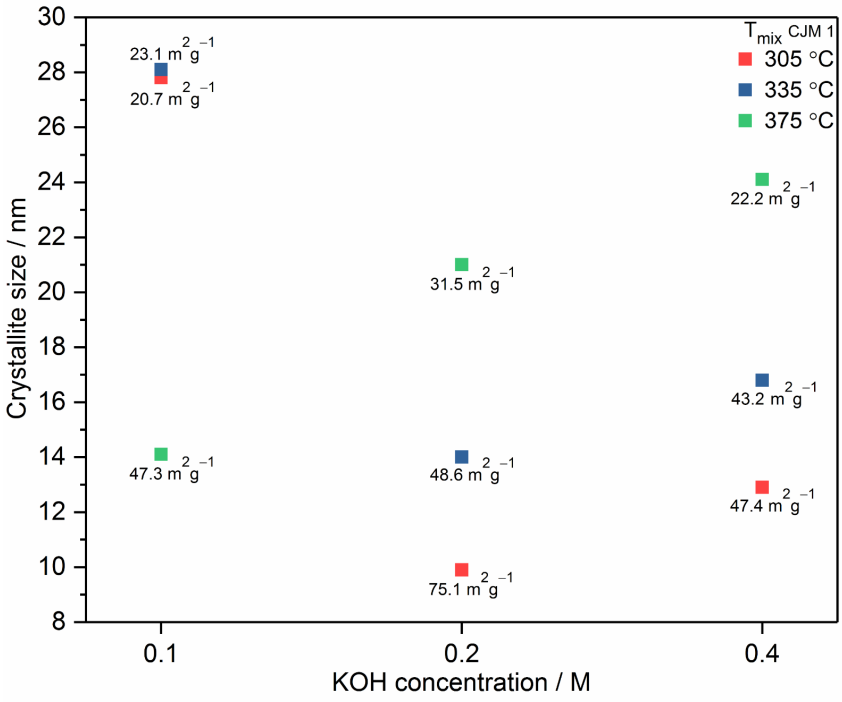

Figure 3-8 – Plot of crystallite size and surface area of CuO synthesised from copper sulfate at constant copper salt concentration and KOH concentration of 0.1, 0.2 and 0.4 M and three different mixing temperatures in a dual mixer CHFS set up.

TEM images were obtained for the CuO with the smallest crystallite size synthesised at the optimum conditions, which revealed an average particle size of 15.0 ± 7.3 nm (Figure 3-9). The particles had a cuboid morphology and were similar to CuO nanoparticles formed in the literature during similar hydrothermal flow techniques. The high resolution TEM images showed a d-spacing of 0.25 nm corresponding to the CuO (–111) plane (Figure 3-9b).

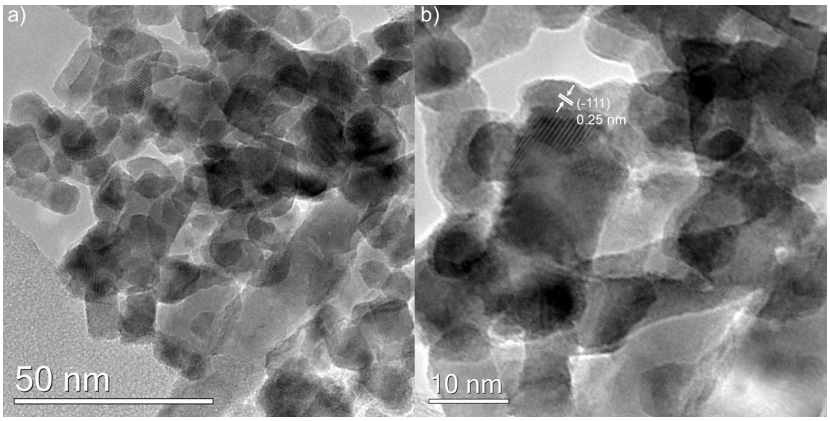

Figure 3-9 – TEM images of sample CuO-1:2/305 synthesised from copper sulfate at base concentration of 0.2 M and mixing temperature of 305 °C.

3.3.1.3 Influence of H_2O_2

The effect of H_2O_2 as an additive was considered in the absence of KOH. CuO was synthesised via the CHFS process (single and dual mixer set up) using copper acetate as a metal salt precursor. Other copper salt precursors (nitrate and sulfate) were also used to synthesise CuO in the absence of KOH, however, resulted in no product formation. The resulting solution from the output of the BPR was blue, which suggested that CuO was either formed in the mixer and then re-dissolved or no CuO initially precipitated. Thus, for copper nitrate and sulfate precursors, KOH was required to achieve the appropriate conditions for the successful synthesis of CuO. Similar results have been observed with nickel and iron based oxides.[122,140,141]

The use of copper acetate as a metal precursor resulted in the direct formation of CuO. The chosen mixing temperature was limited to 305 °C, as the previous experiments (Section 3.3.1.2) suggested that a lower mixing temperature was favourable for the formation of small-sized CuO nanoparticles. Initially, the effect of metal salt concentration was evaluated, where the metal salt concentration was varied in the range 0.05 to 0.3 M. The yield remained high for all samples synthesised using copper acetate precursor alone (in the range 80 to 90 %) (Table 3-5). The PXRD was obtained of the as-prepared dried nanopowders, shown in Figure 3-10.

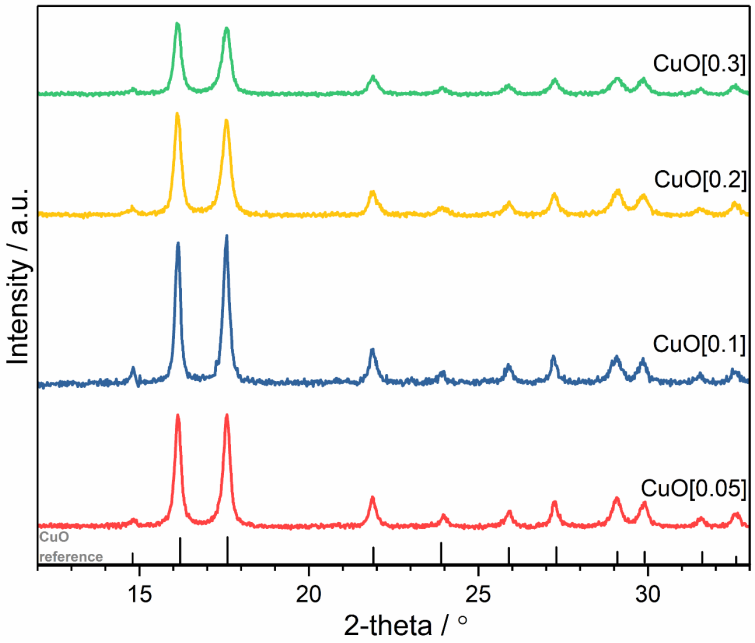

Figure 3-10 – PXRD pattern of CuO synthesised via the dual mixer CHFS set up, using copper acetate only (with increasing metal concentration, in the range 0.05 to 0.3 M) at a mixing temperature of 305 °C.

At all concentrations and within the conditions tested, pure CuO was formed, with no other impurity phases, such as $Cu(OH)_2$, Cu_2O and Cu. The peaks observed matched well with the reference pattern presented (JCPDS 01-089-2529). Broadening of the CuO peaks were observed with increasing concentration, which was reflected in the decreasing crystallite size (Table 3-5), as determined by the Scherrer equation. It was also expected that increasing the copper acetate concentration would result in the decrease of the output slurry pH, as more acetic acid was formed. Acetic acid formed as the copper acetate decomposed, at the same time copper hydroxide formed, which was subsequently dehydrated to CuO (as shown in the scheme below, Equation 3.3 and 3.4). The dehydration pathway (Equation 3.4) also shows the decomposition of acetic acid into CO, CO_2, H_2 and CH_4, but this not stoichiometrically represented as a range of products are possible from acetic acid decomposition, dependent on the reaction conditions.[142]

$$Cu(CH_3COO)_2 + 2H_2O \rightarrow Cu(OH)_2 + 2(CH_3COOH) \quad \text{Equation 3.3}$$

$$Cu(OH)_2 + 2(CH_3COOH) \rightarrow CuO + H_2O + [CO + CO_2 + H_2 + CH_4] \quad \text{Equation 3.4}$$

It was expected that as the copper acetate concentration increased, increasing amounts of acetic acid would be formed, however, the output pH did not decrease, as shown in Table 3-5. A similar observation was observed when Co_3O_4 was formed using the same CHFS reactor, where a quench was used in the synthesis process. The authors observed the pH decreased with increasing cobalt acetate concentration in a single mixer set up, however, with the addition of the quench, the pH increased due to the dilution effect from the quench feed, which was also operating at 160 mL min^{-1}.[113]

For each copper acetate concentration, 1 v/v% H_2O_2 was added in the Pump 3 feed (used for KOH typically) to understand the effect of H_2O_2 on the CuO nanoparticle formation. Similarly, the addition of H_2O_2 did not result in any impurity phases and pure phase CuO was formed, as observed in the PXRD patterns confirmed with the reference pattern (Figure 3-11). Peak broadening was apparent but did not significantly vary between each sample. The addition of H_2O_2 decreased the pH despite the increasing concentration of copper acetate and the presence of the quench feed. The yield was also affected by the addition of the H_2O_2 as it decreased in the range 60 to 70% (Table 3-5). This may be expected, considering the copper Pourbaix diagram, where due to the decreasing pH the Cu^{2+} ion becomes increasingly stable at pH lower than 6 in an oxidising environment.[143,144] Therefore, some dissolution of CuO is possible as the output pH is in the range 3.8 to 4.7.

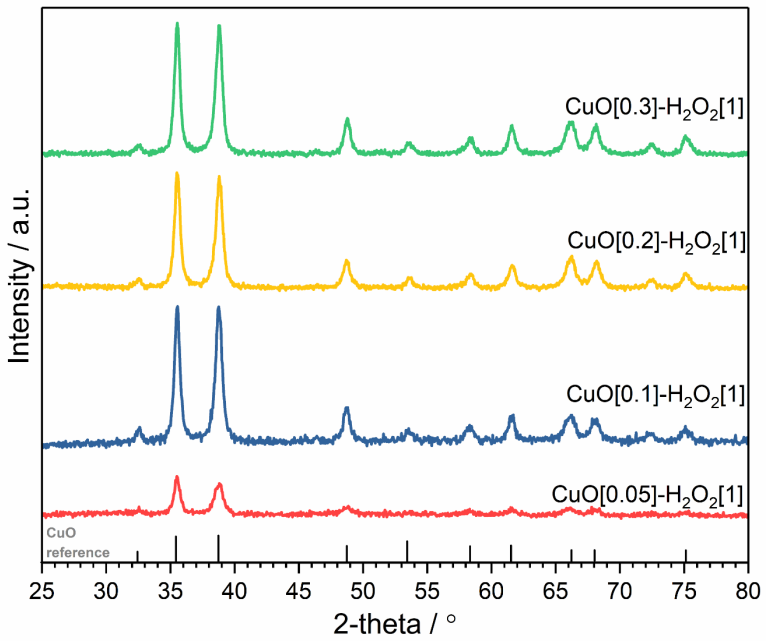

Figure 3-11 - PXRD pattern of CuO synthesised via the dual mixer CHFS set up, using copper acetate only (with increasing metal concentration) and 1 v/v% H_2O_2 fed through pump 3 at a mixing temperature of 305 °C.

Table 3-5 - Summary of pH, yield, crystallite size, surface area and particle size for CuO synthesised using the dual mixer set up, with increasing copper acetate concentration (0.05 to 0.3 M) with and without the addition of 1 v/v% H_2O_2.

Sample	pH	Yield / %	Crystallite size / nm (PXRD)	Surface area / $m^2\ g^{-1}$	Avg. particle size / nm (TEM)	SD for particle size / nm
CuO[0.05]	4	83	15.3	26.4	38.0	14.7
CuO[0.1]	3.5	87	16.9	27.7	38.5	15.1
CuO[0.2]	4	92	12.3	27.2	32.4	15.5
CuO[0.3]	4.2	91	12.1	33.1	24.0	9.2
CuO[0.05]-H_2O_2[1]	4.2	74	15.7	27.8	29.5	16.8
CuO[0.1] -H_2O_2[1]	4.7	67	13.8	35.9	10.9	4.2
CuO[0.2] -H_2O_2[1]	3.8	68	13.2	33.2	19.6	15.6
CuO[0.3] -H_2O_2[1]	3.9	72	12.9	31.4	30.9	13.9

The surface area increased slightly with decreasing crystallite size as expected but the measured surface area was significantly lower than estimated surface area, determined by the equivalent sphere diameter (in the range 60 to 85 $m^2\ g^{-1}$). The particles were also characterised by TEM (Figure 3-12). Figure 3-12 a-d showed the CuO particles formed without the addition of H_2O_2 and with increasing concentration from figures a to d. With increasing concentration, the particles decreased in size and became less aggregated. A change in the morphology was not observed between the samples,

however, an average size reduction from 38 to 24 nm was observed between samples CuO[0.05] and CuO[0.3], respectively. For samples with the addition of H_2O_2, Figure 3-12 e-h, a significant difference was not observed for samples CuO[0.05]H_2O_2[1], CuO[0.2]H_2O_2[1] and CuO[0.3]H_2O_2[1] compared to the particles synthesised without the addition of H_2O_2. However, the addition of 1 v/v% H_2O_2 was significant for the CuO[0.1]H_2O_2[1] sample. The particles were significantly smaller and less aggregated compared to its counterpart with no H_2O_2 addition (Figure 3-12b). The formation of small (sub-5 nm) spherical CuO nanoparticles were also observed (see inset Figure 3-12f) along with slightly larger spherical CuO nanoparticles. The high resolution TEM image of the CuO[0.1]-H_2O[1] sample revealed a d-spacing of 0.23 nm corresponding to the (111) plane, which was confirmed to be CuO (Figure 3-13).[135]

D90, D50 and D10 analysis highlighted the significance of increasing copper acetate concentration within the precursor feed as well as adding H_2O_2 in the auxiliary feed (Figure 3-14). The decrease in the size of CuO nanoparticles could be confirmed if the D90 number was considered between samples CuO[0.05] and CuO[0.3]. The size distribution also became significantly narrower with sample CuO[0.3]. The measured yield increased from ca. 83 to 92 % between the samples. This change is significant and unexpected. For the synthesis of Co_3O_4 in the literature, Denis et al. used a single and double mixer in both a turbulent and laminar mixing regime. Turbulent mixing regimes ensure complete and efficient mixing, whereas, laminar mixing remains in parallel layers without complete mixing. Denis et al. observed that when a turbulent mixer was used, the particle size increased with increasing metal salt concentration.[145] In the Co_3O_4 study, cobalt acetate was used as a metal salt precursor in the absence of KOH, with H_2O_2 added through the heaters.[113]

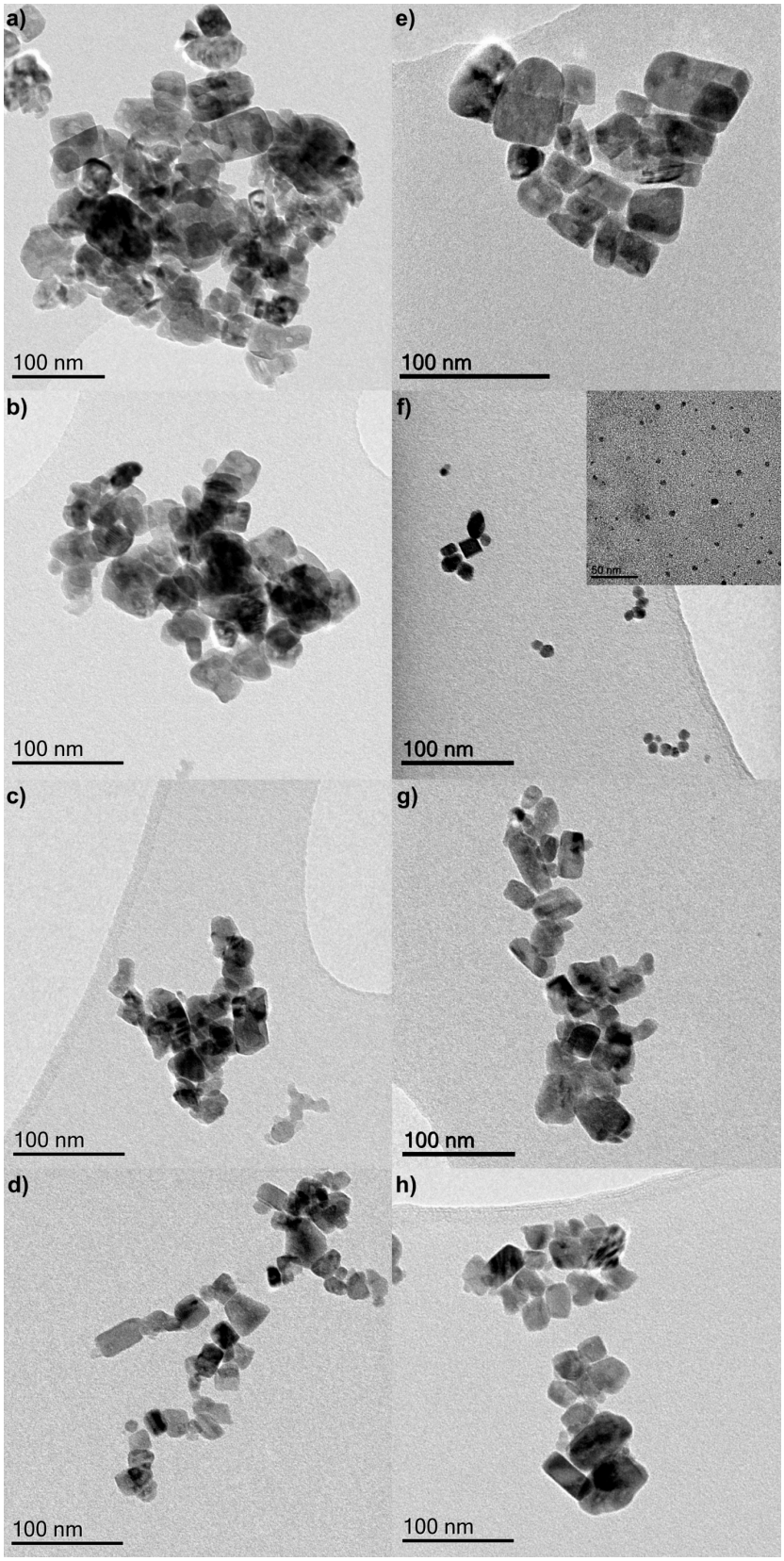

Figure 3-12 - TEM images of CuO synthesised using copper acetate at different concentrations in the absence of KOH, at a mixing temperature of 305 °C – a) 0.05 M, b) 0.1 M, c) 0.2 M and d) 0.3 M e) 0.05 M and 1 v/v% H_2O_2, f) 0.1 M and 1 v/v% H_2O_2, g) 0.2 M and 1 v/v% H_2O_2, f) 0.3 M and 1 v/v% H_2O_2.

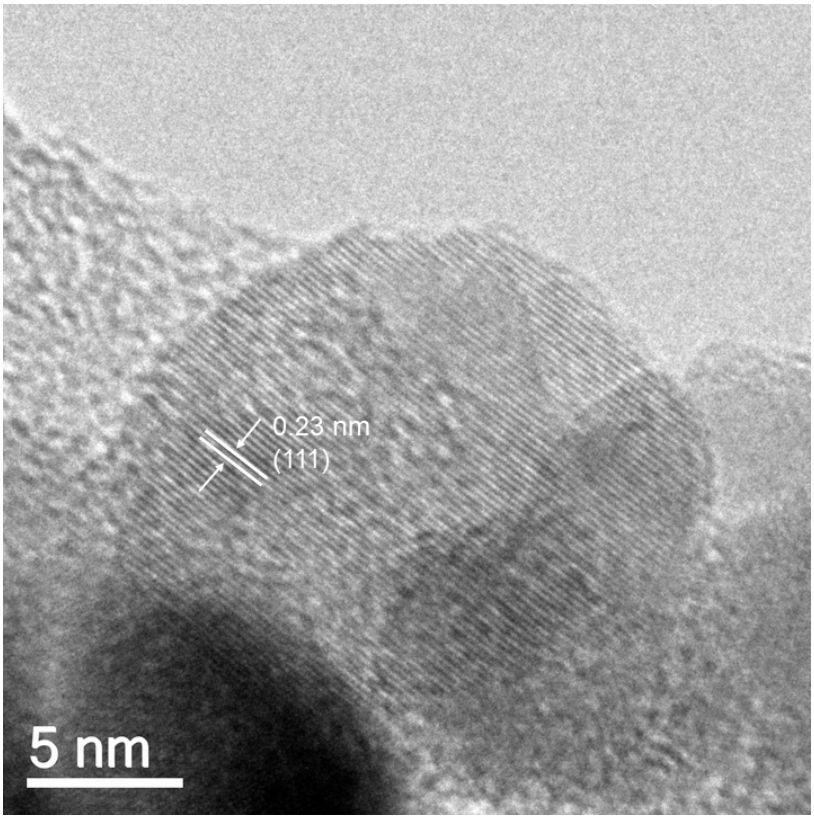

Figure 3-13 – High resolution TEM image of sample CuO[0.1]-H_2O_2[1] showing the (111) plane with a lattice spacing of 0.23 nm.

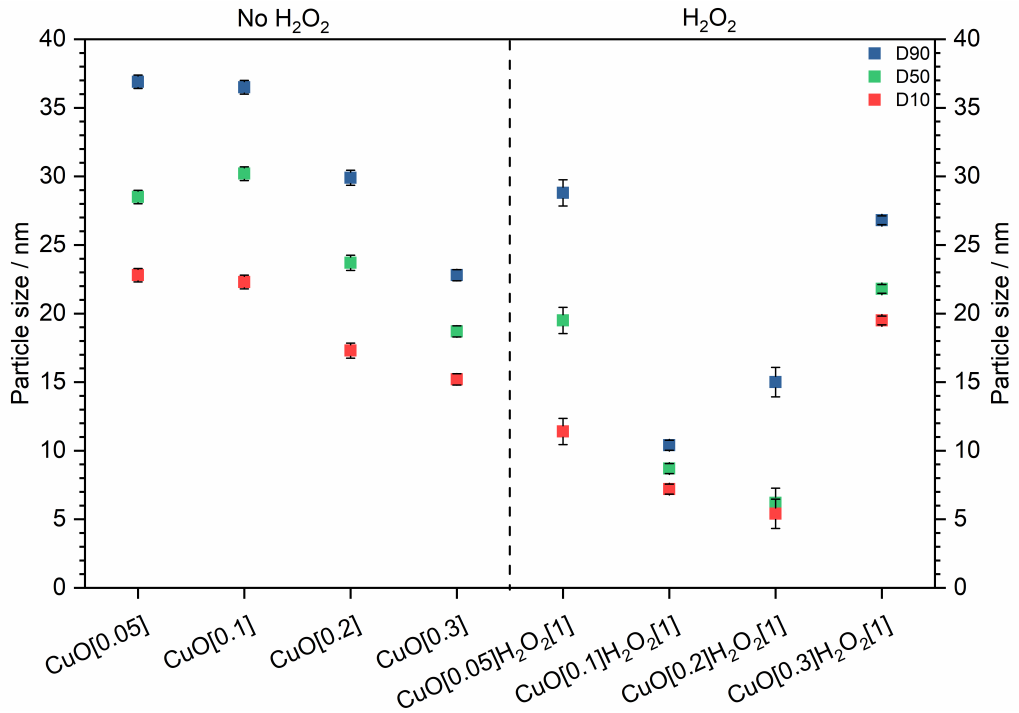

Figure 3-14 – D90, D50, D10 analysis of CuO synthesised with increasing copper acetate precursor (0.05 – 0.3 M) with and without the addition of 1 v/v% H_2O_2.

This is in contrast to CuO synthesised with increasing copper acetate concentration in a turbulent mixing regime. At high concentrations, at significantly high nucleation rates, results in the formation of small nuclei. This reaction is effectively halted as the solution prematurely runs out of Cu^{2+} ions to react and grow, leading to smaller particles at high concentrations. In the case of Co_3O_4 synthesised via the same CHFS reactors at UCL, a similar trend was not observed. A comparison in the absence of H_2O_2 was not possible for Co_3O_4 as H_2O_2 was required to form the correct phase of Co_3O_4 and enhance the oxidation of cobalt.[113] For Co_3O_4, in a turbulent mixer, particles grew larger with increasing concentration. This was due to the readiness of Co_3O_4 to grow through coalescence in a highly turbulent regime which increased the collision rates between the particles and this was not the case for CuO. The results suggested that CuO synthesised under these parameters favoured a nucleation domination pathway and a turbulent mixing regime in combination with high precursor concentration could be exploited to form small nanoparticles.

In the case of H_2O_2, sample CuO[0.05]H_2O_2[1] did not vary significantly to the sample synthesised in the absence of hydrogen peroxide, although there was a minor particle size reduction with the addition of H_2O_2. Indeed, the size distribution remained significantly broad for this sample. However, for CuO[0.1]H_2O_2[1], the D90-D10 parameters showed the particle size distribution had significantly narrowed and the average particle size decreased (from 38.5 to 10.9 nm), when compared to the CuO sample synthesised without the addition of H_2O_2.

With increasing metal salt concentration, the addition of H_2O_2 did not reduce the particle size or narrow the particle size distribution. For sample CuO[0.2]H_2O_2[1], D90 increased to 15 nm, however, the D50 and D10 numbers were lowered, suggestive that small size CuO nanoparticles were also being formed, similar to the previous sample. As the concentration

increased to CuO[0.3]H_2O_2[1], the D90 number increased further to 27 nm. It is expected that there was not enough H_2O_2 compared to the copper ions to have a significant impact to the particle size or shape. Further increase of H_2O_2 concentration compared to the copper species would be expected to decrease the particle size and decrease the particle size distribution.

Following these observations, the metal salt concentration was kept constant at 0.1 M and the H_2O_2 concentration was varied in the range 0.5 to 4 v/v%. This experiment was carried out in the dual mixer (see design in Figure 3-1) at a mixing temperature of 305 °C, consistent with previous CuO synthesis. The PXRD of the as-obtained dried nanopowders (Figure 3-15) showed that pure phase CuO formed, however, no significant difference was observed in the peak broadness with increasing H_2O_2 concentration. The increasing H_2O_2 concentration led to an increase of the pH when sample CuO[0.1] was compared to sample CuO[0.1]-H_2O_2[0.5] and changed from pH 3.5 to 4.6, respectively (Table 3-6). Further increase in H_2O_2 concentration did not alter the pH or the yield. Similarly, the crystallite size decreased significantly from sample CuO[0.1] to sample CuO[0.1]-H_2O_2[0.5] from 16.9 to 12.8 nm, respectively, and further increase of H_2O_2 did not significantly affect the crystallite size. Generally, samples synthesised with the increasing H_2O_2 did not show significant variation in the crystallite size. The surface area was highest for the sample with the lowest crystallite size, as expected and little variation was observed, when the H_2O_2 concentration was altered.

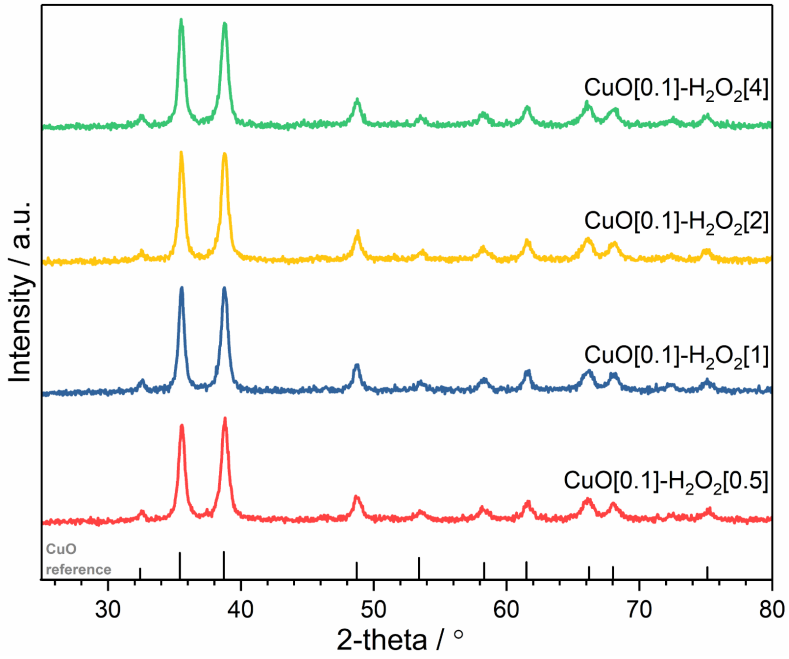

Figure 3-15 – CuO synthesised via the dual mixer set up, using copper acetate at 0.1 M and H_2O_2 in the range 0.5 to 4 v/v% at a mixing temperature of 305 °C.

Table 3-6 - Summary of pH, yield, crystallite size, surface area and particle size for CuO synthesised using the dual mixer set up, with increasing H_2O_2 content (0.5 to 4 v/v%) with and without the addition of H_2O_2.

Sample	pH	Yield / %	Crystallite size / nm (PXRD)	Surface area / $m^2\ g^{-1}$	Avg. particle size / nm (TEM)	SD for particle size / nm
CuO[0.1]	3.5	61	16.9	27.7	38.5	15.1
CuO[0.1]-H_2O_2[0.5]	4.6	74	12.8	40.9	14.1	4.4
CuO[0.1]-H_2O_2[1]	4.7	67	13.8	35.9	10.9	4.2
CuO[0.1]-H_2O_2[2]	4.6	67	14.1	34.4	12.6	5.4
CuO[0.1]-H_2O_2[4]	4.5	66	13.1	34.8	12.9	4.7

The particles were examined by TEM (Figure 3-16 a-d showing increasing H_2O_2 concentration). Compared to the CuO samples synthesised in the absence of H_2O_2 (Figure 3-12), the CuO particles were less aggregated and smaller with an average particle size reduction from 38.5 to 14.1 nm with the addition of 0.5 v/v% H_2O_2 and a significant narrowing of the size distribution from 15.1 to 4.4 nm. The addition of increasing concentration of H_2O_2 did not show a significant variation in the particle size and the size distribution remained ca. 4 to 5 nm. During the synthesis of sample CuO[0.1]-H_2O_2[4], it was observed that pumping 4 v/v% H_2O_2 became problematic and led to unpriming of the P3 (due to gases produced). It was deemed that less than 4

v/v% was required for the successful synthesis of CuO without limiting the operation of the pumps.

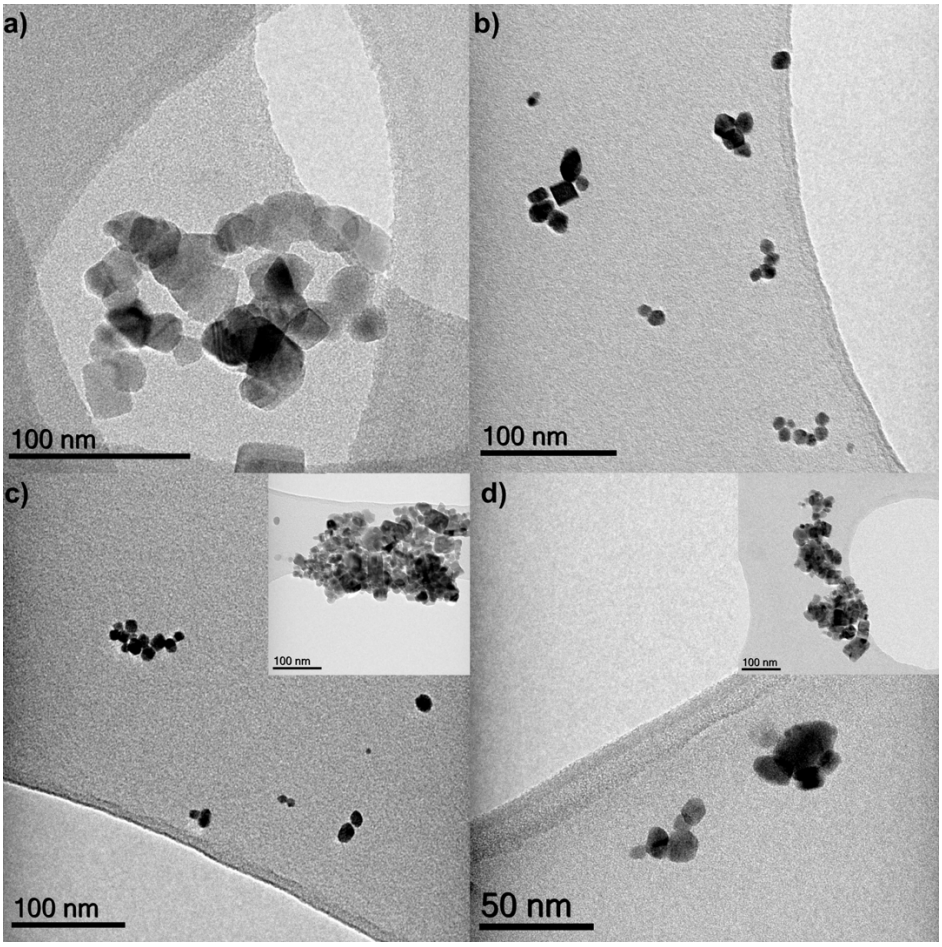

Figure 3-16 - TEM image of CuO synthesised using copper acetate (0.1 M) in the absence of KOH and with the addition of a) 0.5 b) 1 c) 2 and d) 4 v/v% H_2O_2, at a mixing temperature of 305 °C, using the dual mixer.

D90, D50, D10 showed the stark contrast between the copper acetate only sample and the effect of adding H_2O_2 (Figure 3-17). The addition of 0.5 v/v% H_2O_2 resulted in the D90 number to reduce from 36.5 to 13.8 nm, which further decreased to 10.4 nm with 1 v/v% H_2O_2. As observed with the TEM and further supported by the statistical analysis, little variation was observed with samples with >1 v/v% H_2O_2.

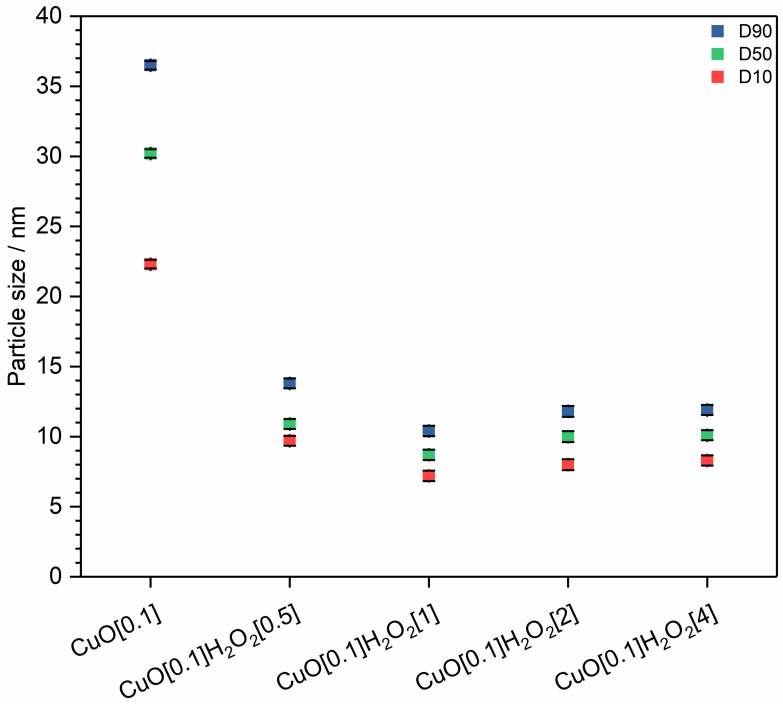

Figure 3-17 – D90, D50 and D10 parameters for CuO synthesised using copper acetate (0.1 M) in the absence of KOH and with the addition of H_2O_2 in the range 0.5 to 4 v/v%, at a mixing temperature of 305 °C, using the dual mixer.

To understand the effect of the mixer type, CuO was synthesised in the single mixer using copper acetate precursor in the absence of KOH with H_2O_2 as an additive, in the range 0.05 to 2 v/v% (added through P3). For all samples synthesised via the single mixer, the yield was signficiantly lower >50% when no or limited amounts of H_2O_2 was added and this was lowered to >40% when the H_2O_2 concentration increased (Table 3-7). The lower yield may be due to processing issues, Cu dissolution or the incomplete precipitation of CuO. The presence of a blue supernatant confirmed that it was unlikely to be a processing issue as Cu^{2+} were present in the output slurry. The output pH was around 3.3 for all samples and did not vary with increasing H_2O_2. The pH was more acidic compared to the samples prepared via the dual mixer (see Table 3-6), where the quench was present and an increase of pH was observed, due to dilution effects. However, this was not the case, herein, as no quench was present. All samples resulted in pure phase CuO (Figure 3-18), as confirmed with the CuO reference. The PXRD patterns presented with narrower and sharper peaks confirmed that CuO

formed via the single mixer had higher crystallinity. The crystallite size, however, did not vary between the samples prepared via the single mixer and dual mixer (being in the region 10-15 nm for both, see Table 3-6 and Table 3-7 to compare).

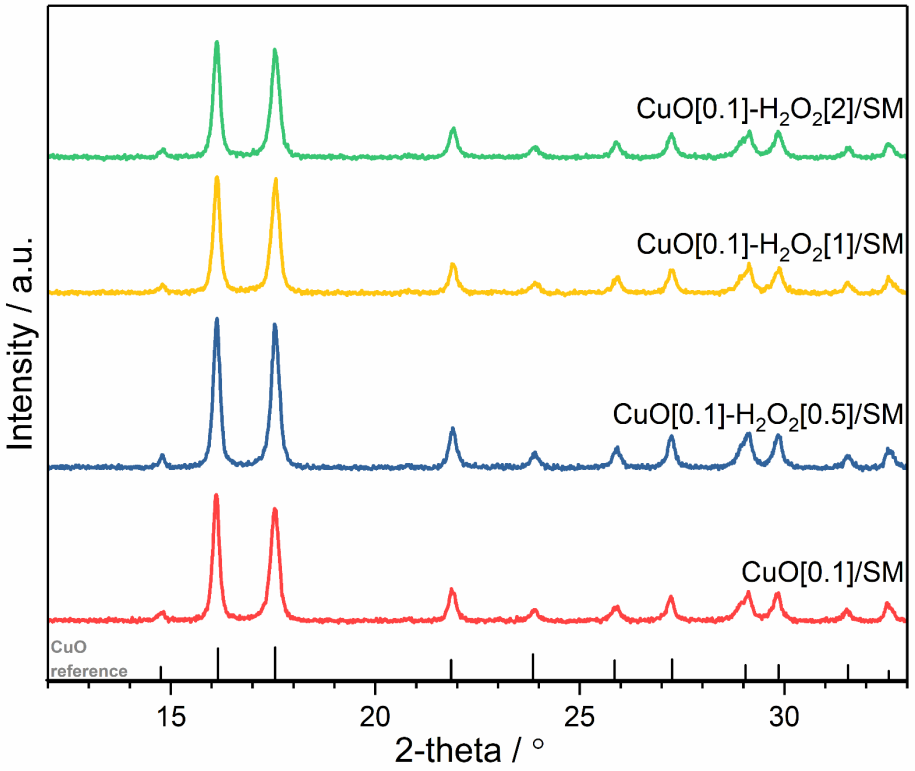

Figure 3-18 – PXRD pattern for CuO synthesised using copper acetate (0.1 M) and H_2O_2 in the range 0.5 to 2 v/v%, in the absence of KOH using the single mixer set up at a mixing temperature of 305 °C.

Table 3-7 - Summary of crystallite size, surface area and particle size for CuO synthesised using the single mixer set up, with increasing H_2O_2 content (0.5 to 2 v/v%).

Sample	pH	Yield / %	Crystallite size / nm (PXRD)	Surface area / $m^2\ g^{-1}$	Avg. particle size / nm (TEM)	SD for particle size / nm
CuO[0.1]-H_2O_2[0]/SM	3.2	46	6.1	19.8	53.9	26.5
CuO[0.1] - H_2O_2[0.5]/SM	3.3	43	15.2	21.9	49.7	22.0
CuO[0.1] - H_2O_2[1]/SM	3.3	38	15.2	21.1	56.8	32.4
CuO[0.1] - H_2O_2[2]/SM	3.3	38	14.9	22.1	55.2	20.8

The samples were also analysed by TEM (Figure 3-19) and the particles were generally well-defined and presented with a rhombic and cuboid morphology, which did not vary between samples. This was in contrast to samples prepared via the dual mixer in the same conditions, where the particles were significantly smaller and also presented with more spherical morphology. The average particle size for samples prepared via the single mixer was in the range 50 to 55 nm with a significantly broad size distribution. Samples prepared via the dual mixer were in the range 11 to 14 nm, with a significantly narrower size distribution (ca. 4 nm). It was evident that the quench, along with the use of H_2O_2 has a significant effect in reducing the particle size, either by hindering the particle growth or through enhanced nucleation rates of CuO.

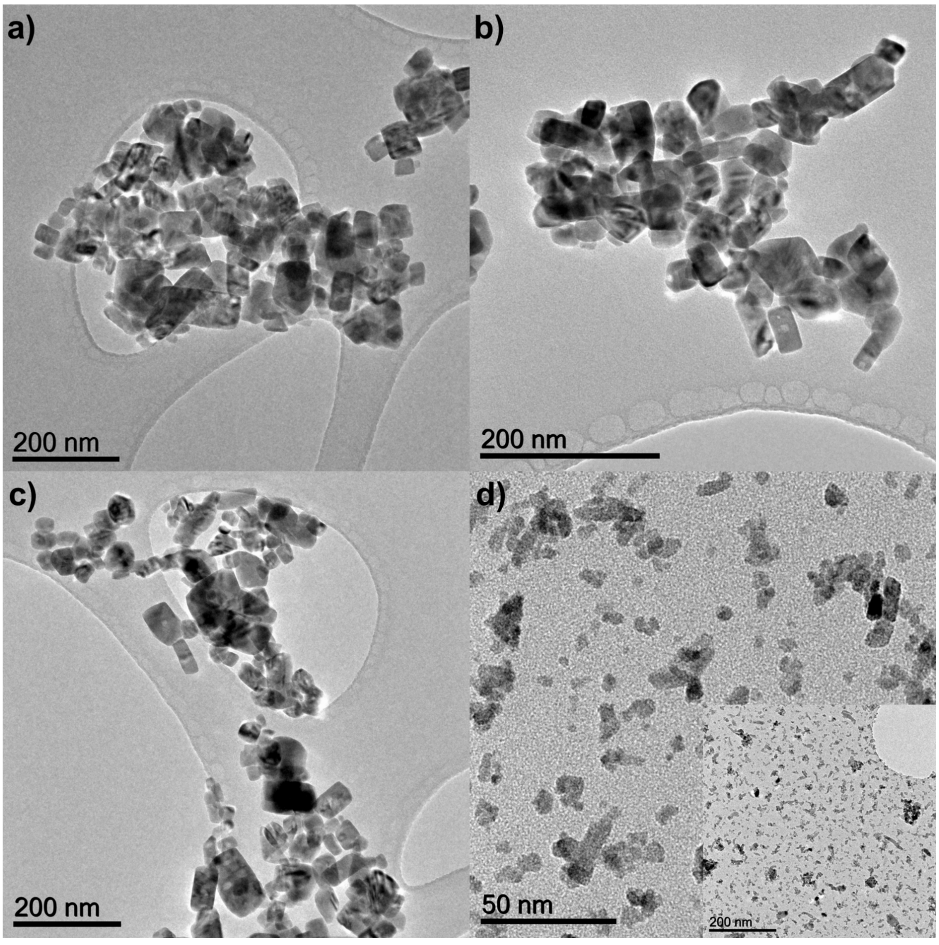

Figure 3-19 – TEM image of CuO synthesised using copper acetate precursor with H_2O_2, in the absence of KOH, using the single mixer set up – a) CuO with no H_2O_2, b) 0.5 c) 1 and d) 2 v/v% H_2O_2.

Despite the addition of H_2O_2, the mixer type had a more profound effect on controlling the CuO particle nucleation and growth. It is expected that the initial formation of copper hydroxide was increased upon the addition of H_2O_2, as it created a more hydrolysing environment. However, the longer residence time from the mixing point to the cooling point, contributed to the CuO growth. This was the case as there was little variation between the particle size as confirmed by the D90, D50 and D10 parameters (Figure 3-20). In the case of the CuO samples prepared by the dual mixer, the presence of the quench rapidly hindered further particle growth and the increased supersaturation could be maximised as the shortened residence time meant that CuO did not continue growing. Considering the effect of KOH (Table 3-5), the particle size was lower for CuO synthesised in the absence of KOH and in the presence of H_2O_2 with a dual mixer. However, the reaction conditions were not favourable for the synthesis of small sized CuO via the single mixer using H_2O_2, in the absence of KOH. Indeed, the particle size was considerably larger on average when CuO was synthesised in the single mixer in these conditions compared to KOH.

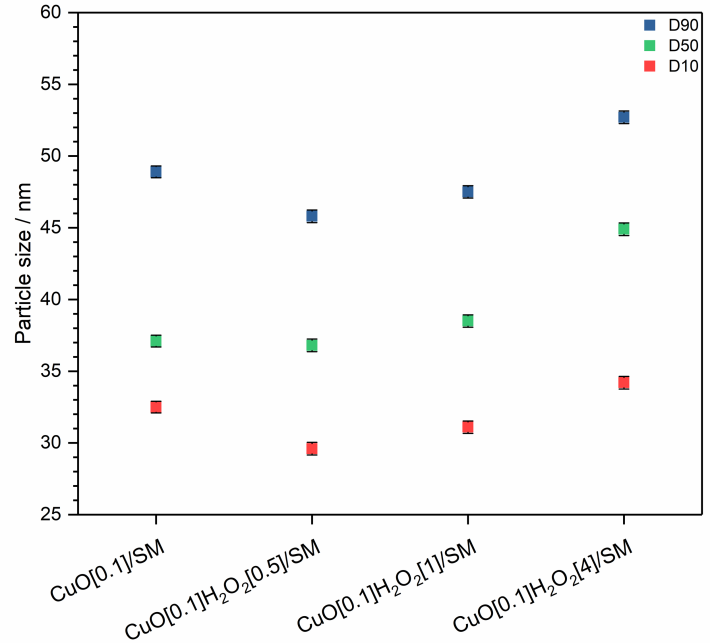

Figure 3-20 – D90, D50 and D10 parameters for CuO synthesised using copper acetate precursor with H_2O_2 (in the range 0 to 2 v/v%), in the absence of KOH, using the single mixer set up at a mixing temperature of 305 °C.

The lower yields, in both mixer types, in the presence of H_2O_2, indicated that it was possible that CuO was redissolving. This may be further supported as the interaction of H_2O_2 with acetic acid (from copper acetate decomposition) and copper ions results in the formation of copper acetate by the following equation:

$$Cu + H_2O_2 + 2CH_3COOH \rightarrow Cu(CH_3COO)_2 + 2H_2O \qquad \text{Equation 3.5}$$

Hence, there may be an equilibrium shift where as CuO was formed, it re-dissolved. It is also more likely that as smaller particles re-dissolved more readily (see Equation 1.21, Chapter 1), CuO grew at the expense of smaller particles, through Ostwald ripening. However, the growth rate was more dominant, as the particles continued to grow to ca. 50 to 55 nm. Another plausible reason for the larger particles may be that the reaction conditions were not optimised and hence the particles grew through a reaction limited pathway.

Phase pure CuO was directly synthesised through the CHFS reactor and the particle size could be modulated by altering the reaction parameters such as precursors and additives including copper metal salt, KOH concentration and H_2O_2. The temperature was also found to affect the supersaturation behaviour of CuO as the solubility was altered in sub and supercritical conditions. The use of a dual mixer was found to be crucial for controlling the particle size by rapidly quenching the particle growth. Cu_2O and Cu nanoparticles have not been previously synthesised via the lab scale CHFS reactor at UCL and is discussed in the following section.

3.3.2 Synthesis of Cu_2O and Cu

3.3.2.1 Effect of mixer type

Cu_2O and Cu nanoparticles were synthesised via the lab-scale CHFS reactor using H_2 derived from formic acid, where two mixer types were investigated;

pre-mixer and dual mixer. Design of the pre-mixer can be found in Section 3.2.2 and involved a 1/4" cross prior to the 3/8" CJM, where formic acid was fed through (via Pump 4) to meet the supercritical water. The pre-mixer was utilised to decompose the formic acid with supercritical water to H_2 and CO. When the formic acid met the supercritical water, the mixing temperature was ca. 330 °C (as calculated from the model described by Wagner and Pruβ on the properties of water), which upon mixing the metal salt feed, resulted in a mixing temperature of 305 °C.[146] The distance between the pre-mixer and the mixing point was ca. 10 cm. In the case of the pre-mixer set-up, the use of copper sulfate (0.1) and formic acid at ratio of 1:5, resulted in predominantly Cu_2O with minor amounts of Cu for sample Cu_2O/Cu-PM-1:5, as confirmed with the PXRD pattern (Figure 3-21a). Increasing the formic acid ratio to 1:50 resulted in predominantly Cu with minor Cu_2O formation. The peaks matched well with the JCPDS 01-071-3645 for Cu_2O and JCPDS 01-089-2838 for Cu. The sharp peaks in the diffraction data indicated highly crystalline samples. The crystallite size for the reduced phases was in the range 20 to 45 nm (Table 3-8). CuO was not observed as an impurity phases during the synthesis of Cu_2O and Cu phases.

Formic acid was also added with the copper sulfate precursor to attempt to synthesis Cu_2O and Cu and evaluate the need for a pre-mixer for formic acid decomposition. When the metal salt and formic acid ratio was limited to 1:1, only CuO formation was observed. This indicated that the formic acid content was not high enough within the CJM to reduce and drive the formation of Cu_2O and Cu (sample CuO-FA-1:1). In the case of Cu_2O-FA-1:3, phase pure Cu_2O was formed (JCPDS 01-071-3645). In the case of Cu formation (sample Cu/Cu_2O-FA-1:5), there was significant amounts of Cu_2O present (Figure 3-21b), where it was evident, an increase in the formic acid content was required. Samples prepared with higher formic acid content (>1:5), where the final product pH was fairly acidic (pH <3), resulted in eventual redissolving as Cu^0 was converted to Cu^{2+} upon exposure to air.

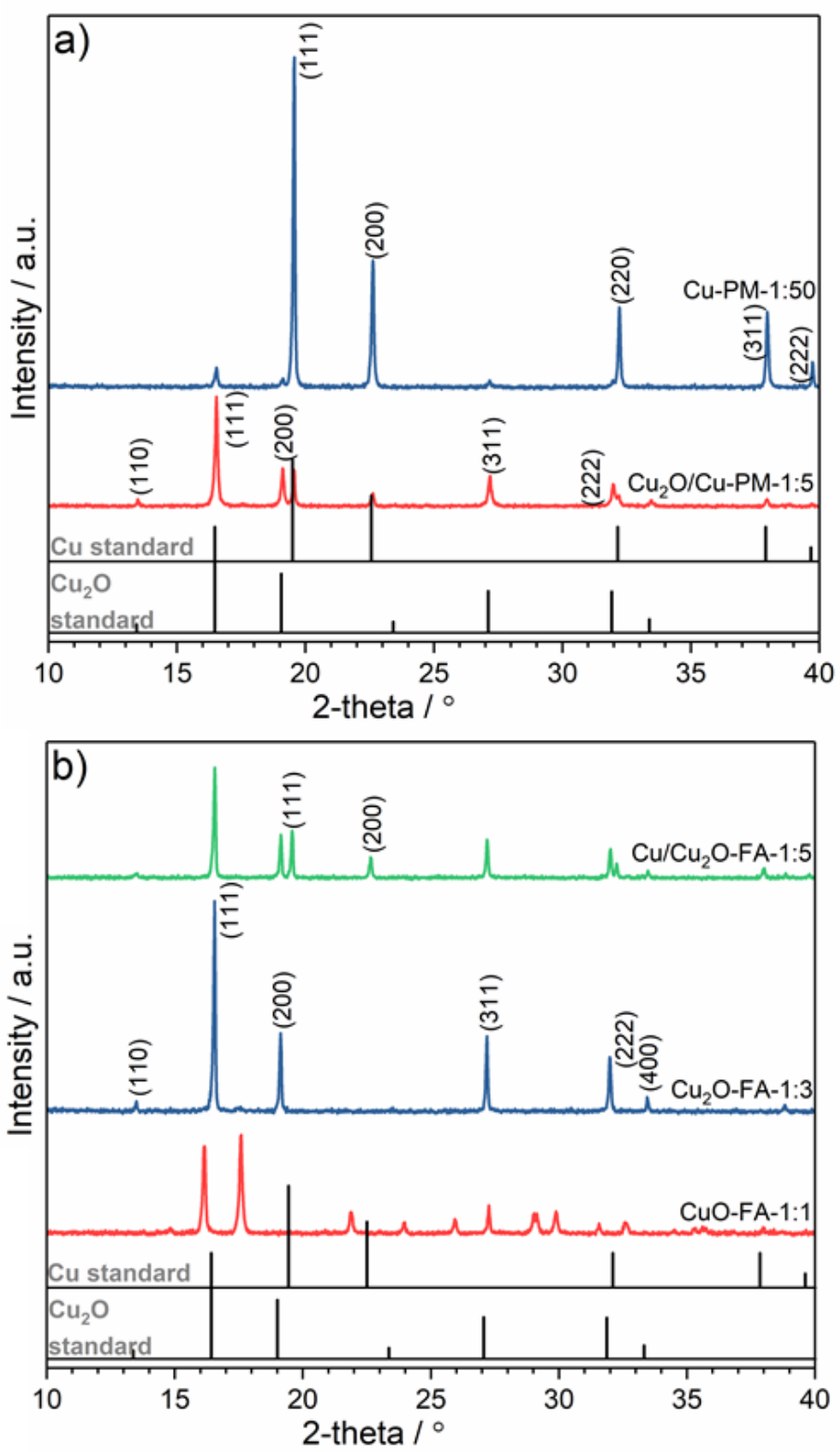

Figure 3-21 - PXRD patterns for the synthesis of Cu_2O/Cu from copper sulfate at constant copper salt concentration with increasing formic acid concentration comparing different mixers a) pre-mixer where the formic acid was introduced to the supercritical water feed prior to meeting the precursors and b) where formic acid was introduced with the copper salt in the first CJM. The synthesis was carried out at ca. 300 to 335 °C depending on the mixer type.

It was possible to directly synthesise Cu_2O and Cu phases without the need of surfactants (to protect the reduced phases during the synthesis process). It was also evident that there was no added benefit for the use of a pre-mixer for the decomposition of formic acid. In the case of most samples synthesised, oxidation of Cu_2O and Cu was facile and therefore no further characterisation was possible. Therefore, surface functionalisation was required to hinder further oxidation as well as particle growth. Table 3-8 summarises the crystallite size, phases observed, particle size, yield and pH measurements pertaining to the synthesis in this section.

Formic acid has been used to synthesise copper metal nanoparticles in flow previously.[126,147] The decomposition of formic acid in sub and supercritical water has been investigated, where the decomposition of formic acid in water is favoured above 320 °C.[148] The temperature, concentration and residence time can affect formic acid decomposition. The decomposition pathway follows a dehydration (Equation 3.6) or a decarboxylation (Equation 3.7) pathway.

Table 3-8 - Data summary for Cu_2O/Cu synthesis via copper sulfate with increasing formic acid concentration including crystallite size, particle size, yield and pH. * refers to the crystallite size for the secondary phases observed in the PXRD pattern (Cu).

Sample	Phase	Yield	pH	Crystallite size / nm (PXRD)
Cu_2O/Cu-PM-1:5	Cu_2O/Cu	65	5.5	35/41*
Cu-PM-1:50	Cu_2O/Cu	3	6	24/38*
CuO-FA-1:1	CuO	64	6	31
Cu_2O-FA-1:3	Cu_2O	5	5	47
Cu_2O/Cu-FA-1:5	Cu_2O/Cu	26	4	41/35.5*

$$HCOOH \rightarrow CO + H_2O \qquad \text{Equation 3.6}$$

$$HCOOH \rightarrow CO_2 + H_2 \qquad \text{Equation 3.7}$$

According to Zhang et al. the formic acid decomposition is catalysed by supercritical water.[149] Water acts as a catalyst by transferring a proton along the locally formed hydrogen bond network. Thus, decarboxylation becomes

more favourable in such conditions (Equation 3.7). CO remains a minor product during formic acid decomposition at high temperatures and the ratio of H_2 to CO_2 is affected by the formic acid concentration and the temperature. At higher temperature, H_2 is favoured, and with increasing formic acid concentrations, the H_2 gas molar fractions decrease and CO_2 and CO increase. Kubota et al. also suggested that the synthesis of Cu_2O nanoparticles using formic acid in supercritical conditions was made possible as the ratio of H_2 to Cu^{2+} ions was not high enough but also as the kinetics of the formation of the oxide occurred too quickly compared to the release of hydrogen from the formic acid decomposition (which affected the oxidation state of the final product).[126]

3.3.2.2 Addition of Polyvinylpyrrolidone (PVP)

The synthesis of Cu_2O and Cu nanoparticles was possible without the addition of any surfactants via the CHFS reactor, both in the pre-mixer and the CJM mixer. However, the long-term stability was poor as the particles rapidly oxidised as they were exposed to air. Surface modification is required to protect the surface from further oxidation and to limit particle growth. The synthesis of Cu nanoparticles via continuous flow has been previously targeted and surfactants such as PVP, EDTA, alkanethiol have been used.[125–127,147] Herein, different concentrations of PVP (in the range 1 to 5 w/v%) were added to the quench feed at 160 mL min^{-1} and Cu_2O was the targeted phase, as this has been shown to be a promising catalyst for CO_2 electroreduction (as discussed in Chapter 1).

The PXRD pattern shows the formation of pure phase Cu_2O as confirmed with JCPDS 01-071-3645 (for Cu_2O-PVP1 to Cu_2O-PVP2) (Figure 3-22). Increasing the PVP concentration in the quench feed decreased the pH of the outlet stream (Table 3-9). For sample Cu_2O-PVP3, CuO was formed directly (JCPDS 01-089-2529) and further increase of PVP, likely formed Cu_2O, based on visual observations, as the slurry colour was yellow.

However, this sample subsequently re-dissolved within a short amount of time (few hours) and therefore no further characterisation was possible.

The particles were also characterised by TEM and revealed particles with rounded cube and spherical morphology with a size range of 140 to 165 nm. The increasing addition of PVP did not appear to make any observable difference to the morphology and the size. It was possible that the synthesis of Cu_2O was complete in the first CJM before reaching the quench feed, where the addition of PVP did not make a significant difference to the size and shape of the Cu_2O formed. It may be expected that water (in the absence of PVP) may quench the reaction (in the dual mixer). Sample Cu_2O-PVP0 was not examined by TEM due to the low yields and subsequent oxidation to CuO. However, the crystallite size was comparable for sample Cu_2O-PVP0 and Cu_2O-PVP2, which did not suggest the quenching the Cu_2O synthesis was possible, as Cu_2O nucleation and growth was complete in the first mixer.

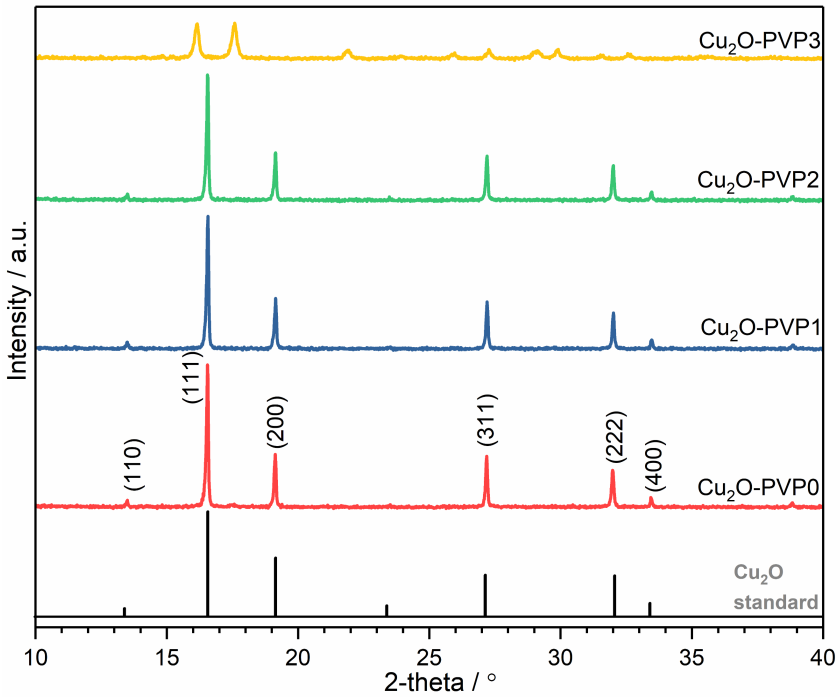

Figure 3-22 – PXRD pattern of Cu_2O synthesis using copper sulfate and formic acid ratio of 1:3, with increasing PVP capping agent (in the range 1 to 5 w/v%) added via the quench feed in the dual mixer set up. The synthesis was carried out ca. 335 °C.

Table 3-9 - Data summary for Cu_2O synthesis using PVP as a capping agent including pH, yield, crystallite, particle size and XPS peak position for Cu^{2+} $2p_{3/2}$. Cu_2O-PVP4 is marked as * as no recoverable product was obtained.

Sample	Phase	pH	Yield / %	Crystallite size / nm (PXRD)	Particle size / nm	XPS (Cu^{2+} $2p_{3/2}$)	
						Cu^{+}	Cu^{2+}
Cu_2O-PVP0	Cu_2O	5.5	5	47	-	932.7	933.9
Cu_2O-PVP1	Cu_2O	6	15	41	165 ± 79	932.5	933.5
Cu_2O-PVP2	Cu_2O	6	6	48	141 ± 60	932.6	
Cu_2O-PVP3	CuO	5	0.7	17	47 ± 23	932.1	933.8
Cu_2O-PVP4*	Cu_2O	4	-	-	-	-	-

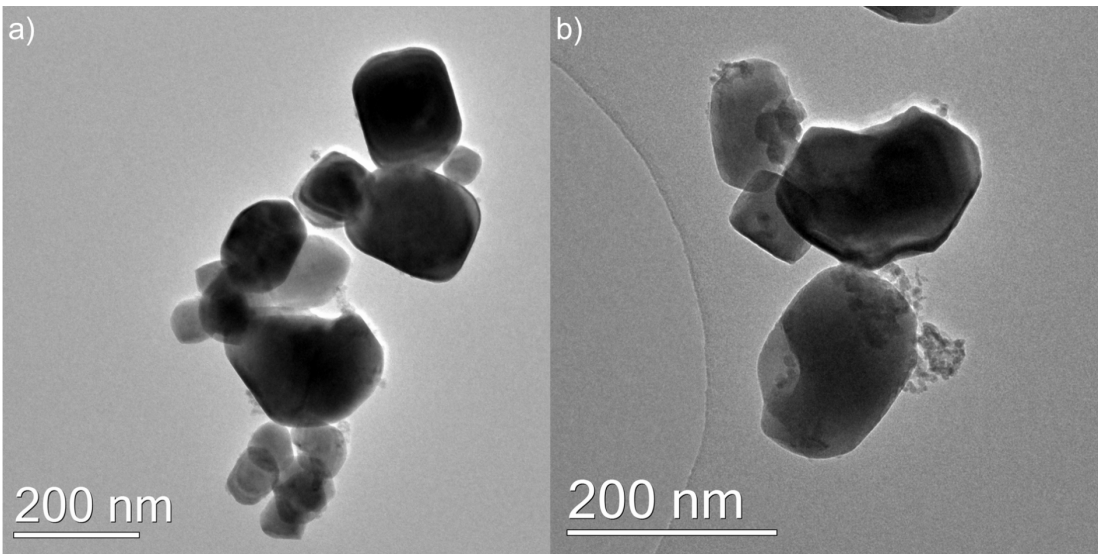

Figure 3-23 – TEM images for Cu_2O synthesis using PVP as a capping agent – a) with 1 w/v% PVP and b) 2 w/v% PVP.

To confirm if Cu_2O nucleation was complete in the first CJM, PVP was added with the metal salt feed, to evaluate if PVP addition with the copper ions could control the particle growth. This led to formation of CuO only and eventual re-dissolving of the particles that formed, as the measured pH was <3. PVP thermally decomposes at 483 °C and Aksomaityre et al. investigated PVP degradation in supercritical water (>400 °C) and showed

some breakdown of the polymer chain, as measured by ^1H NMR.[150,151] However, in this study, the mixing temperature was limited to 335 °C, so it is not expected that PVP would begin to degrade in the conditions tested.

The stability of Cu_2O should be considered in sub and supercritical conditions. At room temperature, according to the Pourbaix diagram, Cu_2O is stable in the pH region 9 to 12, in slightly reducing conditions.[143] $Cu(OH)_2(s)$ and $HCuO_2^-$ species are dominant in slightly basic and oxidising conditions (Figure 3-24a), as the temperature is increased, in supercritical conditions, these species become non-existent and CuO becomes more dominant. (Figure 3-24b). The stability field of Cu_2O (cuprite) significantly diminishes in supercritical conditions. The stable formation of Cu_2O requires fine-tuning of the reducing conditions as well as controlling the pH. The pH within the mixer is not known and it is only measured at the outlet of the BPR as the product stream is further diluted (from the quench feed). As the synthesis of Cu_2O is sensitive to variations in pH and temperature, changes locally within the reactor during the synthesis (for example, the flow rates of the precursors feed being altered) may result in the formation of CuO. The mechanism of Cu metal nanoparticle synthesis in flow has been suggested, where the formation of $Cu(OH)_2$ follows CuO synthesis which is subsequently reduced to Cu_2O and Cu.[125,127]

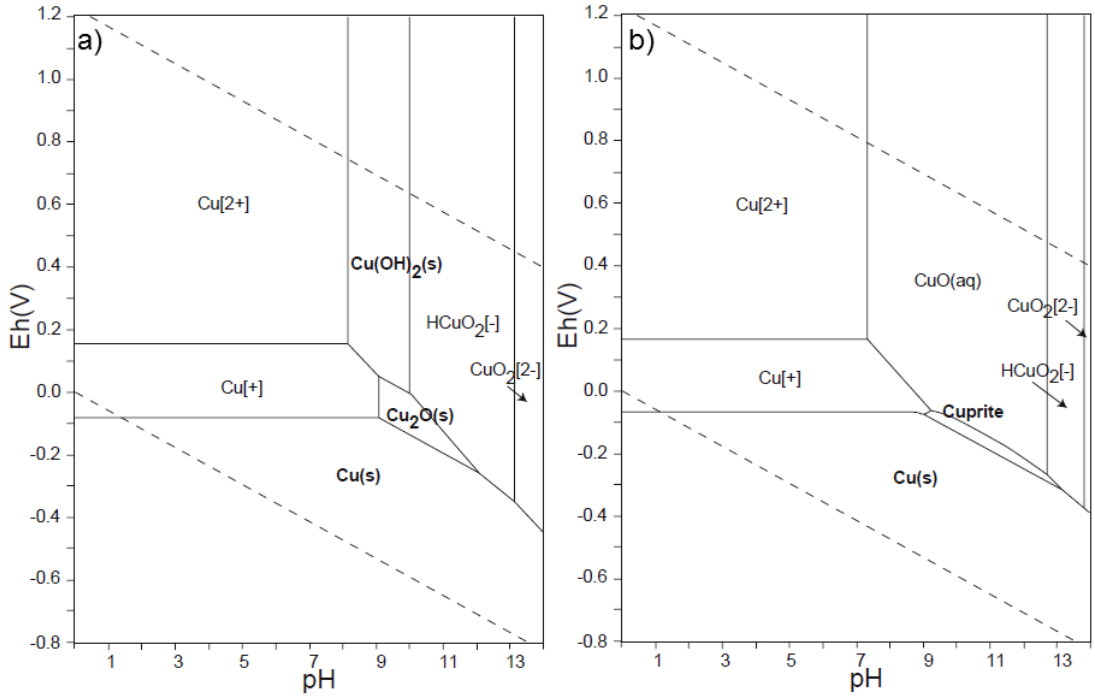

Figure 3-24 – Pourbaix diagrams for Cu species in water – a) at room temperature and b) in supercritical conditions (adapted from ref[143])

This mechanism was suggested as when the NaOH concentration was increased in the experiments, Cu was more readily formed, because CuO formation was facile in basic conditions.[127] When this was repeated in the CHFS process used in this thesis, and the KOH concentration was increased, only CuO was formed and the formation of Cu was suppressed. The outlet pH was measured at 8, which was in the stability region of CuO formation. The formic acid concentration was kept the same as previously used.

In the literature, the pH of the solution was found to also affect formic acid decomposition, where in acidic conditions the dehydration pathway (Equation 3.6) was favourable and in basic conditions (pH >4), the decarboxylation pathway was favoured.[152] Despite the basic environment, the product was favoured to be CuO, when additional KOH was added. This suggested and confirmed that the kinetics of CuO formation was faster than the release of hydrogen from the formic acid decomposition in the conditions tested. For the synthesis of reduced copper species, weakly acidic conditions were required

to optimise hydrogen generation from formic acid decomposition as highly basic conditions promoted and stabilised the formation of formate.

3.3.2.3 Fructose as a reducing agent

Formic acid and formaldehyde have been typically used as reducing agents for the synthesis of Cu nanoparticles via hydrothermal flow processes. Copper acetate has also been used as a precursor, where the acetate decomposes to create a reducing atmosphere and drives the formation of Cu_2O and Cu phases.[125] Fructose has not been used as a reducing agent for the synthesis of Cu_2O and Cu nanoparticles via the CHFS processes. There is also a likelihood that the presence of carbon from the decomposition of fructose on the surface of the particles could act as a protective layer to prevent further oxidation of the reduced phases. Two different copper metal precursors were used; copper sulfate and acetate. The mixing temperature was also kept to ca. 335 °C for the experiments with fructose.

The PXRD pattern for copper sulfate (Figure 3-25a) revealed the formation of Cu_2O at a Cu^{2+} to fructose ratio of 1:3 and Cu formation at a ratio of 1:5. Considerably less fructose was required compared to formic acid to drive forward this reaction. It should be noted that the formation of brochantite was not observed for any copper sulfate samples due to the acidic pH from the decomposition of the reducing agent. Sodium pyrophosphate was added to the precursor to modify and buffer the pH in situ in some samples. Similar to the fructose ratios used, the formation of Cu_2O and Cu nanoparticles was successful and indeed no impurity phases were observed for copper sulfate. The use of pyrophosphate also increased the yield of Cu_2O phases from 25 to 56 % in the case of Cu_2O-SO_4/1:3C/P, however, the yields for the Cu phases were still significantly low (Table 3-10). Issues with blockages (from the formation of larger particles) were observed during the experiments where the rapid formation of copper led to pipe blockages after the first mixer. It is expected the yield was low due to this issue during the synthesis.

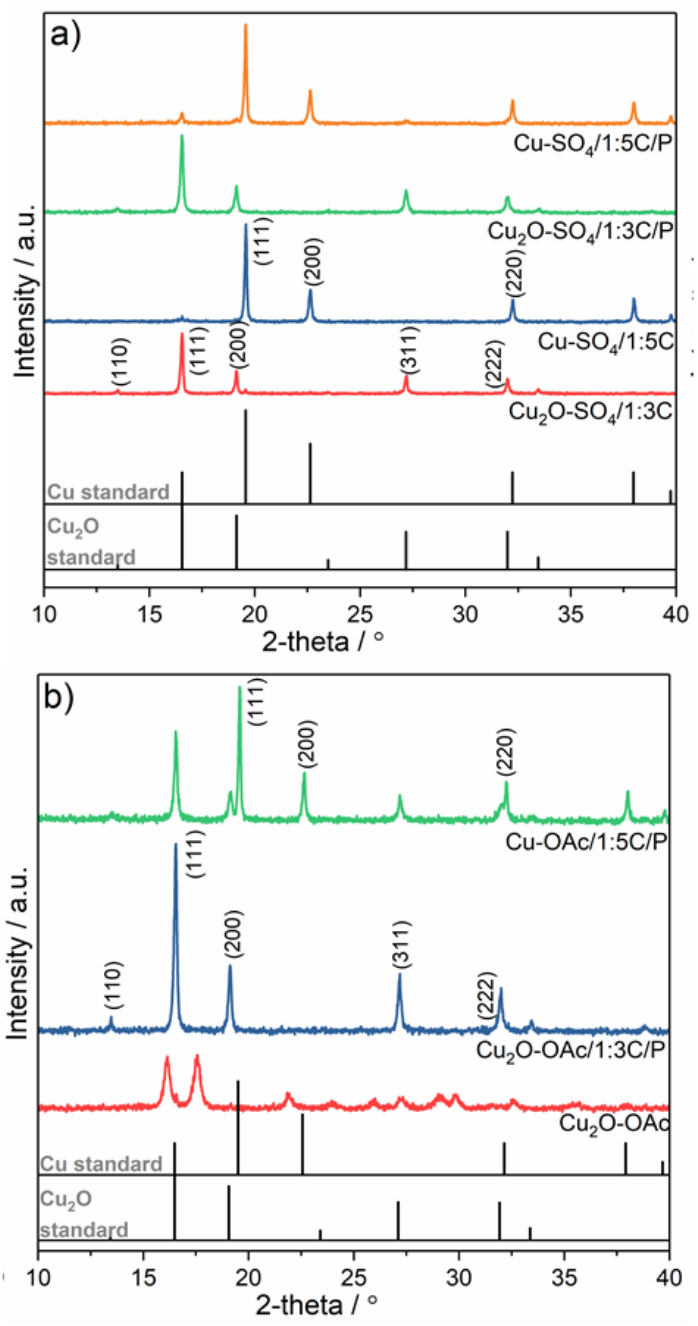

Figure 3-25 - PXRD pattern for Cu_2O/Cu synthesis using fructose as a reducing agent – a) using copper sulfate as a precursor and b) copper acetate as a precrusor.

Table 3-10 - Data summary of Cu_2O and Cu synthesised via the dual mixer using fructose as a reducing agent, showing the pH, yield, crystallite size and particle size.

Sample	Phase	pH	Yield / %	Crystallite size / nm (PXRD)	Particle size / nm
Cu_2O-SO_4/1:3C	Cu_2O	5	25	29	-
Cu_2O-SO_4/1:5C	Cu	4	2	27	-
Cu_2O-SO_4/1:3C/P	Cu_2O	5	56	25	86 ± 38
Cu_2O-SO_4/1:5C/P	Cu	5	9	28	-
Cu_2O-OAc	CuO	11	59	11	-
Cu_2O-OAc/1:3C/P	Cu_2O	5	49	26	84 ± 34
Cu_2O-OAc/1:5C/P	Cu	4	4	32	-

When no reducing agent was added and copper acetate was solely used, the formation of CuO was observed and therefore the addition of a reducing agent was necessary. This was in contrast to a Cu nanoparticle study in the literature were the use of copper acetate without the addition of a reducing agent resulted in the formation of Cu_2O and Cu mixture phases, however, temperatures >400 °C were used during the batch hydrothermal synthesis, where the thermal decomposition of the precursor was aided with higher temperatures.[125] In the case of copper acetate (Figure 3-25b), only the pyrophosphate samples are shown as no recoverable product was observed for the copper acetate sample synthesised with fructose. The synthesis of Cu_2O and Cu was also possible, with minor impurity phases observed for sample Cu-OAc/1:5C/P, being similar to standard reference patterns JCPDS 01-071-3645 and 01-089-2838 for Cu_2O and Cu, respectively.

The XPS samples for Cu_2O-SO_4/1:3C/P and Cu_2O-OAc/1:3C/P were compared between the copper sulfate and acetate samples, where the survey scans for both samples (Figure 3-26a and Figure 3-26f) confirmed the presence of Cu, C and O as expected. No other detectable impurities were present on the surface, related to the synthesis or processing of the samples. The high-resolution Cu 2p scans were also compared, where the presence of a reduced Cu oxidation state was evident from the fitting of the $2p_{3/2}$ peak. The peak at 932.4 eV corresponded to the Cu^+ or Cu^0 oxidation state, as confirmed from literature reports.[153] It was not possible to distinguish

between the two oxidation states. The presence of the satellite peaks as well as the peak at ca. 934.5 eV showed the presence of Cu^{2+} on the surface of Cu_2O. This is expected as Cu_2O readily undergoes oxidation due to the unstable +1 oxidation state. However, in the case of the copper acetate sample, considerably more Cu^{2+} was observed, mainly due to the presence of the satellite peaks. Deconvolution of the oxygen 1s scan confirmed the presence of O related to the metal-oxygen bond and oxygen species from the carbonate bond at 531.3 and 532.8 eV, respectively (sample Cu_2O-SO_4/1:3C/P). The high-resolution C scan confirmed the presence of surface carbonates at ca. 287 eV and adventitious carbon at 284.9 eV for both samples. There was no significant difference for the C and O scans between the samples prepared by copper sulfate or acetate precursors.

TEM measurements were conducted to investigate the morphology and size of the Cu_2O samples. Differences in the samples prepared via different precursors was observed. In the case of sulfate sample (Figure 3-27a), there were small spherical particles (ca. 5 nm) present in a carbon type matrix, as observed due to the contrast in the TEM. There were large Cu_2O particles (average size 86 ± 38 nm) also formed in conjunction with the small particles and the large particle size distribution was evident. The Cu_2O samples synthesised via copper sulfate were not as well defined as the samples prepared via copper acetate. In the case of copper acetate, smaller spherical particles were not observed as seen with copper sulfate. The particles had an average size of 84 ± 34 nm and presented with some faceting and generally were spherical in nature. The high resolution TEM image confirmed the presence of Cu_2O as the d-spacing of 0.25 nm (111) and 0.29 nm (110) was observed for sample Cu_2O-SO_4/1:3C/P (Figure 3-27b) and Cu_2O-OAc/1:3C/P (Figure 3-27d). Ziegler et al. also observed size differences for the synthesis of Cu and Cu_2O when using $Cu(NO_3)_2$ or $Cu(CH_3COO)_2$ as precursors, where the acetate precursor resulted in particles with larger size and a broader size distribution.[125]

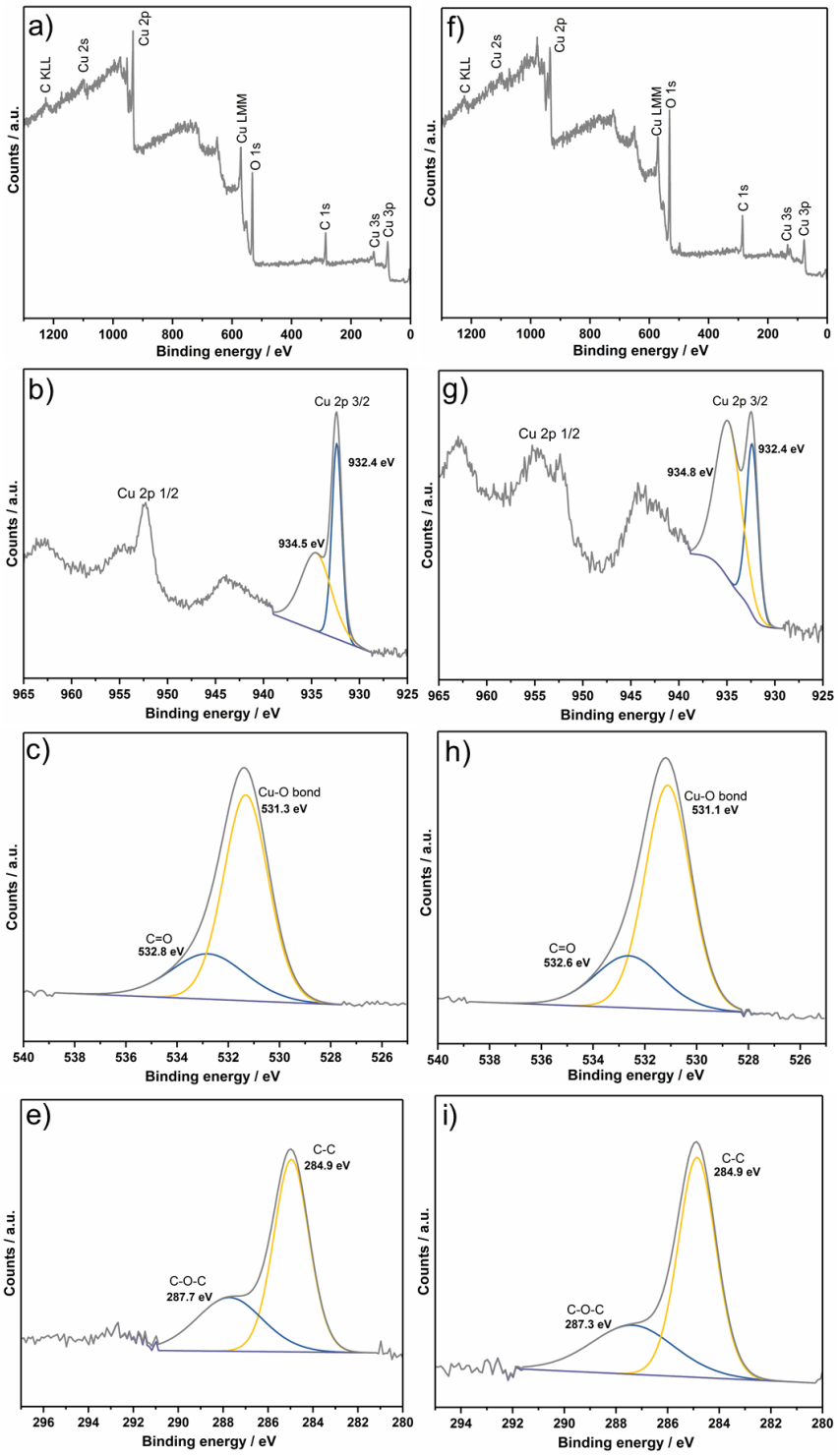

Figure 3-26 – XPS spectrum for Cu_2O samples prepared by using fructose as a reducing agent – a-d) sample prepared via copper sulfate showing the a) survey, b) Cu 2p, c) O 1s and d) C 1s and e-h) sample prepared via copper acetate showing the e) survey, f) Cu 2p, g) O 1s and h) C 1s.

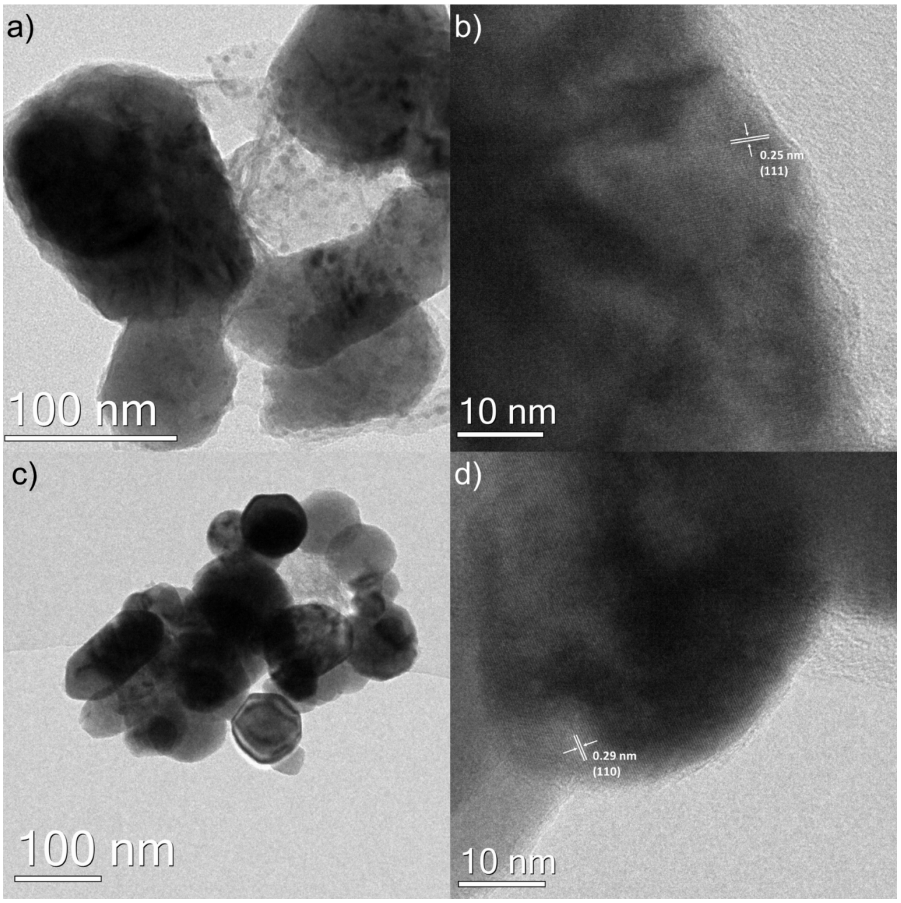

Figure 3-27 - TEM image of Cu_2O nanoparticles synthesised using fructose as a reducing agent a) synthesised from copper sulfate, b) high resolution image showing a d-spacing of 0.25 nm (111) plane and c) synthesised from copper sulfate and d) high resolution image showing a d-spacing of 0.29 nm (110).

The decomposition of fructose in sub and supercritical conditions has been previously investigated where typical decomposition products from fructose in the temperature range 300 to 350 °C at 25 MPa include dihydroxyacetone, glyceraldehyde, erythrose, pyruvaldehyde, acetic and formic acids, where erythrose further decomposes to acetic and formic acids. Fructose, along with other reducing sugars, has been used to form copper nanoparticles via other synthesis routes. Komarneni et al. investigated the solvothermal/hydrothermal (batch) route of Cu synthesis with and without microwave irradiation.[154] The authors observed that fructose promoted the growth of Cu nanoparticles, also synthesised with copper sulfate, as with the use of glucose, smaller particles were observed. The use of dual mixer was required for the synthesis of Cu_2O/Cu as the formation of soft Cu metal within

the reactor in the single mixer set-up led to significant blockages in the experimental parameters tested. Despite having a quench feed, the particle growth was not limited. This indicated that upon mixing of the precursors with supercritical water, Cu^{2+} ions were rapidly reduced to Cu^{+} or Cu^{0}.

3.4 Conclusions and Future Work

To summarise, the synthesis of pure-phase CuO was successful via CHFS. The particle size could be controlled by introducing a quench feed to rapidly cool the nascent nanoparticle slurry and therefore limit the particle growth. In the context of CO_2 electrocatalysis, it is important to be able to control catalyst properties (such as particle size) to tailor structure-property relationships to optimise catalytic performance. The information gained through this Chapter can be utilised for subsequent synthesis of nanocatalysts via CHFS and exploit the scalability of the process for scale-up of CO_2 utilisation.

It was confirmed that the anion of the copper salt does not affect the CuO morphology or size significantly in the conditions tested. The importance of finding the optimum base concentration and mixing temperature was also shown, where the optimum mixing temperature of 305 °C and metal to base ratio of 1:2 was ideal for synthesising the smallest particles using a copper sulfate precursor. Copper sulfate was found to be sensitive to the pH and mixing temperature as the mineral brochantite was easily formed at low base concentrations and mixing temperatures. The influence of H_2O_2 was also studied and it was shown that the presence of H_2O_2 created a superior hydrolysing environment resulting in the formation of sub-15 nm CuO nanoparticles, which has not been reported using continuous hydrothermal flow methods.

Cu_2O and Cu phases were also successfully formed using two different reducing agents; formic acid and fructose. By varying the ratio of Cu to

reducing agent and the pH, Cu_2O or Cu could be formed. However, the long-term stability of particles needs to be evaluated and similarly, the effect of other capping agents need to be investigated. Preliminary results of a range of capping agents used with CuO have shown triethanolamine to be an excellent capping agent by reducing the crystallite size from 23 to 12 nm. Therefore, this needs to be assessed for the reduced phases. Limiting the growth of the Cu_2O and Cu nanoparticle needs to be also evaluated. During the synthesis of Cu_2O and Cu, issues with blockages were observed and therefore, emergency reactor shutdowns were necessary. This may be overcome by lowering the metal salt concentration as attempted previously.[125,126] This can however can limit the scalability of the process, as significantly longer collection times are required to synthesise the same amount of material. It also limits the sample processing as the volume collected increases. Mixer types, specifically laminar mixers, may be advantageous in this case. Denis et al. were able to show the influence of laminar mixers at high metal salt concentrations, where smaller particles were formed.[113] This may be applied to the synthesis of Cu and Cu_2O nanoparticles to attempt to limit the particle growth.

Chapter 4. The Role of Nafion in the Electrochemical Reduction of Carbon Dioxide

4.1 Introduction

Inks play a significant role in depositing functional materials in a range of applications in the electronics, fuel cells, pigments, automobiles and packaging industries.[155] The composition, casting and adhesive properties are key aspects of ink formulations that impact on their suitability for particular applications. In terms of catalysis, inks are commonly used as a vehicle to transfer catalysts on desired substrates, such as inert electrodes, carbon cloths or polymers.[29,156] For the electrochemical reduction of CO_2, inspiration for catalytic inks can be sought from extensive research conducted within fuel cells to improve the electrochemical performance and stability for their catalyst inks.[157] Studies considering their impact on the electroreduction of CO_2 remain limited and are a significant focus of this chapter.

4.1.1 Electrode structure

The electrode structure and role of GDE was discussed in detail in Section 1.11.4. The microstructure of the catalyst layer can often be overlooked and has been found to be an important aspect of the catalytic process in proton exchange membrane fuel cells (PEMFCs), however, has been poorly evaluated in the context of CO_2 conversion. A key parameter to consider is the inter particle distance, where the ionomer can play a crucial role in altering the microstructure of the catalyst layer.[158] This has implications for the mass transport of reactants and products during the catalytic reaction.

Typically, Nafion has been used in PEMFCs but other ionomers such as polytetrafluoroethylene (PTFE) and polyvinylidene fluoride (PVDF) have also been used.

4.1.2 The role of ionomers

The importance of optimising the catalyst layer is crucial. The catalyst layer is deposited from a suspension, which typically consists of the active material, an ionomer and solvent mixture. The ionomer can be described as a polymer composed of non-polar macromolecules in which approximately 10 to 15 % of the units have ionic groups.[159] Due to this polymer structure, ionomers are known to have unique properties and morphologies from the formation of cross links, resulting from the phase separation of the ionic groups from the non-polar hydrophobic groups. A group of fluorinated ionomers have been used extensively in numerous applications, initially in the chloro-alkali industry and more recently in fuel cell applications.[159] In partially and perfluorinated polymers, ionic groups typically include sulfonic and carboxylic acids.[159] A popular commercial ionomer, which is a focus of a number of different applications has been Nafion. Nafion is based on a modified Teflon structure with strong ionic groups in the form of sulfonic acid groups, which is illustrated in Figure 4-1, also showing the cross-links possible in the Nafion structure.[38] It is extremely resistant to chemical attack, except from attack from alkali metals. Compared to other polymers, it also has a high working temperature (up to 190 °C), a high ionic conductivity so it can function as a cation exchange polymer as well as being highly permeable and selective towards water. Nafion is able to absorb large amounts of water and can 'swell' up to 22 wt%, allowing for hydration control.[160]

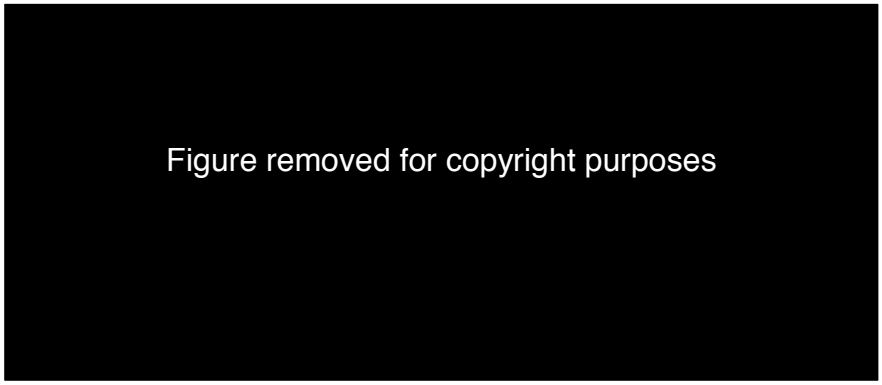

Figure 4-1 – Nafion ionomer structure (obtained from reference D. Dunwoody and J. Leddy, *Electrochem. Soc. Interface*, 2005, **14**, 37–39[161]).

Recently, PEMFC-like designs were adopted for CO_2 electrochemical CO_2 reduction (ECR), where Nafion ionomer was incorporated in the catalyst layer to help improve CO_2 reduction.[162] Nafion can act as a binder, creating a continuously connected ionic conductive matrix, which allows the reactants and products to be transported between the active catalytic sites and the reactant.[163] The ionomer is considered a direct hindrance to the coalescence or detachment of the catalyst during the catalytic process.[164] Several studies have shown that the performance of PEMFCs is often sensitive to the Nafion fraction, where an optimal fraction is typically in the range 25 to 40 wt% (depending on Pt fraction and Pt particle size, in the case of PEMFCs). Recent studies have also investigated the effect of Nafion and PTFE as binders on the electrochemical reduction of CO_2 on Sn-based catalysts. Wang, Q. et al. reported the highest Faradaic efficiency for HCOOH formation using Sn-based catalysts (Sn GDEs under ambient pressure), where an optimal loading of 5 mg cm^{-2} and 50 wt.% Nafion fraction resulted in a Faradaic efficiency of 72 %.[165] Similarly, Wu, J. et al., also investigated the use of Nafion with Sn nanoparticles and observed an optimal Nafion fraction varied in the range 17 to 20 % resulting in high Faradaic efficiencies.[166]

To the author's knowledge, no systematic study considering the Nafion fraction with nano-copper-based catalysts for CO_2 reduction has been previously investigated. Copper and its oxides, both bulk and nanostructured,

remain the only system to electrochemically convert CO_2 to 1C and 2C products such as formic acid, methanol, ethanol and acetic acid, with significant improvements to the energetic efficiency of the process, compared to other catalysts. As the microstructure of the final catalyst layer plays a significant role in the catalytic performance, it is imperative to understand the correlation between Nafion content and electrocatalytic activity for CO_2 reduction. This also becomes critical when scaling up from conventional three electrode cells typically used in electroreduction of CO_2, to fuel-cell like designs, which have the potential to convert CO_2 to chemicals at pilot scale level.[64]

4.1.3 Ink formulations

The ink solutions used to fabricate catalyst layers typically consist of a solvent mixture, an ionomer and the catalyst. The molecular interaction of Nafion (and any other ionomers) with the solvents is crucial as this will determine the homogeneity and stability of the dispersion. Common solvents that have been used with Nafion are isopropyl alcohol (IPA), water, ethanol, methanol, ethylene glycol mixtures, ethers and glycerol.[163] Depending on the dielectric constant, ε, of the solvent, Nafion will either remain in a solution state ($\varepsilon > 10$), colloidal state ($10 > \varepsilon > 3$) or precipitate ($\varepsilon < 3$).[167] Often dual solvent mixtures are used to obtain the optimal conditions to allow for homogeneous dispersions, allowing to modulate the ε at both the mixing and deposition stages.

The importance of the homogeneity of the ink solution becomes apparent when the inks are cast onto a substrate to form thin films. Poor dispersions of inks will lead to non-uniform distribution of the catalyst on the substrate, leading to poor surface contact or small islands of particles. This has a detrimental effect on the performance of the catalyst, as has been reported by several studies in PEMFC.[163,164,167–169] A number of casting methods are commonly used in the literature:

1. Drop casting – This method involves dropping a solution and allowing for solvent evaporation. This is a very simple method and has no waste of material, however, it can be challenging to cover large areas and can be difficult to control film thickness as well as homogeneity. The combination of solvents is crucial to control differing evaporation rates of mixtures.
2. Spin coating – This is a popular method as it leads to good uniformity and control of thickness, however, can be much more wasteful and does not cover large areas as well. The film thickness may be controlled by altering the rotation speed or solution viscosity.
3. Dip coating – The substrate is dipped into the solution and moved at a controlled speed. It allows for reasonable uniformity of the film and can cover a large area. The film thickness may be controlled by changing the viscosity and withdrawal speed of the substrate.
4. Doctor blade – This uses a moving blade to spread the ink onto a stationary substrate. The film thickness is controlled by altering the fluid viscosity, blade speed, blade height and pressure of the blade. This method allows to cover large area and is less wasteful, however, requires precise control of the blade and any inhomogeneity of the substrate will lead to surface roughening, which may not be uniform or repeatable.

A key part of the ink formulation process is the method used to make the ink. Common processing methods include ultra-sonication, high shear mixing, stirring and ball milling.[170] The optimisation of these methods is also a crucial part of the ink formulation process. Ultra-sonication remains the most common method, especially in preparation of Nafion based inks for PEMFCs. Although the impact of the ionomer content, solvent system, casting method as well as the ink dispersion method have been studied for PEMFCs, there is a lack of understanding of how this relates to the performance of electrochemical reduction of CO_2.

A systematic approach is required for development of catalysts and catalyst inks in order to improve and optimise the performance of the electrochemical reduction of CO_2. This will also deepen our understanding on the process and how it could translate into a larger scale process. The optimisation of the catalyst layer is also crucial for improving the stability of the active material during testing and subsequent commercial use (in terms of years). Therefore, key considerations regarding the catalyst layer have to be made during the testing phase.

This chapter will consider a systematic approach to the ink formulation of copper-based catalysts. The effect of the Nafion fraction on the Faradaic efficiency and overpotential for the conversion of CO_2 to formic acid was studied. The effect of the applied potential (in the range –0.6 to –1.4 V) on the performance of the CuO catalysts, was also explored. Electrochemical impedance spectroscopy (EIS) was used to provide an insight into the influence of the Nafion fraction on the performance of CO_2 reduction to formic acid.

4.2 Method

4.2.1 Materials

Copper(II) nitrate trihydrate [$Cu(NO_3)_2{\cdot}3H_2O$, technical grade, >98 %] and potassium hydroxide pellets (KOH) were used in the synthesis of ultrafine CuO. All reactions were conducted in deionised water (>10 MΩ). Nafion (5 wt% in a mixture of lower aliphatic alcohols and 45 vol% water) and high purity LC-MS chromasolv isopropanol (IPA) and methanol were used in the ink formulation. All chemicals, unless stated otherwise, were supplied by Sigma Aldrich, (Dorset, UK). High purity $KHCO_3$ was supplied by Alfa Aesar, (Lancashire, UK). All chemicals were used as purchased.

4.2.2 Synthesis of CuO

Pure copper(II) oxide nanoparticles were synthesised using a dual continuous hydrothermal flow system, which uses four high-pressure diaphragm pumps (Chapter 2). Briefly, a room temperature aqueous solution of 0.1 M copper nitrate trihydrate was pumped (via pump 2 at 40 mL min^{-1}) to mix with an aqueous flow of 0.2 M potassium hydroxide solution (via pump 3 at 40 mL min^{-1}) in a dead volume T-piece. The resulting mixture was then mixed with a superheated water feed at 400 °C (delivered via pump 1 at 80 mL min^{-1}) inside a confined jet mixer, (CJM) (Chapter 2). This CJM was designed to mix the reagents without blockages under a turbulent mixing regime (Reynolds number ≈ 6079). The calculated mixing temperature was ca. 305 °C, with a residence time of ca. 0.8 s before the nanoparticle slurry was quenched rapidly as it mixed with a feed of room temperature deionised water (via pump 4 at 160 mL min^{-1}) in a second CJM (Reynolds number ≈ 2989). The mixing temperature and Reynolds number were calculated based on the model described by Wagner and PruB on the properties of water. The design and sizes of the two CJMs are given in more detail in Chapter 1 and 2 and previous publications.[113] The newly formed and partially cooled nanoparticle laden slurry was then cooled further via a pipe-in-pipe heat exchanger and was then continuously collected from the exit of the back-pressure regulator (BPR), which maintained the pressure in the system at 24.1 MPa. The particle slurry was processed and freeze-dried as described in Chapter 2.

4.2.3 Materials Characterisation

The freeze-dried CuO nanopowder were examined by PXRD, XPS, TEM as described in Chapter 2, Section 2.4. Particle size distribution was determined by measuring the diameter of 300 particles from TEM images.

4.2.4 Ink formulation

4.2.4.1 Testing phase

Processing method

To investigate the effectiveness of the ink formulation, the ink processing method was altered between low and high intensity sonication of the inks. For completeness, high shear mixing was also tested. The ink formulations used the dried CuO nanopowder, IPA, Nafion, water and methanol (in some suspensions) in varying ratios. A VWR USC100T sonic bath was used for samples processed at a lower intensity for 30 mins. For high intensity samples, the suspension was sonicated using a high-power dispersion sonic tip (Branson Sonifiers 250D, Geneva, CH) for 10, 30 and 60 mins at 20 % amplitude, with a pulse sequence of pulse on for 0.2 s and pulse off for 0.5 s. An IKA T18 digital Ultra Turrax high shear mixer was used at 9000 rpm for 30 mins. The samples are named as following: SB1 for sonic bath, SP for sonic probe (where SP1 indicates sample testing for 10 mins and so forth), HSM is used to describe high shear mixer.

Solvent System

The composition of the solvent system was altered to understand its effect on the dispersion of the ink. The water content in the ink was altered (0, 13, 33, 50 and 100 vol%) against IPA. Methanol was added to the system to improve the ink quality (to obtain a homogeneous and stable ink). The methanol content was varied in the range 0 to 3000 μL.

4.2.4.2 Nafion content – Optimised ink formulation

50 mg of CuO nanoparticles were suspended in a mixture of isopropanol (IPA), methanol and D.I. water in a volume ratio of 1:6:6, respectively. The Nafion content was varied at values of 1, 10, 25, 50 and 66 wt% (vs. total solid fraction). The suspension was sonicated using a high-power dispersion sonic tip (Branson Sonifiers 250D, Geneva, CH) for 30 minutes at 20 %

amplitude. The ink suspension was immersed in an ice bath to avoid solvent evaporation and conversion of CuO to copper carbonates.

4.2.5 Electrode preparation

The glassy carbon sheet (1 x 1 cm) (Alfa Aesar, Lancashire, UK) was cleaned by polishing using a 0.05 μm alumina slurry (Buehler, Stuttgart, DE) prior to drop casting. Electrodes were then prepared by casting CuO inks on a glassy carbon sheet to have a loading of approximately 0.3 mg cm^{-2}. Subsequently, the glassy carbon was dried overnight in a vacuum oven at 40 °C to give a homogeneous CuO film, denoted as a catalyst layer (CL). Samples were thus named CL1, CL10, CL25 and CL66 for catalyst layers with 1, 10, 25 and 66 wt% Nafion fraction, respectively. The catalyst film morphology was observed using SEM.

4.2.6 Electrochemical characterisation

Electrochemcial characterisation was carried out on all CL samples, as described in Section 2.6, where cyclic voltammetry, constant potential electrolysis, surface area measurements, EIS and SEM was conducted.

4.3 Results and discussion

4.3.1 Synthesis of CuO

Ultrafine CuO nanoparticles were synthesised via continuous hydrothermal flow synthesis (CHFS) using 0.1 M copper nitrate and 0.2 M KOH, resulting in an aqueous nanoparticle slurry with a pH of 5. The particles in the slurry were cleaned by centrifugation and dialysis to remove any possible unreacted precursors and by-products. The wet solids were freeze-dried, resulting in a black powder (yield = 76 %). The PXRD pattern (Figure 4-2a), confirmed that pure phase CuO was formed, with a monoclinic structure (similar to standard reference pattern of CuO, JCPDS 01-089-2529), with the

most intense reflections arising from (–111), (111) and (–202) peaks. The broad nature of the peaks suggested a small crystallite size for the CuO, which was estimated from application of the Scherrer equation to be ca. 15 nm.[171] Surface analysis of the particles by XPS confirmed the presence of Cu^{2+} species, as indicated by the XPS peaks for Cu $2p_{3/2}$ at 933.9 eV and Cu $2p_{1/2}$ at 953.7 eV (Figure 4-2b). Additional confirmation of the Cu^{2+} state was seen with the broad shake-up satellite peaks at higher binding energy than the main peaks. Shake up satellites are not normally seen with Cu^{+} or Cu^{0} oxidation states, as reported previously in the literature, which suggested the presence of only Cu^{2+} species on the surface.[60,85]

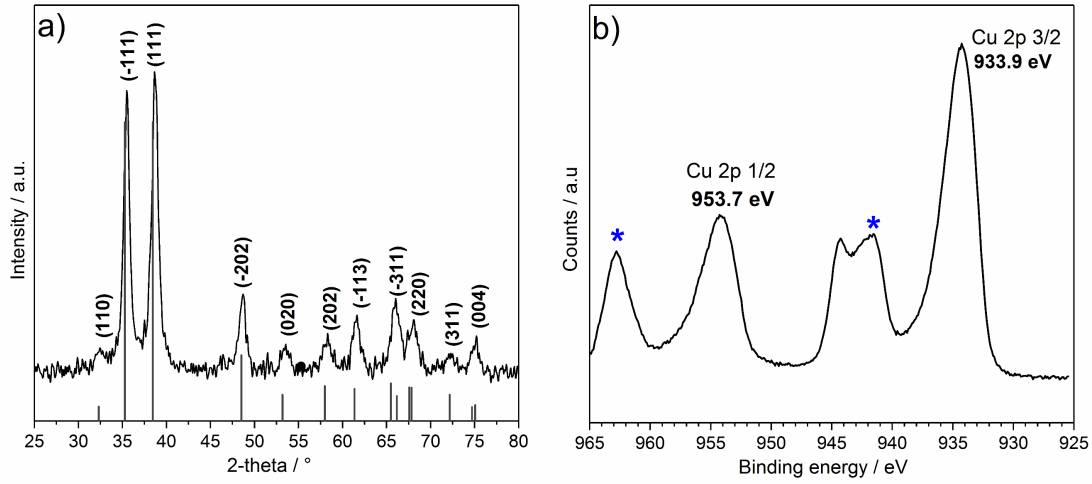

Figure 4-2 - a) PXRD pattern of CuO synthesised via CHFS (JCPDS 01-089-2529) and b) high resolution Cu 2p scan of CuO as prepared via CHFS, Cu 2p 3/2 at 933.9 eV and Cu 2p 1/2 at 953.7 eV. Satellite peaks are highlighted by asterisks.

As synthesised nanopowders were also analysed by Transmission Electron Microscopy (TEM) (Figure 4-3a). The CuO particles appeared to be well defined with some faceting, monocrystallinity and a rhombic morphology, with an average size of 17 ± 5 nm (300 particles measured, Figure 4-3b). The average particle size matched well with the crystallite size of ca. 15 nm as estimated from the Scherrer equation. Higher magnification analysis showed a lattice planar spacing of 0.23 nm, which was in agreement with literature value for the (111) plane (Figure 4-3c) of 0.23 nm.[135] The BET surface area was found to be 52 $m^2\ g^{-1}$ and was in close agreement with the

estimated BET surface area based on a hard sphere model (57 m^2 g^{-1}). The crystallinity and phase purity of the nanoparticles were consistent with previous observations reported for the formation of metal oxides synthesised via CHFS, which suggested the formation of CuO occurred via rapid hydrolysis of a Cu(II) salt to form $Cu(OH)_2$ and subsequent dehydration to form CuO.[101,172] Also, the small crystallite size, high yield and monodispersity of particles, suggested a nucleation dominated mechanism of nanoparticle formation, where a supersaturation of small nuclei was maximised due to the decrease in dielectric constant and the low solubility of inorganic ions under the reaction conditions in the CJM.[113,173,174]

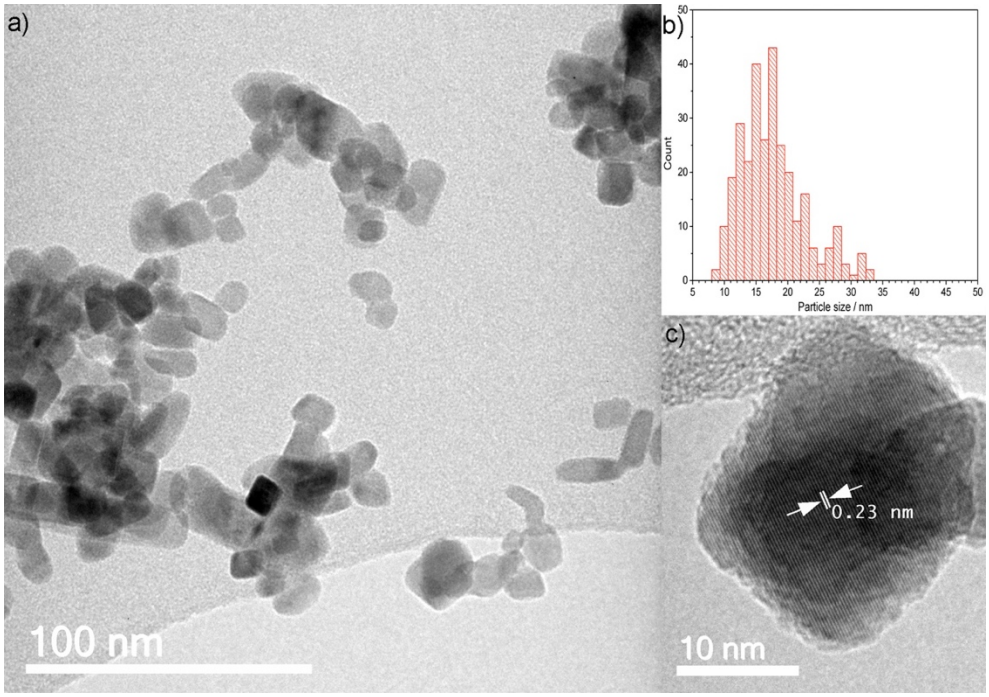

Figure 4-3 - a) TEM image of CuO nanoparticles as prepared by CHFS, b) inset shows histogram of particle size distribution measured from 300 particles and c) high resolution image of CuO nanoparticles showing (111) plane with a d spacing of 0.23 nm.

4.3.2 Catalyst Ink development

A number of factors are known to affect the electrochemical activity of CO_2 electroreduction such as the catalyst type, cell design and operating test conditions, as commonly reported in the literature.[175] Other parameters that can affect the electrochemical activity also include the ink formulation

(type(s) of solvents, binder ratios, ultra-sonication type) and electrode structure (the film quality and uniformity), which is also affected by the deposition and drying process of the film. Reports in this area linked to CO_2 electroreduction are limited and inconclusive, therefore, these factors remain important parameters that have not been defined, for the electrochemical conversion of CO_2.

4.3.2.1 Method of preparation

The ink formulation method was studied to find the optimum preparation method. Three methods were chosen; sonic probe, high shear mixer and sonic bath due to their common occurrence in ink preparation in literature. Intensity and preparation time parameters were altered (Table 4-1). The ink photographs (Figure 4-4) provide examples of the as prepared ink, where the HSM sample clearly shows a poor suspension, where particles are beginning to sediment. A longer and higher shear mixing time was also studied but resulted in equally poorer dispersions.

Table 4-1 - Preparation methods for catalyst inks. *The method highlighted in asterisk was not used for further experiments due to its poor quality.

Sample ID	Preparation method	Time (mins)	Outcome
SB1	Sonic bath	30	Dispersion appeared homogeneous.
SP1	Sonic probe	10	Dispersion appeared homogeneous.
SP2	Sonic probe	30	Dispersion appeared homogeneous.
SP3	Sonic probe	60	Dispersion appeared homogeneous.
HSM1	High shear mixer*	30	Poor dispersion. Particles settle quickly.

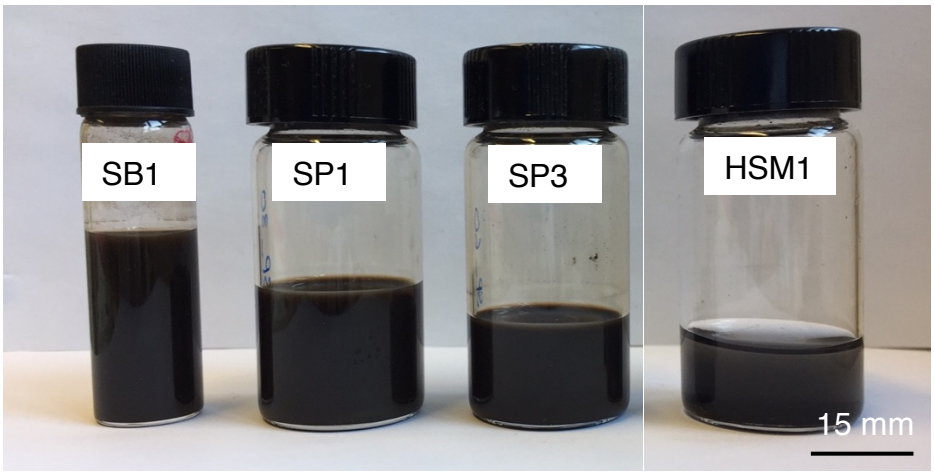

Figure 4-4 - Photograph of catalyst inks prepared with different preparation methods; sonic bath, sonic probe and high shear mixer.

If the dispersion remained homogeneous during the casting phase, it was deemed successful. The size distribution of the catalyst in its ink form was evaluated by DLS in order to effectively understand the optimised preparation method (Figure 4-5). Sample HSM1 was not used for further testing as the dispersion quality was too poor to obtain optimal DLS measurements as well as resulting in significantly poorer films. The effect of the sonication intensity is apparent on the size distribution as well as the Z-ave diameter of the nanoparticle aggregates in the inks, especially when the SP3 is compared to SB1. The sample prepared using sonic bath showed dual aggregation behaviour where some significantly larger aggregates remained in the ink, which the sonic probe may be able to reduce in size. The irradiation time does not make a significant difference between the 10 and 30 min samples when using a sonic probe and similarly, the difference between the 60 min samples to the rest is minimal. Ultrasonication may further polymerise or degrade the Nafion polymer.[176] The effect of ultrasound on fuel cell catalyst inks has been evaluated by Pollet and Goh, where Pt/C in Nafion and IPA was subjected to different sonication intensity.[168] It was observed the longer irradiation times resulted in changes in composition and particle morphology. To prevent such issues with this system, all further ink

formulations were subsequently only subjected to 30 min ultrasonic irradiation times.

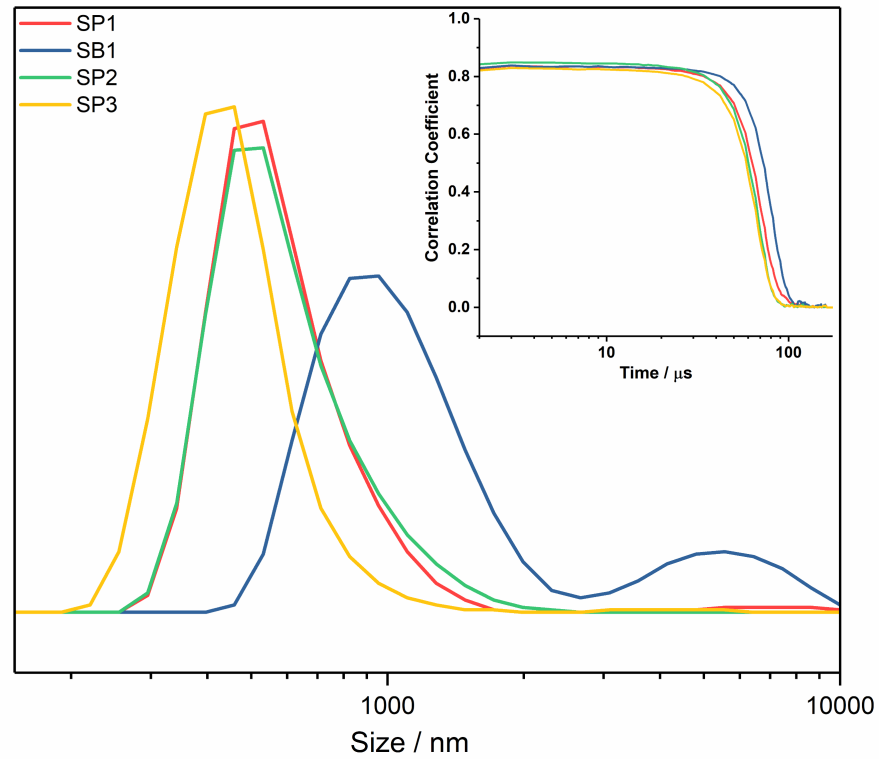

Figure 4-5 – Particle size distribution of catalyst inks prepared by sonic bath and sonic probe. Inset shows correlation curves for each sample.

The quality of the dispersions was also evaluated on glassy carbon electrodes to assess their wetting and drying properties on the chosen substrate for electrochemical testing. The electrode films were subsequently assessed by SEM (Figure 4-6).

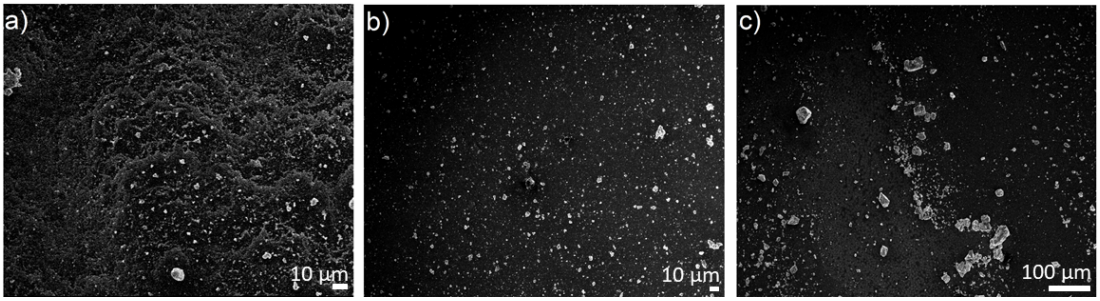

Figure 4-6 – SEM images of catalyst inks prepared a) sonic bath, b) sonic probe and c) high shear mixer on glassy carbon substrate.

For the sonic bath (Figure 4-6a), the SEM images showed that the particles are more homogeneously deposited than other samples on the glassy carbon but that can also be significantly influenced by how the film dried. The sonic bath provides poor control over the sonication intensity and generally low ultrasonic power is transmitted through the bath. A common problem is that the position of the suspension in the sonic bath affects the consistency of the ink, as the sonication waves are not always consistently distributed. The sonic probe allows for the sonicating power to be directly delivered to the solution rather than dissipated through a bath but more importantly the intensity can be controlled and tuned to find the optimal effect.[168,177] From the SEM images, it is evident that high shear mixing the ink, is a poor choice for this system as the film looks inhomogeneous with significant exposed substrate areas where large aggregates are also present with smaller particles (Figure 4-6).

4.3.2.2 Solvent system optimisation

The solvent system was also evaluated by changing solvent types and solvent ratios. The solvents tested were isopropyl alcohol (IPA), methanol (MeOH) and water (H_2O). Initial ink formulations involved using IPA and water only, as it was adopted from the solvents and compositions used in the literature, which were basis for the initial ink formulations (Table 4-2). Ink photographs are also shown in Figure 4-7, where initial visual appearance suggested the ink dispersions were of good quality to be casted.

It is well known, particularly in the field of PEMFC that the solvent system has a significant effect on the Nafion conformation, which in turn affects the film development and its electrochemical activities.[178] Reports concerning PEMFC and Pt/C based materials show that the ratio of IPA/H_2O or MeOH/H_2O play a significant role in enhancing the electrochemical activity of a fuel cell and the performance of the catalysts. The most common solvent systems that have been used in the literature, both in the case of PEMFC

and CO_2 electroreduction have been IPA and water with Nafion. The solvent system that is effective is also significantly dependent on the particles that are being utilised, in terms of their composition, size and morphology.

Table 4-2 - Optimisation of solvent system. All inks included the same amount of catalyst (~20 mg) and were sonicated for 30 minutes using a sonic probe. The Nafion content remained constant in all experiments.

Sample ID	Ink formulation	Outcome
SS1	IPA to water ratio 3:1	Poor dispersion
SS2	IPA:H_2O 6:1, with Nafion	Poor dispersion
SS3	IPA 100 % with Nafion, no H_2O	Poor dispersion
SS4	H_2O 100% with Nafion, no IPA	Poor dispersion
SS5	IPA:H_2O 1:1, with Nafion	Poor dispersion

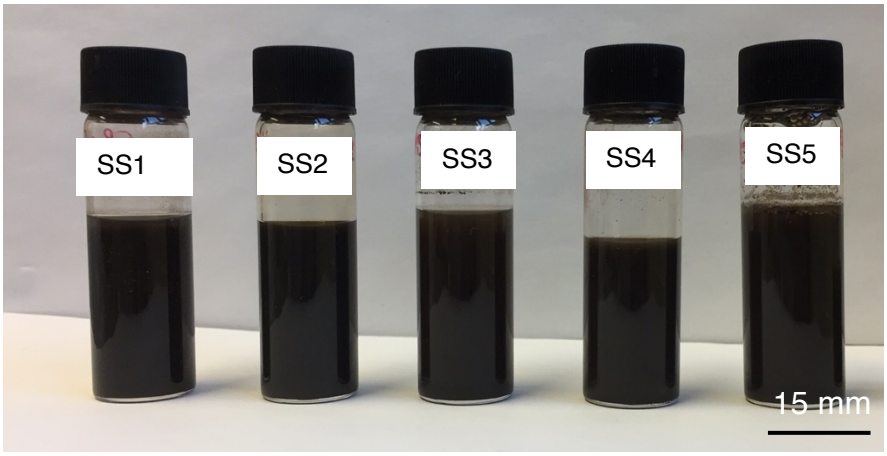

Figure 4-7 – Image of catalyst inks prepared with different ratios of IPA and water.

Commonly studied materials include Pt/C and therefore comparisons with CuO systems are limited. With the catalyst used in this Chapter, initial ink formulations (SS1 – Table 4-2) using IPA and water alone as solvents for the ink dispersion, were found to be unsatisfactory in providing homogeneous uniform inks. Upon deposition of those inks onto the electrode surface, the film was visibly inhomogeneous and dried in 'patches' or resulted in wide coffee rings. Coffee rings appear due to different evaporation rates for liquids in the ink, as more particles are carried to the edge than that remain in the centre, leading to the coffee ring effect (Figure 4-8).

Figure 4-8 – IPA and water ink deposited on glass slides showing presence of coffee rings.

This is a clear indication that the catalyst film is inhomogeneous and non-uniform. The inks could be further improved by altering the solvent system. A systematic approach was used to evaluate an optimised solvent system, where the ratio of IPA to water was altered. Incorporation of water in the ink formulation improved the homogeneity of the ink, as observed from the DLS measurements of the different inks (Figure 4-9a). The Z-ave parameter decreased with increasing water content within the ink (Figure 4-9b), with the exception at 13 vol % water in the ink. The density and viscosity of IPA and water mixtures changes with the composition of the solvents; where the viscosity goes through a maxima at high IPA content (>40 wt% IPA).[163] DLS measurements are strongly affected by the viscosity and the particle size of the dispersion. A more viscous solution leads to slower Brownian motion of particles and therefore is shown by the broader particle size distribution and an increased Z-ave diameter.

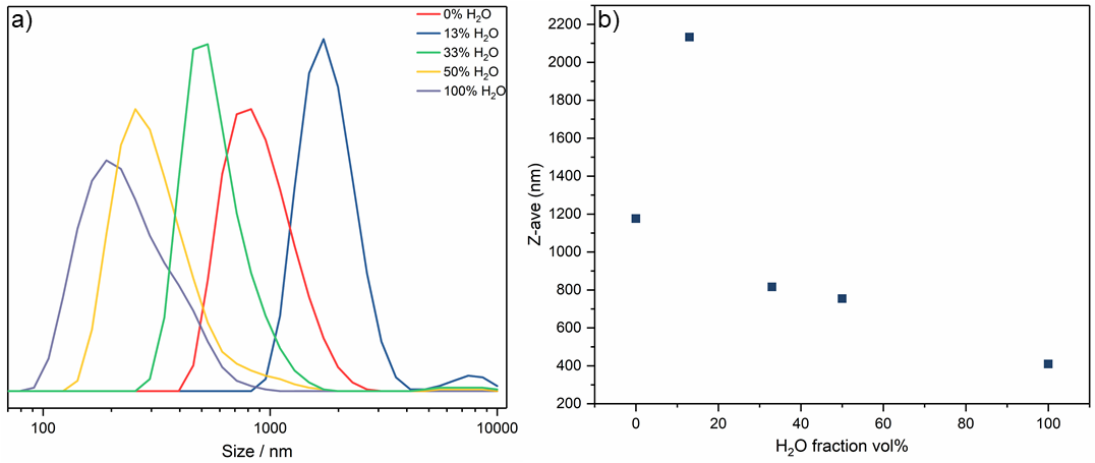

Figure 4-9 – a) Particle size distribution of catalyst inks where the solvent system is systematically altered to find the optimum solvent ratio. The water content is altered 0, 13, 33, 50 and 100 vol % H_2O, b) corresponding correlation curve for the sample measured and c) plot of Z-ave (nm) versus the water fraction (vol%) in the ink formulation.

Nafion consists of a hydrophobic perfluorocarbon backbone and hydrophilic vinylether sulfonated side chains. As these are incompatible,[179] i.e. will not interact with each other to form aggregated particles, the presence of the solvent and the catalyst plays a bigger role in the final morphology of the Nafion polymer. The behaviour observed in the DLS measurements may be attributed to the solvent interactions towards the backbone or the side chains of Nafion. The compatibility of the solvent with the hydrophobic perfluorocarbon backbone is thought to drive the formation of the primary aggregated particles. For example, if a solvent is not compatible with the backbone, it is likely that the aggregated particles will be larger.[163] Similarly, the negatively charged sulfonate (SO_3^-) side chains groups in the Nafion will interact with positively charged H_3O^+ ions (derived from water). The dielectric constant of the solution is known to affect the Nafion morphology and therefore, will also affect the compatibility with the sulfonate side chains. The combination of solvents will subsequently affect the dielectric constant and the final particle size distribution and ink behaviour. In investigations considering IPA/water ratios and their impact on the Nafion clusters in the literature, it has been reported that another form of intermolecular interaction is the hydrogen bonding between alcohol and water. IPA may be able to break the H-bond network in water, if the IPA ratio is sufficiently high, to form IPA-IPA intermolecular hydrogen bonds. The excess water molecules may then interact with the negatively charged ions and form SO_3^--- H_3O^+-- SO_3^- ionic interactions leading to the formation of secondary clusters.

Furthermore, the inclusion of more IPA than water can result in a shift of the mean hydrodynamic radii to smaller radius.[163,180] However, this is not observed in the case of the inks formulated with the CuO catalysts in the DLS measurements. As the water and IPA ratio was altered, the mean Z-ave varied widely and when the water ratio was higher than IPA or no IPA was used in the solvent, the Z-ave was considerably smaller than if more IPA was used. Indeed, the IPA may interact with H^+ ions and form $(CH_3)_2CH\text{-}OH_2^+$,

however, due to the lack of compatibility of IPA with the fluorocarbon backbone, it is more likely to drive the formation of SO_3^- ions from SO_3H due to the H^+ ions.[163] This could also be encouraged due to the lower steric hindrance from the H_3O^+ ions rather than the $(CH_3)_2CH\text{-}OH_2^+$.

With increasing water content versus IPA, the dielectric constant is also increased, resulting in the formation of more negatively charge sulfonate groups and therefore, smaller primary Nafion aggregates.[163] It should be noted that usually the interactions of the solvents and Nafion is considered without the catalyst in the literature. The presence of CuO and its surface behaviour is likely to alter the behaviour of the Nafion, water and IPA. Indeed, it is apparent from the DLS measurements, the effect of utilising water as a major solvent in ink formulations, results in a more homogeneous ink. The surface coverage of CuO nanoparticles may include a high proportion of surface hydroxyls due to the synthesis and processing method used. Thus, it could be assumed that the interaction of the catalyst with water as a solvent would be favoured due to formation of a hydrogen bond network. This could further substantiate the Nafion, water and IPA interactions as observed through DLS measurements, where water is favoured as a major solvent and the Z-ave is smaller.

During the deposition and drying phase of an ink on a substrate, the wetting and adhesion properties play a key role in producing inks with an acceptable print quality. Water-based inks can have inherent issues due to the surface tension effects of the ink and the surface energy of the film.[181] It was observed during the deposition of high water content inks, that ink droplets formed beads on the surface of the glassy carbon electrode, where the ink would not distribute evenly on the surface. This was despite the DLS data that suggested that the resultant ink had a narrower size distribution and therefore more homogeneity. In order to achieve satisfactory wetting of the ink onto the substrate, the surface tension of the ink and the surface energy

of the film should be altered to achieve optimum results. Pre-treatment of the substrate with IPA or methanol to alter the surface energy of the substrate was also investigated. However, this resulted in poor ink distribution and also led to some physical contamination of the substrate and was subsequently not investigated further.

Methanol was chosen as a third solvent choice, in order to alter the surface tension properties of the ink and to aid the distribution and wetting properties of the ink on the glassy carbon substrate. However, triple solvent systems with Nafion have not been reported, so comparisons of the optimised solvent system used in this Chapter cannot be made to the literature. Methanol with water and Nafion as an ink (without IPA) was unsuccessful and resulted in faster sedimentation of particles than others. However, when methanol was added systematically (0 – 3000 μL methanol) to the ink mixture (containing IPA, water and Nafion), it was observed through DLS (Figure 4-10) and ink deposition that the ink wetting properties improved significantly and resulted in wetting of the ink onto the glassy carbon electrode rather than forming droplets. The size distribution was also altered with the addition of methanol; addition of a small amount to the ink mixture did reduce the mean hydrodynamic diameter and the addition of 400 μL increased the Z-ave diameter (Figure 4-10c) and the particle size distribution showed bi-modal distribution, which may be due to this particular composition of IPA, methanol and water being unfavourable for a homogeneous ink. With increasing methanol addition, the Z-ave decreased and increasing amounts of methanol were found to result in a narrower size distribution compared to the standard and 200 μL sample.

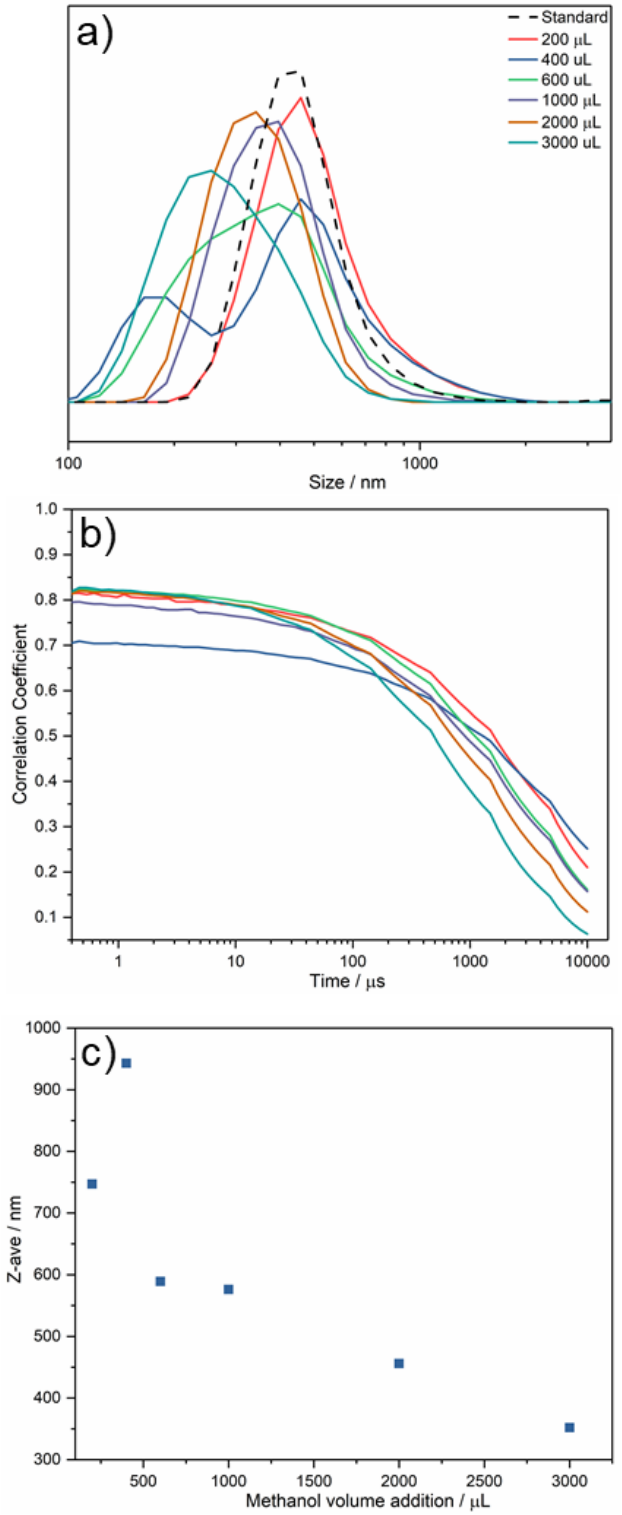

Figure 4-10 – Particle size distribution of catalyst inks versus methanol added systematically to a pre-prepared ink mixture of catalyst, Nafion, IPA and H_2O.

4.3.2.3 Deposition and drying method

Another crucial factor that has been considered in ink development is the process of ink deposition and drying. The drying process of the film has a significant role to play in the final uniformity of the film. As mentioned in the previous section, the prevalence of coffee rings after drying is suggestive of different evaporation rates of solvents, which leads to particles being carried to the edge of the film, resulting in an uneven distribution of particles in the film. Herein, two different drying temperatures were investigated; room temperature air drying and vacuum oven at 40 °C (Figure 4-11).

Figure 4-11 – CuO ink deposited on glass slide – (left) shows ink dried in air at room temperature and (right) shows ink dried in vacuum oven at 40 °C.

It was found that the air drying at room temperature resulted in wider coffee rings due to the slow evaporation rates. As the drying process was significantly aided by the raised temperature under vacuum, the solvent evaporation was faster, allowing less time for the redistribution of the particles to the edge. This resulted in a significantly more homogeneous film on the glassy carbon electrode and this drying method was adopted for subsequent ink depositions.

4.3.3 Contamination during testing

During the electrochemical reduction of CO_2, it is critical to ensure no organic contaminants are present in the electrolyte or during any processing stages. During early stages of establishing this set up, it was observed that contaminants may originate from various sources, such as the CO_2 feed, the water purification source and use of any sterilised plastics (pipette tips or Nalgene bottles). Contaminants could also be traced to leaching of solvents

from the ink, if it was not dried for long periods of time. Following this, all inks were dried under vacuum overnight after any deposition stage. The NMR shows the level of contamination that may be found when the CO_2 feed and sterilised plastics were used (Figure 4-12). In general, contaminants may include products of interest from the electrochemical conversion of CO_2 (such as CH_3OH and HCOOH), so it was even more critical to ensure all sources of possible contaminants were made redundant and protocols were in place to prevent such issues.

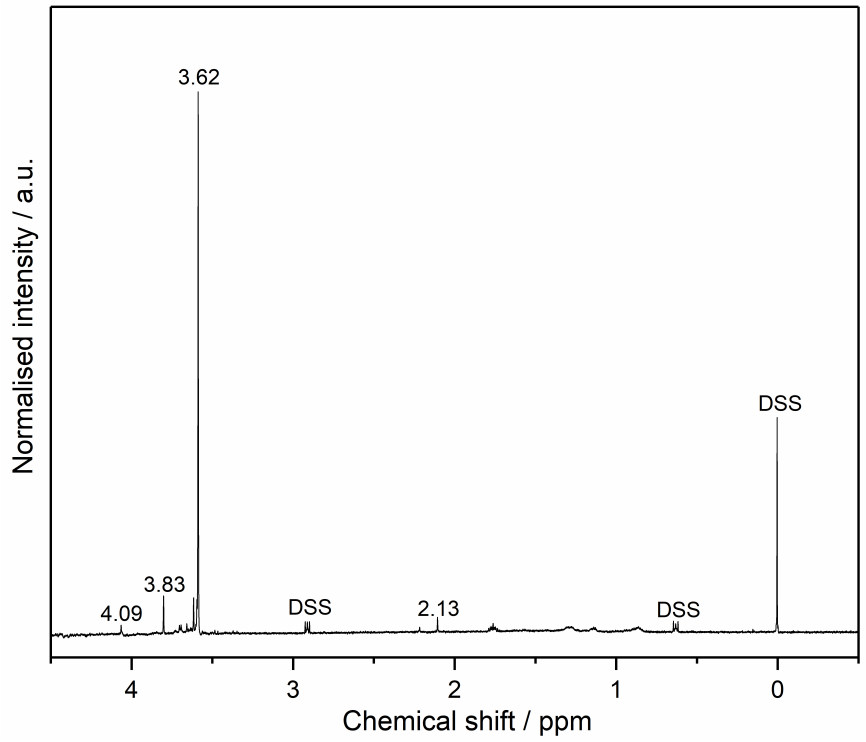

Figure 4-12 - ^1H NMR of contaminants present in the bubbler after CO_2 saturation. DSS peaks are highlighted, where DSS was used as a reference control.

To avoid this, the CO_2 was first fed through clean deionised water in a bubbler and then passed onto the electrochemical cell. When this was not carried out, contaminants could be found in the electrolyte. The water in the bubbler was regularly cleaned and checked for contaminants. Similarly, sterilised plastics (pipette tips) were avoided and mainly glass syringes and needles were utilised. If pipettes were used during any stage, they were thoroughly washed with deionised water, prior to use.

4.3.4 Role of Nafion

4.3.4.1 Ionomer content

Following the optimisation of the solvent system, ink preparation method and the drying process, inks with different Nafion content were evaluated to understand the impact of this on the electrochemical performance of CO_2 reduction. The Nafion content was varied by 1, 10, 25 and 66 wt% versus the solid fraction. 50 wt% Nafion content was also investigated, however, this resulted in a poor ink dispersion. The inks were also characterised by DLS (Figure 4-13). According to the DLS measurements, the sample with 25 wt% Nafion content showed inks with a more homogeneous ink formulation, as with 1 wt%, a bimodal aggregate was observed, despite a lower Z-ave. At 10wt% Nafion the size distribution narrowed but this was shifted to higher Z-ave and 66 wt% Nafion had a larger Z-ave than the sample at 25 wt% Nafion.

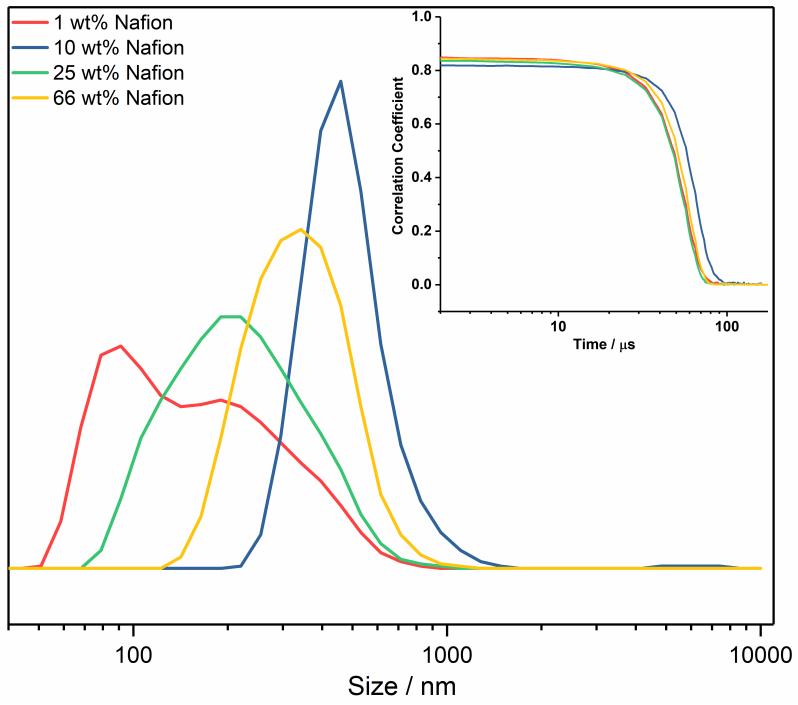

Figure 4-13 – Particle size distribution of the catalyst ink where the ionomer content was altered between 1 and 66 wt% Nafion. Inset shows correlation curve for each sample.

4.3.4.2 Cyclic Voltammetry

The as-prepared nanoparticles were suspended into inks containing IPA, methanol and D.I. water in a total volume ratio of 1:6:6, respectively. The Nafion content was varied between 1, 10, 25 and 66 wt% Nafion (vs. total solid fraction). The inks were cast on glassy carbon electrodes and the redox behaviour of CuO to Cu (via Cu_2O) was characterised by cyclic voltammetry in CO_2 saturated 0.5 M $KHCO_3$.[182] Samples were thus named CL1, CL10, CL25 and CL66 for catalyst layers with 1, 10, 25 and 66 wt% Nafion fraction, respectively, where the catalyst layer was described as CL. Typically, CuO reduction followed a small peak for CuO to Cu_2O reduction (peak labelled I) and the appearance of a nucleation loop and a crossover point characteristic of nuclei formation and growth process could be observed in the potential range from –0.2 to –0.6 V vs. Ag/AgCl. This is typically higher than the equilibrium potential as the metal ions were deposited on a substrate that was crystallographically different, resulting in a substrate metal misfit. Distinct cyclic voltammograms were observed in this case for glassy carbon coated with CuO inks with different Nafion fractions (Figure 4-14).

A nucleation loop was observed for all samples, however, the position and size of the nucleation loop varied greatly between each sample. The initial reduction from CuO to Cu_2O was observed at –0.1 V and is represented as "I" in Fig. 4. The onset of the crossover potential was similar for sample CL1 (Figure 4-14a) and sample CL10 (Figure 4-14b), and appeared at –0.3 V. The crossover potential for sample CL25 (Figure 4-14c) was lower than the previous example, at –0.2 V, indicative of a lower overpotential requirement for Cu_2O reduction to Cu on CuO. A considerable difference was observed for CL66 (Figure 4-14d), where the crossover potential was shifted to more negative potential at –0.6 V, indicative of a significant overpotential requirement for Cu_2O reduction to Cu on CuO. The appearance of the sharp anodic stripping peak was consistent with the dissolution of the Cu layer that previously formed on CuO represented by "II" (Figure 4-14). Small cathodic

and anodic peaks were also observed in samples CL1, CL10 and CL66 and were attributed to the reduction and oxidation of copper species taking place on inhomogeneous sites, potentially arising from inconsistencies in the film deposition. Similarly, splitting of the anodic peak for sample CL66 was observed, where the secondary peak showed some asymmetric behaviour and was likely a contribution from the oxidation of Cu_2O to CuO as represented by peak III in Figure 4-14d. The differences in the cyclic voltammetry each sample tested, could be linked to the variation in the Nafion fraction in the catalyst layer. Indeed, the presence of 66 wt.% Nafion within the catalyst layer was hindering the copper oxide reduction process, as shown by the shifting of the crossover position.

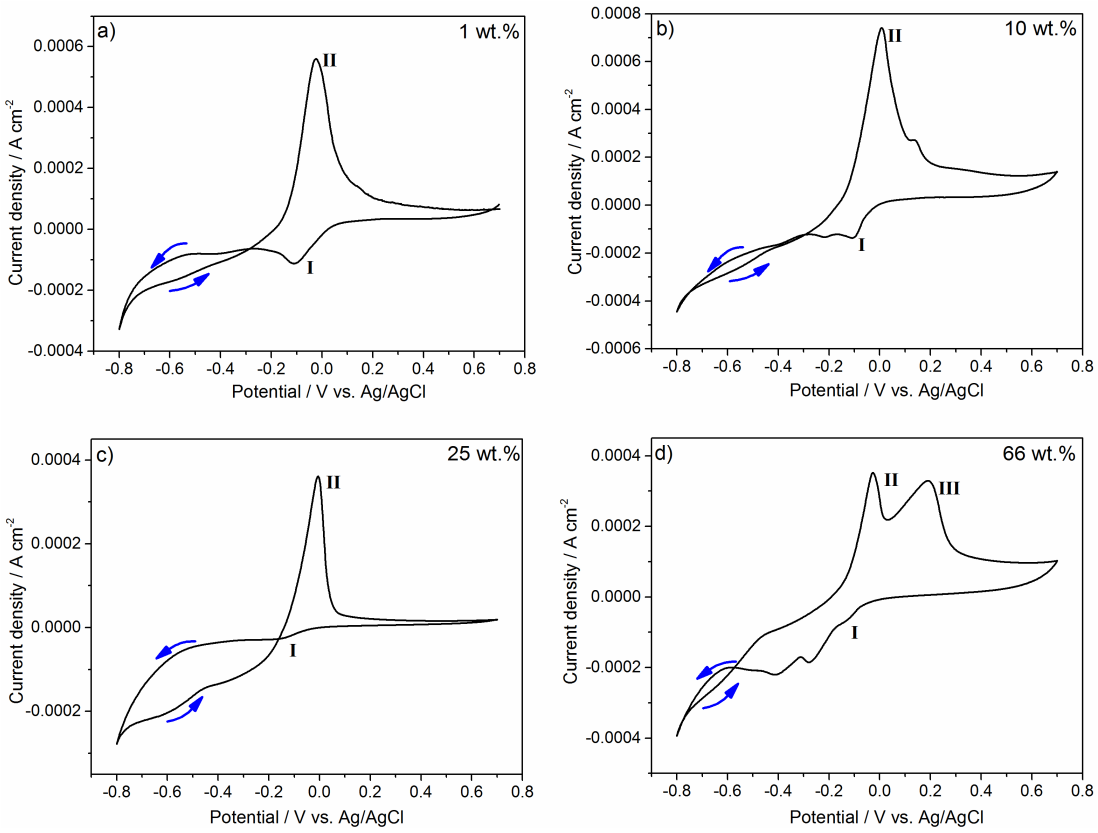

Figure 4-14 - Cyclic voltammograms of samples a) CL1, b) CL10, c) CL25 and d) CL66 in 0.5 M $KHCO_3$ saturated with CO_2 at a scan rate 5 mV s^{-1}, during the second cycle.

4.3.4.3 Constant Potential Electrolysis

CuO inks with different Nafion fractions were examined by constant potential electrolysis to determine the correlation between Nafion fraction, Faradaic

efficiency and the overpotential of CO_2 reduction to formic acid. Glassy carbon electrodes prepared with CL1, CL10, CL25 and CL66 inks were held at various potentials (range of –0.6 to –1.4 V) and the effect on the Faradaic efficiency was studied (Figure 4-15). The catalyst layer with 1 wt% Nafion fraction showed high Faradaic efficiency for applied potentials of –1.0 and –1.2 V. At –1.4 V, some delamination of the CuO/Cu film from the glassy carbon electrode was also observed (attributed to excessive formation of hydrogen bubbles from water splitting). As the film was damaged during electrolysis under these conditions, no product was observed via NMR or GC. Furthermore, the current density increased steadily with increasing applied potential, with a significant increase at –1.4 V (–16 mA cm^{-2}) as a result of substantial water splitting reaction.

For sample CL1, trace levels of formic acid were observed at –0.6 and –0.8 V, as the overpotential was not sufficient to drive the reduction at a rate, where measurable products were obtained. As the Nafion fraction was increased from 1wt% to 10 wt%, with increasing negative potential applied across the electrode; the Faradaic efficiency for formic acid production reached a maximum of 11 % at –1.2 V. Increasing the potential to –1.4 V resulted in a sudden drop to a Faradaic efficiency of 1.8 % as CO_2 reduction competed further with water splitting. With increasing Nafion fraction in the catalyst layer to 25 wt%, at –0.6 V and –0.8 V, formic acid production was suppressed, with Faradaic efficiencies tending towards 0.6 and 1.8 %, respectively. A significant increase in the Faradaic efficiency was observed at –1.4 V (61 %), which to the author's knowledge is one of the highest Faradaic efficiency achieved on copper-based catalysts for the formation of formic acid. Recently reported comparable results using electrodeposited copper nanofoams have shown formic acid production at a Faradaic efficiency of 37 % at –1.5 V vs. Ag/AgCl.[59] In another report, copper oxide/copper electrocatalysts synthesised via batch hydrothermal methods showed high Faradaic efficiency for formic acid production of 59.3 % at –0.9

V vs. Ag/AgCl and reached 62.2 % at −1.3 V vs. Ag/AgCl after 20 hours of electrolysis time.[156] High Faradaic efficiencies in this case were attributed to the distinct morphology of the electrocatalysts, however, the batch synthesis of nanostructured catalysts is inherently difficult to scale up reproducibly. Additionally, the rate of formation of formic acid was also found to be very high, at 4.2 mmol g^{-1} hr^{-1}. There was no report of the rate of formation mentioned by Qiao et al., so a direct comparison cannot be made regarding the kinetics of formic acid formation.

Herein, a significant drop of Faradaic efficiency was observed as the Nafion fraction was increased to 66 wt%. No products were observed until −1.0 V was applied, suggesting a larger overpotential compared to lower Nafion fractions, was required to form any products. A shift to more negative overpotentials with increasing Nafion content, was also observed. Similarly, the current density decreased with increasing Nafion fraction in the catalyst layer. Thus, the best performing fraction of 25 wt% Nafion gave the highest Faradaic efficiency and good stability to the catalyst layer.

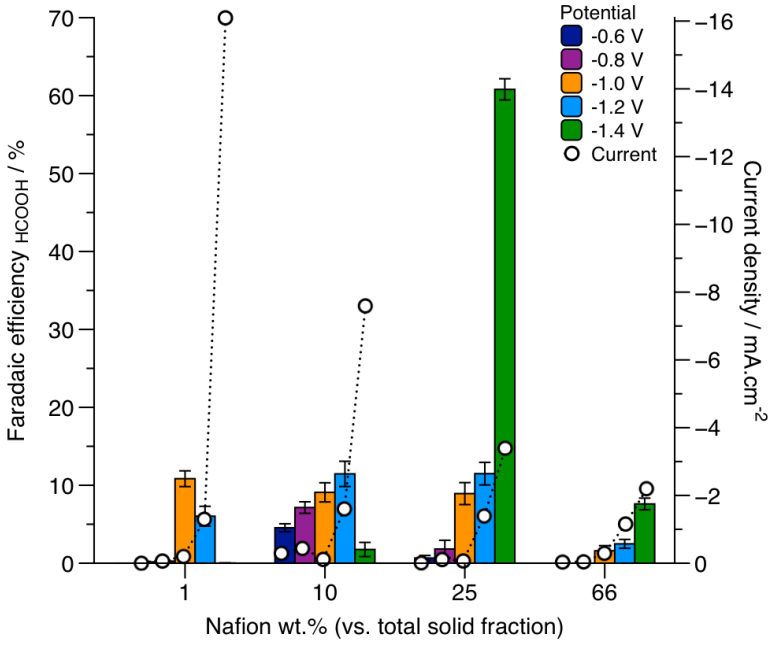

Figure 4-15 - Faradaic efficiency for formic acid formation from electrocatalytic reduction of CO_2 on a nano-copper electrocatalyst, where the Nafion content is varied in the range 1 to 66 wt% in the catalyst layer.

4.3.4.4 Structural Examination of the catalyst layer

Selected catalyst layers with different Nafion fraction held at –1.0 V for 3 hours, were examined by SEM post electrolysis (Figure 4-16) and showed some significant changes to the morphology and size of the particles before electrolysis (Figure 4-17), also confirmed further by surface analysis via XPS (Figure 4-18). The initial CuO phase had undergone electrochemical reduction to Cu during the electrolysis process (Figure 4-16 a-d). From the structural characterisation and cyclic voltammetry, the active catalyst is inferred to be the copper phase, as the initial CuO phase was reduced in situ to Cu. The Cu particles remained nano-sized with a narrow size distribution. Some growth in size was observed from CuO electroreduction to Cu (from sub 20 to ca. 50 nm).

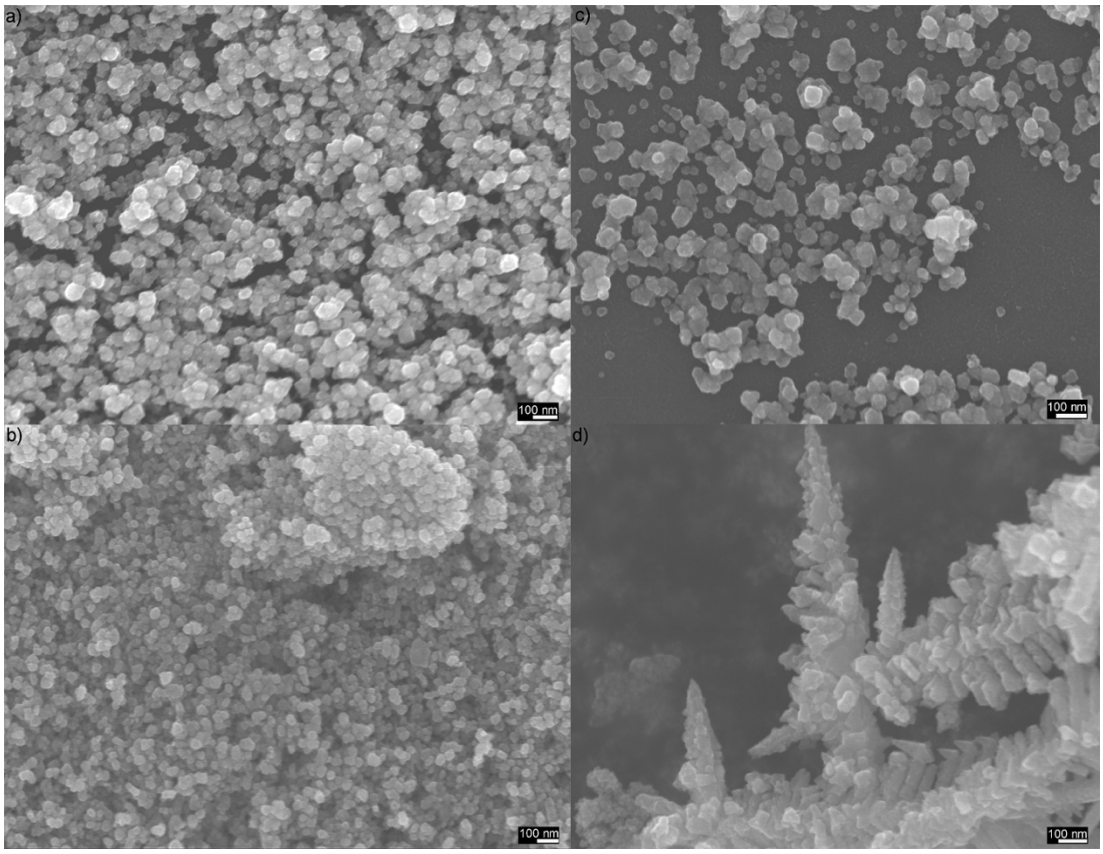

Figure 4-16 - Post electrolysis SEM images of catalyst layer on glassy carbon electrode a) 1 wt%, b) 10 wt%, c) 25 wt% and d) 66 wt% Nafion fraction.

The catalyst layer with a Nafion fraction of 66 wt%, showed dendritic growth of Cu during the electrolysis process, which was not observed with the other

samples. The growth of this type of structure may be facilitated by the negatively charged sulfonic acid groups present in Nafion, which can inhibit the mass transport of Cu nuclei, allowing the growth of dendritic branched structures.[183] With the presence of excess Nafion in the catalyst layer, dendritic structures may have been more favourably formed in this instance, rather than at lower Nafion fraction. The Faradaic efficiency was significantly lower for sample CL66 compared to sample CL25 due to the presence of excess Nafion in the catalyst layer.

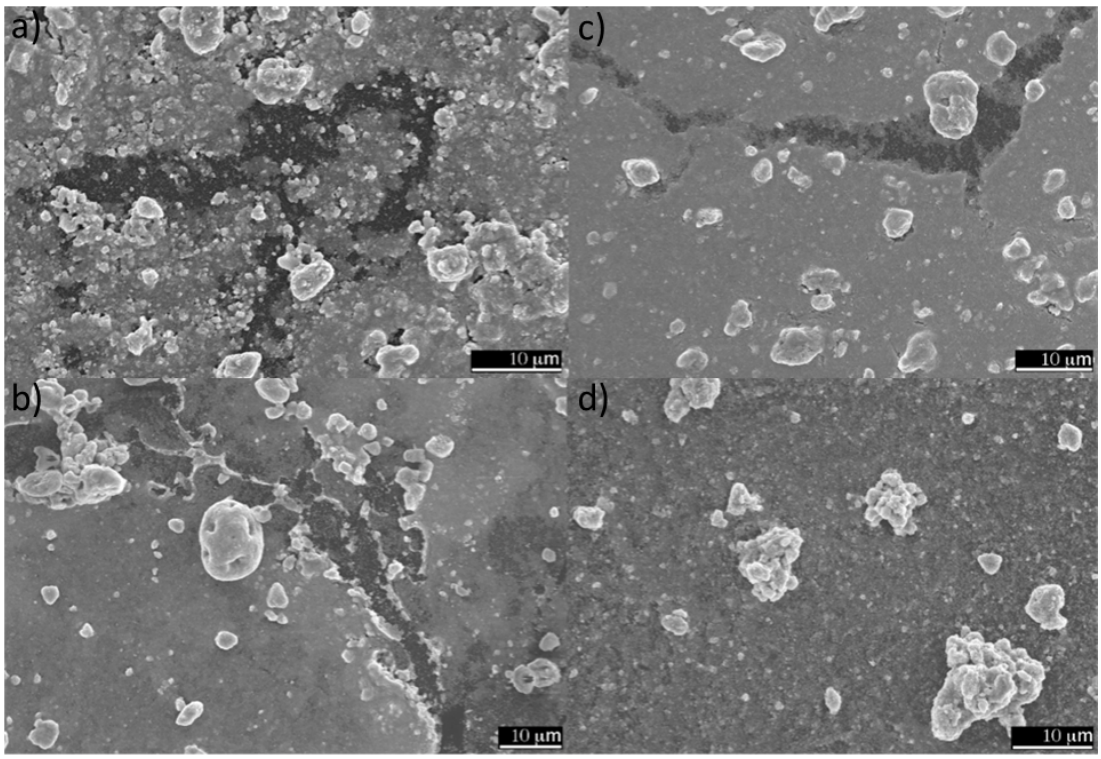

Figure 4-17 - SEM of CuO deposited on glassy carbon electrode with a) 1 wt.%, b) 10 wt.%, c) 25 wt.% and d) 66 wt.% Nafion fraction before electrolysis.

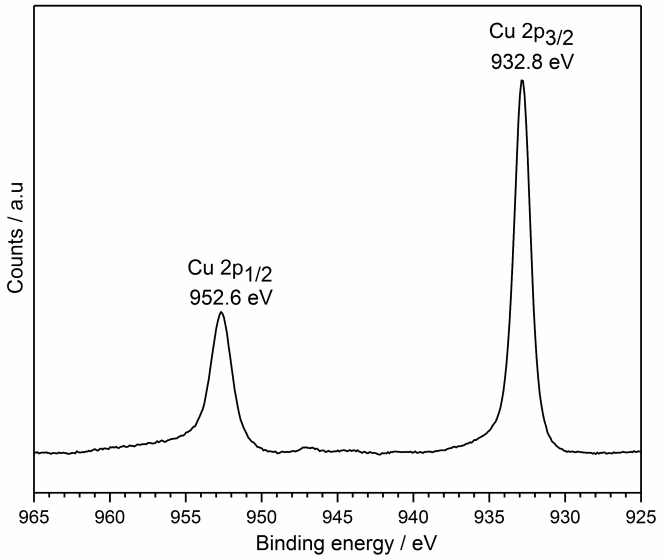

Figure 4-18 - XPS spectra of sample CL1 post electrolysis (–1.0 V vs. Ag/AgCl for 3 hrs) showing Cu $2p_{3/2}$ 932.4 eV and Cu $2p_{1/2}$ 952.6 eV for Cu^0. No satellite peaks typically seen with Cu^{II} were observed, confirming the presence of Cu^0 on glassy carbon after electrolysis.

Cross sectional SEM of the as prepared CuO ink with a fraction of 66 wt% Nafion was conducted to investigate the distribution of fluorine originating from the perfluorocarbon backbone in Nafion and copper (Figure 4-19). A homogeneous distribution of fluorine, copper and oxygen was observed within the film layer. The high C count derived from the film was due to the film being supported on glassy carbon electrodes. This is in agreement with a film deposition that resulted in consistent distribution of Nafion within the catalyst layer without the formation of Nafion layers blocking access to the copper surface or contact of the catalyst with the electrode surface, even at significantly high fractions of Nafion.

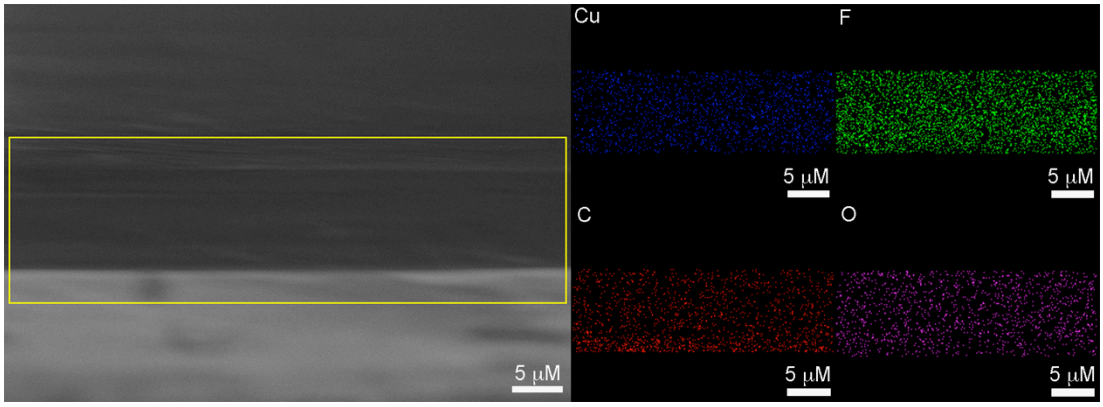

Figure 4-19 - a) Cross section of CuO film with 66 wt% Nafion fraction b) showing elemental mapping of Cu, F, C and O.

4.3.4.5 Surface Area Measurements

The surface roughness factor was calculated for samples with 1, 10, 25 and 66 wt% Nafion fraction, using capacitance where only the non-Faradaic region was explored. The CuO inks were reduced at –1.0 V in CO_2 saturated 0.5 M $KHCO_3$ for 1 hour before conducting cyclic voltammetry in the non-Faradaic region in 0.1 M H_2SO_4. The capacitance was calculated from a linear plot of current vs. scan rate (see Figure 4-20 for plot). The capacitance and surface roughness factor (Table 4-3) indicated the surface roughness factor increased with increasing Nafion content up to 10 wt% Nafion fraction, however, a sharp decrease was observed at 25 wt% Nafion content. The bare glassy carbon had a low capacitance value, indicative of low surface area as expected for a glassy carbon surface, and the incorporation of the catalyst film increased the surface roughness factor.

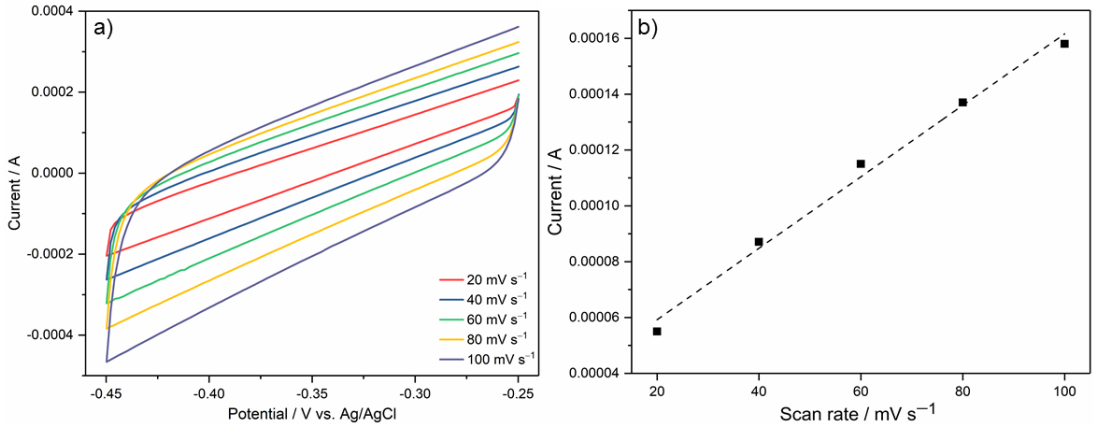

Figure 4-20 – a) Plot of current vs potential of CL10 in 0.1 M H_2SO_4 cycled between –0.25 and –0.45 V vs. Ag/AgCl at scan rates in the range of 20 – 100 mV s^{-1} and b) shows plot of current vs scan rate where the linear regression gives capacitance information.

A decrease in the surface area was observed for catalysts with >10 wt% Nafion fraction, however, the Faradaic efficiency for formic acid production was still particularly high for sample CL25 at 61% Faradaic efficiency (at –1.4 V), which suggested the high activity at CL25 was due to other factors (discussed below) and not entirely due to the high surface area of nano-sized Cu. Some insights into the mechanism of formic acid production on copper, have been highlighted in theoretical calculations by Norksov et al., which suggest that a formate pathway (F-intermediated pathway, Equation 4.1 – 4.3) on copper surfaces, leads to exclusive formation of formic acid whereas a carboxyl pathway (C- intermediate), leads to the production of formic acid and some other higher order hydrocarbons.[184,185]

Table 4-3 - Capacitance values and surface roughness factors for catalyst layers with varying Nafion content measured using cyclic voltammetry in a region where only non-Faradaic processes are present. The factor is given as a ratio, where the blank glassy carbon electrode is assumed to be 1.

Nafion fraction (wt%)	Capacitance (uF cm^{-2})	Surface Roughness Factor
Glassy carbon	0.03	1
1	1.14	37
10	1.37	44
25	0.70	23
66	0.39	13

$$CO_2 + H^+(aq) + e^- + * \rightarrow HCOO^* \text{ (F intermediate)} \quad \text{Equation 4.1}$$

$$HCOO^* + H^+(aq) + e^- \rightarrow HCOOH^* \quad \text{Equation 4.2}$$

$$HCOOH^* \rightarrow HCOOH + * \quad \text{Equation 4.3}$$

Headspace analysis via gas chromatography (GC), did not reveal the presence of hydrocarbons such as methane, ethane, or CO. Formic acid was the major product observed in ^1H NMR experiments with trace levels of methanol and acetic acid in some cases (Figure 4-21). The dominance of (111) and (100) surfaces on Cu are likely to be linked to the production of formic acid via the formate pathway, whereas the presence of (200) surfaces leads to the production of formic acid via the carboxyl intermediate. Post electrolysis analysis of the copper particles via TEM (Figure 4-22) showed the presence of (111) copper surfaces (d_{111} spacing = 0.21 nm), which is in agreement with 0.21 nm for d_{111} lattice spacing in literature, which may explain the high selectivity for formic acid over other products.[186]

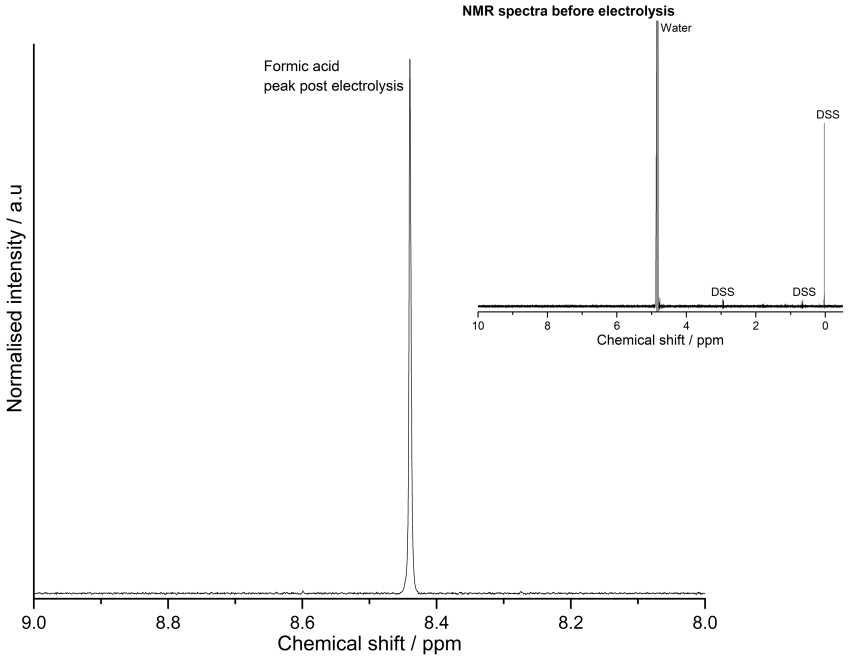

Figure 4-21 - shows NMR spectra after electrolysis and presence of a strong formic acid peak. Inset shows DSS peaks are highlighted, where DSS was used as a reference control and a strong water signal is observed at 4.75 ppm.

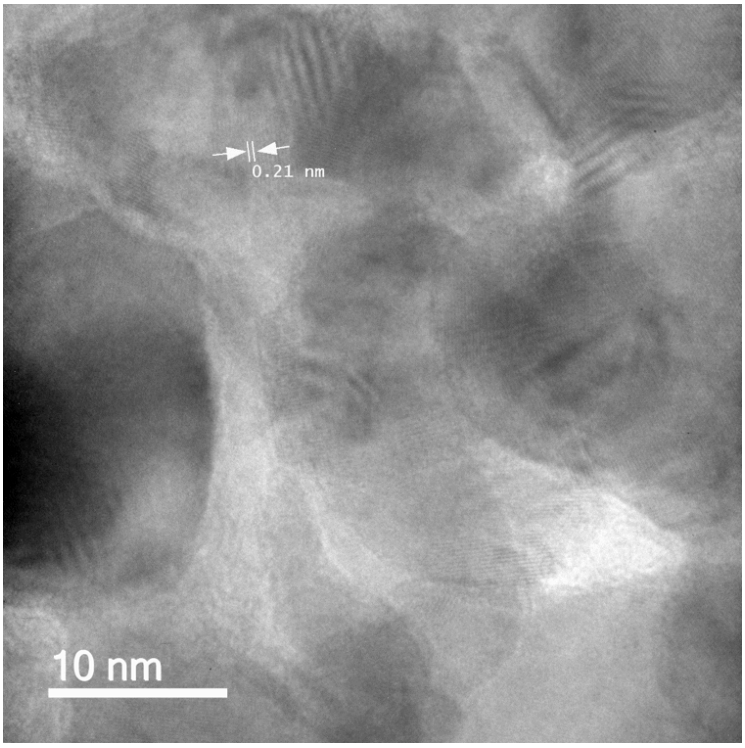

Figure 4-22 - TEM of CL25 post electrolysis at –1.0 V for 3 hrs showing (111) surface plane with a d-spacing of 0.21 nm consistent with Cu d_{111}.

4.3.4.6 Electrochemical Impedance Spectroscopy (EIS)

The particularly high Faradaic efficiency observed herein, was also attributed to the 3-dimensional network that was formed when using the optimum Nafion, catalyst and reactants ratio. Electrochemical impedance spectroscopy (EIS) was conducted to further elucidate the effect of Nafion content within the catalyst layer. The CuO catalyst layers with different Nafion fractions were subjected to an AC perturbation of 5 mV over a frequency range from 10 KHz to 0.1 Hz at a DC voltage of –1.4 V. Nyquist plots of CuO catalyst layers with different Nafion fractions were compared (Figure 4-23) and the equivalent circuit was modelled (Figure 4-24) to obtain simulated values of charge transfer resistance, R_{ct} and mass transport resistance, R_{mt}. The CuO catalyst layer with 1 wt% was not considered due to mechanical degradation of the film at –1.4 V, which would have resulted in poor impedance data. A significant R_{ct} difference was observed between the CuO catalyst layer with 25 wt% (14 Ω) and 66 wt% (63 Ω) Nafion, whilst the CuO10 sample had a R_{ct} of 17 Ω. The R_{mt} was also significantly higher for

the 66 wt% Nafion fraction (10 Ω) compared to the catalyst layers with lower Nafion content. The Nafion content is a crucial factor when considering the performance of the catalyst and has previously been explained through the percolation threshold.

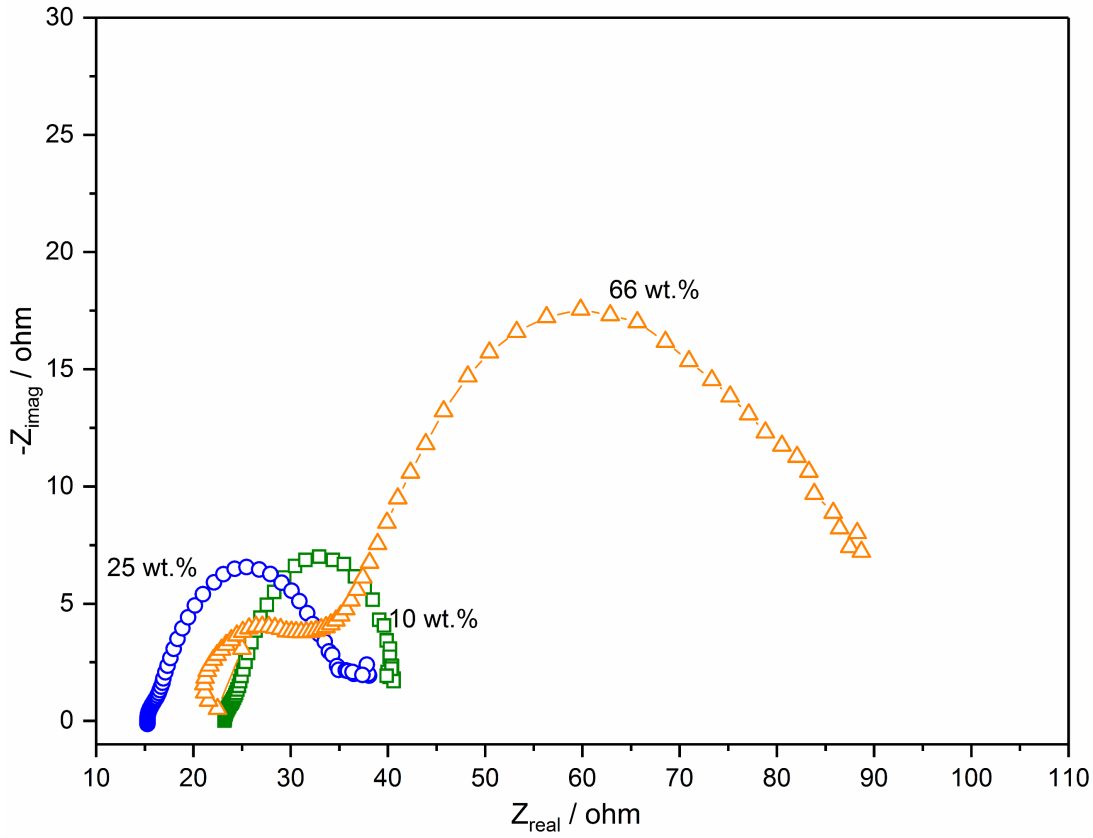

Figure 4-23 - Nyquist plot comparing different Nafion content (□ 10 wt%, ○ 25 wt% and △ 66 wt%) at a DC voltage of –1.4 V.

Suzuki et al. modelled a three-dimensional (3D) meso-scale structure of the catalyst layer in the context of a proton exchange membrane fuel cell (PEMFC), where three different percolating pathways were modelled.[169] A network of catalyst grain contacts is necessary for electronic conduction, the Nafion network that forms around the particles allows ionic conduction and the resultant channels formed in the catalyst layer allow for gas diffusion. This is significant as the channels allow the transport of CO_2 and products (formate). The Nafion can promote H^+ conduction and the copper oxide derived catalyst can provide good electronic conduction.

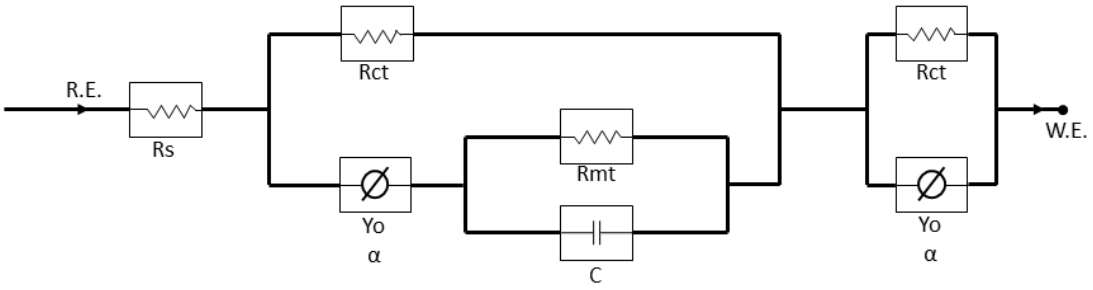

Figure 4-24 - Equivalent circuit model of three electrode set up with Nafion thin film coating on the glassy carbon electrode.

At a low Nafion fraction, although the particles form a percolating pathway for electronic conduction there is likely to be poor catalyst utilisation, which is also observed in the increased charge transfer resistance for CL10 (Figure 4-23) as there was not enough Nafion to allow good ionic, including proton conduction. Subsequently, when the Nafion fraction was too high, the Nafion can form aggregates or micelle structures, which are more thermodynamically stable at certain ionomer content.[164] This resulted in particle separation at large distances where good electronic conduction was likely to have been inhibited. From the modelled impedance data, it is evident that the presence of excess Nafion also impeded gas transport and increased mass transport resistance within the catalyst layer leading to a reduced performance. This can be confirmed as only the Nafion fraction was altered between each impedance experiment. At the optimal Nafion fraction of 25 wt%, the three percolating pathways resulted in good catalyst utilisation for electronic conduction, sufficient Nafion for proton conduction and gas channels for gas transport without adverse mass transport issues. This can be figuratively represented in the following illustration (Figure 4-25).

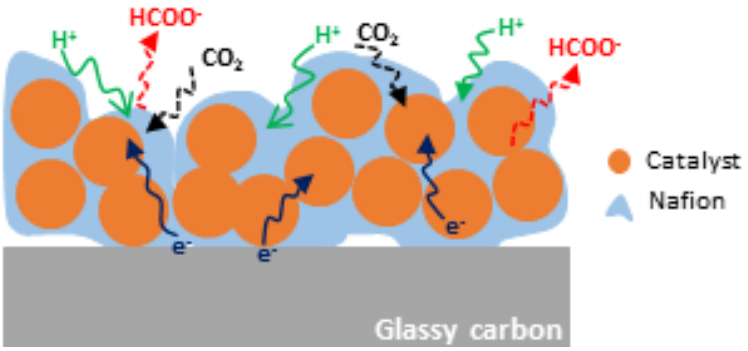

Figure 4-25 – Illustration of the Nafion and catalyst interaction during the electrochemical reduction of CO_2.

As CO_2 reduction is sensitive to the competing water splitting reaction, the presence of Nafion was essential in proton transportation. Protons are also crucial for the synthesis of formic acid (Equation 4.1 to 4.3). At –1.4 V, in the case of CL25, significant water splitting could be advantageous as the significant fraction of Nafion assisted proton conduction through the ionomer, providing protons without impeding the flow of electrons to form formic acid at high Faradaic efficiencies.

4.3.5 Stability Measurements

The long-term stability of sample CL25 at –1.4 V was conducted over a 24-hour timescale. The chronoamperometric curve (Figure 4-26) indicated excellent stability with minimal current loss over the time tested, with an average current of –3.0 ± 0.5 mA, and a Faradaic efficiency of 53 % for the production of formate.

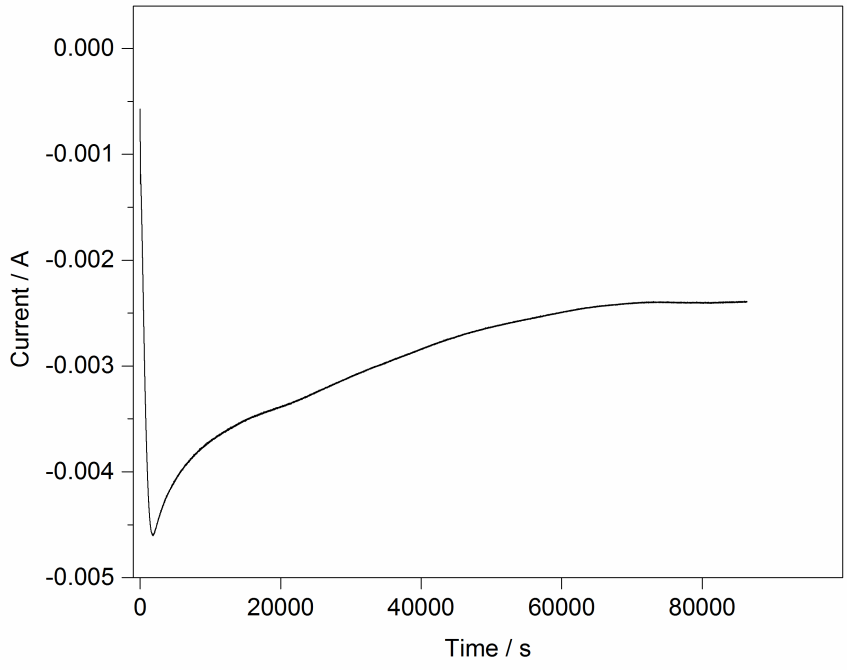

Figure 4-26 - Long term stability test of sample CL25 held at –1.4 V vs. Ag/AgCl for 24 hours in CO_2 saturated 0.5 M $KHCO_3$ solution.

Although this experiment was conducted over 24 hours, further experiments would be required to determine the catalyst's long term stability (over 100 hours). A key issue with Cu, often reported in the literature, is the formation of carbon on copper catalyst, which can significantly impede the catalyst's ability to further convert CO_2 efficiently. Other reported deactivation routes can occur via deposition of heavy metals impurities in the electrolyte, such as Fe^{2+} and Zn^{2+} or also the deposition of trace levels of organic substances can also severely deteriorates catalytic activity.[187] This would need to be evaluated to determine whether this presents an issue in this case.

4.3.6 Control experiments

To ensure the products of CO_2 conversion were due to the presence of the catalyst and from the CO_2 bubbled in the electrolyte, control experiments were conducted where either no CO_2 was bubbled into the electrolyte or no catalyst was deposited on the glassy carbon electrode.

4.3.6.1 No CO_2 saturation in electrolyte

The cell was set up as described in Section 4.2.6, however no CO_2 was bubbled in to the electrolyte (0.5 M $KHCO_3$). Constant potential electrolysis experiments were conducted where the potential was held at the optimum potential of –1.4 V for 3 h to observe if any products were obtained under such conditions. NMR of the electrolyte post-electrolysis indicated that a negligible amount of formic acid was produced (of the order of 1 x 10^{-6} M) (Figure 4-27). Therefore, the formic acid produced under the optimum conditions was due to the CO_2 presence in the electrolyte.

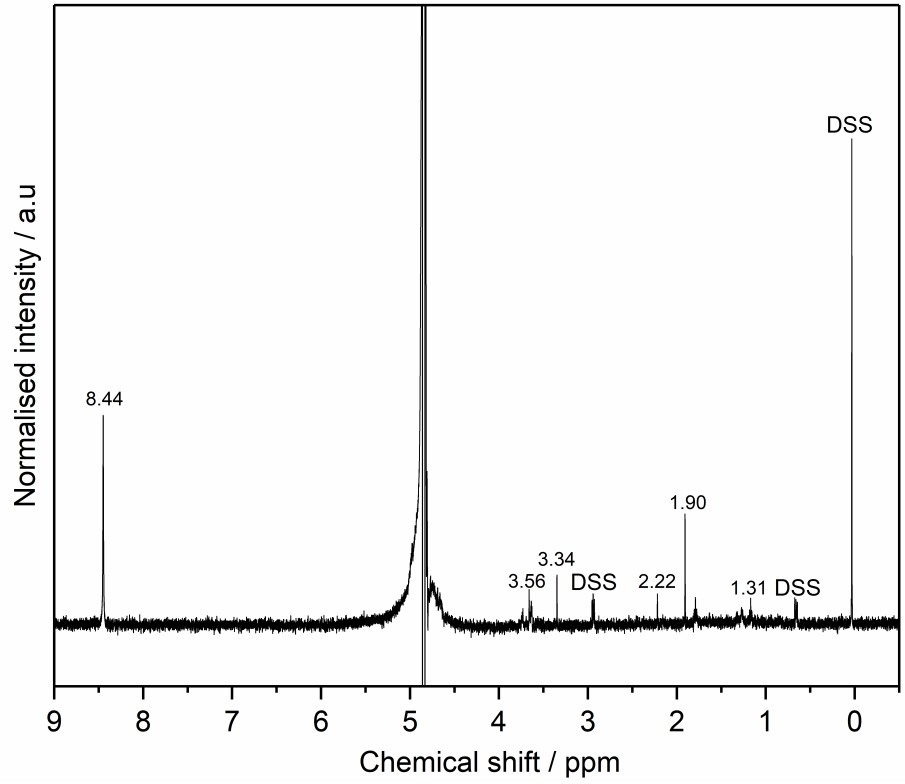

Figure 4-27 - ^1H NMR of 0.5 M $KHCO_3$ post electrolysis (–1.4 V vs. Ag/AgCl for 3 h) with no CO_2 saturation. DSS peaks are highlighted, where DSS was used as a reference control and a strong water signal is observed at 4.75 ppm.

4.3.6.2 No catalyst deposited on glassy carbon

The cell was set up as described earlier. In this case, a cleaned blank glassy carbon electrode was used as the catalyst, where no CuO was deposited on to its surface. Constant potential electrolysis experiments were conducted as described in Section 2.6 and NMR samples of the electrolyte pre and post-

electrolysis indicated that no product was formed during electrolysis confirming the presence of formic acid was only due to the catalyst reducing the CO_2 on its surface rather than through any impurities in the CO_2 or electrolyte feed (Figure 4-28).

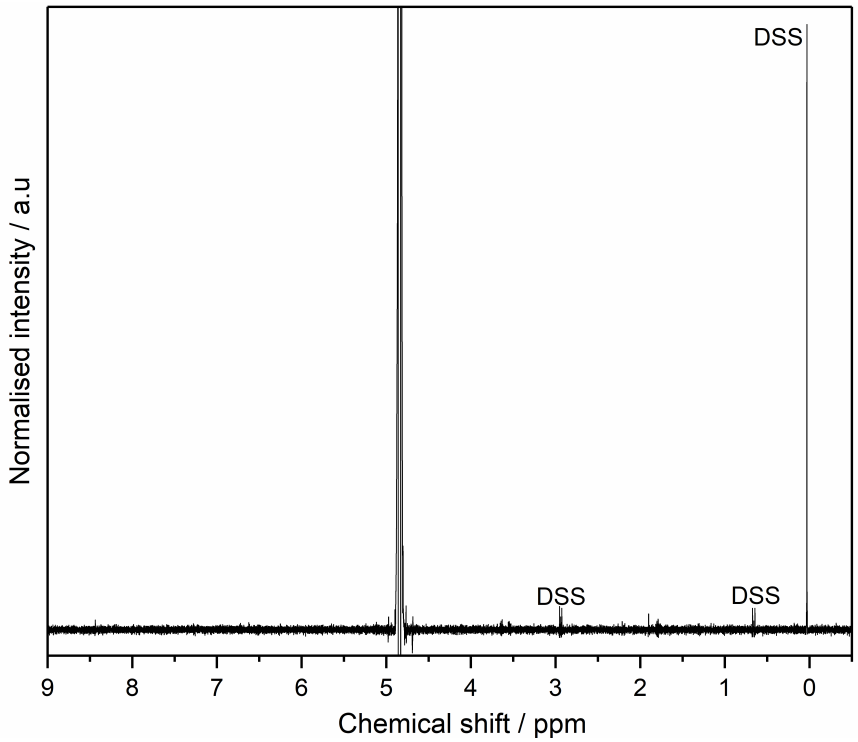

Figure 4-28 - ^1H NMR of 0.5 M $KHCO_3$ post electrolysis (–1.4 V vs. Ag/AgCl for 3 h) saturated with CO_2 but with no catalyst present on the glassy carbon electrode. DSS peaks are highlighted, where DSS was used as a reference control and a strong water signal is observed at 4.75 ppm.

4.4 Conclusion

In summary, ultrafine CuO nanoparticles were successfully synthesised in a large scale via continuous hydrothermal flow synthesis. The resulting 17 ± 5 nm nanoparticles were subsequently formulated in to homogenous Nafion based inks that were employed to prepare stable catalyst layers on glassy carbon electrodes. The ink formulation was systematically evaluated by assessing the impact of the preparation method, solvent system and drying methods. The ink composition was also optimised with varying Nafion fractions to maximise the performance for the electrocatalytic reduction of CO_2 to formic acid on copper surfaces derived from the CuO nanoparticles.

The highest measured Faradaic efficiency was >60%, which was significantly higher than the majority of comparable reports for copper catalysts in the literature and makes the process potentially attractive to larger PEMFC-like designs for CO_2 reduction, especially considering the scale up capabilities, green nature and ease of formulation of the proposed synthetic method. The high Faradaic efficiency for formic acid was explained by the presence of Cu (111) planes, observed by TEM, which favoured the formation of formic acid on copper via the formate pathway. Further evidence of the importance of controlling the Nafion fraction on the electrocatalytic reduction of CO_2 to formic acid was indicated by EIS, where the charge transfer and mass transport resistance were found to be minimal for the optimised Nafion fraction, highlighting the correlation between the catalyst ink formulation and the consequent layer structure on the electrocatalytic performance. This has previously been poorly studied, in the context of the electrochemical reduction of CO_2, particularly for copper-based electrodes.

Future work may consider evaluating the longer-term stability of the catalyst, over 100 hours, potentially in a device set up to consider the scale up of CO_2 conversion to formic acid. A preliminary study was conducted in this thesis, to validate the use of stacked device for CO_2 electroreduction. The design was based on an electrolyser-type device used for water splitting.[64] However, high levels of organic contaminants (in the 100 to 500 μM range) were observed in the ^{1}H NMR after electrolysis. This may be derived from the carbon cloth used within the device (GDE) or breakdown of Nafion membrane. Further work is required to understand the source of contaminants and to engineer prototypes that avoid contaminants to validate the use of devices for CO_2 electroreduction.

Another focal point of future investigations could be studying modified Nafion ionomers to improve its proton conductivity and to further understand the interaction of the ionomer with the catalyst and whether this would improve or

hinder the electrochemical conversion of CO_2. Other binders could be investigated as well; binders which are commonly used in other areas (batteries and fuel cells), such as PVDF or PTFE, may result in improved performance of CO_2 conversion to fuels. The thickness of the catalyst layer is known to affect the electrochemical performance, so this could be evaluated to find an optimal thickness where the CO_2 conversion and film stability may be improved.

Chapter 5. Electrochemical Reduction of CO_2 on Ni Doped CuO

5.1 Introduction

Metal alloys of transition metals have shown superior CO_2 conversion by lowering the overpotential required to efficiently convert CO_2 into useful products, such as fuels and polymer.[188] Alloying may be used as an approach to overcome the challenges faced from using copper and its oxides, in particular high overpotentials and low selectivity. Copper-based alloy nanocatalysts, in particular, have been used to enhance or modify the product distribution from electrocatalytic CO_2 conversion.[189] Two main approaches have been adopted in alloying, to catalyse CO_2 reduction; the choice of metal to be alloyed with copper and altering the metal alloy stoichiometry. For example, Au-Cu alloys have been used extensively in the literature in order to improve the Faradaic efficiency and lower the onset potential required to convert CO_2 into products such as CO, HCOOH, CH_3OH and CH_4. Yang et al. studied composition dependent activity and selectivity with increasing amounts of Cu.[45] The CO selectivity increased with decreasing Cu content, but also resulted in the production of formate, methane and ethane as well as minimal amounts of ethanol and acetate. The Faradaic efficiency for methanol and ethanol could be controlled by selecting the appropriate Au_xCu_{1-x} compositions. Selective alcohol production for $Au_{36}Cu_{64}$ alloys was studied, where the formate to alcohol ratio was higher in Cu rich samples.[190]

Watanabe et al. previously produced a range of transition metals with Cu in electroplated Cu-*M* alloy films (where *M* = Ni, Zn, Cd, Sn, Pb, Au or Ag).[191] The product distribution was found to vary between the pure metals and their alloys. Although, hydrocarbon formation remained unchanged, inclusion of Ni

with Cu produced CH_3OH, which was not formed with pure Cu. Similarly, Cu/Sn alloys showed higher Faradaic efficiency for HCOOH production as well as lowering of the overpotential, which was not observed on the respective pure metals. It is clear that the synergistic effects between the elements in metal alloys can result in a positive effect for the conversion of CO_2 to useful chemicals. It has been suggested that the positive outcome of the alloying approach is due to the stabilisation of intermediates on the catalyst surface and enhanced activation of CO_2 to $CO_2^{-\bullet}$ (which is the key intermediate step in the process).[192]

Ni Cu alloy catalysts show promise in reducing the overpotential required for the electrocatalytic conversion of CO_2 as well as affecting the selectivity towards product distribution.[192,193] Theoretical modelling of the product formation mechanism and CO_2 activation on Ni doped Cu (111) shows intermediate stabilisation due to the inclusion of Ni, and therefore, lower activation energy for CO_2 conversion.[194,195] The knowledge obtained from alloy systems for the electro-reduction of CO_2 may also be applied to oxide systems. To date, studies including *M* (for example *M* = Ni) doped copper oxides for electroreduction of CO_2 have not been investigated and it is possible that as copper oxides can favourably alter the overpotential and product distribution, inclusion of Ni into the copper oxide structure may further enhance the catalytic performance.

It is well known that the synthesis method can alter the catalyst structure and composition, which in turn will affect the catalytic activity, selectivity and stability of the catalyst.[196] For CO_2 reduction, typical synthesis routes for Ni Cu alloy has been limited to Ni coated Cu (111) metal surfaces with molecular beam epitaxy (MBE) under ultra-high vacuum conditions or through electroplating films.[192] The use of nanostructured catalysts in this context, has not been investigated. In the literature, Ni doped CuO has been

synthesised for its unique magnetic properties, commonly through sol-gel, co-precipitation and microwave combustion synthesis methods.[197–200]

As mentioned in Chapter 1, inherent issues with batch processes may be overcome by employing continuous hydrothermal flow syntheses. The CHFS process has been used to make doped materials previously, e.g. the successful synthesis of V doped $LiFePO_4$ and Sn doped TiO_2 for energy storage materials as well as Al and Ga co-doped ZnO as transparent conducting oxides.[201–203] Other reports of doping metal oxide systems for catalytic applications included doping 18 elements at three different levels into TiO_2 and ZnO for applications in photocatalysis.[204,205] The synthesis of doped metal oxides with co-precipitation versus continuous flow techniques has not previously been compared directly in this group or in literature.

This chapter will examine the synthesis of Ni doped CuO via co-precipitation and continuous hydrothermal flow synthesis. A range of Cu and Ni compositions were synthesised. The catalysts were characterised by a range of structural characterisation techniques such as PXRD, TEM, BET, XPS as well as ICP-AES. The catalysts were subsequently tested via electrochemical characterisation for their catalytic performance towards CO_2 conversion.

5.2 Methods

5.2.1 Materials

Copper(II) nitrate trihydrate [$Cu(NO_3)_2{\cdot}3H_2O$, technical grade, >98 %], nickel(II) nitrate hexahydrate [$Ni(NO_3)_2{\cdot}3H_2O$, technical grade, >99 %] and potassium hydroxide pellets (KOH) were used in the synthesis of ultrafine Ni doped CuO. All reactions were conducted in deionised water (>10 MΩ). Nafion (5 wt% in a mixture of lower aliphatic alcohols and 45 % water) and high purity LC-MS chromasolv isopropanol (IPA) and methanol were used in the ink formulation. High purity K_2HPO_4 was used as an electrolyte for some

reactions. All chemicals, unless stated otherwise, were supplied by Sigma Aldrich, (Dorset, UK). High purity $KHCO_3$ was supplied by Alfa Aesar, (Lancashire, UK). All chemicals were used as purchased.

5.2.2 Synthesis of Ni doped CuO

5.2.2.1 Co-precipitation

Stochiometric amounts of $Cu(NO_3)_2.3H_2O$ and $Ni(NO_3)_2.6H_2O$ were mixed to achieve 1, 5 and 10 at% Ni content. KOH was added as a precipitating agent and the resultant pH was 9. The precipitate was subsequently centrifuged and cleaned until the conductivity of the supernatant was below 50 μS measured by a conductivity probe. The concentrated paste was dried in a vacuum oven at 40 °C and heat-treated at 800 °C for 5 h in air.

5.2.2.2 CHFS - Double mixer

Ni doped CuO nanoparticles were synthesised using a modified dual mixer CHFS system, which uses four high-pressure diaphragm pumps (Chapter 2). Briefly, in the process, a room temperature aqueous solution of 0.1 M copper nitrate trihydrate and nickel nitrate hexahydrate was pumped (via pump 2 at 40 mL min^{-1}) to mix with an aqueous flow of 0.2 M potassium hydroxide solution (via pump 3 at 40 mL min^{-1}) in a tee-piece mixer. The resulting mixture was then mixed with a superheated water feed at 400 °C (via pump 1 at 80 mL min^{-1}) inside a confined jet mixer (CJM) (Chapter 2). The calculated mixing temperature was ca. 335 °C (Reynolds number ≈ 6939), with a residence time of ca. 0.7 s before the nanoparticle slurry was quenched rapidly as it mixed with a feed of room temperature deionised water (via pump 4 at 160 mL min^{-1}) in a second CJM (Reynolds number ≈ 3354). The copper and nickel nitrate solution was altered to achieve 0.1 M total concentration over a range of different dopant percentages. Nickel content was varied between 0, 1, 5, 10, 15, 20, 30, 40, 50 and 100 at%. The design and sizes of the two CJMs are given in more detail in the Chapter 1 and 2 and previous publications.[113] The newly formed and partially cooled

nanoparticle laden slurry was then cooled further via a pipe-in-pipe heat exchanger and was continuously collected from the exit of the back-pressure regulator (BPR), which maintained the pressure in the system at 24.1 MPa. The samples were processed as described in Section 2.3.

5.2.2.3 Single mixer

Ni doped CuO nanoparticles were also synthesised using a single mixer CHFS system. The single mixer set up used three high-pressure diaphragm pumps. The reactions were run similar to the dual mixer set up with the exception of the quench feed. The Ni content was limited to 10, 20 and 30 at% Ni.

5.2.3 Materials Characterisation

The freeze-dried Ni doped CuO nanopowder was examined by powder X-ray diffraction (STOE STADI P, Mo $K_{\alpha 1}$, λ = 0.709 Å) The patterns were collected between a 2θ range of 2 to 40°, at a step size of 0.5° and count time of 5s per step. Rietveld refinement was carried out to obtain lattice parameter and unit cell volume for Ni doped CuO samples. It was performed on FullProf suite software by Dr. Tom Ashton at the Clean Materials Technology Group. A pseudo-voigt peak shape was employed for the peak fitting.

BET and XPS measurements were undertaken as described in Section 2.4 and XPS depth profiles of the Ni doped CuO samples were measured with an Al X-ray source and Ar^+ ion at 2000 eV with a sputter rate of 0.2 nm/min and XPS measurements were carried out for 5 levels with measurements taken at each level.

Detailed morphology and size analysis was carried out using high-resolution transmission electron images. Images were obtained on a JEOL JEM 2100 TEM with 200 KeV accelerating voltage and a $LaBF_6$ filament. HRTEM samples were prepared by dispersing the particles in methanol 99.9 %

(Sigma Aldrich, Dorset, UK) by ultra-sonication before dropping the resulting dispersion onto 300 mesh Holey gold film grids (Agar Scientific, Stansted UK). The copper and nickel distribution was examined by Energy dispersive X-ray spectroscopy (EDX) and was conducted on the JEOL JEM-2100 TEM fitted with an Oxford Instruments X-MaxN 80 T Silicon Drift Detector (SDD). When samples for EDS were prepared, the dispersed particles were dropped onto 300 mesh Holey gold film grids. Particle size distribution was determined by measuring the diameter of 100 particles from TEM images.

Inductively Coupled-Plasma Atomic Emission Spectroscopy (ICP-AES) was conducted to study the composition of Cu and Ni. Samples were diluted and dissolved in 1 % HNO_3 (aq). Calibration standards were prepared in the at% range for Cu and Ni used in the as synthesised $Cu_{1-x}Ni_xO$ samples. Copper and nickel nitrate salts were dissolved and diluted in 1 % HNO_3 (aq). Measurements were conducted using a Varian 720 ICP-AES (axial configuration) equipped with an autosampler at the Department of Earth Sciences, University College London, by Mr. Ian Johnson from the Clean Materials Technology Group, supported by Prof. John McArthur at the Department of Earth Sciences.

5.2.4 Electrochemical characterisation

The Ni doped CuO catalysts were prepared as inks as described in detail in Chapter 2, as was the electrochemical cell. The inks were characterised by cyclic voltammetry prior to any other electrochemical testing. 0.5 M $KHCO_3$ electrolyte was saturated with CO_2 for 30 mins before cycling. The electrode was cycled in the range 0.7 and –0.8 V vs. Ag/AgCl at 100, 50, 20 and 5 mV s^{-1}, respectively. The potential window was expanded and the electrodes were also cycled in the range 0.5 and –1.4 V vs. Ag/AgCl to evaluate Ni interaction. Subsequent testing (constant potential electrolysis, surface area and impedance measurements) were carried out as described in Chapter 2.

For some samples, the catalysts were also tested in 0.5 M K_2HPO_4; the electrodes were held at a potential range –1.0 to –1.4 V vs Ag/AgCl.

5.2.5 Sample coding

The samples are coded as CuO-Ni[x] where the x indicates the nominal value of Ni within the sample. In some cases, the actual value of Ni content is given, as determined by ICP-AES, however, this has been clarified in the Chapter. The synthesis method may be highlighted and would be displayed as CuO-Ni[x]/CP (for co-precipitation), CuO-Ni[x]/DM (CHFS dual mixer), CuO-Ni[x]/SM (CHFS single mixer).

5.3 Results and discussion

5.3.1 Synthesis of Ni doped CuO

5.3.1.1 Synthesis of $Cu_{1-x}Ni_xO$ via co-precipitation

Ni doped CuO was synthesised via co-precipitation following a synthesis route described by Meneses et al. in the literature.[200] The copper and nickel nitrate salts were pre-mixed to obtain a nickel dopant level of 1, 5 and 10 at%. The addition of KOH resulted in the formation of blue precipitate assumed to be a copper nickel hydroxide phase and this was subsequently heat-treated. The dried, brown CuO powder was characterised by PXRD (Figure 5-1). The PXRD patterns indicated (1 and 5 at% Ni) the formation of a single phase monoclinic CuO, as confirmed by the reference pattern CuO (JCPDS 01-089-2529). The most intense diffraction peaks were observed at 2θ = 16.2°, 17.6° and 21.9° corresponding to the (–111), (111) and the (–202) planes, respectively. It was evident from the diffraction data for 1 and 5 at% Ni, there was no presence of other phases corresponding to nickel oxide, nickel hydroxide or any other binary copper nickel phases. However, as the Ni content was increased to 10 at%, additional NiO peaks (*) were present (Figure 5-1c). This was suggestive of a limit to Ni inclusion in to the

CuO host structure, consistent with reports in the literature, where similar synthesis routes have been used to synthesise Ni doped CuO.[197–200]

Ramya et al. synthesised Ni doped CuO via a similar co-precipitation route but samples were heat-treated at 400 °C for 3 hours, observing a limit to Ni inclusion at ca. 10 at% into the CuO host structure.[199] Similarly, Amaral et al. investigated Ni, Fe and Zn doping of CuO via co-precipitation and observed a limit of Ni inclusion from 5 at%.[198] Static simulation techniques were conducted to understand the defect disorder within the structure. This analysis indicated that the substitution of Zn^{2+} into the CuO structure was more favourable than Ni^{2+} substitution into CuO. It is expected that Ni^{2+} would substitute the Cu^{2+} site and this is assumed to be favourable as the ionic radius for Ni^{2+} (0.69 Å) and Cu^{2+} (0.73 Å) are not significantly different.

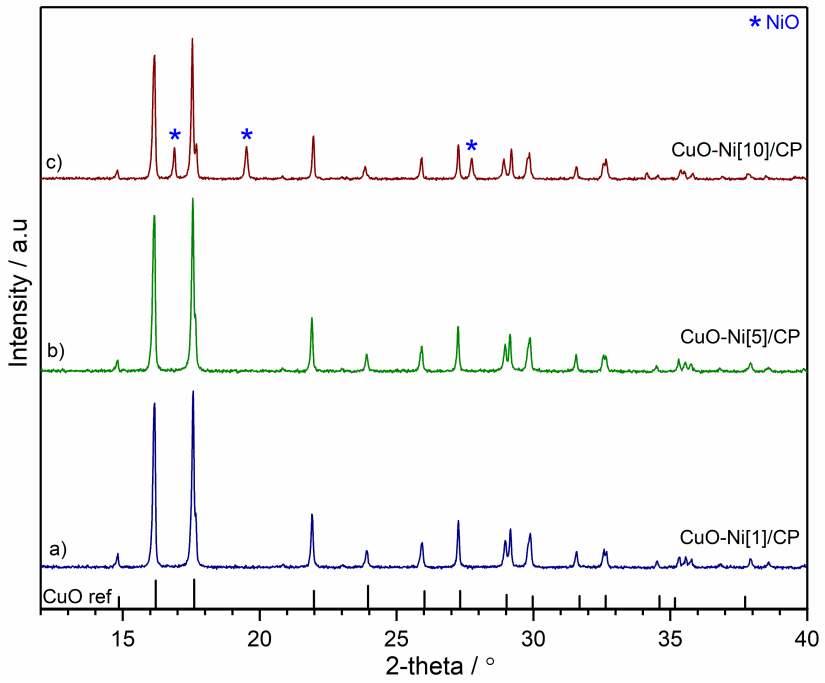

Figure 5-1 - PXRD patterns of as-prepared $Cu_{1-x}Ni_xO$ samples synthesised via co-precipitation. The Ni content was varied from a) 1, b) 5, and c) 10 at% Ni. Spurious NiO peaks are highlighted by *.

Rietveld refinement was performed on the samples prepared by co-precipitation and this revealed a slight decrease in lattice parameters *a* and *c* and a minor increase in lattice parameter *b*, with increasing size as more Ni

was added (Figure 5-2). This was consistent with observations in literature where a similar trend was observed with Basith et al.[197]

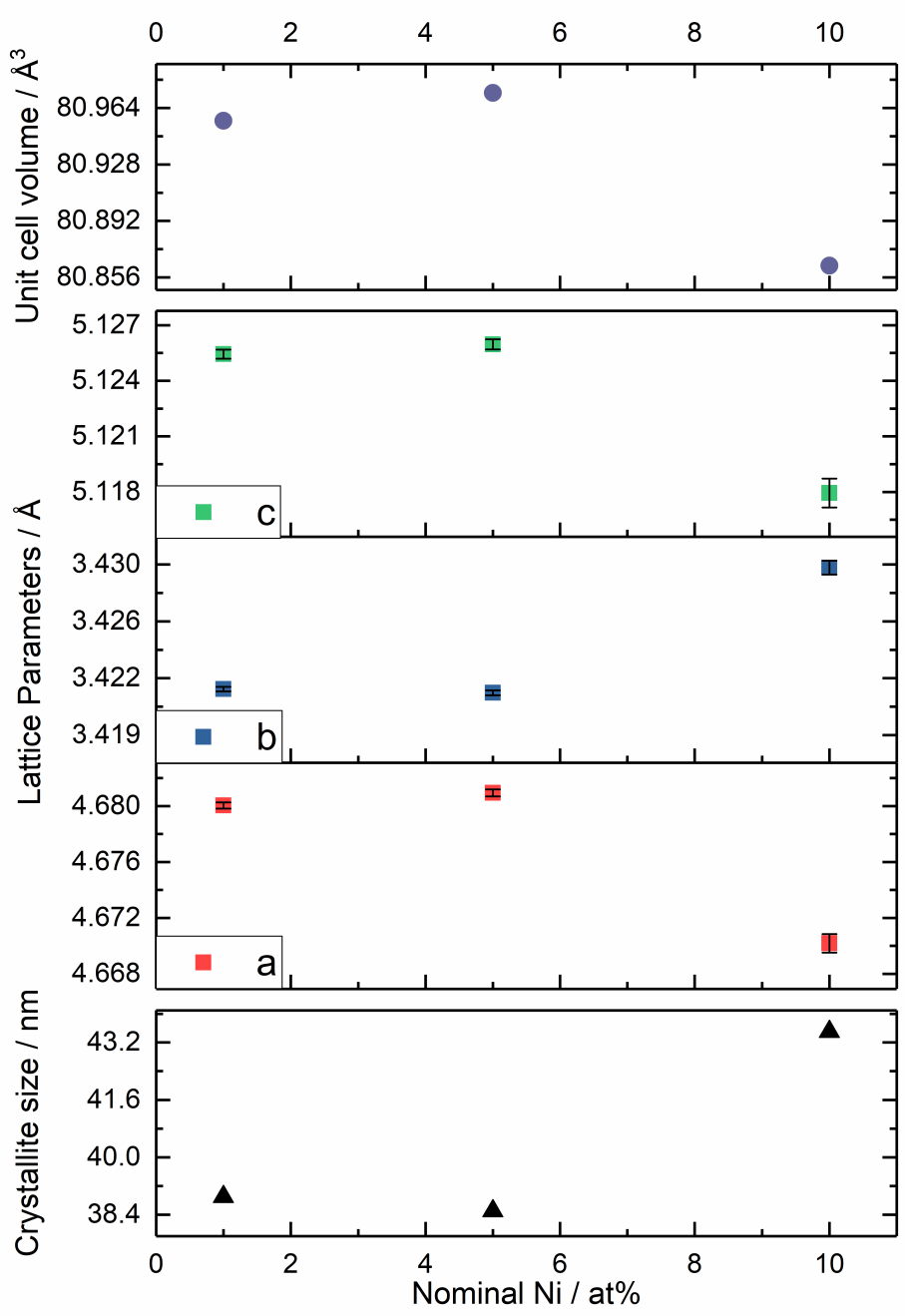

Figure 5-2 – Lattice parameter variations with increasing Ni for samples synthesised via co-precipitation. Lattice parameters are shown as *a* (■), *b* (■) and *c* (■) with crystallite size symbolised as (▲) and unit cell volume as (●).

XPS measurements were carried out to evaluate the oxidation state of Ni doped CuO and quantify the Ni content on the surface of the CuO nanoparticles synthesised by co-precipitation. Surface analysis of samples

containing 1 and 5 at% Ni did not indicate the presence of Ni on the surface of CuO. Figure 5-3 shows the high resolution scans for Cu 2p, Ni 2p and O 1s for the sample doped with 10 at% Ni. Cu was found to be in a +2 oxidation state, as confirmed by the presence of the satellite peaks and the position of the $2p_{3/2}$ (933.1 eV) and $2p_{1/2}$ (952.8 eV) peaks.[60,85] Ni was also confirmed to be in the +2 oxidation state, confirmed by the presence of satellite peaks similar to Cu and $2p_{3/2}$ (853.2 eV) and Ni $2p_{1/2}$ (871.9 eV).[206] Peak fitting of O 1s scan indicated the presence of two peaks corresponding to the metal oxide bond and contribution from carbonate on the surface of the particles.

The samples synthesised by room temperature co-precipitation were also characterised by TEM to understand the particle morphology and size. As an example, the TEM images from the 5 at% Ni doped sample are shown (Figure 5-4). There was no observable difference between the samples synthesised by co-precipitation, consistent with the PXRD pattern (Figure 5-1). Figure 5-4a shows the low resolution TEM image and the particle size was in the range 200 nm to 1 μm. As the particles were heat treated for 5 hours at 800 °C, the CuO nanoparticles coarsened significantly during the calcination process. The high-resolution TEM image showed the (111) planes with a d-spacing of 0.23 nm, which was consistent with observations in the literature for CuO.

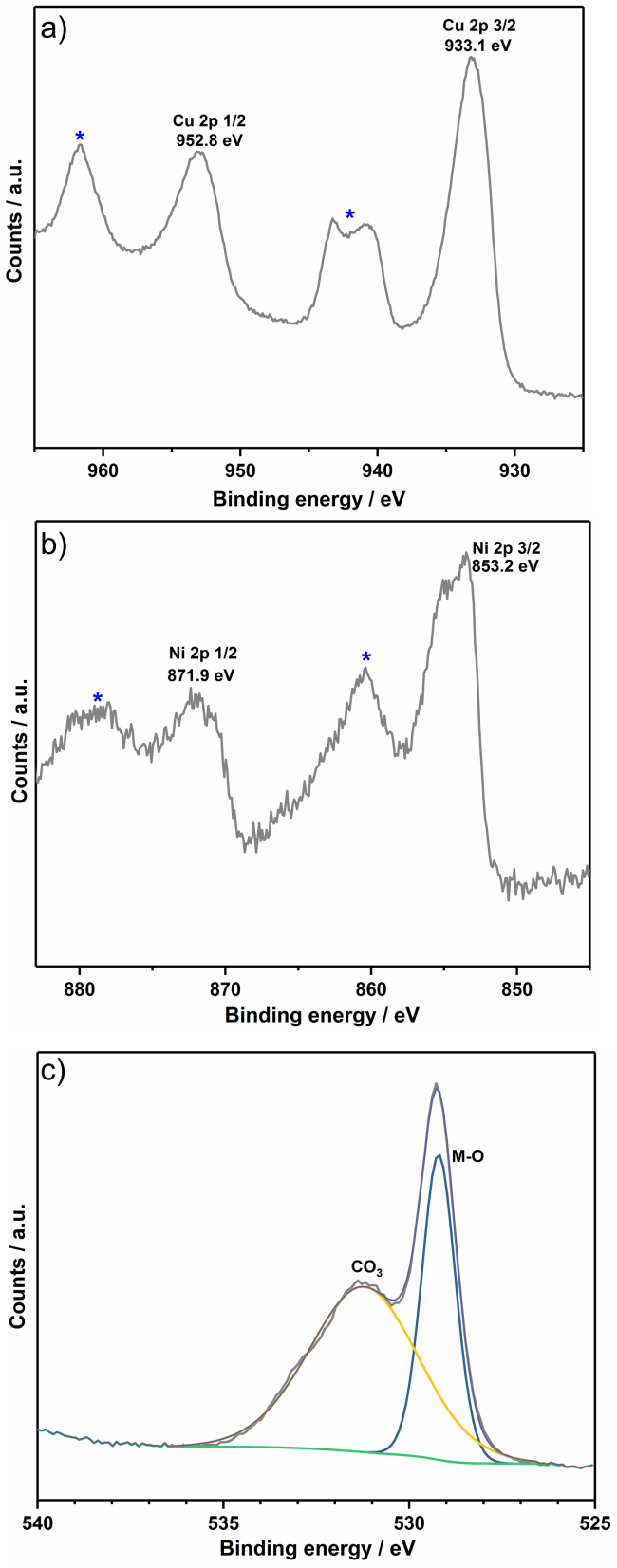

Figure 5-3 – XPS spectra of sample CuO-Ni[10]/CP showing high resolution scans for a) Cu 2p, b) Ni 2p and c) O 1s scan. Satellite peaks are marked by an asterisk.

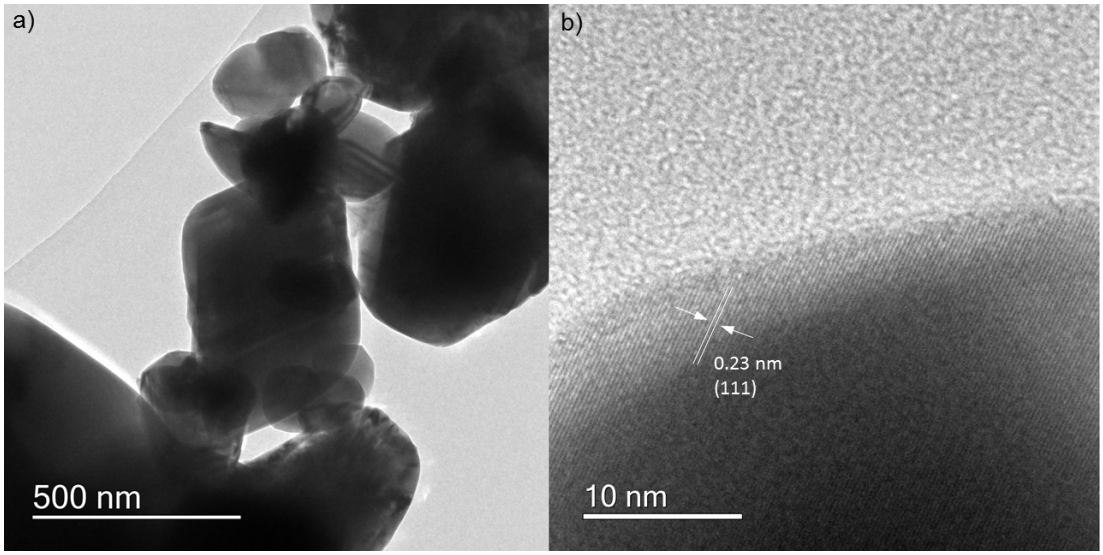

Figure 5-4 – a) Low resolution TEM image of CuO-Ni[5]/CP and b) high resolution TEM image showing the (111) lattice plane with a d-spacing of 0.23 nm.

The particle size and morphology of nanoparticles is affected by the synthesis route and equally, in this case, the Ni content that can be successfully doped into the CuO host structure. The co-precipitation method used in this Chapter was consistent with observations that the Ni inclusion is limited to 5 at% into the CuO host structure. However, it appears this method is limited as ICP-AES of the samples revealed no Ni in the 1 and 5 at% Ni and an actual Ni value of 0.75 at% Ni for CuO-Ni[10]/CP. The synthesis of doped CuO structures has not been investigated by CHFS previously. Heterometallic oxides such as $MnCu_2O_4$, have been synthesised in a single step, however, minor CuO impurities were also present.[207] To verify the suitability of CHFS for the synthesis of Ni doped CuO, samples were prepared by CHFS with Ni content in the range 0 to 50 at%.

5.3.1.2 Synthesis of $Cu_{1-x}Ni_xO$ nanoparticles using a dual mixer set up

$Cu_{1-x}Ni_xO$ nanoparticles (Ni in the range 0 to 50 at%) were synthesised using CHFS with a dual mixer set up. Chapter 3 highlighted the effectiveness of a quench feed (via a dual mixer) to modulate the CuO particle size. Hence, for the synthesis of Ni doped CuO, the dual mixer set up was used. The yield obtained of the $Cu_{1-x}Ni_xO$ nanoparticles from the CHFS dual mixer synthesis

was generally >70 % (Table 5-1). As samples were settled by the addition of NaCl and dialysed, it is expected that loss of material occurred during these stages. Changes in the pH were observed, where a lower Ni content was added in the sample, the outlet pH decreased from 4.6 to 4.2 and increased again after the addition of more than 20 at% Ni to pH 5.5 at 50 at% Ni.

Table 5-1 - Summary of the pH (as measured from the outlet of the BPR using a pH probe), surface area (BET) and crystallite size (as measured from Scherrer equation) for $Cu_{1-x}Ni_xO$ samples prepared by CHFS dual mixer set up.

Sample	pH	Crystallite size / nm	Surface Area / $m^2\ g^{-1}$
CuO	4.6	23.4	23.6
CuO-Ni[1]/DM	4.5	24.1	21.3
CuO-Ni[5]/DM	4.2	26.2	17.9
CuO-Ni[10]/DM	4.4	15.5	35.4
CuO-Ni[15]/DM	4.3	15.4	43.9
CuO-Ni[20]/DM	4.2	15.7	35.4
CuO-Ni[30]/DM	5.0	8.2	76.2
CuO-Ni[40]/DM	5.3	5.8	75.9
CuO-Ni[50]/DM	5.5	2.4	67.0
NiO/NiOOH	5.2	9.8	123.2

The PXRD patterns of $Cu_{1-x}Ni_xO$ nanoparticles showed the presence of pure phase monoclinic CuO structure up to 30 at% Ni and the peaks could be indexed to JCPDS 01-089-2529 (Figure 5-5). The lack of impurity peaks relating to NiO, NiOOH and other Cu/Ni mixed phases supported that Ni may have been successfully included into the CuO host structure. Equally, from the data, it may be that Ni did not go in to the CuO host structure and it formed satellite Ni nuclei, that were not detected. A significant peak shift was not observed with increasing Ni content and is consistent with previous observations in the literature.[197–200] It is expected, as mentioned by Vegard's law, that doping a metal ion into a host structure would result in gradual peak shifts.[208] It states that the lattice parameters should vary linearly with increasing dopant concentration and deviation from this arises due to phase transitions or segregation. It should be noted that changes in peak shifts become further complicated when nano-phase domains are concerned as the peaks broaden.[209] As the Ni content was increased to 50 at% Ni, the CuO peaks became broader, indicative that the Ni inclusion in the CuO

structure significantly reduced the size of the CuO nanoparticles, as confirmed from the Scherrer analysis (Table 5-1). An increase in the peak broadness was observed for sample CuO-Ni[30]/DM, which could be due to the significantly high amounts of Ni being added to the CuO structure and causing lattice distortion of the monoclinic structure. For samples CuO-Ni[40]/DM and CuO-Ni[50]/DM, the diffraction peaks were significantly broadened but also showed some asymmetrical behaviour possibly arising from phase segregation (overlapping CuO and NiOOH peaks) and suggested the presence of two peaks. For the attempted synthesis of NiO via CHFS (in the balanced mixer conditions), at a mixing temperature of 335 °C, a mixture of NiO and NiOOH phases were formed as confirmed with the reference patterns for NiO (JCPDS 01-071-1179) and NiOOH (JCPDS 01-073-1520).

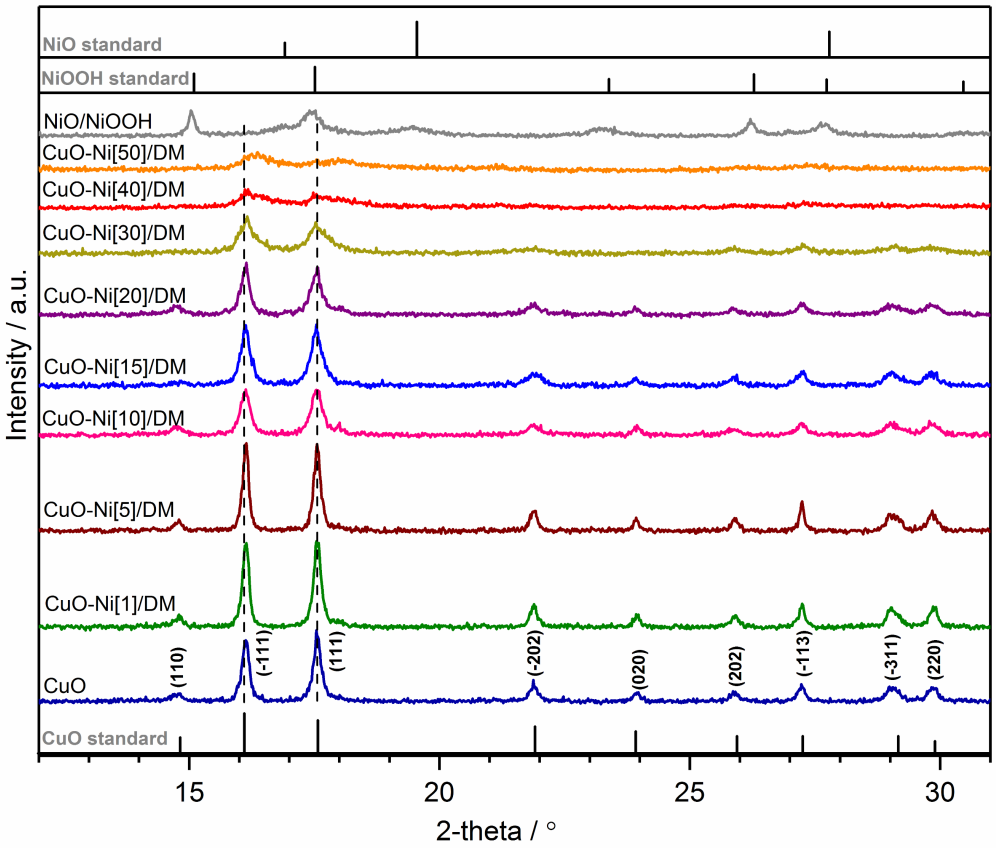

Figure 5-5 – PXRD pattern of as-prepared $Cu_{1-x}Ni_xO$ samples synthesised using CHFS dual mixer set up. The Ni content was varied from 0 to 50 at%. A pure Cu and Ni only samples are shown. The reference patterns are given for CuO (JCPDS 01-089-2529), NiO (JCPDS 01-071-1179) and NiOOH (JCPDS 01-073-1520).

The lattice parameters were obtained by Rietveld refinement by fitting the experimental data with PXRD data obtained from the literature for CuO. A plot of the variation of the lattice parameter with nominal Ni content and the crystallite size (as obtained from Scherrer), is given in Figure 5-6. The Scherrer equation was applied to obtain the crystallite size of the $Cu_{1-x}Ni_xO$ nanoparticles. The crystallite size decreased as the Ni content increases as expected, from the broadening of the peaks observed in the PXRD (Figure 5-6). Similarly, the BET surface area increased with increasing Ni content and decreasing crystallite size (Table 5-1).

The crystallite size decreased from ca. 23 nm (undoped CuO) to ca. 6 nm (30 at% nominal Ni). No significant change in the lattice parameters was observed at low Ni content. However, a significant increase was observed for lattice constant *a* (4.693 to 4.735 Å) when the nominal Ni content was increased to 30 at% (compared to the undoped CuO). Generally, *b* decreased with increasing Ni content and *c* increased slightly but not as significantly as *a*. According to literature reports, the reverse trend was observed when Basith et al. synthesised Ni doped CuO by microwave combustion method.[197] With increasing Ni, the authors observed that *a* and *b* decreased slightly and *c* increased overall, as Ni content increased. However, the changes were minimal (0.09 % change on average between undoped and 2 wt% sample). The authors suggested that the doping of Ni was not ordered and the variation in the lattice parameter was not significant, which may be due to the complexity of the monoclinic crystal structure of CuO and the anisotropic variation in the lattice.[197] The crystal structure is shown in Figure 5-7 for reference, with the monoclinic unit cell and Cu is represented by blue and O by red balls. The same group reported an increase in crystallite size with increasing Ni content, which was not observed here, where the reverse trend was observed compared to samples made via co-precipitation (in Section 5.3.1.1). This is due to the calcination step in the co-precipitation method, which allowed for the CuO particles to be

sintered and therefore continue growing to large crystallite sizes. However, samples prepared via CHFS had a considerably shorter residence time and the presence of the turbulent mixing conditions, rapid hydrolysis and dehydration, small sized crystallite sizes were possible.

Interestingly, Al-Amri et al. reported the synthesis of Ni doped CuO via a sol-gel combustion method and observed a decrease in crystallite size with increasing Ni content. The group observed a similar trend, where the lattice parameter *a* and *c* increased (4.669 to 4.723 Å) and (4.947 to 5.168 Å), respectively with increasing Ni, whereas, *b* decreased (3.788 to 3.427 Å).[210] This was in keeping with the results herein for CHFS made materials. It is possible the lattice parameter variations observed in this thesis are due to the decreasing crystallite size, as a consequence of increasing Ni in the system. It is evident that there is a variation in the structural properties of the Ni doped CuO, dependent on the synthesis method. The change in the lattice observed with samples synthesised via CHFS is suggestive of successful inclusion of Ni into the CuO host structure up to a nominal value of 30 at% Ni. Above 30 at%, successful refinement was not feasible due to the peak broadness and limited intensity. The PXRD patterns and refinements suggest, that the use of continuous hydrothermal flow synthesis allows for the doping of significantly more Ni in to the structure, compared to the literature, including co-precipitation synthesis as attempted in Section 5.3.1.1.

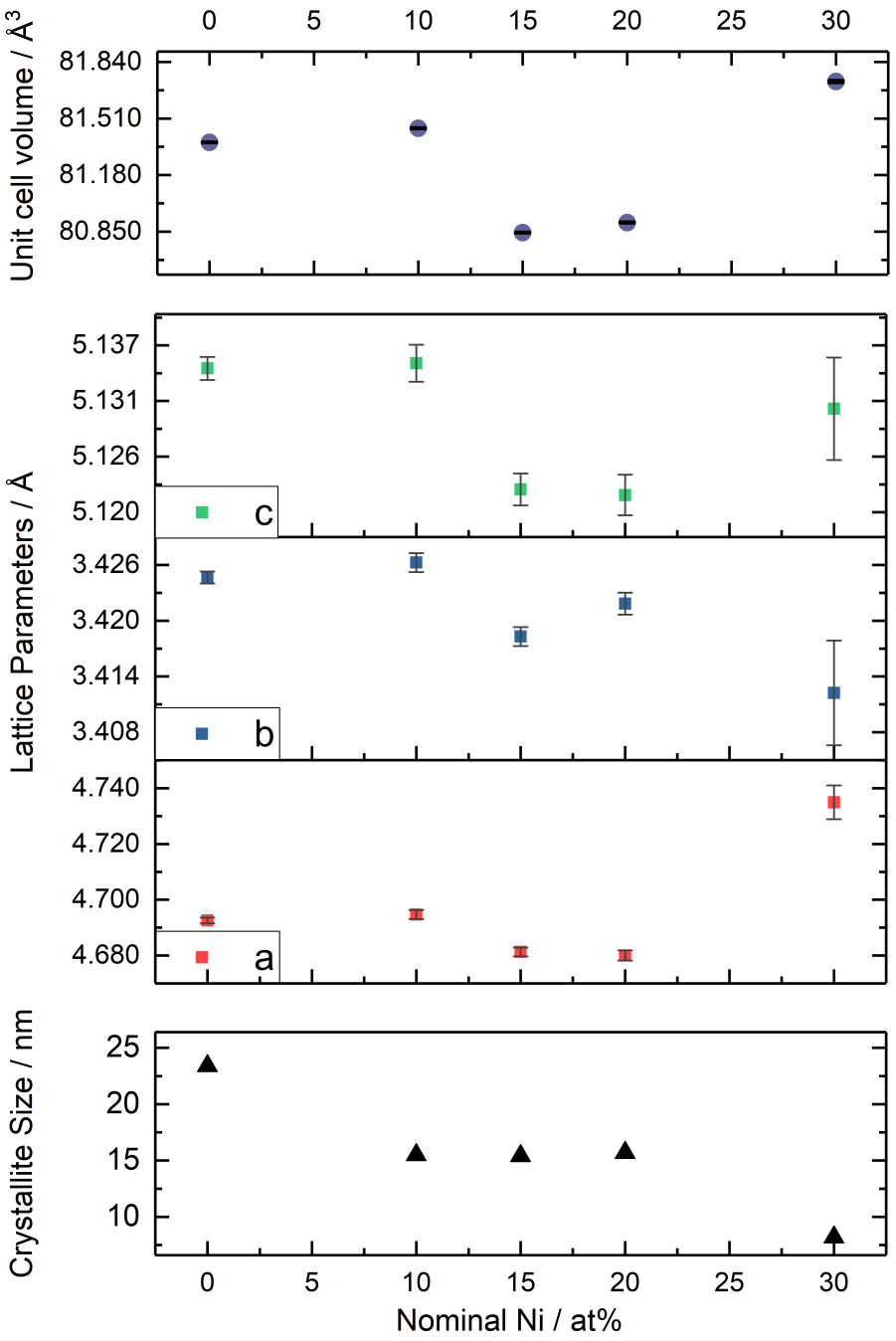

Figure 5-6 – Plot of lattice parameter variation as nominal Ni at% is increased within CuO as synthesised via the double mixer set up. Lattice parameters are shown as *a* (■), *b* (■) and *c* (■) with crystallite size symbolised as (▲) and unit cell volume as (●).

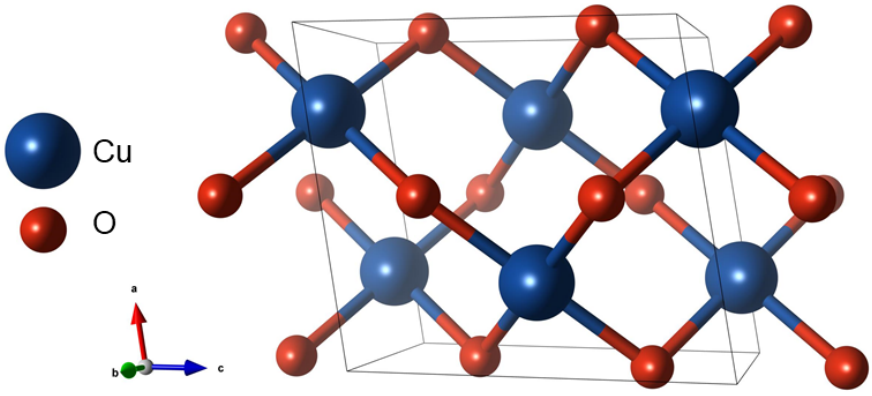

Figure 5-7 – CuO crystal structure for reference, showing the monoclinic unit cell, where Cu is shown as ● and O as ●.

Lattice strain is the deformation of a lattice which can be caused by stress (tension), resulting in lattice contraction or expansion. It is well known that a lattice contraction is observed with metal nanoparticles with decreasing particle size,[211–213] due to the high surface energy. To compensate, the atoms compress to reduce the surface area and surface energy. The reverse trend is observed with metal oxide nanoparticles, as has been reported for a range of materials (CeO_2, rutile TiO_2, MgO, $BaTiO_3$ and Cu_2O).[211,214–218] In these cases, the lattice expands as the particle size decreases. A number of models have been suggested including oxygen vacancies, Madelung model for ionic crystallites and negative surface stress effects to explain this phenomenon.[211]

Initial observations from the PXRD data and peak broadening, indicated the crystallite size was decreasing with increasing Ni, which suggested that Ni hindered the growth of the Ni doped CuO nanoparticles. This was further complicated by the presence of a quench feed downstream of the mixing point (0.76 s residence time), which rapidly quenched the nanoparticle growth. The effectiveness of the quench feed in reducing the particle size was verified by comparison of CuO nanoparticle formation using a single mixer versus a dual mixer (Chapter 3), which showed particle size reduction with the use of the quench. This was also observed with the formation of Co_3O_4 nanoparticles as shown by Denis et al.[113] It is possible that the

combination of using Ni^{2+} ions and the turbulent mixing of the precursor feeds with supercritical water, resulted in a high degree of supersaturation resulting in a decrease of particle size. It did not suggest that the formation of Ni doped CuO was growth dominated, comparable to observations in Chapter 3, where CuO formation could be modulated accordingly by altering the pH, temperature, mixer design or through the addition of H_2O_2.

Considering the ionic radii of Ni^{2+} (0.69 Å) and Cu^{2+} (0.73 Å), doping Ni into a CuO lattice would result in lattice contraction as Ni is smaller than Cu. This trend was not observed here, as shown in Figure 5-6. The data confirmed that a decreasing crystallite size resulted in an increase in the cell volume as Ni content increases. It may be speculated that due to this lattice expansion of CuO, higher amounts of Ni can be successfully included into the CuO host structure compared to methods reported in the literature, which are limited by the respective synthesis method in producing small size CuO.

Surface analysis was carried out using XPS to understand abundance of Ni on the surface of the Ni doped CuO nanoparticles synthesised by CHFS. The XPS spectrum of sample CuO-Ni[20]/DM is shown in Figure 5-8. The survey scan (Figure 5-8a) confirmed the presence of Cu, Ni, O. The C 1s peak was due to the carbon tape used in the measurements and adventitious carbon. The high-resolution Cu 2p scan confirmed the presence of Cu^{2+} species, as indicated by the $2p_{3/2}$ peak (932.9 eV) and the $2p_{1/2}$ (953.7 eV). The satellite peaks (marked by *) were typical of Cu^{2+} and have been previously confirmed in the literature.[60,85] The presence of copper carbonate was thought to be due to surface contamination of the surface of copper from exposure to the atmosphere. Similarly, the Ni high resolution scan also confirmed the presence of the Ni^{2+} by the position of Ni $2p_{3/2}$ (855.6 eV) and $2p_{1/2}$ (873.8 eV) and the presence of the satellite peaks.

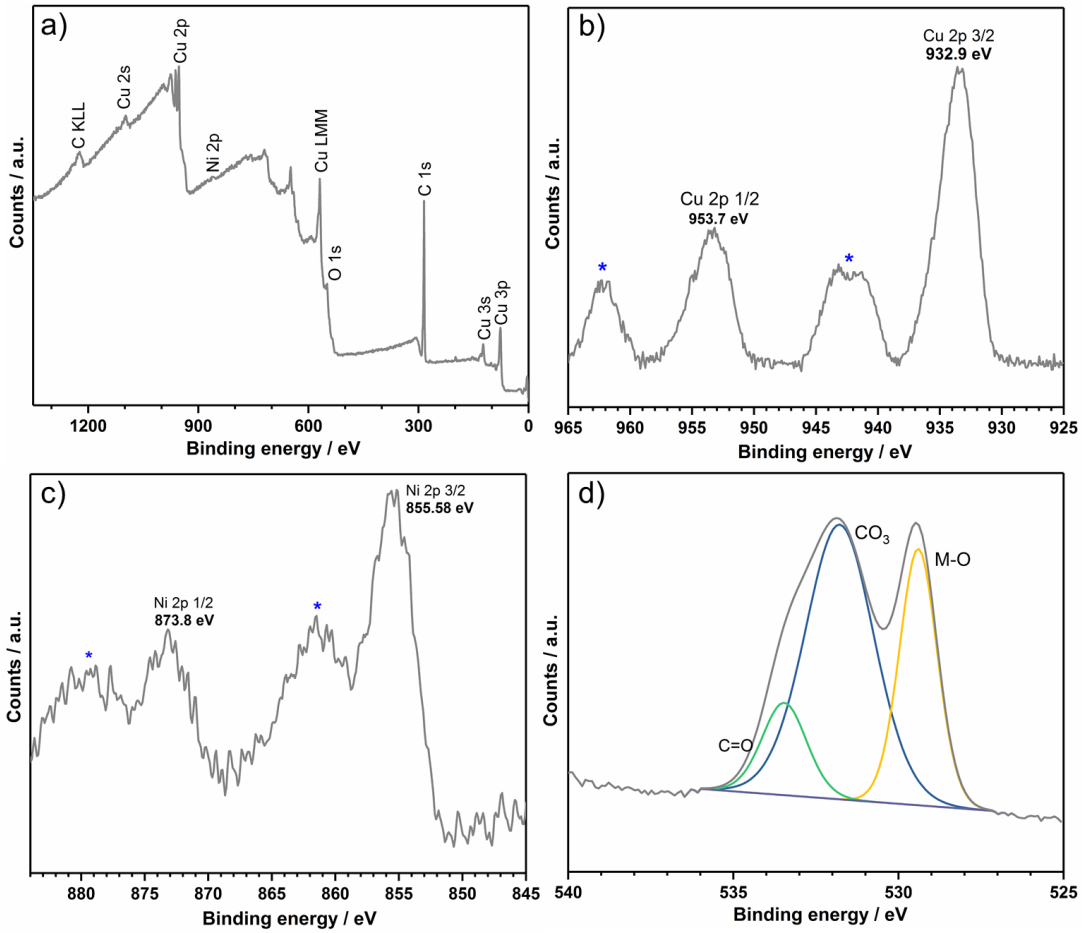

Figure 5-8 – XPS spectra of CuO-Ni[20]/DM sample a) survey scan, b) high resolution Cu 2p scan, c) high resolution Ni 2p scan and d) high resolution O 1s scan. Satellite peaks are indicated by asterisks.

The as-synthesised $Cu_{1-x}Ni_xO$ nanoparticles were also characterised by TEM (Figure 5-9). The images are shown for samples with increasing Ni content in the CuO nanoparticles. The undoped CuO sample (Figure 5-9a) shows CuO particles that were of an average size of 17 ± 5 nm with a rhombic morphology. As the Ni content was increased, a reduction in the average particle size was observed from 17.0 ± 5 nm to 6.5 ± 3 nm.

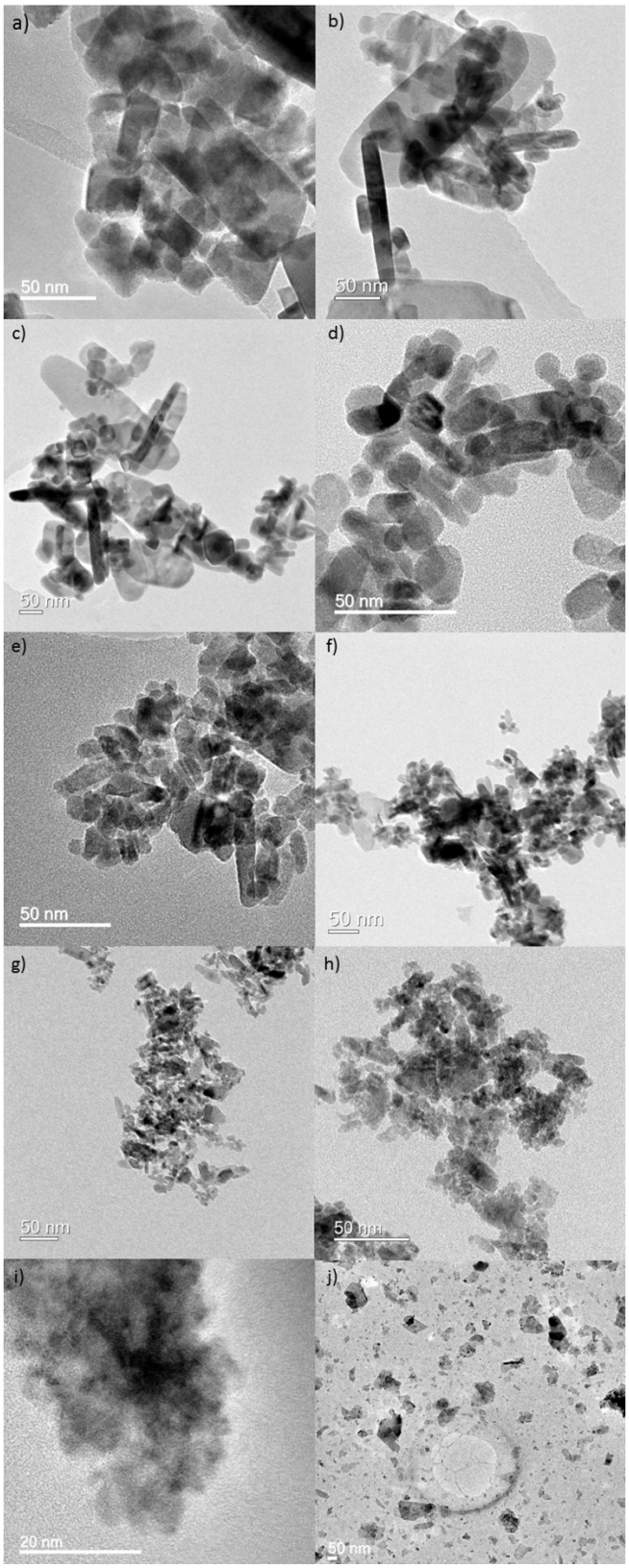

Figure 5-9 – TEM images of $Cu_{1-x}Ni_xO$ nanoparticles synthesised by a dual mixer set up – a) CuO, b) Ni-1 at%, c) Ni-5 at%, d) Ni-10 at%, e) Ni-15 at%, f) Ni-20 at%, g) Ni-30 at%, h) Ni-40 at%, i) Ni-50 at% and j) NiO/NiOOH.

At lower Ni content, the CuO particles had a well-defined rhombic morphology. As Ni content was increased there was a marked decrease in the definition of the particles, particularly for samples greater than 30 at% Ni in the CuO structure. The pure NiO/NiOOH sample (Figure 5-9j) formed sheets which is common for NiO/NiOOH phases.[219] An example of a higher magnification TEM of the CuO-Ni[10]/DM sample in Figure 5-10 showed lattice spacing of 0.26 and 0.24 nm corresponding to the (–111) and the (111) interplanar spacing of CuO, respectively.

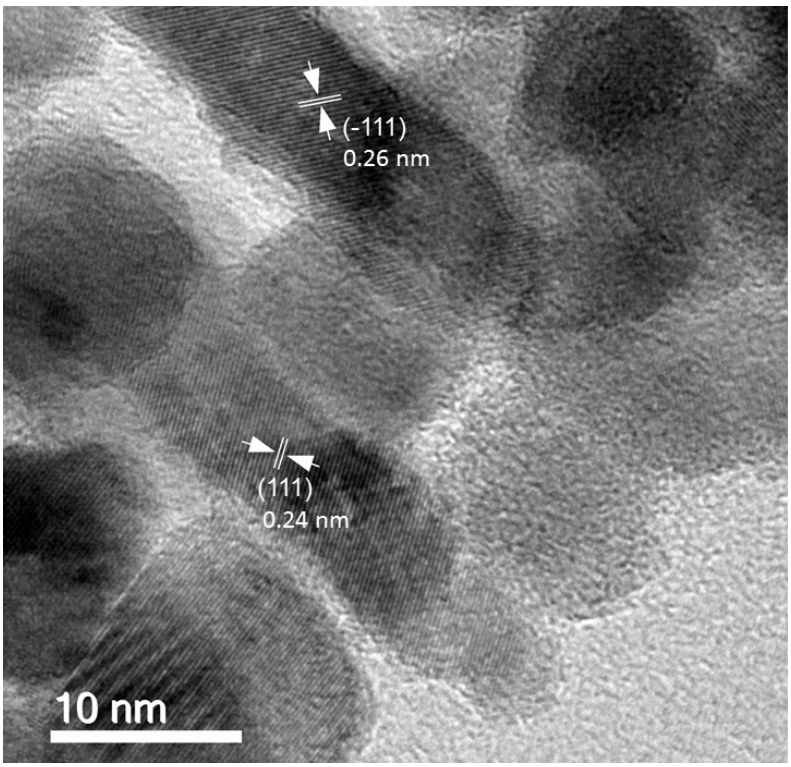

Figure 5-10 – High magnification TEM image of sample CuO-Ni[10]/DM showing a d-spacing of 0.24 nm corresponding to the (111) plane and 0.26 nm for the (–111) plane.

An EDS map was measured to evaluate the Ni and Cu distribution within the CuO nanoparticles. An example of the CuO-Ni[40]/DM sample (Figure 5-11) shows a diffuse distribution of Cu and Ni within an aggregate of doped CuO particles with no localisation of Ni, even at higher amounts of Ni (>20%) in the structure. This suggested that the distribution was homogeneous within the particles. The ratio of Cu to Ni within all $Cu_{1-x}Ni_xO$ nanoparticles was examined and is summarised in Table 5-2.

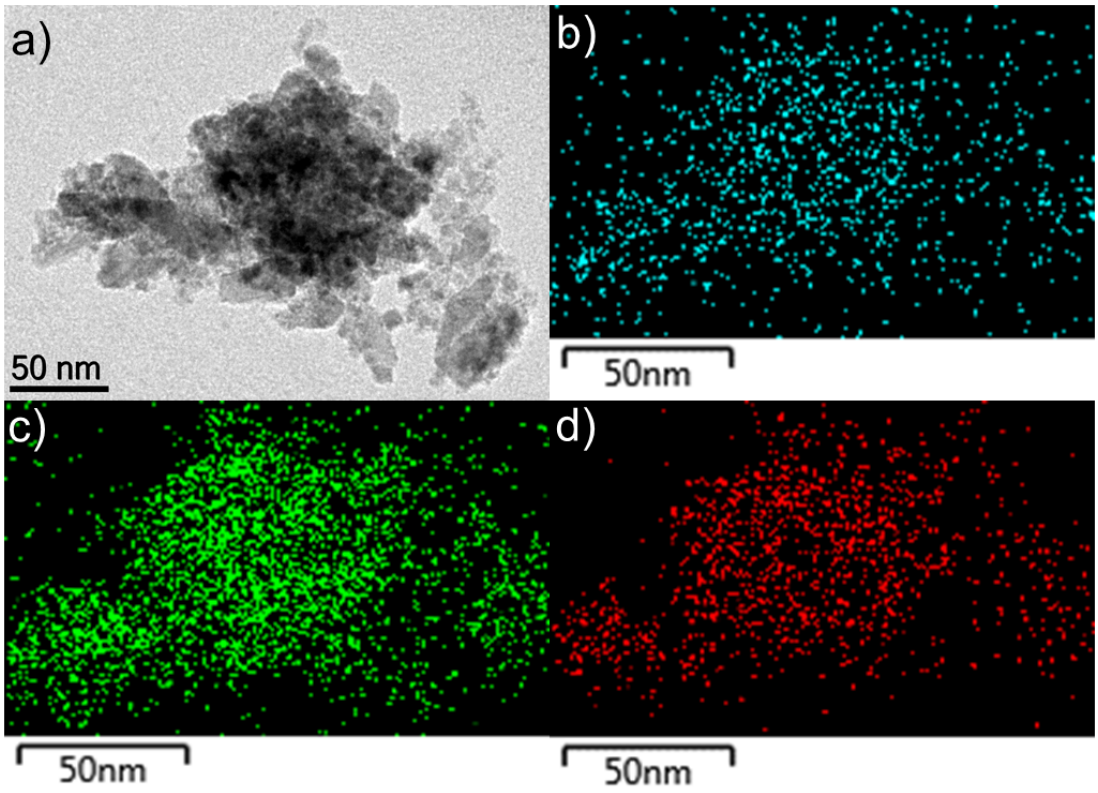

Figure 5-11 – EDS map of CuO-Ni[10]/DM sample, a) corresponding TEM image, b) Cu, c) Ni and d) O elemental maps.

Ni was not detected by EDS in samples below 20 at% nominal Ni. There was a significant discrepancy in the amount of nominal Ni and actual Ni detected by EDS. To verify the amount of Ni within the CuO structure, ICP-AES was performed and Cu and Ni composition is tabulated in Table 5-2. The ICP-AES measurements revealed the sample containing a nominal 1 and 5 at% Ni did not have any measurable Ni present. A possible reason for this was due to the quench feed used in the synthesis. It may be possible that after the formation of Ni doped CuO in the first mixer, some dissolution or leaching of Ni took place as the nascent nanoparticles were rapidly cooled in the second mixer or during the processing stages.

It is possible that the turbulent mixing of the precursors (including dopant metal) in the confined jet mixer, allowed for the rapid synthesis of potentially metastable (kinetic) doped variants of metal oxides, which may not be possible through co-precipitation methods. Equally, it is possible that the

efficient mixing regime in the mixer, also allowed higher dopant amounts that are not accessible via batch processes. The as-prepared samples were then tested to evaluate their electrochemical activity for CO_2 electroreduction.

Table 5-2 - Cu and Ni ratio obtained from EDS analysis and ICP-AES for samples synthesised by a dual mixer set up, given in at%.

Sample	XPS / at%		EDS / at%		ICP-AES / at%	
	Cu	Ni	Cu	Ni	Cu	Ni
CuO	100	0	100	0	100	0
CuO-Ni[1]/DM	100	0	100	0	100	0
CuO-Ni[5]/DM	100	0	100	0	100	0
CuO-Ni[10]/DM	98.9	1.1 ± 0.9	100	0	99.4	0.6 ± 0.05
CuO-Ni[15]/DM	97.9	2.1 ± 0.6	100	0	98.3	1.7 ± 0.07
CuO-Ni[20]/DM	97.1	2.9 ± 0.9	99.3	0.7 ± 0.1	98.0	2.0 ± 0.3
CuO-Ni[30]/DM	80.9	19.1 ± 2.0	97.6	2.4 ± 0.3	88.7	11.3 ± 0.5
CuO-Ni[40]/DM	72.6	27.4 ± 2.1	79.7	20.3 ± 0.7	74.4	25.6 ± 3.2
CuO-Ni[50]/DM	61.2	38.8 ± 2.9	73.1	26.9 ± 1.5	62.5	37.5 ± 2.3
NiO/NiOOH	0	100	0	0	0	100

5.3.2 Electrochemical reduction of CO_2 using $Cu_{1-x}Ni_xO$ nanoparticles

5.3.2.1 Cyclic voltammetry

Selected samples were formulated into inks and deposited onto glassy carbon electrodes with a mass loading of 0.3 mg cm^{-2}. Cyclic voltammograms were obtained for selected samples (Figure 5-12). Samples that indicated no Ni was present, from ICP-AES results, were not used in further testing. The following samples were used for electrochemical reduction of CO_2; CuO-Ni[0.5]/DM, CuO-Ni[2]/DM, CuO-Ni[11]/DM, CuO-Ni[25]/DM. Samples tested for CO_2 reduction will be referred to by how much actual Ni content was within CuO as determined by ICP-AES. In order to fairly assess the Ni doped CuO samples, all inks were formulated following the same protocols (described in Chapter 2 and 4) to obtain homogeneous films. Due to the poor ink dispersion and quality of the catalyst films for CuO-

Ni[38]/DM, the subsequent catalyst deposition resulted in uneven drying of the catalyst film and therefore, it was not used further.

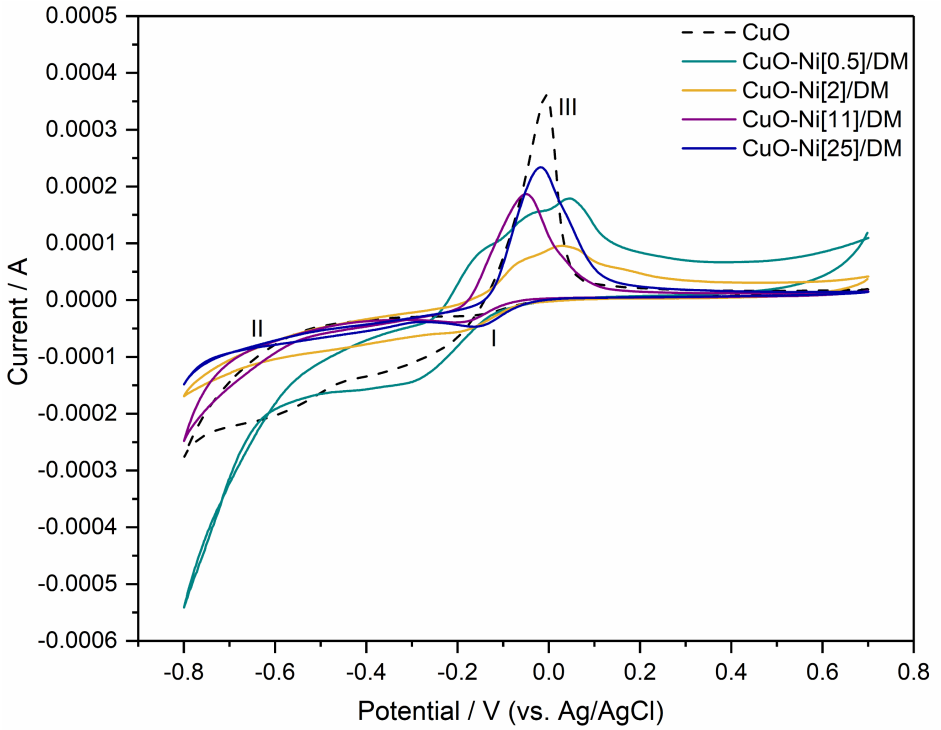

Figure 5-12 – Cyclic voltammograms of selected $Cu_{1-x}Ni_xO$ electrodes in 0.5 M $KHCO_3$ saturated with CO_2, scanned at 5 mV s^{-1}, cycle 2.

The electrodes were cycled from 0.7 to –0.8 V vs. Ag/AgCl at a scan rate of 5 mV s^{-1} to evaluate the redox behaviour of the nickel doped CuO. Generally, CuO was reduced to Cu_2O as shown by peak I and then further reduced to Cu as shown by peak II. As the electrodes were cycled back to more positive potentials, the presence of the anodic stripping peak was observed (peak III). Anodic stripping refers to the characteristic sharp peak that relates to the oxidation of the metal. Although, the sample containing no Ni showed a singular anodic stripping peak, the samples containing Ni dopants showed the presence of broad oxidation peaks and the appearance of three different species. This was more prominent in the sample containing 0.5 at% Ni and was observed somewhat in the 2 at% Ni sample. It may be possible that the presence of such peaks was due to a contribution from oxidation of Ni species that are reduced in the cathodic cycle. Comparison of such behaviour is limited in the literature as the development of such catalysts for

the electrocatalytic reduction of carbon dioxide has not been previously investigated. However, copper nickel alloy films have been developed by electrodeposition, which could provide some insight into the electrochemical behaviour of co-deposited nickel and copper observed here. Nickel deposition, and therefore, its electrochemical response, is typically not observed in the potential window studied, as it occurs in the hydrogen evolution region. Crousier and Bimaghra reported that the copper deposition in Na_2SO_4 was shifted to more anodic potentials with increasing nickel in the solution.[220] This appears not to be the case for samples investigated here. There is no clear trend to shifts of the copper oxide reduction step with increasing nickel. Only the 0.5 at% Ni sample showed higher cathodic currents in the potential region –0.6 to –0.8 V, which is assumed to be a contribution from hydrogen evolution.

On the anodic sweep, samples with higher nickel content showed singular anodic stripping peaks; lack of additional peaks suggested that nickel remained within the copper oxide structure as a solid solution. This may also be applied to the samples containing less Ni. The additional features observed in the broad anodic peak may be due to the interaction of the catalyst ink with the substrate or due to issues with the film drying on the substrate (as observed in Chapter 4). During cycling, if Ni was reduced separately, the anodic peak corresponding to the Ni oxidation would appear in a more anodic region than the copper oxidation peak, as the overpotential for Ni oxidation would be higher than for Cu. As Ni deposition and reduction occurs in the hydrogen evolution region (standard potential range 0 to –1.23 V), the potential window was extended from range 0.5 to –1.4 V vs. Ag/AgCl (Figure 5-13). Despite cycling to more negative potentials, there was no additional anodic peak for Ni oxidation on the reverse sweep and this was not observed when the potential window was extended to further positive potentials to 0.8 V vs. Ag/AgCl.

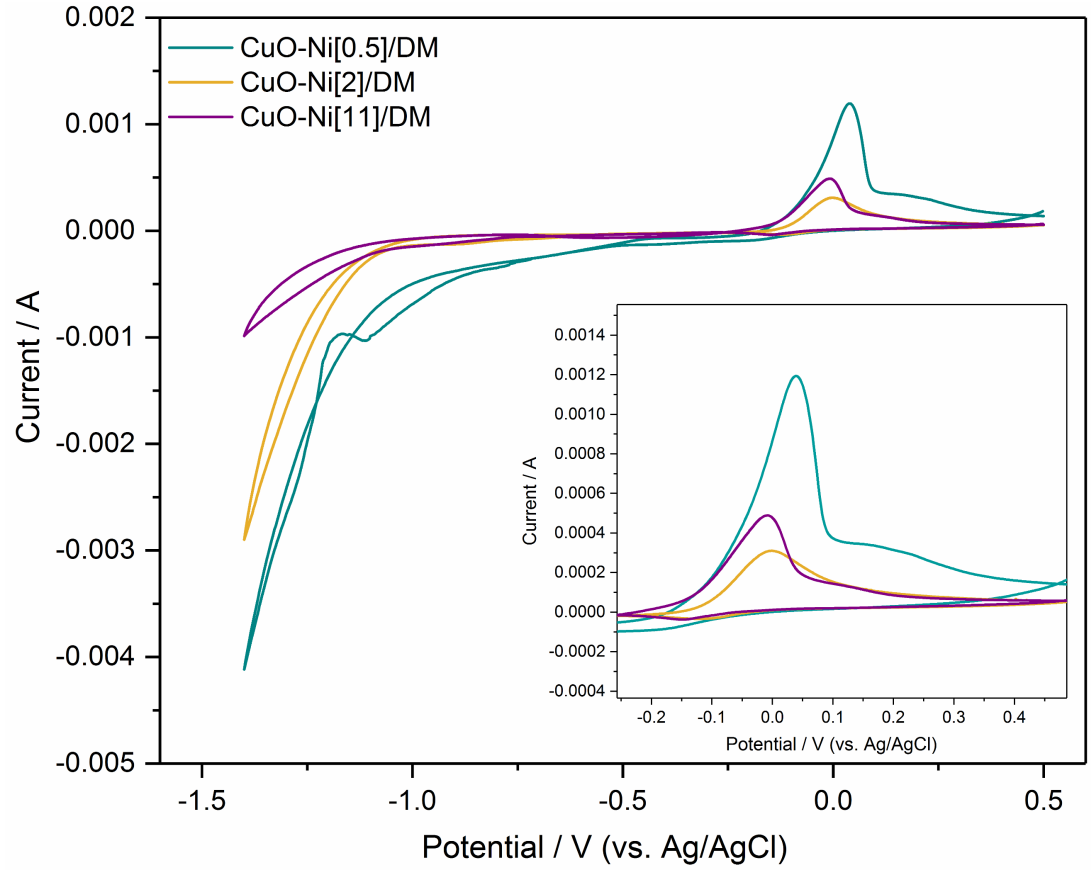

Figure 5-13 – Cyclic voltammetry curves of CuO-Ni[0.5]/DM, CuO-Ni[2]/DM and CuO-Ni[11]/DM in an extended potential window, cycled from 0.5 to –1.4 V vs. Ag/AgCl. Inset shows zoomed in anodic region between –0.2 and 0.5 V vs. Ag/AgCl. All scans represent the second cycle and a scan rate was 5 mV s^{-1} in a CO_2 saturated 0.5 M $KHCO_3$ electrolyte solution.

5.3.2.2 Constant potential electrolysis

Constant potential electrolysis was carried out by holding the electrodes at a fixed potential for 3 h to generate products from CO_2 electro-reduction. The glassy carbon electrodes were prepared with samples containing 0.5, 2, 11 and 25 at% Ni and held at various potentials (range of –0.6 to –1.4 V) and the effect on the Faradaic efficiency was studied (Figure 5-14). All samples were compared to 0 at% Ni sample for reference. Figure 5-14 shows the Faradaic efficiency for formic acid production. Other products were not observed in the ^1H NMR or via gas phase chromatography. At –0.6 V, no formic acid was observed for any samples containing Ni. As the potential was increased to –0.8 V, the formic acid production increased for samples containing Ni. Interestingly, the sample containing 2 at% Ni showed higher

Faradaic efficiency at –0.8 V compared to the sample containing no Ni. This was also the case for sample containing 11 at% Ni. However, the inclusion of only 0.5 at% Ni did not have a positive effect on the Faradaic efficiency of formic acid. Increasing the Ni content to 25 at% also did not have a positive effect and no formic acid was produced at this potential. At –0.8 V, the Faradaic efficiency was highest in the order 2 > 11 > 0 > 25 > 0.5 at% Ni.

As the potential was increased to –1.0 V, significant increase in the Faradaic efficiency for formic acid was observed for all samples. For the CuO sample, the Faradaic efficiency increased from 1.8 % at –0.8 V to 8.9 % at –1.0 V. A significant increase in Faradaic efficiency was observed for the sample containing 0.5 at% Ni, where the Faradaic efficiency increased from 0 % at 0.8 V to 11 % at –1.0 V. This was higher than the sample containing no Ni. However, increasing the nickel content to 25 at% did not lead to particularly higher production rates of formic acid. At –1.0 V, the Faradaic efficiency was highest in the order 0.5 > 0 > 25 > 11 > 2 at% Ni.

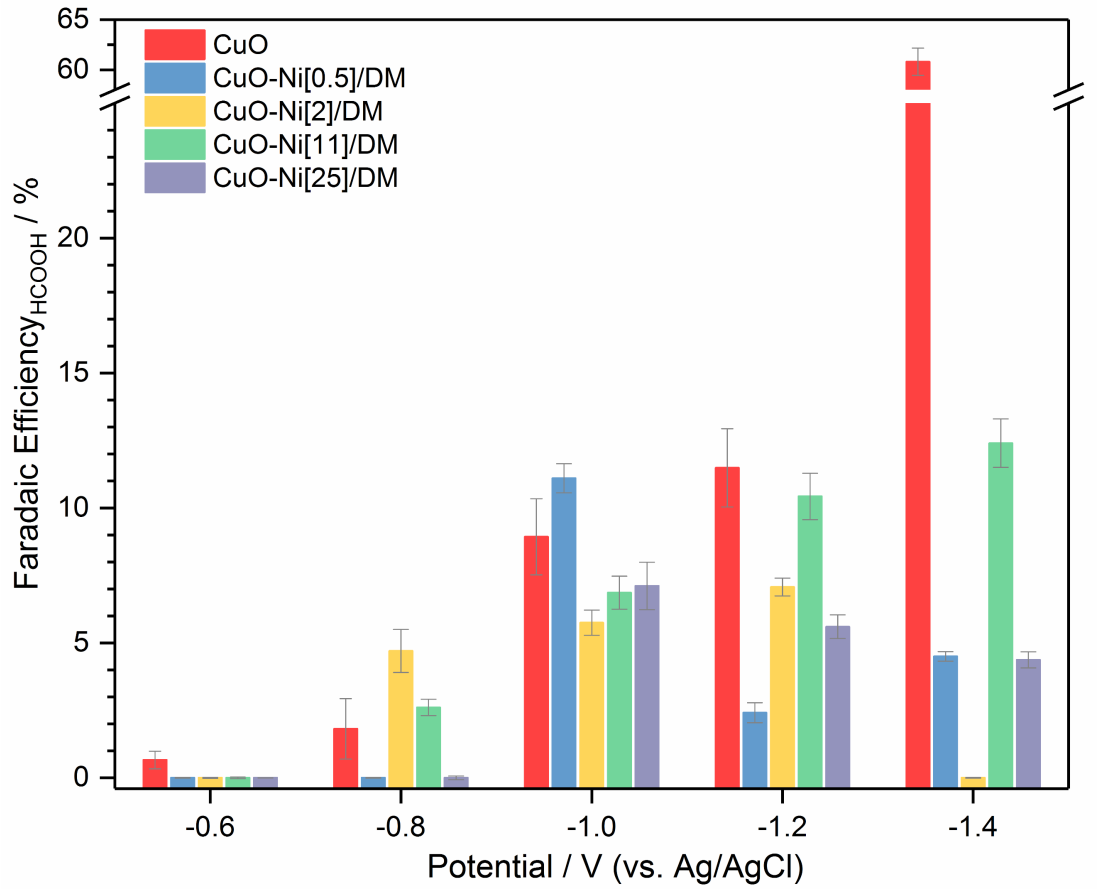

Figure 5-14 – Faradaic efficiency of HCOOH formation of samples containing 0.5, 2, 11 and 25 at% Ni in 0.5 M $KHCO_3$, saturated with CO_2, held in the range –0.6 to –1.4 V vs. Ag/AgCl.

At –1.2 V, the sample containing no Ni showed increased production of formic acid. The Faradaic efficiency for the sample containing 0.5 at% Ni decreased significantly from 11 % at –1.0 V to 2.4 % at –1.2 V. The Faradaic efficiency for the sample containing 2 at% Ni resulted in a slight increase from 4.7 % at –1.0 V to 5.8 % –1.2 V. A more significant increase was observed for the sample containing 11 at% Ni compared to the other nickel containing samples. A decrease in Faradaic efficiency was observed for sample containing 25 at% Ni. At –1.2 V, the Faradaic efficiency was highest in the order 0 > 11 > 2 > 25 > 0.5 at% Ni. At –1.4 V, including Ni into copper oxide based catalyst did not appear to improve the Faradaic efficiency significantly. A further increase of Faradic efficiency was observed for the samples containing 0.5 at% and 11 at% at –1.4 V, however, the increase for 0.5 at% sample was not more significant compared to –1.2 V. The data suggested that in general, CuO catalysts doped with <11 at% Ni performed

better than samples containing higher Ni content. Also, there was a potential dependency, where increasing the potential from –0.6 to –1.4 V, the Ni doped catalysts tended to perform worse than samples with no Ni.

As observed in Chapter 4, the copper oxide based catalyst reduces to copper metal during the CO_2 electro reduction process, it is expected that the nickel doped copper oxide is also reduced to a copper nickel alloy during the electroreduction process. This can be verified by the cyclic voltammograms (Figure 5-12) where the nucleation loop is observed, characteristic of copper metal formation.

Doping of transition metals can alter the mechanism pathway of CO_2 electro-reduction and reduce the activation barriers for key reaction steps, leading to the reduced overpotential and increased catalytic activity. Theoretical insights into the mechanism of CO_2 reduction on doped transition metal oxides is limited, however, a number of reports provide an insight into why and how doping may lead to enhancement of catalytic activity. Recently, Ou et al. investigated the effect of doping transition metals (Ni, Pd and Pt) on Cu(111) surfaces to understand the mechanism of CH_4 and CH_3OH formation.[193] In the same DFT study, the authors suggested a decrease in the activation barrier of the initial CO_2 activation to $CO_2^{-\bullet}$ was considerably lower when Cu(111) was doped with Ni, Pd and Pt. This may explain why an increased Faradaic efficiency for formic acid was observed at lower overpotentials when CuO was doped with small amounts of Ni. The selectivity was not altered when Ni was doped into CuO, as no other products were observed during the electroreduction process. According to Ou, L., Ni doped Cu(111) was capable of the facile formation of CO and the further reduction of CO to CHO that was shown to be the preferred pathway on Ni doped Cu(111).[221] The formation of CHO required a higher activation barrier than its dissociation to CO and H on both pure Cu(111) and Ni doped Cu(111). This step was found to be of hindrance for the successful formation

of CH_4 and CH_3OH. This could explain why detectable amounts of CH_3OH or CH_4 were not observed with Ni doped CuO samples in this investigation.

Formic acid can be formed on copper surfaces, as highlighted in Chapter 4 and as suggested by theoretical calculations of Nørskov et al. who highlighted that the formation of formic acid may be favoured by the formate pathway due to the dominance of Cu (111) and (100) surfaces.[184,185] As Ni doping is known to stabilise intermediates, it is possible that the HCOO* intermediate formed during the formation of HCOOH, is stabilised better by Ni doping compared to the pure Cu. This is due to high carbon and oxygen affinity of Ni, which stabilises all intermediates during the CO_2 reduction.

At higher overpotentials (> –1.0 V), the Faradaic efficiency was lowered for samples containing Ni compared to pure CuO. Ni metal is known to catalyse the hydrogen evolution reaction (HER),[222] which could suggest that as the CO_2 reduction is competing with HER, electrons for CO_2 reduction are being consumed for HER instead. Furthermore, the formation of water, following the protonation of adsorbed OH from the CO_2 reduction, is a key step in the electroreduction of CO_2. The presence of adsorbed OH on the surface of the catalyst can lead to deactivation of the catalyst via surface poisoning from OH. Ou et al. calculated the activation barriers for OH removal from the surface of doped Cu(111) surface. Ni doped Cu(111) was found to have the highest activation barrier of the three transition metals dopants (Ni, Pt and Pd) for OH removal.[193] Ni has a high affinity for OH, which can explain the reduced formic acid production at higher overpotentials as more HCOOH may be formed locally but the rate of formation of the product subsides eventually.

5.3.2.3 Effects of the catalyst surface area

The electrochemically active surface area of the catalyst was also measured to evaluate if including Ni in the catalyst altered the available active sites for CO_2 reduction. The active surface area was calculated via the double layer

capacitance in 0.1 M H_2SO_4 and cycling in the non-Faradaic region at scan rates from 20 to 100 mV s^{-1} (Figure 5-15a). The difference in current at a particular potential was plotted against the scan rate and the slope from the linear regression gave the capacitance (Figure 5-15b). The surface roughness factor (SRF) was calculated as a ratio of the samples versus the substrate (glassy carbon) (Table 5-3). The sample containing no Ni was also given as a reference. The roughness factor for samples containing Ni, did not change significantly compared to the undoped CuO sample, despite smaller particle size with increasing Ni. It does not appear that including the Ni increases the availability of active sites in, which may also explain why the Faradaic efficiency was not significantly increased with the inclusion of Ni as compared to the optimised unmodified CuO sample. It may also suggest that during electroreduction, the catalyst surface is altered and hence the true representation of the active surface is not provided, as the surface measurements are carried out post electrolysis. To further understand this, the catalyst layers were examined by SEM.

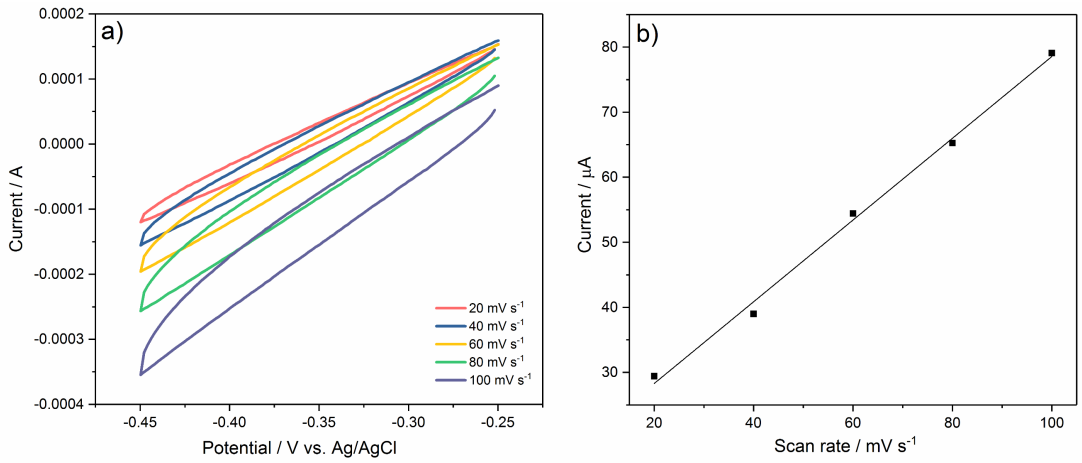

Figure 5-15 – Surface area evaluation from double layer capacitance measurements a) cyclic voltammetry scans of CuO-Ni[2] samples in the non-faradaic region, cycled between –0.25 and –0.45 V vs. Ag/AgCl at scan rates of 20, 40, 60, 80 and 100 mV s^{-1}, b) current from the cyclic voltammetry scans are plotted against scan rate and the linear regression gives the capacitance values which is tabulated in Table 5-3.

Table 5-3 - Table of samples tested in this chapter including their capacitance values as extracted from the method described above to give the surface roughness factor. Glassy carbon refers to 1 and SRF calculations for subsequent samples are done versus glassy carbon.

Sample	Capacitance / uF cm^{-2}	Surface Roughness Factor
Glassy carbon	0.03	1
CuO	0.70	23
CuO-Ni[0.5]/DM	0.63	21
CuO-Ni[2]/DM	0.65	22
CuO-Ni[11]/DM	0.62	21
CuO-Ni[25]/DM	0.61	20

5.3.2.4 Structural characterisation of catalyst layers

The catalyst layers were examined before and after constant potential electrolysis, to evaluate if any changes to the morphology or the particle size occurred during CO_2 electroreduction. As indicated by the SEM images (Figure 5-16 left row with increasing Ni), the catalyst inks before electrolysis displayed an even deposition of the catalyst on the glassy carbon electrode, with the presence of some larger aggregates, as expected from the ink formulation process and deposition stages. This was consistent with earlier examples of catalyst inks (Chapter 4). The inclusion of Ni in the catalyst did not appear to make a significant difference to how the inks dried on the glassy carbon electrode. Following constant potential electrolysis at –1.0 V for 3 h, the electrodes were re-examined by SEM; the sample containing 0 at% Ni is given as reference (Figure 5-16 a and b). The sample containing 0.5 at% Ni (Figure 5-16 c and d) did not vary significantly before and after constant potential electrolysis. The particle size remained relatively similar and was consistent in appearance with the sample containing no Ni.

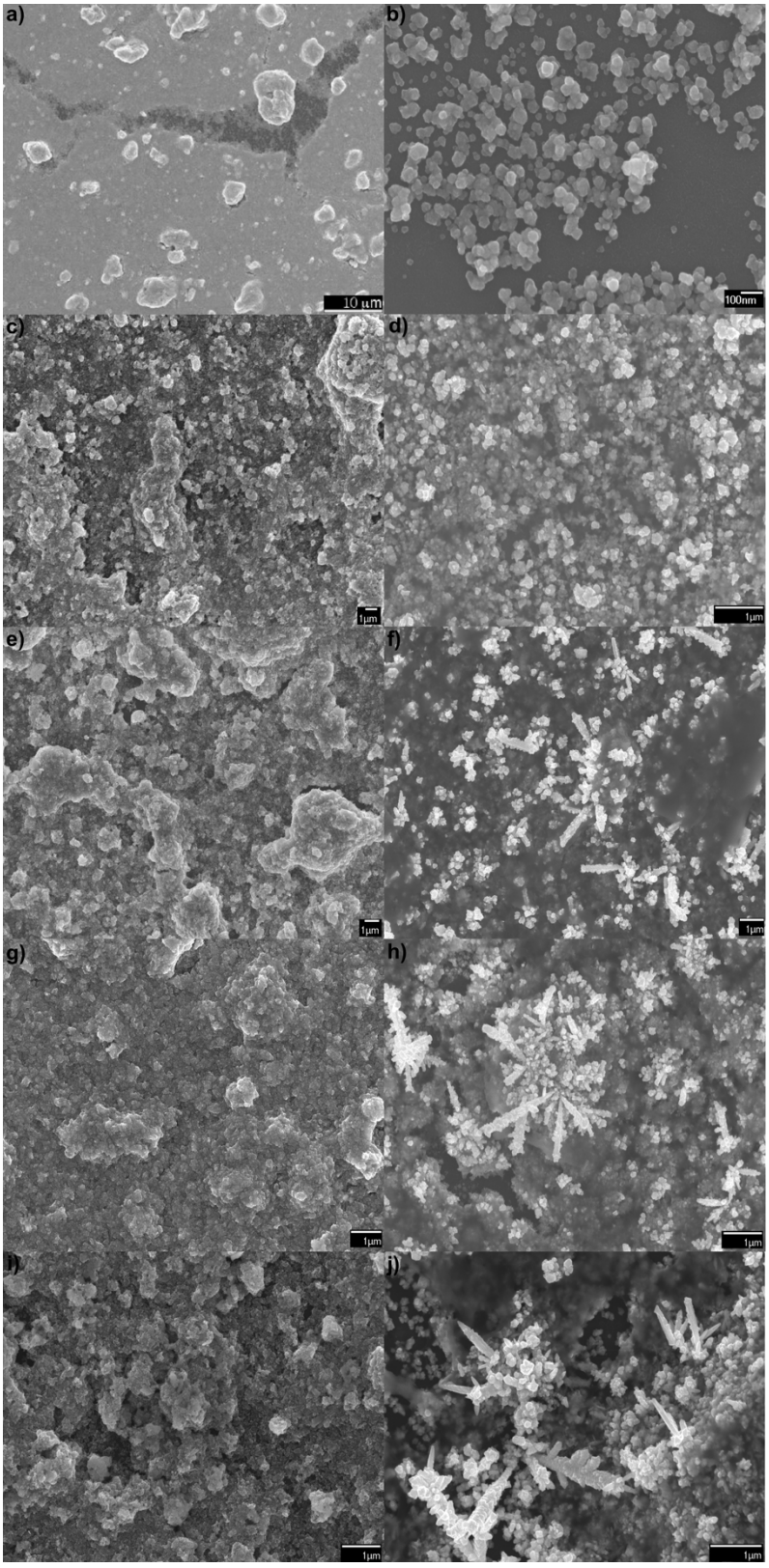

Figure 5-16 – SEM images of catalyst layer before and after electrolysis conducted at –1.0 V for 3 h, left row shows the catalyst before electrolysis and right row shows the catalyst after electrolysis – a, b) unmodified CuO, c, d) 0.5 at% Ni, e, f) 2 at% Ni, g, h) 11 at% Ni and i, j) 25 at% Ni.

As the Ni content was increased (Figure 5-16 e and f), a significant change was observed for the sample containing 2 at% Ni, where the formation of dendrite structures was observed as well as the presence of the smaller particles, as seen in the sample before electrolysis. This was consistently observed for all samples containing higher amounts of Ni (Figure 5-16 h-j). The high magnification SEM images in Figure 5-17 show the copper dendrite formation that occurred in situ during constant potential electrolysis experiments, with increasing Ni from 2 to 25 at%.

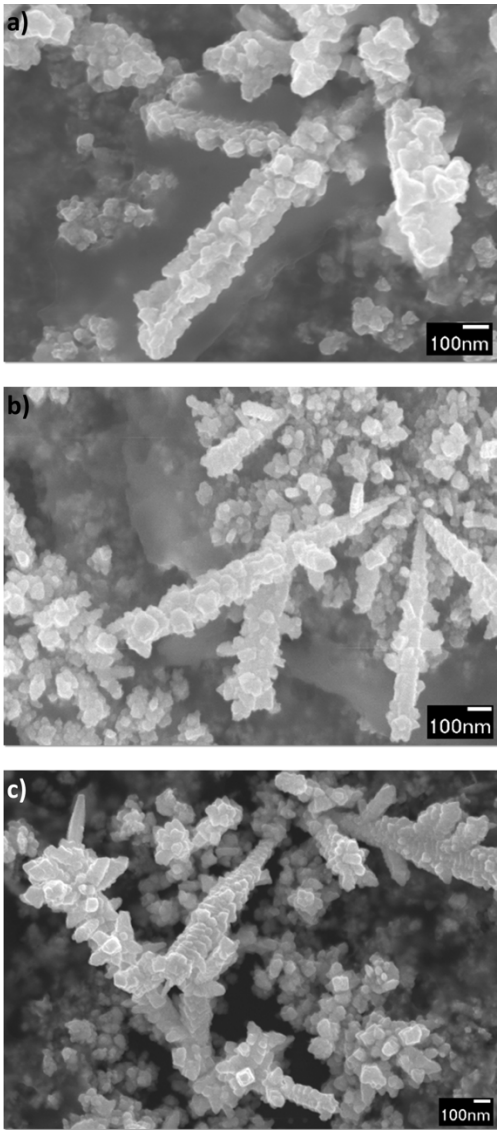

Figure 5-17 – Higher magnification SEM images of Ni doped CuO on glassy carbon electrode, after constant potential electrolysis experiments at –1.0 V for 3 h, showing copper dendrite formation for samples containing a) 2, b) 11 and c) 25 at% Ni

Dendrite growth was observed in Chapter 4, when the Nafion content in the catalyst layer was increased to 66 wt% (vs. the solid-state fraction). The formation of dendrites was linked to the presence of negatively charged sulfonic acid groups in Nafion, which would inhibit the mass transport of Cu nuclei, promoting the growth of dendrite structure. However, here, the Nafion content was limited to 25 wt%, as it was found to be the optimum Nafion content to achieve the optimal catalytic activity. Electrochemical dendrite growth is commonly seen with the electrodeposition of copper and can be affected by the concentration of the copper ions, concentration of the supporting electrolyte, increase in the viscosity or decrease in the temperature as well as the velocity of motion of the bulk solution.[223]

The formation of dendrites has been reported in the literature during the electrodeposition of copper when nickel is co-deposited with copper on a glassy carbon electrode. Crousier and Bimaghra observed the formation of copper and nickel dendrites when Na_2SO_4 was used as an electrolyte.[220] As the deposits were obtained by scanning the potential rather than conducting potentiostatic polarisation, there was also a presence of larger copper crystallites as well as fern shaped crystallites. Dendrites were observed as the potential was scanned to –1.0 V vs. SCE. However, this study also indicated a morphology dependence of the supporting electrolyte, where dendrite formation was hindered by the presence of NaCl electrolyte. It is likely that the significant morphology changes observed in the samples prepared via CHFS were due to the presence of Ni in CuO, which was driving the formation of dendrites. This was also supported by the fact that as the Ni content was increased, there was more dendrite formation at higher Ni content compared to samples with lower Ni content.

Recently, Larrazábal et al. compared undoped Cu_2O with doped Cu_2O (with Sn, In, Ga and Al) to tune the selectivity of CO_2 electroreduction.[224] As well as observing a positive change in the selectivity of CO production with the In

and Sn doped Cu_2O, some restructuring of the particle morphology was observed before and after the catalysts were used. The authors observed the formation of small but well defined nanostructured polyhedral features on the surface of the particles after the catalysts had been used for CO_2 electroreduction. This was, however, observed in the undoped Cu_2O as well as the doped Cu_2O to some extent and the authors argued the morphological changes were due to the irregularity of the starting material, which could lead to major re-structuring process in situ.

The morphology changes observed with Ni doped CuO were significant and it is also possible that the interaction of the supporting electrolyte and the Ni doped CuO could play a role in driving the formation of dendritic structures in situ. To further understand the role of the supporting electrolyte in the formation of dendrites, the samples were tested in 0.5 M K_2HPO_4. The anionic species were changed in order to better understand their role as it has been highlighted through previous studies that anions such as Cl^- can play a role in promoting dendrite growth.[225]

5.3.2.5 Effect of the supporting electrolyte

The supporting electrolyte plays a key role on the electroreduction of CO_2 to fuels and chemicals. To further understand the impact the supporting electrolyte had on dendrite formation and subsequently Faradaic efficiency of HCOOH formation, the catalysts were tested in 0.5 M K_2HPO_4. Only catalysts containing 0.5, 2 and 11 at% Ni were tested as these catalysts showed the most promising activity with 0.5 M $KHCO_3$.

The constant potential electrolysis experiments were limited to –1.0, –1.2 and –1.4 V as potentials lower than –1.0 V vs. Ag/AgCl generally showed poor selectivity towards CO_2 electroreduction. The Faradaic efficiency of HCOOH formation vs. the applied potential is shown in Figure 5-18. Other products were not observed in the liquid or gas phase similar to testing conducted with

0.5 M $KHCO_3$. Faradaic efficiency for HCOOH formation in 0.5 M $KHCO_3$ is also presented for reference.

At –1.0 V, the Faradaic efficiency was negligible for all samples in 0.5 M K_2HPO_4 and significantly higher for samples tested in 0.5 M $KHCO_3$ electrolyte. An improvement in the Faradaic efficiency with increasing potential was not observed, as the catalysts were held at –1.2 V. A similar trend was observed at –1.0 V and –1.2 V, where the Faradaic efficiency increased marginally with increasing nickel content. However, this change was not significant enough to positively associate increasing Faradaic efficiency with increasing Ni content in the catalyst layer. As the potential was held at –1.4 V, a more significant increase in the Faradaic efficiency for HCOOH formation was observed in 0.5 M K_2HPO_4 compared to 0.5 M $KHCO_3$. However, the reverse trend was observed where the Faradaic efficiency only decreased marginally with increasing Ni content at –1.4 V.

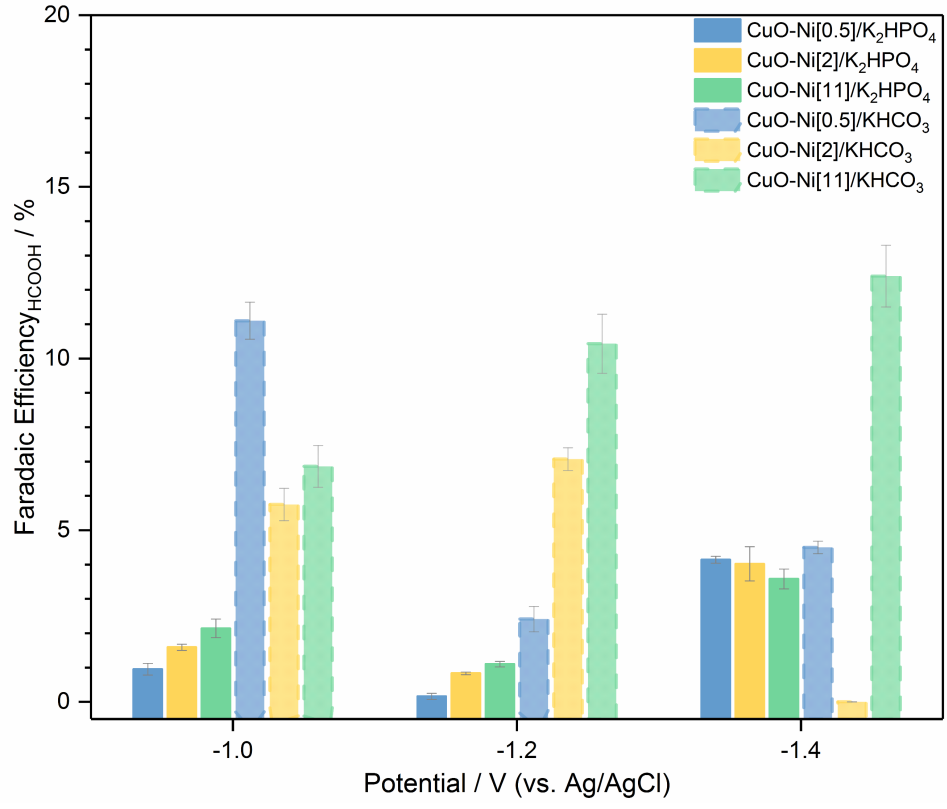

Figure 5-18 – Faradaic efficiency for HCOOH formation for samples 0.5, 2, 11 at% Ni in 0.5 M K_2HPO_4 and 0.5 M $KHCO_3$, saturated with CO_2.

Generally, the samples tested in 0.5 M $KHCO_3$ had a higher Faradaic efficiency for HCOOH formation than samples in 0.5 M K_2HPO_4. However, a significant decrease was observed for the sample containing 2 at% Ni in $KHCO_3$ compared to K_2HPO_4 at –1.4 V. Some studies have attempted to evaluate the impact the anion in the electrolyte has on the electroreduction of CO_2. A study by Wu, J. explored the impact of the electrolyte on Sn electrodes; specifically, investigating the effect of anions ($KHCO_3$, K_2SO_4 and KCl) as well as the cations and electrolyte concentration.[226] $KHCO_3$ was found to be the optimal electrolyte as it showed the higher formate production rates. K_2SO_4 showed relatively high Faradaic efficiency at lower overpotentials, but the authors did not discuss the significance of this observation in detail. The authors argued that $KHCO_3$ was more suitable as it supplied the most availability of reactants (dissolved CO_2) to the electrode for CO_2 reduction.

It is clear from the literature that there is a lack of understanding of how in situ morphological changes of the catalysts during CO_2 electroreduction play a major role in the enhancement or degradation of catalytic activity and selectivity. The presence of Ni in the catalyst layer further complicates understanding of HCOOH formation as the question remains whether the HCOOH formation is depended on dendrite formation (as observed here) or through Ni interacting and stabilising the intermediates. The catalyst layers were examined post electrolysis in 0.5 M K_2HPO_4. The changes in the morphology as observed by SEM before and after electrolysis with 0.5 M K_2HPO_4 were minimal as compared to 0.5 M $KHCO_3$ (Figure 5-19).

The particles did not show any dendritic growth with increasing Ni content (Figure 5-19 a-c). The particles remained nanostructured but some roughening and clustering of aggregates was also observed. This is a stark difference to the catalysts tested in 0.5 M $KHCO_3$, where significant morphology change was observed for samples containing >2at% Ni and

dendrite growth was observed. This was not the case with K_2HPO_4. However, the corresponding Faradaic efficiency remained negligible. It has been highlighted in a number of studies that electrocrystallisation (in this case CuO reduction to Cu on CuO) can be influenced by the blocking of deposition sites by specific anion adsorption, which can influence electrochemical kinetic parameters. Carneval and Cusminsky studied the influence of the anion on copper electrocrystallisation and compared sulfate, pyrophosphate, chloride, citrate, cyanide and amine-sulfate solutions.[227] A difference in morphology was observed with different anions; dendrite formation was observed with sulfate and pyrophosphate solutions. The authors suggested that the morphological changes were predominantly influenced by the adsorbed components as they observed different morphologies with varying current densities and anion type.

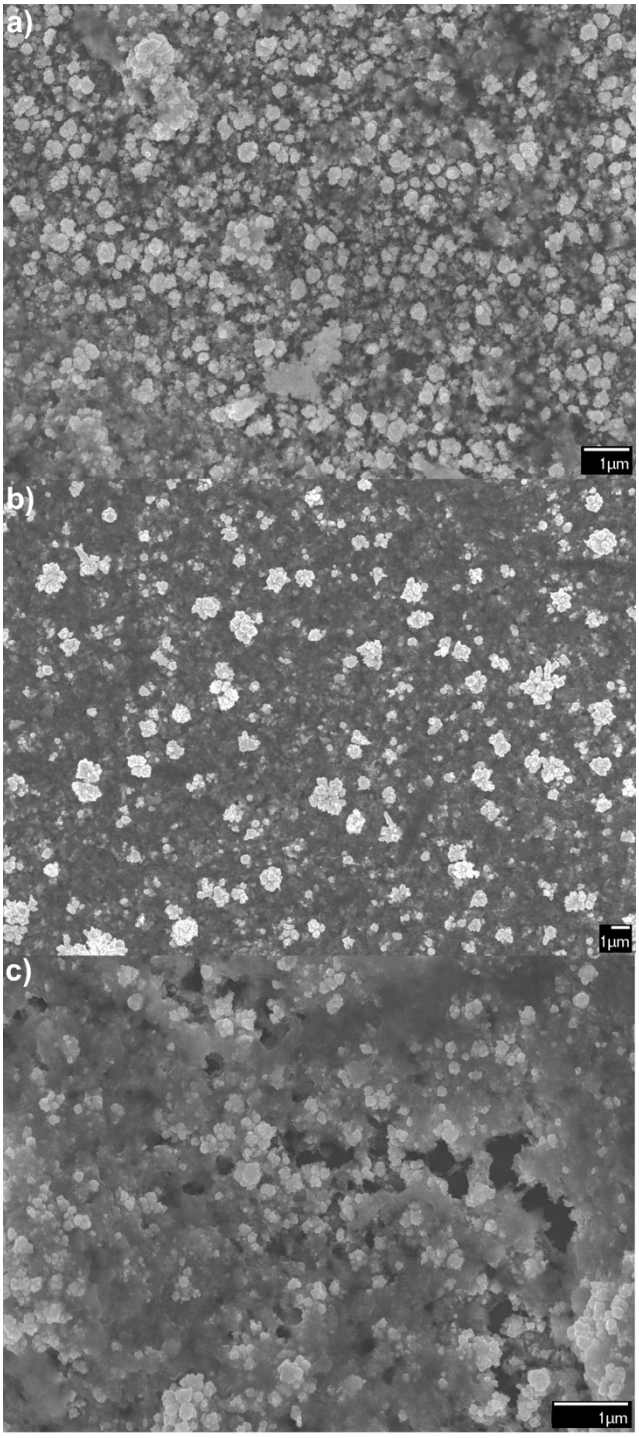

Figure 5-19 – Post electrolysis SEM images of Ni doped CuO in 0.5 M K_2HPO_4, a) 0.5 at%, b) 2 at% and c) 11 at% Ni.

The effect of the potential on the catalyst layer (in PO_4^{-2}) was also examined (Figure 5-20). However, no significant changes were observed with the catalyst layer as the potential was increased from –1.0 to –1.4 V for the sample containing 11 at% Ni. This was also the case for the samples

containing lower Ni content. It has been shown that the formation of dendrites has been due to higher overpotentials at the electrode surface but this was not observed, which implied the role of the electrolyte and specifically the anion was more significant in controlling the morphology.

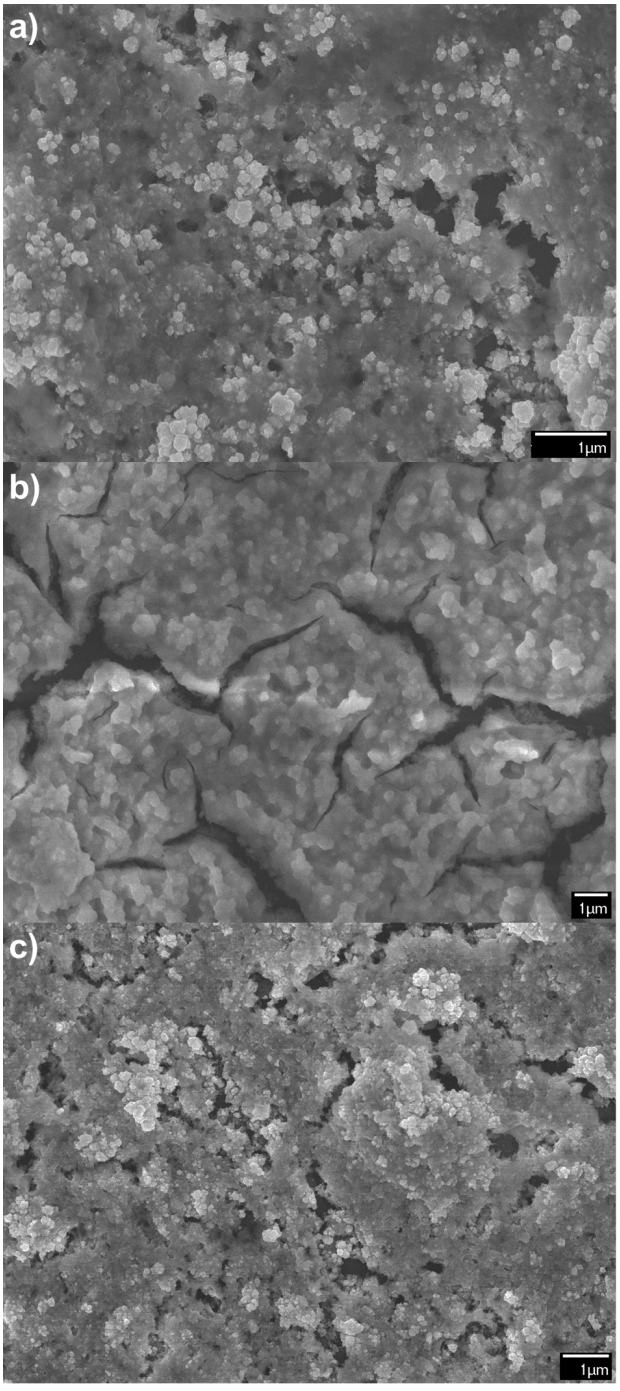

Figure 5-20 – Post electrolysis SEM images for sample CuO-Ni[11]/DM in 0.5 M K_2HPO_4, a) –1.0 V, b) –1.2 V and c) –1.4 V.

The significant cracks shown in Figure 5-20b are likely to be due to volume changes to the catalyst layer during the reduction process.[228] However, the particles also remained nanostructured and did not display significant morphological changes compared to samples tested in 0.5 M $KHCO_3$. Damjanovic et al. also noted that the presence of small amounts of organic substances (10^{-12} mol cm^{-2}) may influence morphological changes of a growing crystal.[229] However, this is not observed in this case as HCOOH formation has not caused any morphological changes as shown by the SEM images taken of the CuO sample tested in Chapter 4 even when significantly high amounts of HCOOH was produced.

Varela et al., investigated changes in the catalytic activity, selectivity and the surface morphology of Cu in the presence of halides and observed a positive effect for CH_4 production with I^-.[230] The authors observed some morphology changes when Br^- and I^- were added to 0.1 M $KHCO_3$. Nanostructuring at the surface of the electrode was observed and the formation of well-defined cubes was seen. The authors, however, argued that the enhanced selectivity of methane formation with I^- was not as a result of in situ formation of nanocubes, but due to the interaction of the I^- ion with the catalyst surface and the stabilisation of intermediates, specifically for CO protonation to CH_4.

Ren et al. studied the electrochemical reduction of CO_2 to ethylene and ethanol on copper (I) oxide films with varying thicknesses and used 0.1 M $KHCO_3$ and 0.1 M phosphate buffers (K_2HPO_4 and KH_2PO_4) during testing.[228] Morphology changes were observed as the Cu_2O films were potentiostatically polarised and the formation of small nanoparticles on the surface of the catalyst was observed. The catalyst films were subsequently tested in a phosphate buffer and an enhancement of CH_4 production was not observed and the formation of C_2H_4 decreased. The authors suggested that changes in the local pH were not the sole factor for the enhanced activity with $KHCO_3$ and the local structure and morphology made a significant

difference to enhance the catalytic activity and selectivity. The authors, however, did not present any evidence of morphological changes of the Cu_2O films with phosphate buffer.

Impedance analysis was carried out on samples in both 0.5 M $KHCO_3$ and K_2HPO_4 to elucidate the mechanism of CO_2 reduction. The Nyquist plots for sample CuO-Ni[2]/DM at –1.4 V are given in Figure 5-21. The two plots show very different impedance plots, where the sample in $KHCO_3$ revealed a small semi-circle, however, the sample in K_2HPO_4 revealed two large semi circles. Fitting the impedance plots (to the equivalent model described in Chapter 4) revealed a charge transfer resistance, Rct of 7.0 Ω in $KHCO_3$ and Rct of 30.5 Ω in K_2HPO_4.

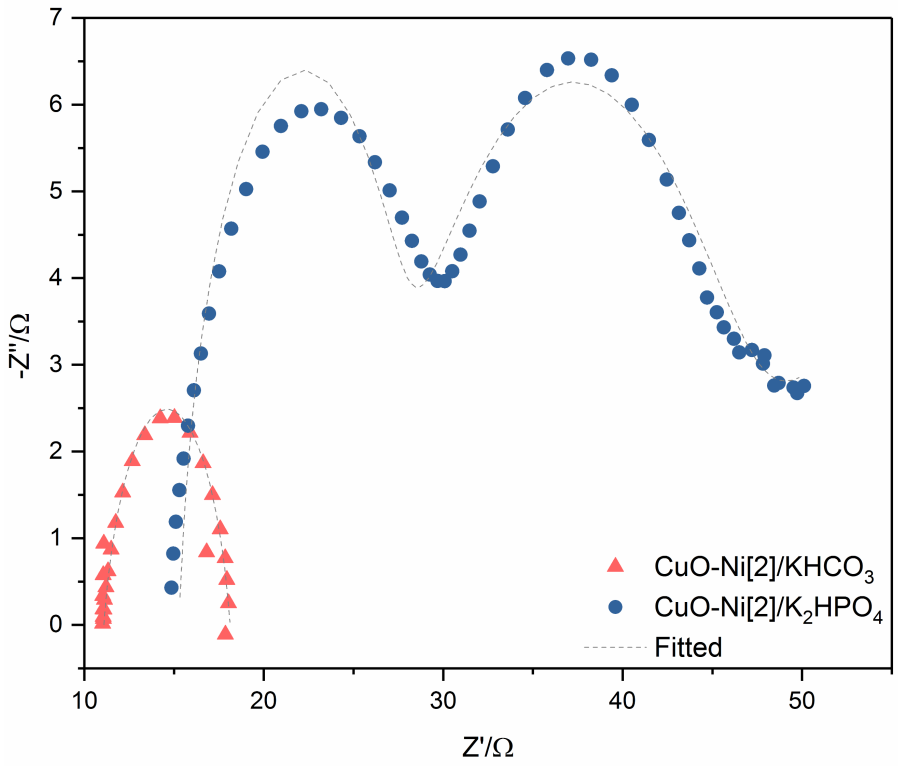

Figure 5-21 - Nyquist plot of CuO-Ni[2] in 0.5 M $KHCO_3$ and 0.5 M K_2HPO_4, carried out in 3-electrode cell, saturated with CO_2 for 30 mins, at a potential of –1.4 V vs. Ag/AgCl.

The existence of two different Nyquist plots suggests that different mechanisms of CO_2 electroreduction took place in the different electrolytes tested here. The presence of two semi circles was also observed by Lates et

al. (gold nanoparticles for CO_2 reduction), who suggested that the existence of two semi circles correspond to two different time constants.[231] The considerably higher charge transfer resistance with K_2HPO_4 suggested that CO_2 electro-reduction took place easily in $KHCO_3$ compared to in K_2HPO_4. It is possible that the presence of dendritic structure observed with $KHCO_3$ assisted in facile electron transfer from CO_2 to the $CO_2^{\bullet-}$.

From the electrochemical reduction of $Cu_{1-x}Ni_xO$, it is evident that doping CuO with Ni has some effect in terms of marginally increasing the production of formic acid at lower overpotentials compared to the unmodified CuO (Figure 5-14). There was a morphology change and the formation of dendritic structures was observed when $Cu_{1-x}Ni_xO$ nanoparticles were used with 0.5 M $KHCO_3$. The use of a phosphate based supporting electrolyte, resulted in poorer activity and selectivity towards CO_2 electroreduction, but the formation of dendrites was not observed and the morphology changed insignificantly compared to pre-electrolysis. To understand if the presence of Ni at the surface, was driving dendrite formation and therefore, potentially improving the catalytic activity, CHFS synthesis of $Cu_{1-x}Ni_xO$ samples was repeated using a single mixer. It was hypothesised that using a quench feed to rapidly cool the nascent nanoparticles had potentially led to dissolution of Ni from the surface of the particles as the particles were rapidly cooled. This may be why the actual Ni content was lower than the expected values for samples synthesised via the dual mixer.

5.3.3 Synthesis of $Cu_{1-x}Ni_xO$ using a single mixer

For this experiment, Ni doped CuO containing a nominal Ni content of 10, 20 and 30 at% were synthesised using a single mixer set up. The copper and nickel salts were prepared as before and fed through the precursor feeds to achieve the desired ratios. The metal salt solution mixture met with a feed of KOH and subsequently the combined feed was mixed with supercritical water in the first CJM. The particles were then cooled in line and then collected

after the exit of the BPR. The slurries were washed and dried as described in Section 2.3. The residence time for the single mixer (from the mixing point to the cooler) was ca. 4.35 s, compared to only 0.76 s for the dual mixer.

The as-prepared powder samples were characterised by PXRD (Figure 5-22). For the CuO-Ni[10]/SM, the CuO peaks matched well with the JCPDS reference 01-089-2529. As the Ni content was increased to 20 and 30 at%, significant peak broadening was observed and application of the Scherrer equation to the PXRD peaks, where the crystallite size decreased from ca. 8.4 nm (10 at% Ni) to 4.5 nm (20 at% Ni) and 2.7 nm (30 at% Ni). The crystallite size of the samples synthesised via the single mixer were comparable to the samples synthesised via the dual mixer, when the actual Ni content was considered. CuO-Ni[40]/DM (Ni content 25.6 at%) gave a crystallite size of 5.8 nm, which was comparable with CuO-Ni[20]/SM (4.5 nm) and CuO-Ni[50]/DM (Ni content 37.5 at%) gave a crystallite size of 2.4 nm, comparable to sample CuO-Ni[30]/SM (2.7 nm). Similar to the samples previously, asymmetry of the (–111) and (111) peaks was observed, particularly for sample CuO-Ni[30]/SM. It is unclear from the PXRD of CuO-Ni[30]/SM sample whether it is conclusively pure phase, as the shoulder of the peak corresponding to the (111) peak could have contributions from a separate NiOOH phase as compared to the reference NiOOH peaks (JCPDS 01-073-1520).

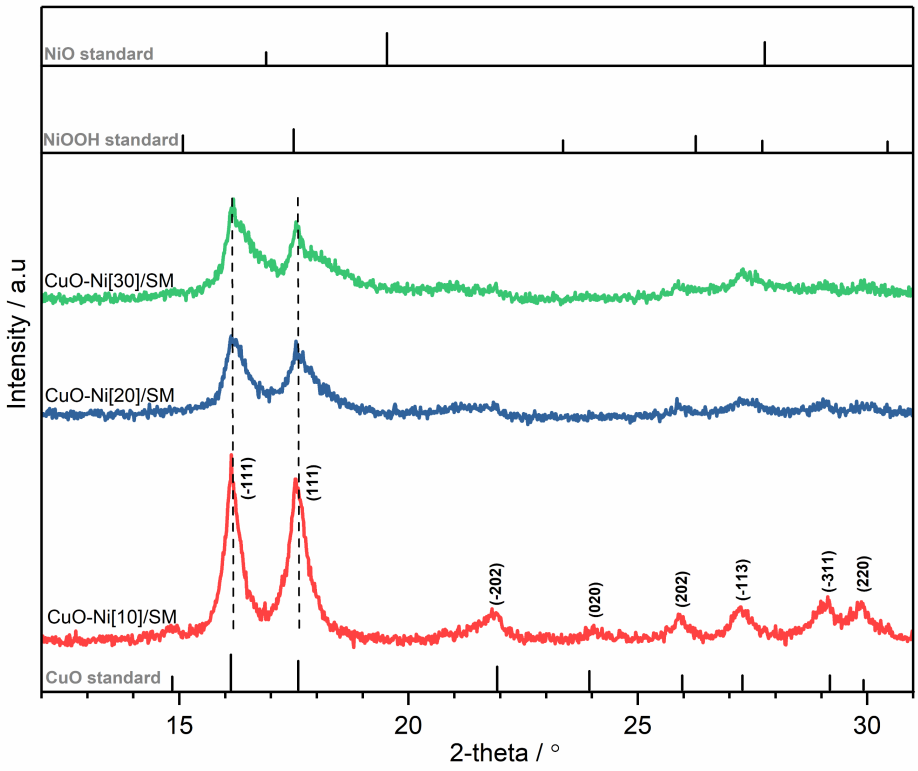

Figure 5-22 - PXRD pattern of as-prepared $Cu_{1-x}Ni_xO$ samples synthesised using single mixer set up. The Ni content was varied in the range 10 to 30 at%. The reference patterns are given for CuO (JCPDS 01-089-2529), NiO (JCPDS 01-071-1179) and NiOOH (JCPDS 01-073-1520).

This suggests that phase segregation of Ni and Cu oxides began to occur at 30 at% Ni for $Cu_{1-x}Ni_xO$ particles synthesised via CHFS. For the samples prepared via the dual mixer, similar behaviour was observed for samples CuO-Ni[40]/DM and CuO-Ni[50]/DM, where the ICP-AES analysis revealed the actual bulk Ni content was 25 and 37 at%, respectively. Compared to co-precipitation syntheses typically seen for Ni doped CuO in the literature and in Section 5.3.1.1, this synthesis technique already allowed for the inclusion of significantly higher Ni content into the CuO structure. ICP-AES revealed the Ni content for sample CuO-Ni[10]/SM was 9 ± 0.3 at%, CuO-Ni[20]/SM was 21 ± 0.5 at% and CuO-Ni[30]/SM was 29 ± 0.4 at%. This also confirmed that dissolution of Ni took place when the dual mixer was used compared to the single mixer, possibly as mixing temperature rapidly cooled or the pH increased (dilution effect). The Pourbaix diagram of the Ni system suggested that in the pH conditions measured some dissolution is possible as Ni^{2+} becomes more stable.[143]

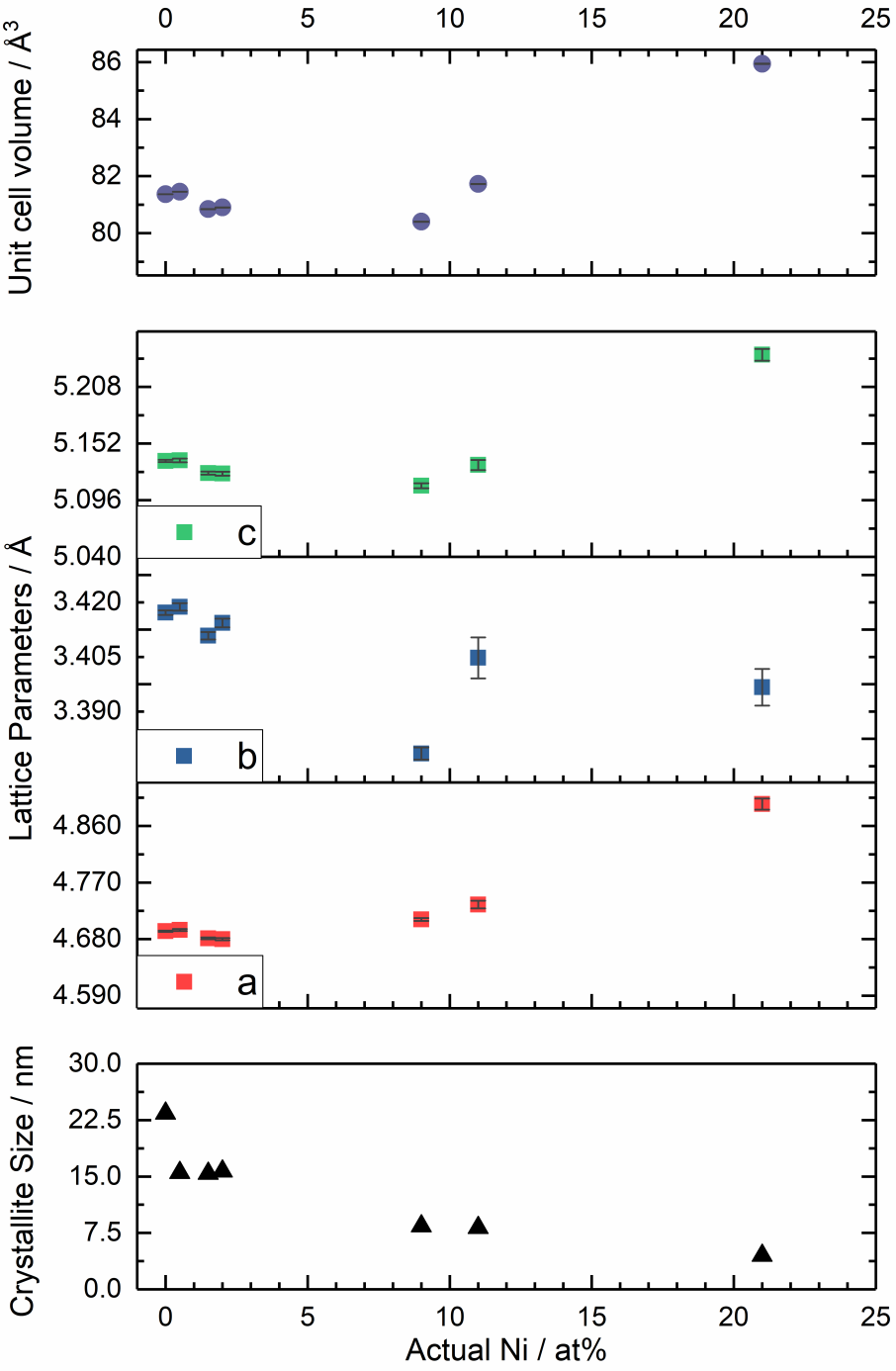

Figure 5-23 - Plot of lattice parameter variation as actual Ni at% is increased within CuO synthesised via CHFS (including dual and single mixer). Lattice parameters are shown as *a* (■), *b* (■) and *c* (■) with crystallite size symbolised as (▲) and unit cell volume as (●).

Rietveld refinement as performed before is plotted in Figure 5-23 where the lattice parameter variations from Ni doped CuO sample synthesised via the double mixer are plotted with samples prepared via the single mixer versus the actual Ni content in the sample (determined by ICP). Refinement of

sample CuO-Ni[30]/SM was not possible due to the broad nature of the peaks. The crystallite size decreased with increasing Ni content within the sample and continued to decrease with higher levels of Ni (ca. 21 at% Ni). The expansion in lattice parameters *a* and *c* is significant. The change in lattice parameter *a* is from 4.692 to 4.894 Å, lattice parameter *b* from 3.424 to 3.404 Å and lattice parameter *c* from 5.134 to 5.239 Å was observed from the undoped CuO to CuO-Ni[21]/SM sample, respectively. This corroborated with the theory mentioned in Section 5.3.1.2 regarding the lattice expansion with decreasing crystallite size. Comparing the crystallite size between single and dual mixer, confirmed that the Ni reduced the particle size by hindering growth of CuO or by enhancing the nucleation rate of CuO, as the crystallite size continued to decrease with samples prepared by the single mixer, despite having a considerably longer residence time than with a dual mixer, where the CuO nanoparticles grew bigger (Chapter 3).

The surface of the particles was analysed by XPS to understand how the abundance of Ni was altered when the particles were synthesised via a single mixer compared to a dual mixer. A summary of the Cu and Ni ratio is given in Table 5-4; comparisons with the dual mixer samples are given for the same nominal content for ease of reference.

Table 5-4 - XPS surface analysis – Cu and Ni ratio for samples synthesised by dual and single mixer as obtained from the survey scans of samples CuO-Ni[10], CuO-Ni[20] and CuO-Ni[30].

XPS surface analysis		**Dual / at%**		**Single / at%**		**EDS (single) / at%**	
Sample	**Nominal Ni at%**	**Cu**	**Ni**	**Cu**	**Ni**	**Cu**	**Ni**
CuO-Ni[10]	10	98.9	1.1 ± 0.9	88.8	11.1 ± 0	96.9	3.1 ± 0.1
CuO-Ni[20]	20	97.1	2.9 ± 0.6	64.1	35.9 ± 0	92.0	8.0 ± 0.5
CuO-Ni[30]	30	80.9	19.1± 0.9	54.8	45.2 ± 0.6	89.8	10.2 ± 0.4

The surface analysis and comparison of the single and dual mixer, showed a significant difference of Ni content compared to the nominal content. Generally, for the dual mixer, the Ni content was significantly lower than expected, indicating the surface was not Ni rich. However, for all samples synthesised via the single mixer, the surface Ni content was considerably higher than the nominal value and that measured by EDS, indicative that the surface was Ni rich as compared to the samples synthesised via the dual mixer. To understand how the Ni content changed from the surface and the near surface of the samples, a depth profile study was conducted. The nickel distribution is given in Figure 5-24a for the dual mixer and Figure 5-24b for the single mixer.

The nickel distribution did not vary significantly over each etch level for samples synthesised via the dual mixer. The general trend showed Ni distributed evenly at the surface and the near surface to bulk of the particles. Figure 5-24b shows samples prepared via the single mixer indicated a Ni rich surface as with etch level the Ni content reduced. As an example, from level 0 to level 4, for sample CuO-Ni[20]/SM the surface Ni content was 35 at% reducing to 24 at% by level 4. This trend was applicable to all samples.

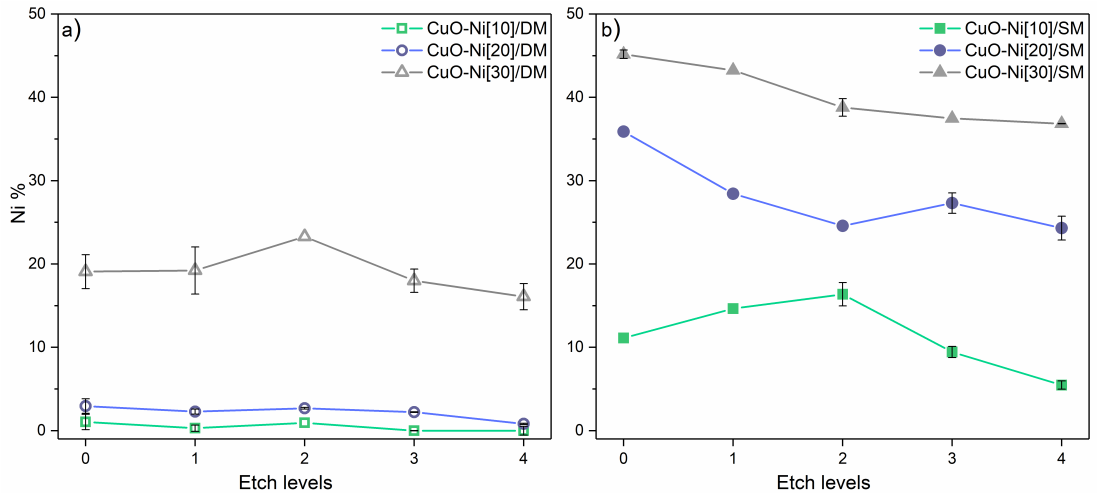

Figure 5-24 – Depth profile analysis of samples CuO-Ni[10], CuO-Ni[20] and CuO-Ni[30]. The Ni content is given versus each etch level for samples synthesised by a) dual and b) single mixer. The etching energy was 2000 eV at each level and the etch depth was 0.22 nm s^{-1}.

The reduction in Ni content with each level (Figure 5-24b) is unlikely to be due to the sputtering or altering of the atomic ratios during the experiment as a similar trend was not observed with samples in Figure 5-24a. The depth profile results are in agreement with the initial hypothesis that the mixer type has a significant effect on the Ni content creating a Ni rich surface with Ni content. For example, CuO-Ni[30]/SM, had ca. 47.5 at% Ni content on the surface prior to sputtering and the depth profile revealed, this dropped to <30 at% Ni at an etch level 4. This was also consistent for samples CuO-Ni[10]/SM and CuO-Ni[20]/SM. In future, this control may allow for some tailoring of the catalytic performance towards CO_2 reduction and to further understand how the Ni content on the surface affected the activity and selectivity as well as driving morphology change.

TEM images (Figure 5-25) showed the formation of cuboid shaped particles for sample CuO-Ni[10]/SM; as the nickel content increased, a decrease in average particle size was observed, CuO-Ni[10]/SM 9.1 nm, CuO-Ni[20]/SM 7.9 nm and CuO-Ni[30]/SM 7.6 nm (average of 100 particles). The particles appeared more well defined in this case compared to samples with the similar Ni content that were synthesised via a dual mixer (Figure 5-25). The high magnification images predominantly showed the (111) plane with a d-spacing of 0.24 nm, which compared well with data from samples synthesised by the dual mixer.

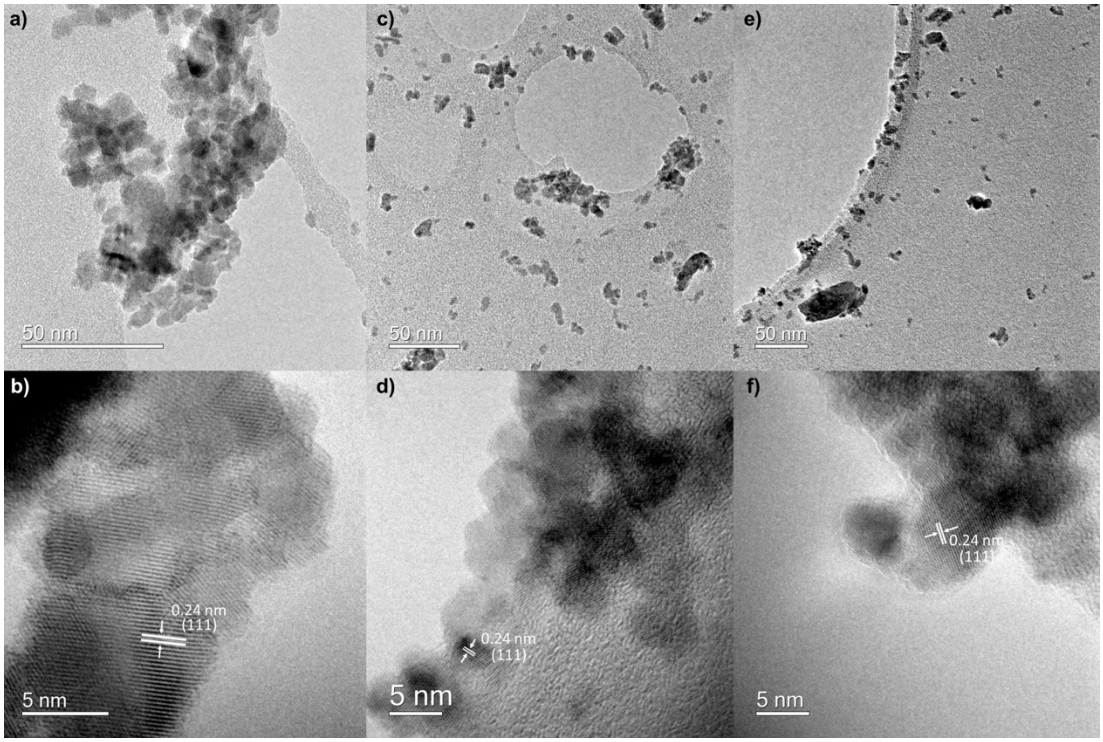

Figure 5-25 - TEM images of $Cu_{1-x}Ni_xO$ nanoparticles synthesised by a single mixer set up – top row shows low resolution images of samples containing a) Ni-10 at%, c) Ni-20 at%, e) Ni-30 at%. Bottom row shows high resolution images corresponding to the particles shown in the top row.

5.3.4 Electrochemical reduction of CO_2 on $Cu_{1-x}Ni_xO$ nanoparticles synthesised via a single mixer

The as-prepared $Cu_{1-x}Ni_xO$ synthesised via CHFS using a single mixer, were prepared as inks following the ink formulation described in Chapter 2. The inks were cast onto glassy carbon and constant potential electrolysis experiments were conducted in the range –1.0 to –1.4 V vs. Ag/AgCl. The main detectable product was found to be HCOOH by ^{1}H NMR. Other products were not observed, consistent with observations with previous samples. The Faradaic efficiency for HCOOH is given in Figure 5-26. The Faradaic efficiency of HCOOH formation for samples prepared via the dual mixer are also given for ease of reference. For sample CuO-Ni[9]/SM, the Faradaic efficiency was the lowest of all samples tested, regardless of the synthesis route at –1.0 V. As the potential was increased to –1.2 V, the Faradaic efficiency increased considerably to 23.1 %. This was the highest

Faradaic efficiency achieved for nickel doped CuO synthesised via CHFS. The Faradaic efficiency for this sample decreased to 1.1 % as the potential was increased to –1.4 V vs. Ag/AgCl.

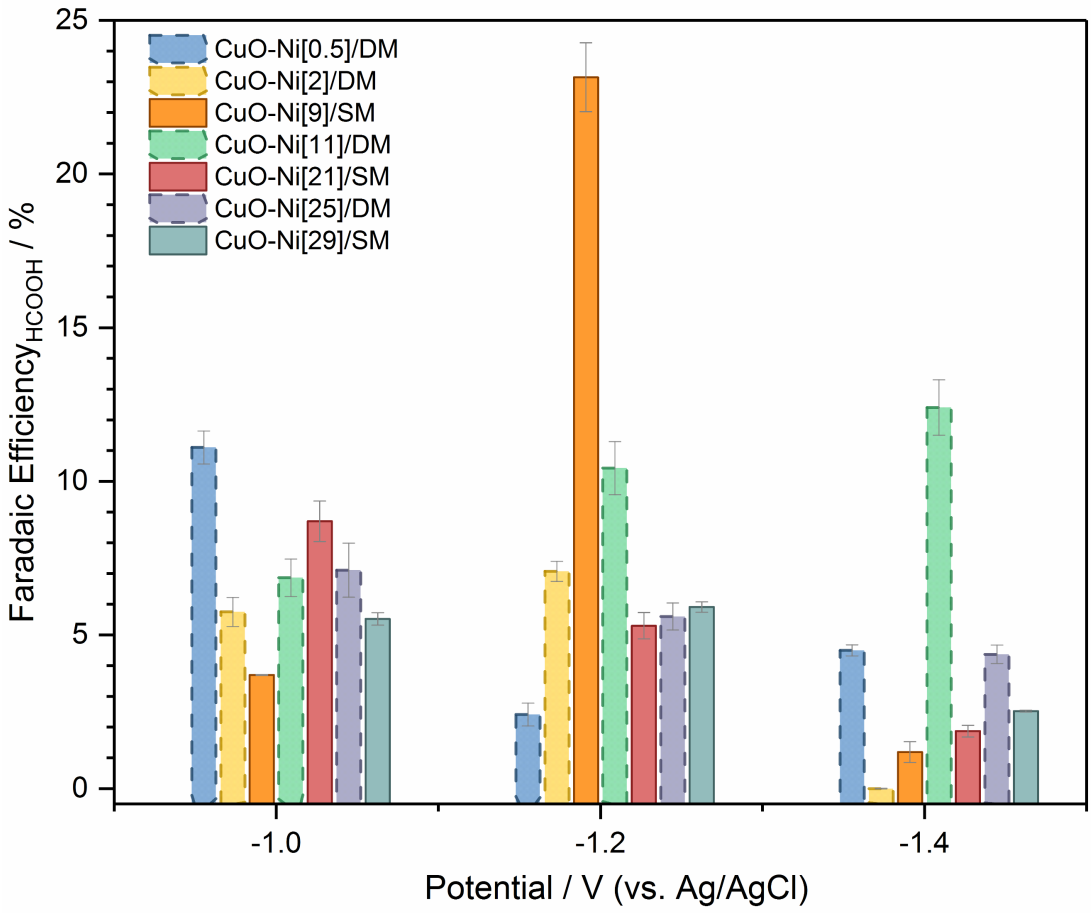

Figure 5-26 - Faradaic efficiency of HCOOH formation of samples containing 9 at%, 21 at% and 29 at% (as synthesised via the single mixer set up) in 0.5 M $KHCO_3$ saturated with CO_2, held in the range –1.0 to –1.4 V vs. Ag/AgCl. The Faradaic efficiency of HCOOH formation for the samples synthesised via the dual mixer is given for reference.

As the nickel content was increased (for samples synthesised via a single mixer), the Faradaic efficiency was higher for sample CuO-Ni[21]/SM containing 21 at% Ni at –1.0 V. For this sample, the Faradaic efficiency decreased with increasing potential. Similarly, sample CuO-Ni[29]/SM, achieved unremarkable Faradaic efficiency for HCOOH formation at all potentials tested. The data suggests that a high Ni content within the catalyst layer does not result in a particularly active or selective catalyst. At low Ni content, the catalyst generally does not achieve particularly high Faradaic

efficiency with the exception of CuO-Ni[0.5]/DM and CuO-Ni[2]/DM at lower overpotential. It appeared an optimum Ni content was required to balance reducing overpotential without reducing the number of active sites significantly.

The catalyst layer was examined by SEM to study the morphological changes pre- and post-electrolysis (Figure 5-27). Figure 5-27 a-c shows the catalysts pre-electrolysis. The catalyst layer showed even distribution of the catalyst on the glassy carbon electrode consistent with previous observations.

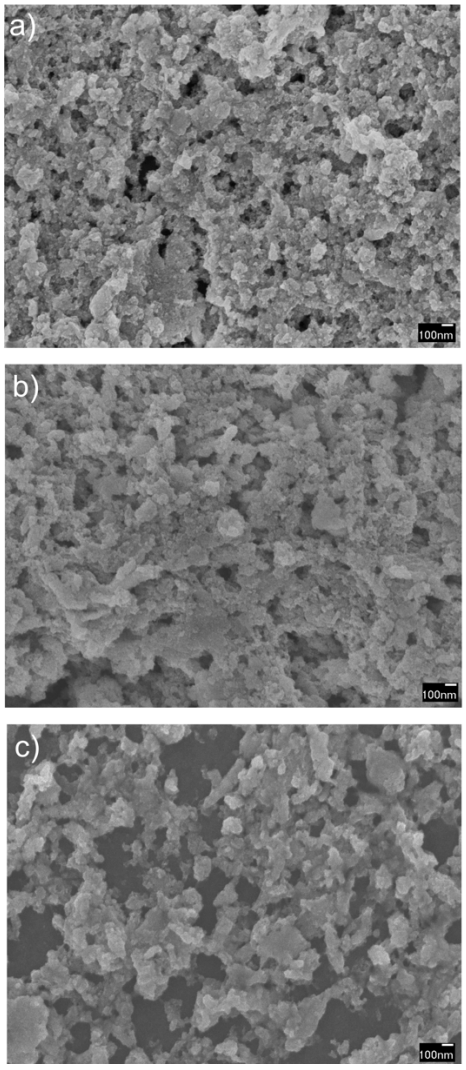

Figure 5-27 – Pre-electrolysis SEM images of Ni doped CuO samples synthesised via the single mixer set up for a) 9 at%, b) 11 at% and c) 21 at% Ni.

Figure 5-28 a-c shows the post electrolysis catalyst layer with increasing potential from –1.0 V (Figure 5-28a), to –1.2 V (Figure 5-28b) and –1.4 V (Figure 5-28c) for sample CuO-Ni[9]. The morphology did not change significantly for samples at –1.0 and –1.2 V. There was a potential dependency observed in this case, where the formation of dendrites was observed in the sample at –1.4 V. This is not consistent with previous observations where dendrite formation was observed for samples prepared via the dual mixer at –1.0 V vs. Ag/AgCl. Morphology change dependent on the potential has been observed in the case of dendrites where it has been shown that there is an overpotential required to begin nucleating and forming dendritic structures.[232]

Figure 5-28 d-e shows the catalyst layers post electrolysis with increasing Ni content from 9 at% Ni (Figure 5-28d), 21 at% Ni (Figure 5-28e) and 29 at% Ni (Figure 5-28f) at –1.2 V. With increasing nickel, dendrite formation was observed for potentials lower than –1.4 V. This observation is also consistent with previous studies where dendrite formation was promoted by the presence of nickel. The dendrites in sample with 21 at% Ni were more well-defined compared to sample with 29 at% Ni. The Faradaic efficiency observed for sample CuO-Ni[9]/SM was considerably higher than other samples and in this particular case, dendrite formation was not observed (Figure 5-27d). It is possible that dendrite formation hinders the catalytic performance towards CO_2 electroreduction. The catalytic performance did not improve with the use of PO_4 based electrolyte where dendrite formation was not observed. The activity and selectivity of CO_2 reduction dependence on the morphology is a tenuous link as dendrite formation does not appear to be consistent.

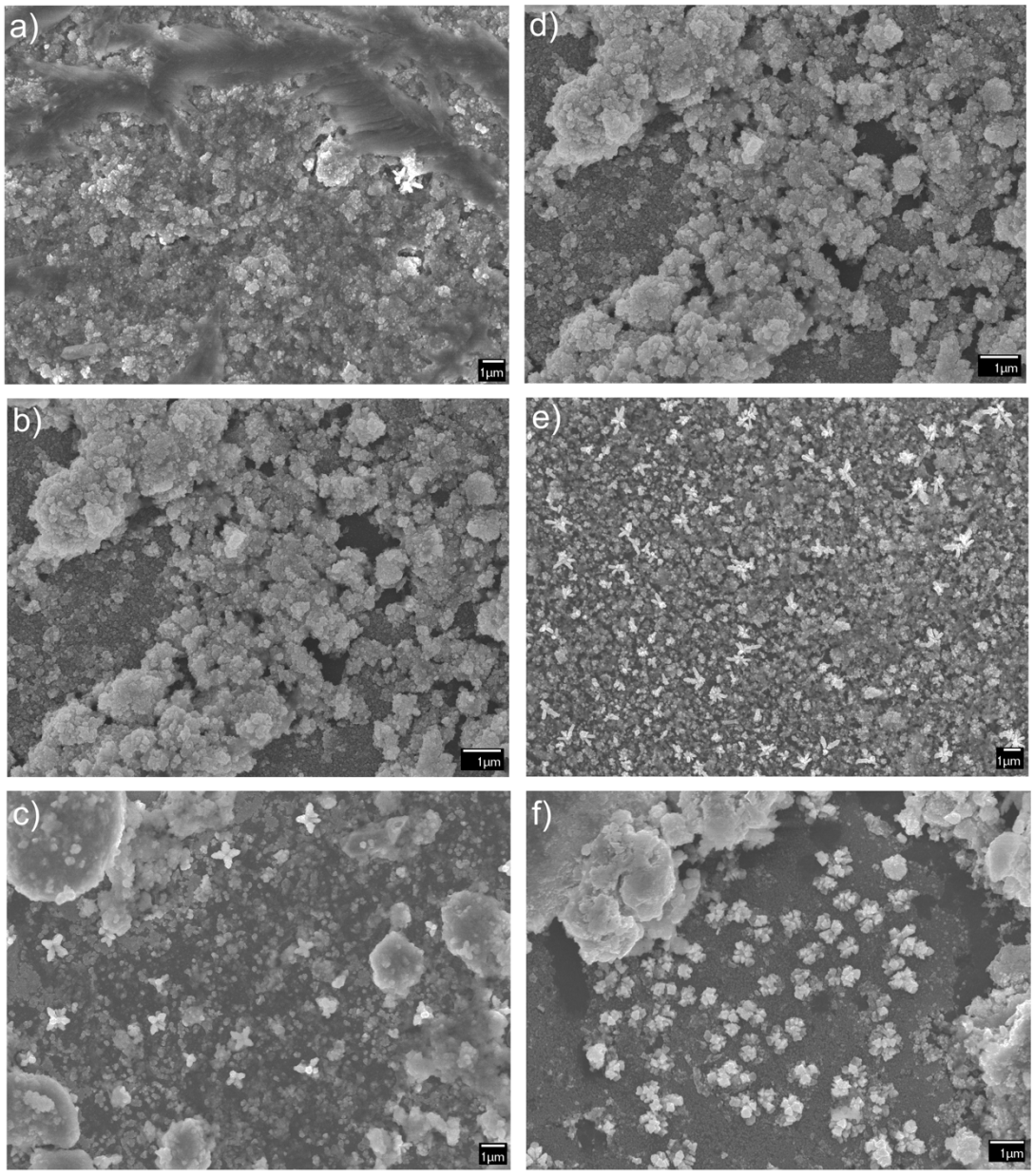

Figure 5-28 – Post electrolysis SEM images for CuO-Ni[9] sample at a) –1.0, b) –1.2 and c) –1.4 V. And the right row shows the post electrolysis SEM images for samples held at –1.2 V containing d) 9 at% Ni, e) 21 at% Ni and f) 29 at% Ni.

To further understand the impact of dendritic growth with Ni doped samples and the presence of Ni in the catalyst layer on the kinetics of CO_2 reduction, Tafel analysis was carried out (Figure 5-29). From the current-potential curves, data was extracted to reveal the overpotential versus log i curve. Linear regression analysis provided the Tafel slope as plotted below for all the samples tested.

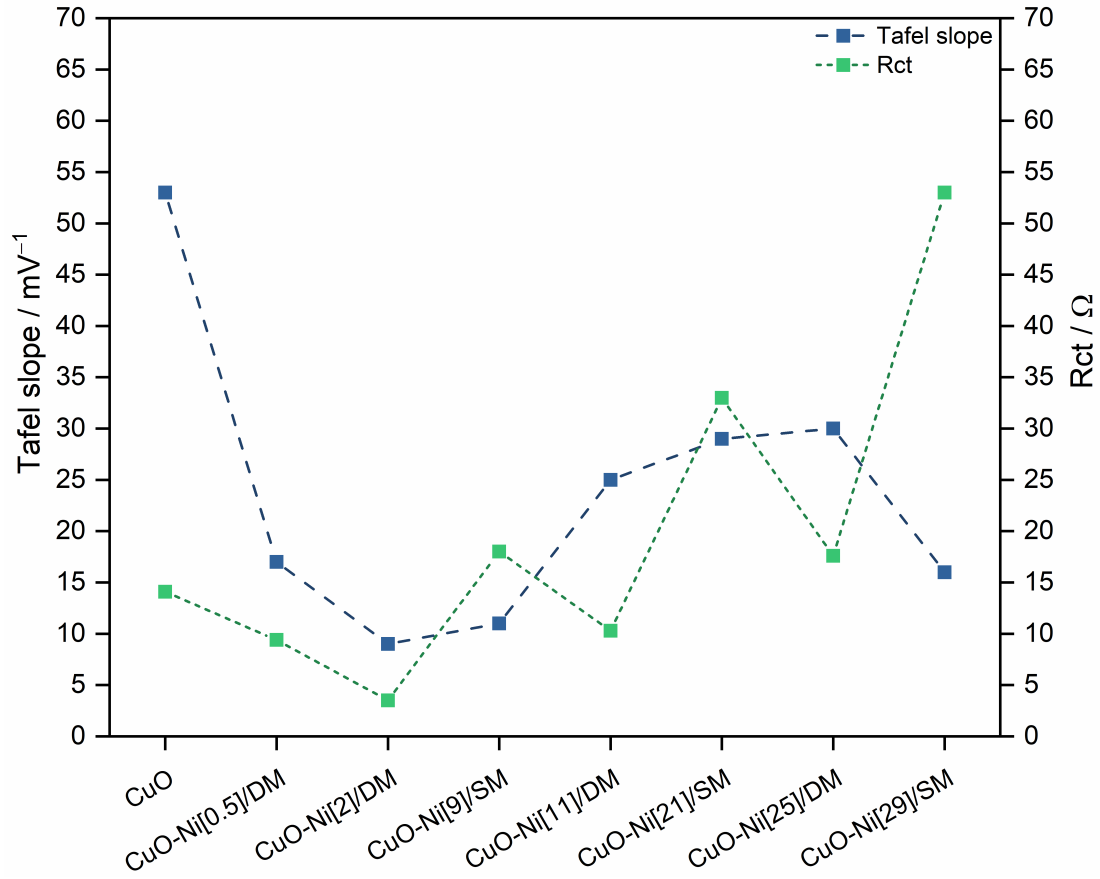

Figure 5-29 – Plot of Tafel slope values obtained from the potential-current curves for all Ni doped CuO samples tested (as synthesised via CHFS). The charge transfer resistance values (Rct) obtained from impedance analysis are plotted.

The CuO sample gave a Tafel slope of 53 mV dec^{-1}, which was considerably lower than observed for similar samples. Previous studies have obtained values of 116 mV dec^{-1} for the Tafel slope with annealed Cu films.[62] The reduction of CO_2 to $CO_2^{-\bullet}$ is commonly thought to be the rate determining step, therefore, the smaller the Tafel slope, the faster this electron transfer takes place. 53 mV dec^{-1} is considerably faster than values reported in the literature, which may also corroborate further with observations that the Faradaic efficiency is significantly higher for the CuO sample (Figure 5-14). The nickel modified sample CuO-Ni[0.5]/DM revealed a further reduction in the Tafel slope, which was also observed with samples containing 2 at% Ni and 11 at% Ni. As the nickel content was further increased to 25 at%, the Tafel slope increased to 30 mV dec^{-1}, suggesting an optimum Ni content was required to promote faster electron transfer. This was also consistent with the

Faradaic efficiency data (Figure 5-14). The samples synthesised via the single mixer revealed higher Tafel slopes for samples containing >20 at% Ni. The Tafel slope did not vary significantly for the sample with 9 at% Ni. The observations for single mixer samples was also consistent with double mixer samples containing higher Ni content, which further supports the idea that higher Ni content is not conducive to faster electron transfer. This also confirms observations from the Faradaic efficiency data that a Ni rich surface does not improve the catalytic activity and selectivity.

To probe the charge transfer processes, impedance measurements were conducted on all samples in 0.5 M $KHCO_3$. The simulated charge transfer resistance, Rct values are plotted with the Tafel slope (Figure 5-29). The Rct values were complimentary of the changes observed with the Tafel slope, further confirming that the addition of an optimal Ni is beneficial to increasing the electron transfer, however, the addition of particularly high amounts of Ni appears to be detrimental to the kinetics of CO_2 reduction.

5.4 Conclusions and future work

In summary, this was the first reported investigation of Ni doped CuO for the electroreduction of CO_2. Ni doped CuO was successfully synthesised via CHFS (in the range 0 to 50 at% Ni) using the dual mixer, where above 30 at% Ni inclusion led to significantly broad peaks, which indicated that phase segregation might have occurred (CuO and NiOOH). The particle size decreased with increasing Ni content, where Ni enhanced the nucleation rate or hinder CuO growth in conjunction with the turbulent mixing environment within the CJM. ICP-AES of the Ni doped CuO, synthesised via the dual mixer, showed a significant discrepancy between the nominal and actual Ni content, caused from dissolution or leaching of the Ni from the host structure as the particles were rapidly cooled.

The Ni doped CuO synthesised via the dual mixer were then tested for the electrochemical reduction of CO_2. Largely, the Faradaic efficiency achieved for HCOOH production was unremarkable (sub-25 %) compared to the undoped CuO. However, marginally higher Faradaic efficiencies were observed for the samples with lower Ni content, at lower overpotentials than the undoped CuO. Morphology change was observed post electrolysis, where dendritic growth was observed with samples with Ni >0.5 at%. The formation of dendrites was linked to the presence of carbonate anion in the $KHCO_3$ electrolyte and Ni. This was confirmed by using K_2HPO_4 as an electrolyte which showed no morphological change during catalysis, however, the Faradaic efficiency was significantly lowered in a phosphate based electrolyte.

Ni doped CuO was synthesised via a single mixer to verify if a Ni rich surface would be beneficial for the electroreduction of CO_2 and how this could affect dendrite growth. Depth profile analysis revealed a Ni rich surface for all samples synthesised via the single mixer compared to the dual mixer. When the samples were tested, the Faradaic efficiency was low at particularly high Ni content suggesting a Ni rich surface was not optimum for CO_2 reduction. At –1.2 V vs. Ag/AgCl, Ni doped CuO with 9 at% Ni had the highest Faradic efficiency for Ni-CuO based catalyst (23 %). Tafel and impedance analysis further supported that an optimum Ni was required to positively enhance CO_2 reduction as electron transfer was faster for samples with lower amounts of Ni (<11 at%).

Further understanding of the Ni distribution within the CuO host lattice is required. Synchrotron based studies, including EXAFS and PXRD, are likely to give an indication of the location of Ni within CuO. This would highlight structure-property and composition relationships, which could be used to alter the synthesis parameters via CHFS to improve the catalytic performance. Similarly, in the literature, other doped elements (Zn, Sn and

Fe) have been incorporated in the CuO structure via co-precipitation but have not been synthesised via CHFS to date. Other dopants need to be screened for their catalytic performance to find a system, which would either significantly improve the Faradaic efficiency, lower the overpotential and/or affect the product distribution.

Furthermore, the formation of dendrites and other morphological changes in situ, is not understood currently. In order to improve the catalyst structure, stability and activity, *in operando* type experiments are required where the phase changes of Ni doped CuO can be understood during real time experiments when a potential bias is applied. Similarly, the mechanism of morphological change and how this affects the catalytic activity needs to be better understood to either facilitate particular morphology change or attempt to hinder the structural changes, to enhance CO_2 reduction. A possible way to understand if dendrites favour CO_2 reduction is to electrochemically grow copper-based dendrites on glassy carbon and subsequently test these for CO_2 reduction. This would provide an insight into the role of morphology dependence on CO_2 reduction.

Chapter 6. Rotating Ring-Disk Study of the Electrochemical Reduction of Carbon Dioxide

6.1 Introduction

Products generated from the electrochemical reduction of CO_2 have been detected and analysed by a number of ex-situ techniques including ^{1}H NMR, GC-MS, mass spectrometry, infrared spectroscopy and high pressure liquid chromatography.[233,234] The analysis or identification of products, can pose a challenge due to the proximity of the CO_2 reduction and hydrogen evolution reaction. Furthermore, the amount of product formed is typically very low (μM range) and their quick diffusion from the catalyst surface through the cell determines low concentrations. This means observing current-potential features in aqueous voltammetry curves can be difficult and becomes a bigger challenge as the carbon dioxide in solution can lower the pH of the medium, so it is acidic.[231,235–237] Typically, analysis is carried out at a fixed potential and products are generated for a period of time and then analysed by the analytical methods described above. Current catalysts that have been investigated are also prone to degradation over time; their use can result in variation of product distribution over the testing period. There is a need for simpler methods, which can detect products in-situ, with higher sensitivity and allow reaction mechanisms and kinetics to be studied. In-situ techniques such as scanning electrochemical microscopy (SECM) with a substrate generation/tip collection (SG/TC) mode have been utilised for screening catalysts prior to bulk electrolysis for CO_2 reduction.[233] However, the collection efficiency is significantly lower for SG/TC mode than the TG/SC mode (tip generator/substrate collection) and there are some challenges in controlling the tip/substrate separation distance, which can affect the image

resolution, especially compared to Atomic Force Microscopy (AFM) and Scanning Tunnelling Microscopy (STM).[238] Some other infra-red spectroscopy based in-situ techniques have been utilised but these have been limited to understand how the catalyst phase changes during the electroreduction of carbon dioxide.[239]

The solubility of CO_2 in aqueous solutions is low (0.08 M) and therefore, mass transport of the reactant to the electrode surface can be a limiting factor. The use of hydrodynamic methods to control the mass transport to increase the transfer rate of reactants to the electrode surface can be beneficial. High-throughput screening of nanocatalysts and their catalytic performance prior to large-scale electrochemical reduction of CO_2 is required and would be highly beneficial to their development, since large-scale and high-throughput synthesis of nanocatalysts is currently possible through methods such as CHFS.

Products from electrochemical CO_2 conversion include formic acid, alcohols and CO, which are electro active chemicals that can be detected electrochemically.[233] Rotating Ring-Disk Electrode (RRDE), developed in the late 1960s, is a very powerful technique for analysing products, side products and short-lived intermediates.[35] The RRDE set up comprises of a disk electrode surrounded by a concentric ring electrode in a cylindrical holder. The disk and ring electrode are separated by an insulating material. A schematic representation is shown in Figure 6-1.

Figure 6-1 - Schematic of Rotating Ring Desk Electrode (RRDE), ω refers to angular rotation. Adapted from Li. et al.[240]

This is a hydrodynamic method and reaches steady-state conditions relatively quickly, allowing high precision measurements with large mass transfer rates compared to stationary electrodes, which rely on diffusion alone.[35] In a stagnant electrolyte, the rate of reaction at the electrode surface is controlled by kinetics and mass transfer of the reactants to and from the electrode. The RRDE allows rigorous experimental control of the mass transport rate so as to isolate the kinetic current by rotating the electrode and introducing forced convection. Reactants are dragged to the disk electrode and the product(s) formed at the disk electrode are swept outwards to the ring electrode by convection caused by the rotating electrode and can be subsequently detected at the ring. This is illustrated in the schematic in Figure 6-2.[35] The gap between the disk and ring and the size of the ring can alter how much of the product the ring can detect and is described as the collection efficiency, N (Equation 6.1).

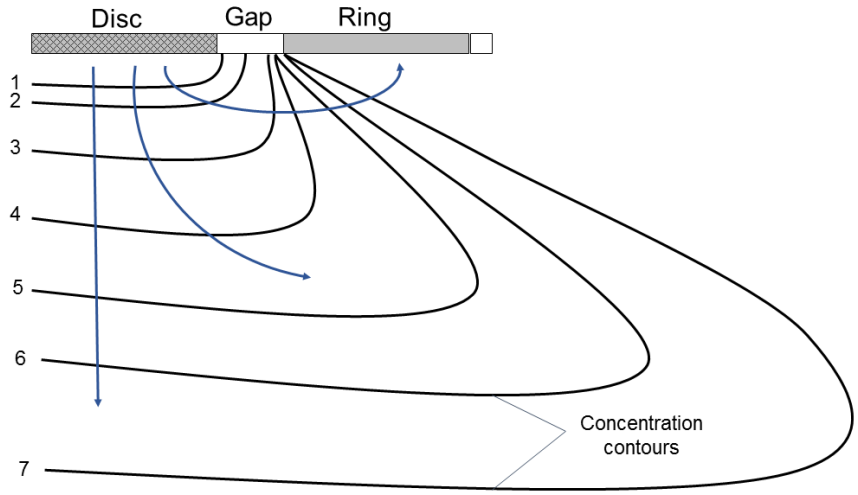

Figure 6-2 – Concentration profile of species R at an RRDE. Concentration increase from 1 to 7. Reproduced with permission from Bard et al.[35]

$$N = \frac{-i_R}{i_D} \qquad \text{Equation 6.1}$$

The hydrodynamics of the rotating disk and rotating ring-disk electrode has been theoretically treated and is based on the diffusion layer approach.[241] The concentration profiles can be described (in three dimensions), based on convection and diffusion (Fick's law). This can be described in cylindrical polar coordinates appropriate to the RDE by Equation 6.2:

$$\frac{\partial c}{\partial t} = D\left(\frac{\partial^2 c}{\partial z^2} + \frac{\partial^2 c}{\partial r^2} + \frac{1}{r}\frac{\partial c}{\partial r} + \frac{\partial^2 c}{\partial \theta^2}\right) - \left(v_r\frac{\partial c}{\partial r} + \frac{v_\theta}{r}\frac{\partial c}{\partial \theta} + v_z\frac{\partial c}{\partial z}\right) \qquad \text{Equation 6.2}$$

This is experimentally simplified to:

$$D\frac{\partial^2 c}{\partial z^2} - v_z\frac{\partial c}{\partial z} = 0 \qquad \text{Equation 6.3}$$

Solving this equation with appropriate boundary conditions, leads to a concentration profile as shown in Figure 6-3. This shows that convection becomes less important near the surface, where there is a stagnant region and diffusion dominates. Away from the electrode, in the bulk solution,

convection dominates and so the concentration does not vary. Levich's quantitative description of the hydrodynamics results in:

$$\partial = \frac{1.61 D^{1/3} \nu^{1/6}}{\omega^{1/2}} \qquad \text{Equation 6.4}$$

Figure 6-3 – Nernst diffusion layer model for the oxidation of R to O at a rotating disk electrode. Adapted from Pletcher.[241]

Equation 6.4 shows that the Nernst diffusion layer, ∂, becomes thinner with increasing rotation rate, where convection becomes more important. This concept allows for a derivation of the current density at the RDE for potentials where the electrode reaction is controlled by mass transport. At such a potential, the surface concentration of the electroactive species is zero so the limiting current density is given by:

$$j_L = nFAD\left(\frac{\partial c}{\partial x}\right)_{x=0} = nFAD\frac{c}{\partial} \qquad \text{Equation 6.5}$$

Combined with Equation 6.4, this leads to the Levich equation:[35,241]

$$j_L = 0.62 \frac{nFAD^{2/3}c}{v^{1/6}} \omega^{1/2}$$ Equation 6.6

where J_L is the limiting current, n is the number of moles of electrons transferred, F is the Faraday constant, D is the diffusion coefficient, ω is the angular rotation rate of the electrode, v is the kinematic viscosity and c is the analyte concentration. The Levich equation indicates that a plot of j_L and $\omega^{1/2}$, which is linear (and passes through the origin), shows mass transfer control. Deviation from this straight line indicates that there is a kinetic limitation involved and that the reaction is electrochemically irreversible. The Koutecky-Levich equation below can be used to obtain the kinetic current density:

$$\frac{1}{j} = \frac{1}{j_k} + \frac{1}{j_L} = \frac{1}{j_k} + \frac{1}{0.62nFAD^{2/3}\omega^{1/2}v^{-1/6}c}$$ Equation 6.7

Herein, j_k represents the current density, in the absence of mass-transfer effects. In other words, it describes the kinetic current at an infinite rotation rate and can be obtained from a plot of inverse current vs. inverse rotation rate. Extrapolation of the linear plot yields the kinetic current, j_k, which would be observed in the absence of mass transport limitations. Through this analysis, it is possible to determine the rate constant and the number of electrons transferred in the reaction and hence begin to understand the mechanism pathway.

Typically, for the RRDE, experiments may be conducted in the following ways:[242,243]

1. Current-potential curves are measured at the disk electrode, whilst the ring is held at a constant potential, where the intermediates or products can be detected as they are reduced or oxidised.
2. The disk can be held at a potential of interest and the ring electrode cycled through a range of potentials to identify products and intermediates.

3. The disk and ring electrodes can be held at a constant potential to allow the intermediates or fragments to undergo further electron transfer.

RRDE has been used extensively to study the oxygen evolution reactions (OER) and oxygen reduction reactions (ORR), however, its use for the electrochemical reduction of CO_2 remains limited. Aoki and Nogami used SnO_2 as a disk electrode and detected HCOOH on a Pt ring.[236] Zhang et al. catalysed the CO_2 reaction with cobalt tetramethylpyridoporphyrazine modified on a glassy carbon disk electrode and detected CO on the Pt ring.[235] Recently, Lates et al. used gold based nanoparticles on disk electrodes to show CO detection on Pt.[231] Through a combination of RRDE measurements and impedance spectroscopy, the authors presented a potential mechanism of CO_2 conversion to CO on gold.

To the author's knowledge, the use of RRDE technique has not been used with copper-based catalysts, which remains an appealing catalyst due to its high energetic efficiency, compared to other catalysts. The only published study using a hydrodynamic based method with copper used a RDE coupled with an online-GC to characterise products.[237] Herein, a RRDE set up was designed, validated and tested for CO_2 reduction on copper-based electrocatalysts. The catalysts tested in this chapter have been previously included in Chapter 4 and 5. The efficacy of the RRDE for electrochemical reduction of CO_2 was evaluated by performing linear sweep voltammetry (LSV), collection experiments, chronoamperometry and cyclic voltammetry.

6.2 Materials and methods

6.2.1 Cell set up

The cell set up is described in detail in Chapter 2, Section 2.6.6.2.

6.2.2 Electrode preparation

The RRDE was cleaned as described elsewhere for the glassy carbon sheet electrode (Chapter 2). The inks were sonicated prior to drop coating on to the electrode, to ensure the inks were completely homogenous. Typically, 30 μL of ink was drop coated on the glassy carbon surface, ensuring the ink did not flow on to the ring or the gap between the disk and ring, to have a loading of 0.3 mg cm^{-2}.

6.2.3 Collection efficiency test

To determine the collection efficiency, a clean RRDE was placed in a solution of 10 mM of $K_3[Fe(CN)_6]$ in 1 M KNO_3. The glassy carbon was not drop coated with the ink, as the presence of the catalyst could influence the outcome of the collection efficiency of the RRDE. The RRDE was operated at rotation rates of 100, 600, 1100, 1600 and 2100 rpm. The RRDE was cycled in the range –0.2 and 0.6 V vs. Ag/AgCl at each rotation rate. The collection efficiency was measured as a ratio of the limiting anodic and cathodic current.

6.2.4 Product calibration

The purpose of the product calibration was discussed in Section 2.6.6.4. Prior to product calibration, the blank Pt ring was cycled in 1 M H_2SO_4 range (0 to 1.5 V vs. Ag/AgCl), 0.5 M $KHCO_3$ and 0.5 M K_2HPO_4 (range –0.65 to 0.5 V vs. Ag/AgCl) to evaluate its electrochemical behaviour without the addition of formic acid and methanol.

For formic acid calibration, 125 mM formic acid was added into 0.5 M $KHCO_3$ or K_2HPO_4, saturated with CO_2. Cyclic voltammetry was performed in the range –0.55 to 0.6 V vs. Ag/AgCl at scan rates of 20, 50 and 100 mV s^{-1}. For methanol calibration, 12 mM methanol was added into 0.5 M $KHCO_3$ or

K_2HPO_4 saturated with CO_2. The cyclic voltammetry was performed in the range –0.55 to 0.6 V vs. Ag/AgCl at the same scan rates as for formic acid and rotation rates in the range 0 to 2100 rpm.

6.2.5 Rotating ring-disk measurements

For each electroreduction experiment, 150 mL of fresh electrolyte (0.5 M $KHCO_3$) was added. The catalyst coated RRDE was immersed in the electrolyte and the electrolyte was degassed with CO_2 for 30 mins. Cyclic voltammetry was performed on the disk, in the range 0 to –1.45 V vs. Ag/AgCl. The ring was held at various potentials (in the range 0.8 to –1.0 V), where products were expected. Chronoamperometric experiments were also conducted, where the disk was held at the same potentials, as mentioned in Section 2.6.3, in the range 0 to –1.4 V and the ring was also held at the relevant potentials to detect products from CO_2 electroreduction.

6.3 Results and Discussion

6.3.1 Collection Efficiency

The collection efficiency test was performed to determine the efficiency of the ring to detect the product (Figure 6-4). A well-known one electron redox reaction was used to conduct this test. The glassy carbon was cycled between –0.2 and 0.6 V at rotation rates in the range 0 to 2100 rpm, whilst the ring was held at such a potential where the product was reduced (0.2 V vs. Ag/AgCl). The limiting current was obtained at 0.6 V and plotted versus the rotation rate (Figure 6-4b).

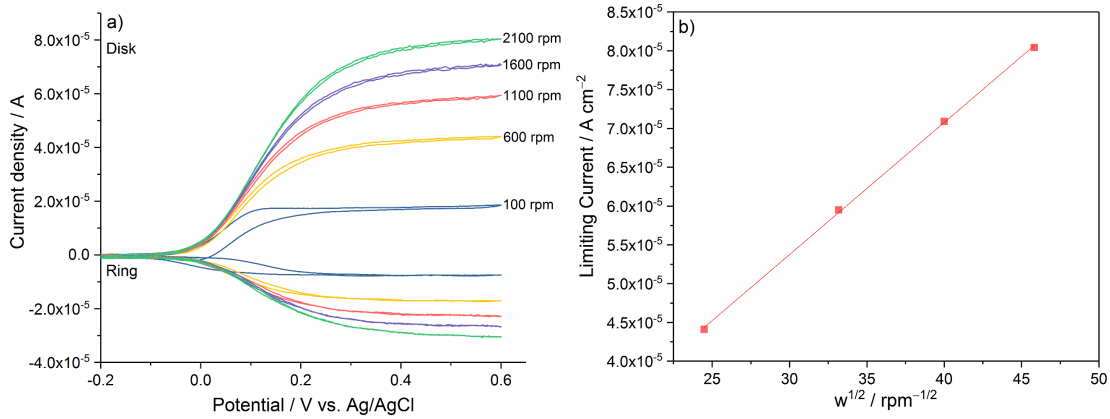

Figure 6-4 - a) Cyclic voltammograms of the ferro/ferricyanide reaction at the disk and ring electrode at rotation rates of 100, 600, 1100, 1600 and 2100 rpm. b) Linear plot of limiting disk current (at 0.6 V) plotted versus the square root of the rotation rates. 100 rpm data point is not included as steady state conditions are not reached.

There was a linear dependency on the limiting current and the rotation rate. The linear fit confirms that the ferro/ferricyanide reactions were mass transport limited at 0.6 V and were electrochemically reversible, as expected. Furthermore, the diffusion coefficient for the ferricyanide was 3.98 x 10^{-6} cm^2 s^{-1}, which agreed well with literature.[244] This further confirmed that the electrochemical set up was operating optimally.

The collection efficiency value is the ratio of the disk and ring limiting current, which presented a collection efficiency of 38 % at all rotation rates, which agreed well with the theoretical collection efficiency value (37 %).[245] The ferro/ferricyanide redox couple is a well-defined reaction and is therefore an ideal way of evaluating that the RRDE set up is operating correctly. There can be issues relating to electrical "cross-talk" between the disk and ring electrode. This occurs when there is uncompensated potential change of one electrode due to change in the current of another, leading to misinterpretation of results in a four-electrode system.[246] This was not observed from the disk and ring potential-current curves obtained from the ferro/ferricyanide redox couple and the potential-current results for ferro/ferricyanide agreed well with literature.

6.3.2 Pt electrode characterisation

The Pt ring electrode was examined independently in H_2SO_4, $KHCO_3$ and K_2HPO_4 to electrochemically characterise its behaviour in three different electrolytes, prior to addition of products derived from the electrochemical reduction of CO_2 (Figure 6-5). H_2SO_4 was chosen as a reference to verify the features observed in the cyclic voltammograms, as Pt has been studied extensively in this electrolyte and its features are well assigned in the literature.[247] The typical features as observed for Pt in H_2SO_4 were observed. In the forward oxidation scan, oxide formation was observed in a potential range 0.75 to 1.25 V vs. Ag/AgCl.

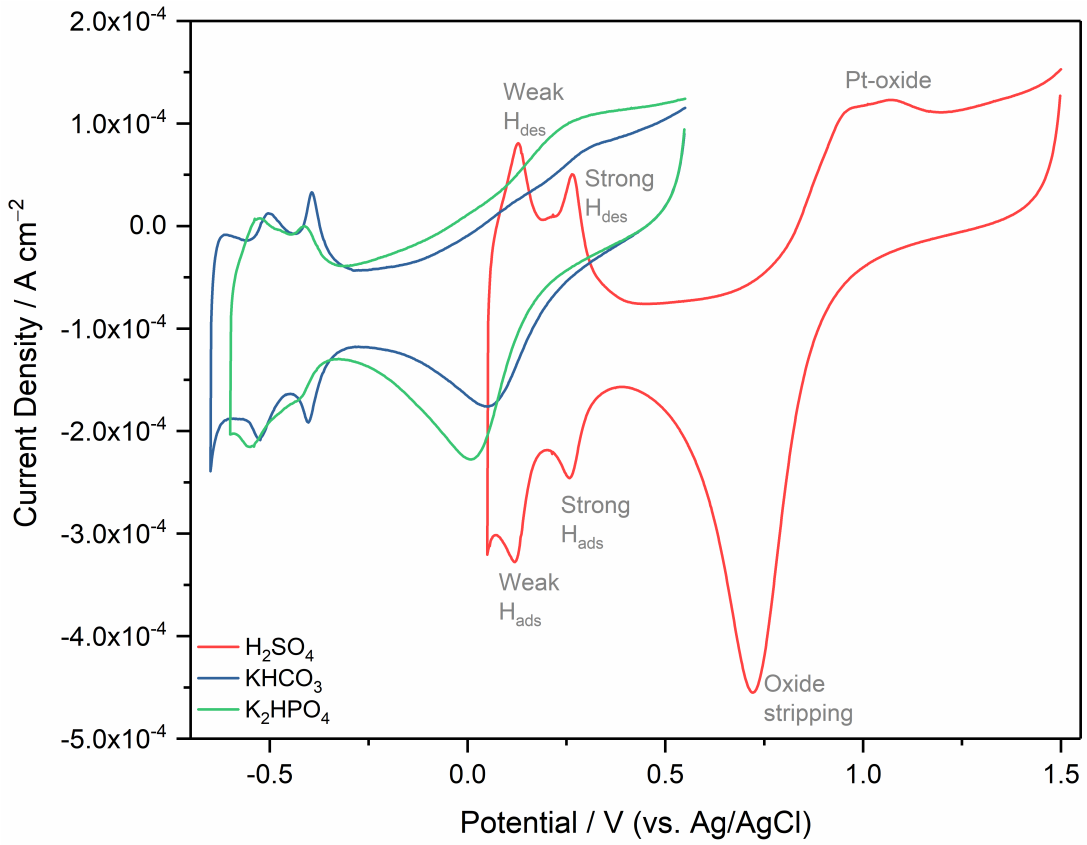

Figure 6-5 – Cyclic voltammograms of Pt ring electrode in 1 M H_2SO_4, 0.5 M $KHCO_3$ and 0.5 M K_2HPO_4 at a scan rate of 100 mV s^{-1}

During the reverse reduction scan, the oxide stripping peak was observed at 0.7 V vs. Ag/AgCl and the Pt – H adsorption region was observed in the range 0.05 to 0.3 V vs. Ag/AgCl, which subsequently desorbed as highlighted

in Figure 6-5. This was typical of a polycrystalline Pt surface cyclic voltammogram in 1 M H_2SO_4. When the Pt electrode was cycled in carbonate and phosphate based electrolytes of a neutral to alkaline pH (0.5 M $KHCO_3$, pH 8.6 and 0.5 M K_2HPO_4, pH 9.3), a shift to more negative potentials was observed (Figure 6-5), which follows the Nernst equation. This is in alignment with observations in the literature, where a similar shift is observed with more neutral and alkaline electrolytes.[247] Equally, the current density is significantly reduced for the Pt electrode in $KHCO_3$ and K_2HPO_4 compared to H_2SO_4. The cyclic voltammograms for Pt electrode in $KHCO_3$ and K_2HPO_4 are shown in more detail in Figure 6-6 for ease of reference.

It is evident from the cyclic voltammograms that the electrolyte environment makes a difference to the features observed. Compared to H_2SO_4, the oxide formation and subsequent oxide stripping peak was suppressed in both $KHCO_3$ and K_2HPO_4. The Pt-H adsorption and desorption regions in $KHCO_3$ were more prominent than in K_2HPO_4. Despite a more alkaline pH, in the case of K_2HPO_4, a shift to positive potentials was observed compared to $KHCO_3$. As the cation for both the electrolyte was the same, it is expected that the anion has a significant effect on the reactivity of Pt. Daubinger et al. investigated nanostructured Pt electrodes in different electrolytes and considered the effect of pH.[247] When the authors investigated the effect of PBS (phosphate-buffered saline), a drastic change was observed in the Pt-H adsorption and desorption regions, which the authors stated was related to the diffusion of proton from the electrolyte. This was considered to be the limiting factor and led to the positive shift in the peaks as well as resulting in less sharp features, which could explain why similar behaviour is observed, herein.

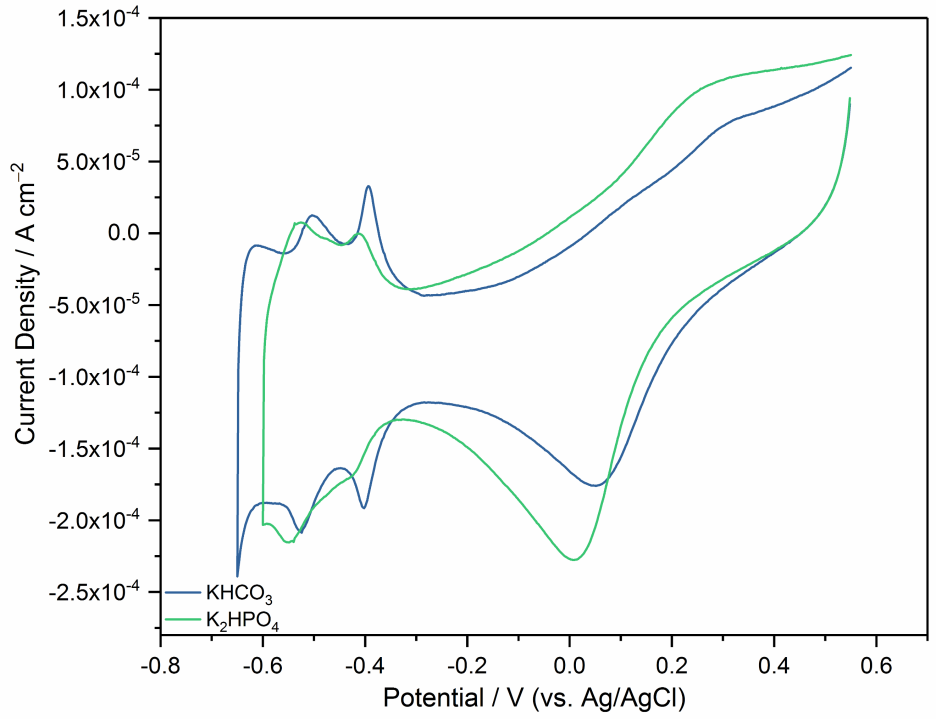

Figure 6-6 – Cyclic voltammograms of Pt electrode in 0.5 M $KHCO_3$ and K_2HPO_4 at a scan rate of 100 mV s^{-1}.

Yu et al. studied the oxidation of methanol in alkaline solutions, namely $NaHCO_3$, Na_2CO_3 and NaOH.[248] The authors observed a similar reduction of current with $NaHCO_3$ and Na_2CO_3 compared to NaOH, which they argued was due to the strong binding of carbonate and bicarbonate anions compared to hydroxyl anions. Similar suppression of the features observed in the Pt voltammogram were seen with $KHCO_3$ (Figure 6-6).

The general agreement in the literature has largely been that the potential region where hydrogen adsorption and desorption occurs is only due to the binding of proton. However, recent studies have also begun to suggest that hydrogen and hydroxide ions co-adsorb onto the surface of Pt and contribute to the features observed in the low potential region. DFT studies indicate that it is thermodynamically favourable for hydroxide anions and protons to co-adsorb.[249] The sub-Nernstian peak shift observed with the phosphate electrolyte may also be explained by the changes of the hydroxide and hydrogen concentrations as the pH changes. The role of the cation in the electrolyte, should also be evaluated. Cations can bind more favourably

relative to proton adsorption, with increasing pH. Crum et al., investigated the effect of potassium ions on the Pt cyclic voltammograms using DFT and observed that the K^+ did not significantly affect proton adsorption but weakened the binding of the hydroxide on the Pt surface.[249]

It is challenging to decouple the effect of pH, cation and anion on the Pt cyclic voltammogram. It appears all factors contribute to the features observed and whilst it is not straightforward to comment on the behaviour observed, an appreciation of the effects of pH and the electrolyte species makes studying the product calibration and the electrochemical reduction of CO_2 more straightforward.

When CO_2 was bubbled in the electrolyte, a significant change was observed in Pt cyclic voltammograms (Figure 6-7). After CO_2 saturation, a positive shift was observed in the peaks, which was related to the acidification of the electrolyte as a consequence of CO_2 saturation. Further evidence of the interaction of carbonate/bicarbonate anions with Pt can also be observed herein, as the features observed in H_2SO_4 compared to $KHCO_3$ were significantly supressed. As $KHCO_3$ is saturated with CO_2, the carbonate equilibrium was still in a region where HCO_3^- species were more prominent in solution (Figure 1-4). Due to the strong binding of carbonate/bicarbonate anions, the adsorption of the hydroxyl anions on the Pt surface was most likely hindered (both in the case of $KHCO_3$ and post CO_2 saturation), the magnitude of the oxide formation and subsequent stripping peak was drastically reduced compared to H_2SO_4.

Evaluation of the Pt cyclic voltammogram behaviour in different electrolytes and with CO_2 saturation, provided an understanding on the effect of electrolyte on the features observed on the Pt surface. It is now possible to verify the addition of products observed during the electrochemical reduction of CO_2, such as methanol and formic acid and aim to understand their

electrochemical oxidation behaviour on a Pt ring surface (in the electrolyte of interest).

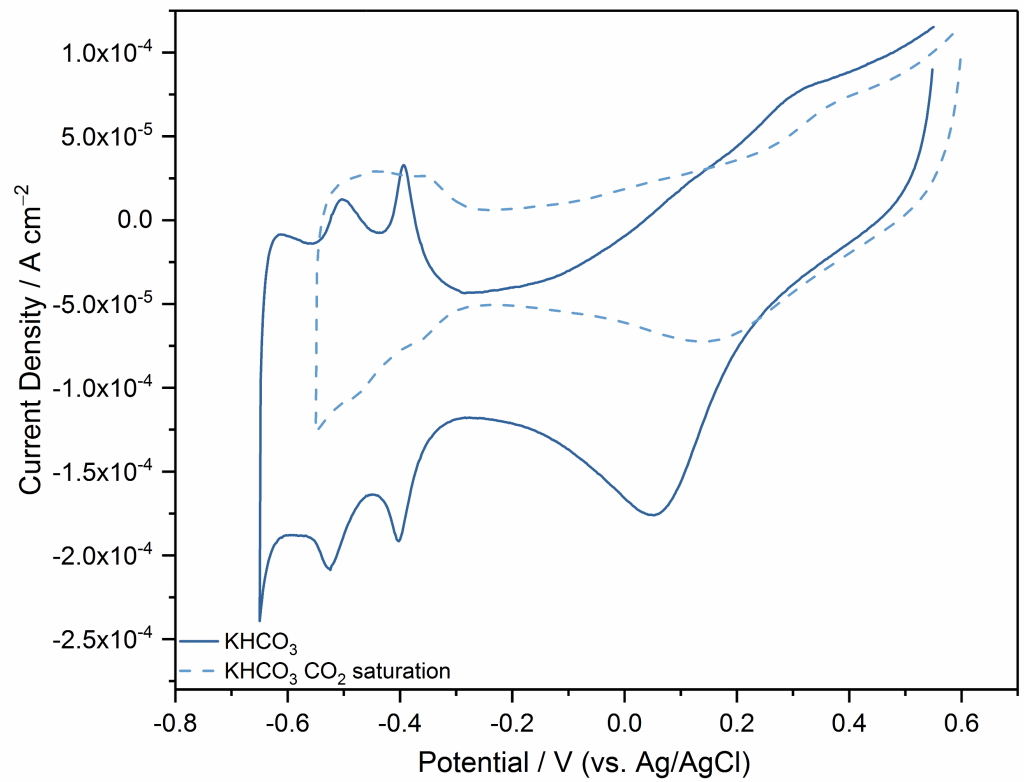

Figure 6-7 - Cyclic voltammograms of Pt electrode in 0.5 M $KHCO_3$ pre (solid line)-and post (dashed line) CO_2 saturation (for 30 min).

6.3.3 Product calibration

In order to understand the behaviour of the electro-active products in the desired electrolyte, a known concentration of formic acid and methanol was added to the electrolyte and their electrochemical behaviour studied. This is not commonly evaluated and as the cell design, electrode area and type can make a significant difference, it is crucial to understand the electrochemical behaviour of products derived from CO_2 electro-reduction.

6.3.3.1 Effect of scan rate and rotation rate

Methanol was added to the electrolyte, saturated with CO_2 and the Pt ring electrode was cycled in the range –0.55 to 0.6 V. The voltammogram (Figure 6-8) shows the oxidation of methanol on Pt at different scan rates (range 2 to

100 mV s^{-1}). The forward scan is represented by the light grey arrow and the reverse scan is represented by the dark grey arrow. The variation in the current between the scan rates was not consistent. For an electrochemically reversible reaction, it would be expected that the current increases with increasing scan rate following the Nernst equation as the hydrogen and hydroxide activity changes with pH.

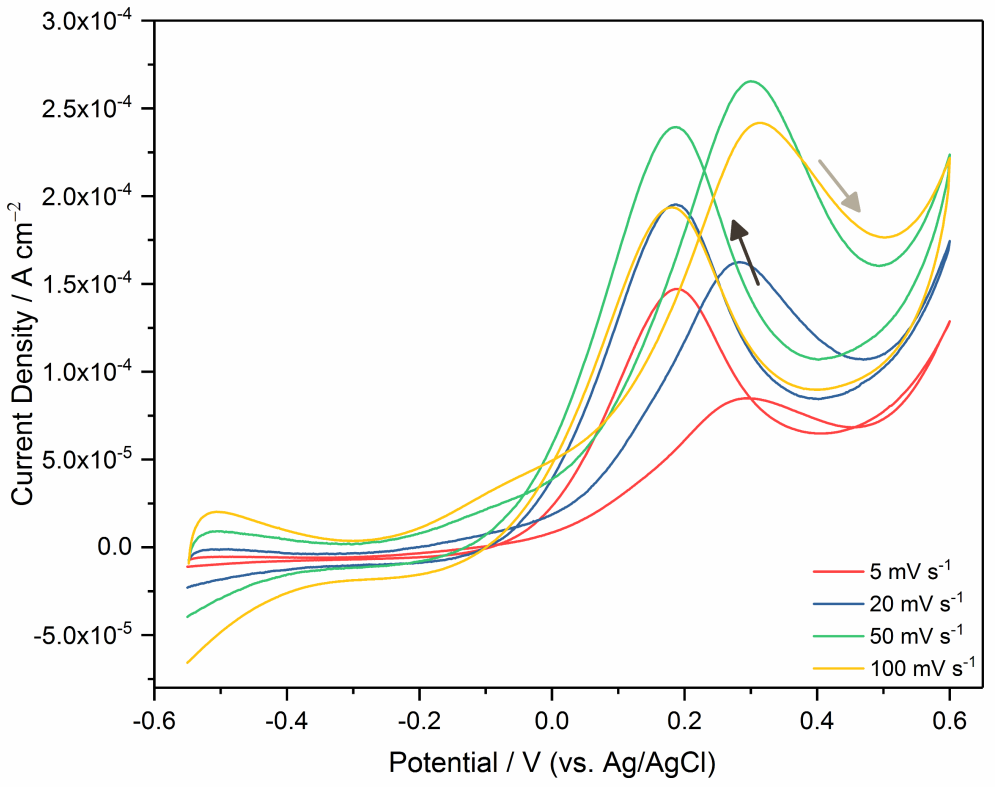

Figure 6-8 – Methanol oxidation on Pt ring electrode at scan rates of 5, 20, 50 and 100 mV s^{-1} in 0.5 M $KHCO_3$ saturated with CO_2. Light grey arrow shows the forward scan and the dark grey arrow shows the reverse scan.

However, the current for 100 mV s^{-1} scan was reduced and in fact, the 50 mV s^{-1} showed the highest current density. Methanol oxidation occurred in a more anodic region than the hydrogen adsorption and desorption region, which was not observed. The rotation rate was also increased to 2100 rpm at a scan rate of 100 mV s^{-1} to understand the influence of increased mass transport to the electrode surface (Figure 6-9). The rotation rate did not have an effect on the current density and a limiting current was not observed, as might be expected with increasing rotation rate, confirming that methanol

oxidation was not mass transport limited. This has previously been observed for formic acid oxidation and in some cases for methanol oxidation, where the rotation rate was varied but appears to be also determined by the catalyst that is used for methanol oxidation.[250]

Two distinct oxidation peaks were observed in this case. It has commonly been thought the first oxidation peak was related to the oxidation of adsorbed methanol and the second oxidation peak on the reverse scan was related to the oxidation of the carbon species from the initial methanol oxidation, rather than the oxidation of further chemisorbed methanol.[251] However, in-situ infra-red spectroscopic measurements suggested that the secondary anodic peak was due to chemisorbed methanol and not residual carbon species such as CO.[252] This was further confirmed by Chung et al. where CV and EIS data confirmed that the secondary oxidation peak was due to methanol oxidation on the free Pt surface.[253]

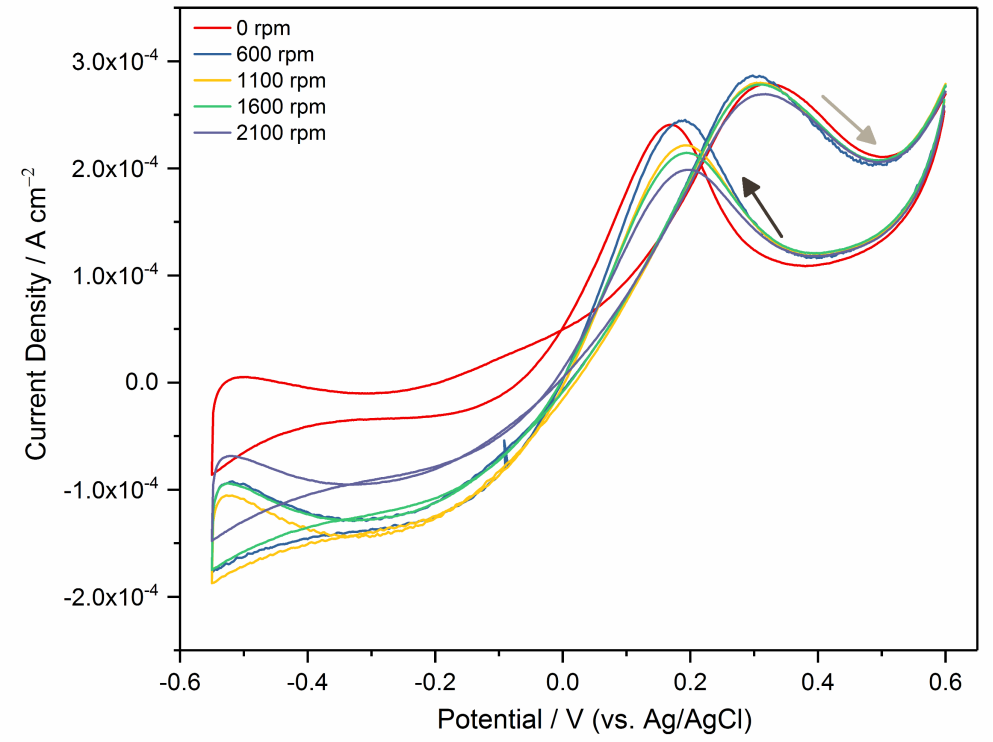

Figure 6-9 - Methanol oxidation on Pt ring electrode at a rotation rates from 0 to 2100 rpm in 0.5 M $KHCO_3$ at a scan rate of 100 mV s^{-1}. Light grey arrow shows the forward scan and the dark grey arrow shows the reverse scan.

Formic acid was added to the $KHCO_3$ electrolyte, post CO_2 saturation and the Pt electrode was cycled in the range –0.55 to 0.6 V and scanned at different scan rates (Figure 6-10). Upon the addition of formic acid to the electrolyte, effervescence was observed as the formic acid reacted with K^+ ions to form formate species ($HCOO^-$), which is the active species involved and was subsequently oxidised. As the scan rate was varied in the range 20 to 100 mV s^{-1}, the current density decreased in both the forward and reverse scan. At higher scan rates the time frame for the catalytic process (of $HCOO^-$ oxidation) to occur becomes narrower and indeed the oxidation of formic acid, is complex, despite being a two-electron process. This also applies to MeOH oxidation ($6e^-$ oxidation process), where a clear trend was not observed for variation in current density with scan rate. A similar trend, as described herein, was also observed for methanol oxidation using Ni based catalysts.[254] Joo et al. also suggested that the $HCOO^-$ binds very strongly to the Pt surface, which leads to a slow oxidation process.[250] This can also be confirmed through the data observed in Figure 6-10, where the current density increased with decreasing scan rate, as at faster scan rates, the oxidation reaction took place too slowly for it to be detected during the cyclic voltammetry scans.

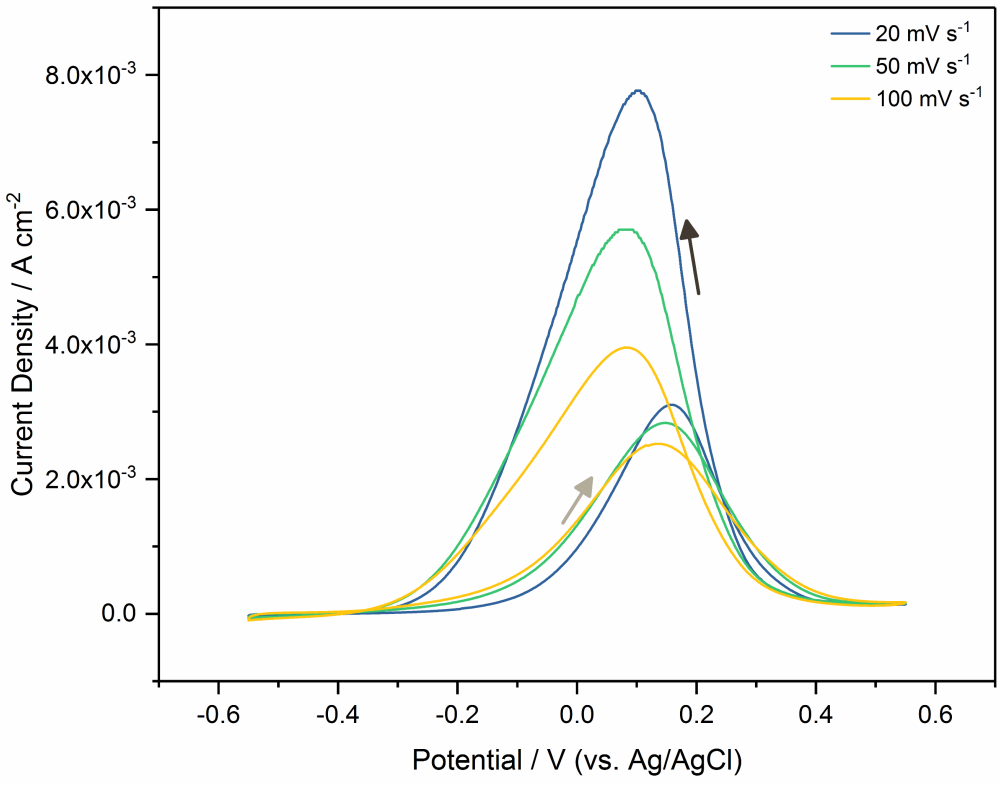

Figure 6-10 – Formic acid oxidation on Pt ring electrode at scan rates of 20, 50 and 100 mV s^{-1} in 0.5 M $KHCO_3$. Light grey arrow shows the forward scan and the dark grey arrow shows the reverse scan.

6.3.3.2 The role of the electrolyte

Methanol oxidation on Pt was tested in $KHCO_3$ and K_2HPO_4 to understand the role of bicarbonate and carbonate anions on the oxidation of methanol (Figure 6-11a). A significant variation was observed in the current density of methanol oxidation in both electrolytes (for the forward and backward scan). Methanol oxidation is known to be more facile in alkaline media (such as NaOH) compared to acidic media due to the formation of poisoning species in acidic media. Yu et al. compared NaOH, $NaHCO_3$ and Na_2CO_3 and observed increased current for methanol oxidation for NaOH compared to Na_2CO_3 and $NaHCO_3$. As carbonate and bicarbonate anions bind strongly to the Pt surface, the hydrogen and hydroxyl adsorption is hindered. MeOH adsorption takes place in the hydrogen adsorption region, which is a reason why hydrogen adsorption and desorption peaks were not observed.

As carbonate and bicarbonate anions are competing and essentially acting as a poison species, carbonate/bicarbonate anions block active sites for ^{-}OH and MeOH coverage, so the current for MeOH oxidation was suppressed in the $KHCO_3$ electrolyte. A small shift to positive potentials was also observed for $KHCO_3$ compared to K_2HPO_4, which was due to the lower pH of $KHCO_3$. The phosphate anions were unlikely to bind preferentially with Pt compared to carbonate and bicarbonate anions, which explains why the current density was significantly higher as more MeOH is preferentially adsorbed onto the Pt surface and subsequently oxidised.

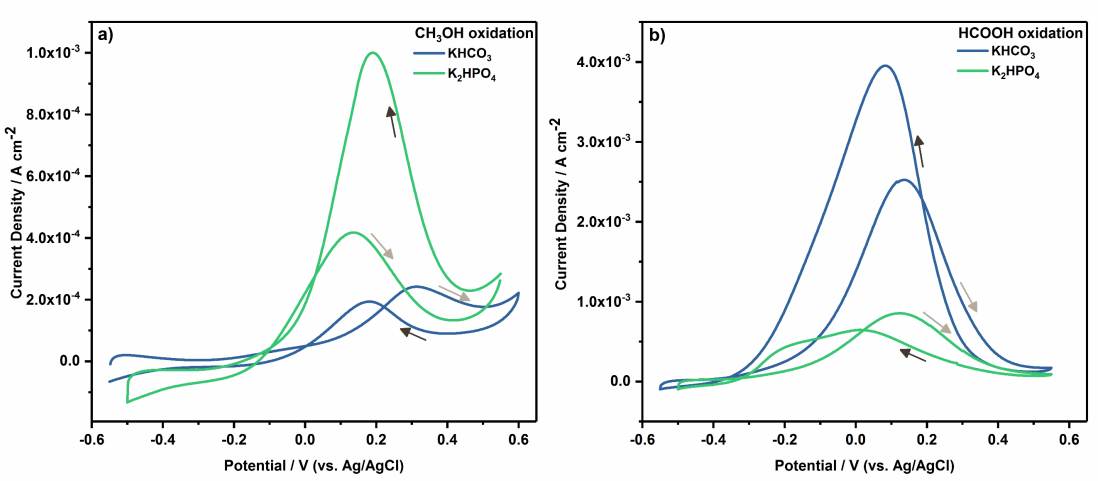

Figure 6-11 – a) Methanol oxidation on Pt ring electrode at scan rates 50 mV s^{-1} in 0.5 M $KHCO_3$ and K_2HPO_4. b) Formic acid oxidation on Pt ring electrode at scan rates 50 mV s^{-1} in 0.5 M $KHCO_3$ and K_2HPO_4. Light grey arrow shows the forward scan and the dark grey arrow shows the reverse scan.

Through infra-red spectroscopy a potential mechanism for methanol oxidation on Pt in alkaline media has been suggested. Generally, it is agreed that methanol is oxidised to formic acid through a direct electrooxidation process. Methanol can also be oxidised to CO via a methanol dehydrogenation pathway, which would then also act as poisoning species on Pt and further block oxidation of MeOH. Tripkovic et al. suggested a mechanism of MeOH oxidation (Equation 6.8 to 6.10). Formate may desorb from the Pt surface or be oxidised further to CO_2.[255]

$$CH_3OH + 3OH^- \rightarrow HCO_{ad} + 3H_2O + 3e^- \qquad \text{Equation 6.8}$$

$$OH^- \rightarrow OH_{ad} + e^- \qquad \text{Equation 6.9}$$

$$HCOOH + OH^- \rightarrow HCOO^- + H_2O \qquad \text{Equation 6.10}$$

Furthermore, formic acid oxidation follows the opposite trend to methanol oxidation, when two different electrolytes were tested (Figure 6-11b). Similar to methanol oxidation, formic acid oxidation takes place in a more anodic region to the hydrogen adsorption/desorption region. The electrochemical behaviour of formic acid oxidation on Pt is complicated by surface oxidation (in the forward scan – light grey arrow) as well as the formic acid oxidation. On the reverse scan, the current density is higher and the oxidation takes place after the Pt oxide reduction and where it is expected that the surface is not significantly poisoned by adsorption of CO.[250]

The majority of studies investigating electro-oxidation of formate on Pt focus on the effect of pH on its oxidation. Joo et al. discovered that the $HCOO^-$ oxidation reaches a maximum current density at a pH close to is pK_a of HCOOH. The authors also suggested a mechanism of formic acid oxidation, which takes place via bridge-bonded adsorbed formate and a weakly adsorbed HCOOH precursor. The oxidation of $HCOO^-$ is found to be worse at higher pH as the hydroxyl adsorption competes with $HCOO^-$ which leads to a decrease in activity. It is possible the slightly higher pH of the phosphate based electrolyte compared to carbonate based electrolyte, might contribute to the lowered activity of formic acid oxidation in the former electrolyte. However, the effect of the anion on the electro-oxidation of HCOOH on Pt has been poorly understood. The specific adsorption of the anion on the Pt electrode could have a bigger influence on the electro-oxidation of formic acid on Pt, in conjunction with the pH of the solution. Perales-Rondón et al. studied the effect of the anion adsorption on the electro-oxidation of formic acid on Pt and observed a stark difference with phosphate based electrolyte compared to sulfate and perchlorate based electrolytes.[256] The current density for HCOOH oxidation was ca. 50% lower in phosphate based

electrolytes compared to the sulfate and perchlorate. If an anion binds more strongly than the desired reactive molecule, this can significantly alter the mechanism pathway and intermediates.

Herein, a stark difference of activity was observed for the electro-oxidation of methanol and formic acid in $KHCO_3$ and K_2HPO_4. The choice of electrolyte plays a critical role both in the electroreduction of CO_2 and the electro-oxidation of the products. Therefore, the use of the correct electrolyte for product detection must be balanced with the expected reaction product. The electroreduction of CO_2 has been shown to be favourable in carbonate based electrolytes and was subsequently used for the study of the RRDE experiment.[253]

6.3.4 Electrochemical reduction of CO_2 – RRDE study

6.3.4.1 Linear Sweep Voltammetry

The catalyst inks were prepared on the glassy carbon disk electrode as described in Section 6.2.2 and the catalyst layer was cycled in the range 0 to –1.4 V vs. Ag/AgCl at a rotation rate of 2500 rpm. Figure 6-12 presents LSV curves where the current versus potential curves did not present a sigmoidal shape, as expected from an electrochemical process that is diffusion controlled (such as for the oxygen reduction reaction or the ferro/ferricyanide reaction (Figure 6-4). Indeed, the current increased monotonically from –1.0 V onwards to higher potentials. Baturina et al. investigated carbon supported copper nanoparticles for CO_2 electroreduction using a RDE set up and observed a similar trend where the current increased monotonically.[237] The authors stated that this was due to the hydrogen evolution reaction competing in parallel with the electroreduction of CO_2, which “masks” the limiting diffusion current for electroreduction of CO_2.

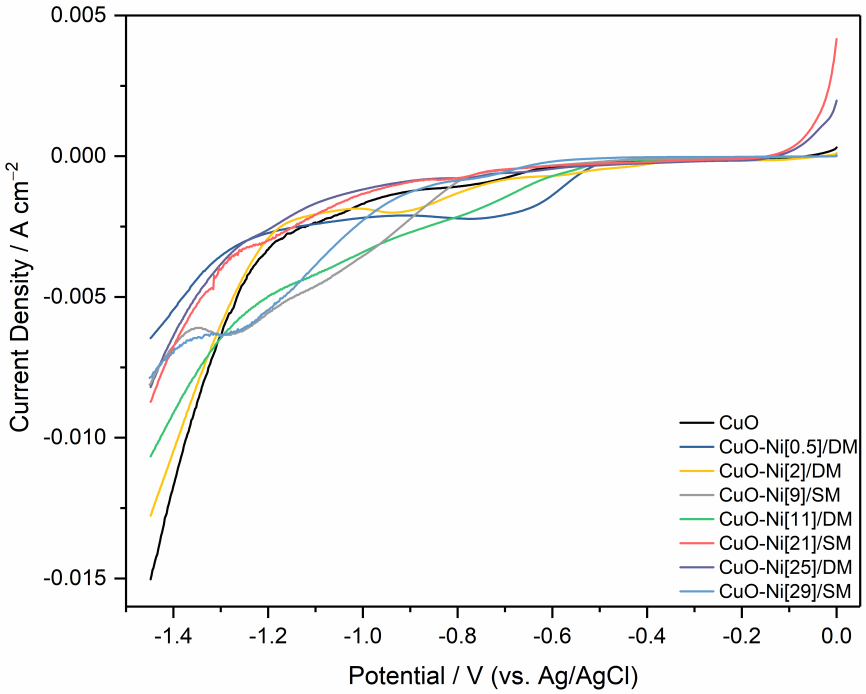

Figure 6-12 – Linear sweep voltammogramms of all catalysts tested in 0.5 M $KHCO_3$ saturated with CO_2 for 30 mins. The rotation rate was 2500 rpm for all scans. The working electrode (disk) was scanned from 0 to –1.45 V vs. Ag/AgCl.

Following characterisation of the catalyst by LSV, the disk electrode was scanned in the range 0 to –1.4 V and the ring was held at such a potential, where products (from the disk) may be oxidised. This potential was chosen from the electro-oxidation of products (Figure 6-11) at the maxima of the peak at 0.14 V vs. Ag/AgCl, in the case of formic acid. An example is shown for sample CuO where the ring is scanned between 0 and –1.4 V vs. Ag/AgCl and the ring is held at 0.14 V (Figure 6-13). The LSV of the disk appeared as before and the ring scan for this potential scan showed minimal current in the range 0 to –1.0 V. However, at –1.0 V, there was a significant increase in the oxidative current density at the ring electrode. The current density increased from 0.02 mA cm^{-2} to 0.32 mA cm^{-2} with increasing negative potential at the disk, an increase of ca. 15-fold. The increasing oxidative current at the ring corresponded to the increasing reductive current at the disk, which was suggestive that as the potential is increased at the disk electrode, CO_2 is converted to HCOOH, which is then detected at the ring electrode, and this does not increase until –1.0 V.

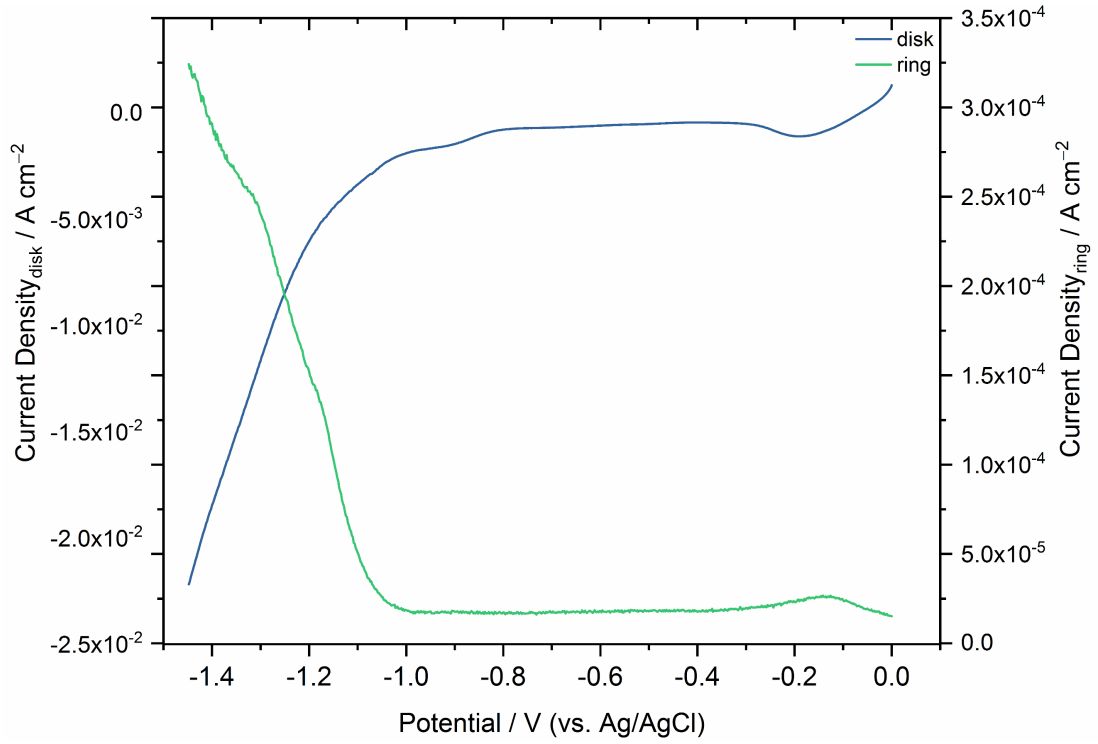

Figure 6-13 – Blue curve: LSV of sample CuO on disk electrode scanned in the range 0 to –1.45 V vs. Ag/AgCl in 0.5 M $KHCO_3$ saturated with CO_2 for 30 mins. Green curve – Corresponding current potential curve for the Pt ring electrode, held at 0.14 V vs. Ag/AgCl, for the electro-oxidation of formic acid as formed on the CuO catalyst.

Furthermore, the current density achieved at the ring electrode at –1.4 V vs. Ag/AgCl is not 38% of the disk electrode, as would be expected from the collection efficiency experiment, which verified that experimentally the ring would be able to detect the 38% of the products formed at the disk. However, this appears not to be the case.

6.3.4.2 Effect of rotation rate on product detection

The rotation was altered to confirm if it affected the product detection at the ring (Figure 6-14). This may be the case, if the electrode was rotated too quickly for the product to be detected at the ring electrode, as the products might have been ‘swung’ downstream and into the bulk of the solution.

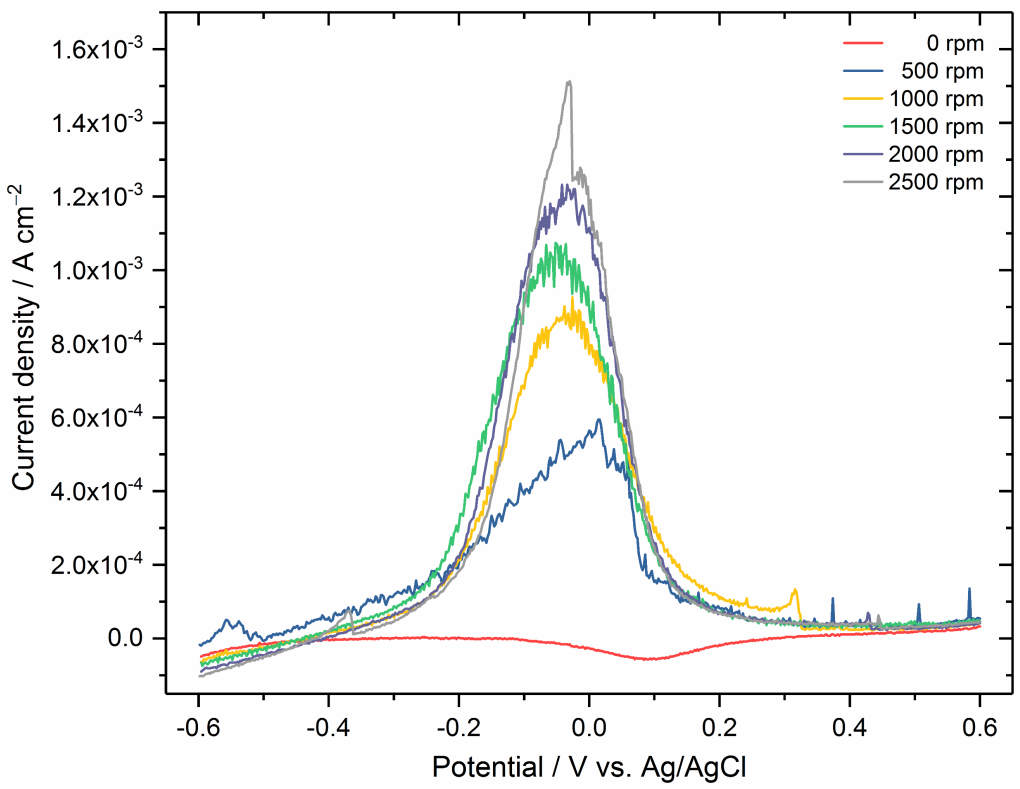

Figure 6-14 – LSV of Pt ring electrode when the ring is swept in the range 0.6 and –0.6 V vs. Ag/AgCl and the disc is held at –1.4 V vs. Ag/AgCl to generate product, at rotation rates of 0, 500, 1000, 1500, 2000 and 2500 rpm, in 0.5 M $KHCO_3$ saturated with CO_2.

As the rotation rate was varied in the range 0 to 2500 rpm, the current density of the peak associated with formic acid oxidation, showed an increase with rotation rates. At 0 rpm, a small negative current was observed at ca. 0.1 V, which was related to reduction of the platinum oxide formed at the surface of the electrode. As the electrode was not rotating in that instance, the HCOOH produced at the disk was not detected by the ring, as the product simply desorbed off the electrode into the bulk solution, hence, no oxidation peak corresponding to HCOOH was observed.

At 500 rpm, an increase in current density was observed, however, the peak was broader and more asymmetrical than the HCOOH formic acid peak observed at this potential, when HCOOH product calibration was conducted in 0.5 M $KHCO_3$. This may be due to a local pH effect as more HCOOH is produced with increased mass transfer of CO_2 to the disk electrode with increasing rotation rate. Joo et al. observed a shift in the formic acid

oxidation peak but did not comment significantly on the reasons, citing the pH change as a potential reason.[250] However, increasing the rotation rate did not alter the peak shape or position significantly. This suggested that the increased production of HCOOH could not be the sole reason for the change in peak shape and position for the 500 rpm scan.

As the rotation rate was increased further, the current density for formic acid oxidation increased, which suggested improved mass transport of CO_2 to the electrode allows higher amounts of HCOOH to be formed at the disc electrode (which is subsequently detected at the Pt ring electrode). Lim et al. investigated the effect of mass transfer on the electrocatalytic reduction of CO_2 on copper electrodes, where the electrode was stirred in the electrolyte.[257] The authors observed a change in hydrocarbon selectivity with rotation rate. Rotating the electrode improved the mass transfer of reactants and products to and from the electrode surface, which led to a decrease in the diffusion layer thickness. This led to a shift in the interfacial pH, close to the bulk pH of the solution and increased the flux of CO_2 to the electrode surface.

As the rotation rate was increased, the mass transfer of OH^- was improved as increasing amounts of it was swept away from the electrode. OH^- was formed during the electrochemical reduction of CO_2 and this also altered the local pH. At lower rotation rates, increasing amounts of OH^- and the lower rotation rate (larger diffusion thickness), could alter the interfacial pH, leading to a change in the peak shape and position of the peak at 500 rpm. However, this was not observed with the higher rotation rate as the diffusion layer thickness decreased further, but also the OH^- ions were swept away faster.

Lim et al. also observed an increase in the production of formic acid (by increase of current efficiency) with increasing rotation rates for the electroreduction of CO_2 on polycrystalline Cu.[257] The authors argued this was due to enhanced mass transfer of CO_2 to the electrode surface. The

observations herein, where the current density increased with increasing rotation rate, agreed with the observations in the literature. It does not suggest that having particularly high rotation rate was detrimental to the detection rates, in fact, 2500 rpm presented with the highest current density for formic acid oxidation. The rotation rate was limited to 2500 rpm, as the maximum safe rotation rate for the RRDE was 3000 rpm. The noise present in the LSV was speculated to be due to the presence of hydrogen bubbles formed during the competing hydrogen evolution reaction (as the disk electrode was held at –1.4 V). The LSV became less noisy with increasing rotation rate, as the hydrogen bubbles were swept away at a faster rate at higher rotation rates.

6.3.4.3 Effect of disk potential on product formation

There is a potential dependency on the electrochemical reduction of CO_2, which has been reported earlier in this thesis as well as in the literature. This was evaluated by using the optimal CuO catalyst, with 25 wt.% Nafion content, (Chapter 4) to coat the disk electrode. The disk electrode was held at the same potentials as it was in previous chapters (in the range –0.6 to –1.4 V) and the Pt ring electrode was scanned in the range 0.6 to –1.0 V vs. Ag/AgCl (Figure 6-15). This was also to observe whether the effect of the disk electrode potential on product formation could be detected by the ring electrode. The independent Pt ring electrode is shown for reference (Figure 6-15a).

When the disk was held in the range –0.6 to –1.0 V, the Pt ring electrode presented itself with CV scans where no product was detected, as compared to the product calibration CVs (Figure 6-15 b-d). This was consistent with the Faradaic efficiencies observed in Chapter 4, where at lower overpotential HCOOH production was significantly diminished.

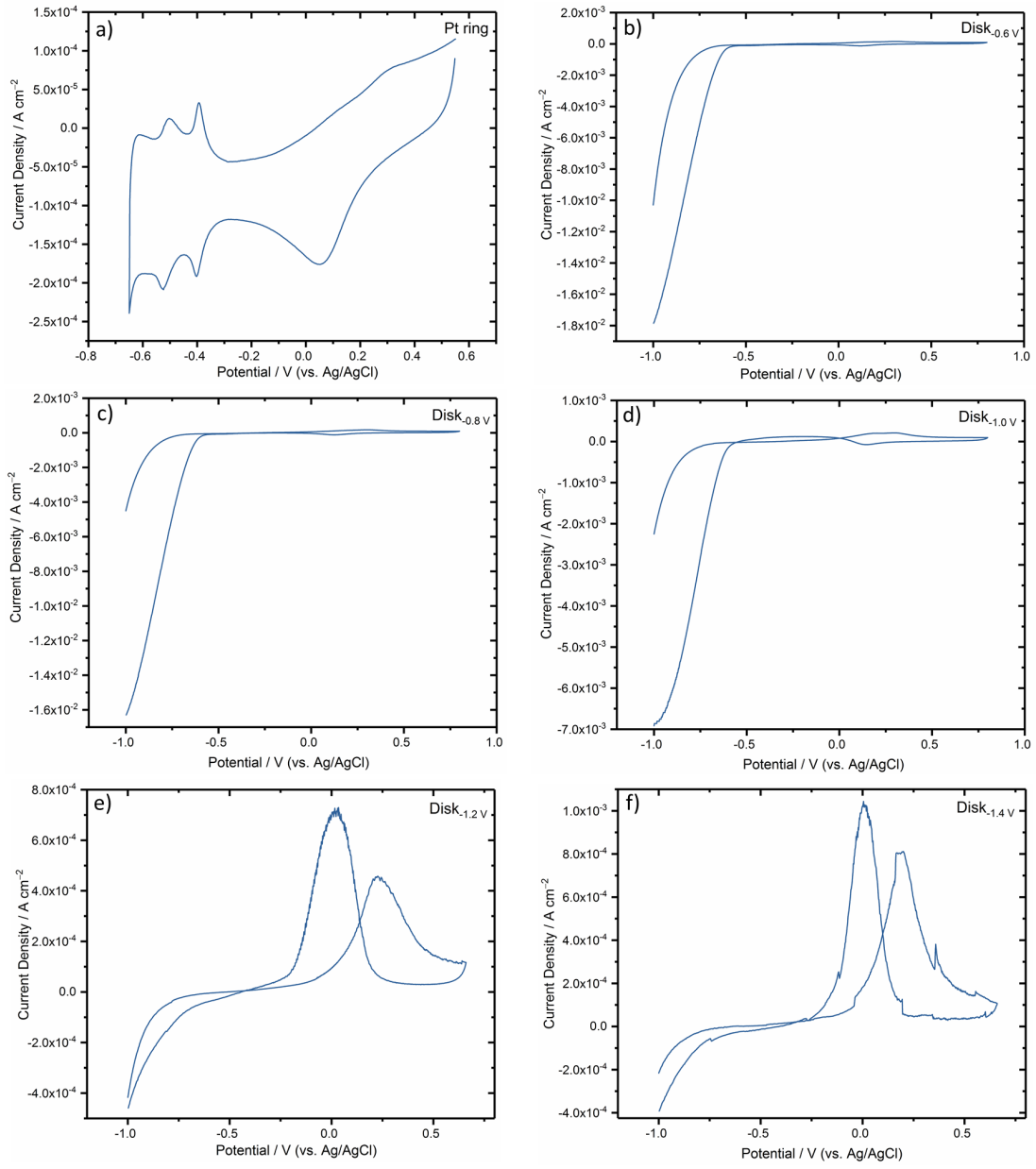

Figure 6-15 - Cyclic voltammetry scans of the Pt ring electrode as it was scanned in the range –0.6 to –1.4 V vs. Ag/AgCl and the CuO coated disk electrode was held at various potentials (in the range –0.6 to –1.4 V) to evaluate the potential dependency at a rotation rate of 2500 rpm.

Features of the Pt ring electrode were observed on the CV scans, further confirming that formic acid was not detected by the Pt ring electrode. This is indicative that the amounts of formic acid formed at the electrode were significantly lowered and hence not detected at the ring. Interestingly, the current on the Pt ring electrode, was likely due to the hydrogen reduction reaction (at potentials of –1.0 V).The current density for hydrogen reduction

at the Pt ring electrode, decreased with increasing disk potential. This is not likely related to the interaction of the electrolyte, as the current is altered for each potential; it would be expected the current density would be the same or similar, if the hydrogen evolution reaction, on the Pt ring electrode was due to the H^+ ions in the electrolyte. This appeared not to be the case, suggesting that it is possible to detect the hydrogen evolution reaction, which occurs simultaneously with the electrochemical reduction of CO_2. The potential dependency is evident; at lower disk potential, the main product formed on the catalyst is hydrogen and other CO_2 based products are not formed as the overpotential is too low to drive forward the reaction. As the disk potential increases to –1.2 V and higher, less hydrogen forms as the CO_2 reaction becomes dominant. However, a significant difference in the current density is not observed when the disk potential is held at –1.2 and –1.4 V (Figure 6-15 e and f). The current density on the Pt ring decreased from –18.0 to –0.4 mA cm^{-2}, when the disk potential was held at –0.6 and –1.4 V, respectively (measured at –1.0 V). The current density related to hydrogen evolution on the Pt ring electrode can be confirmed as a by-product of the ECR of CO2, as the standard Pt ring electrode CV (at –1.0 V), resulted in a current density of ca. 3 mA cm^{-2}, which was significantly lower than when the disk is held at –0.6 V vs. Ag/AgCl.

Prominent formic acid oxidation peaks were obtained for CV scans when the disk was held at –1.2 and –1.4 V vs. Ag/AgCl (Figure 6-15 e and f). The peak shape and position of formic acid oxidation matched well with the formic acid calibration peaks, as observed in Figure 6-11. As other peaks for methanol or CO were not observed in the Pt ring CV scans, it was confirmed that formic acid was the main detectable product on the Pt ring electrode, which also confirmed well with the NMR and GC results (Chapter 4). The maximum current density for the formic acid peak (in the negative going scan), was lower for the sample when the disk was held at –1.2 V, resulting in a current density of ca. 0.7 mA cm^{-2}, whereas at –1.4 V, the maximum current density

was ca. 1 mA cm^{-2}, which was consistent with observations in Chapter 4, where the formic acid production was significantly higher for the sample held at –1.4 V.

The charge passed for the electrochemical oxidation of formic acid on Pt and for the scan at –1.4 V, was 84 mC and at –1.2 V was calculated to be 43 mC. The values were obtained by integrating the formic acid oxidation peak in the negative going scan. The charge passed for the electrochemical oxidation of formic acid on Pt cannot directly be compared to the charge passed for the electrochemical reduction of CO_2 on the glassy carbon sheet, as tested in Chapter 4, as they are two distinct reactions. Similarly, the process design can make a significant difference. For example, differences in the electrode area between the RRDE and the glassy carbon sheet, stagnant vs. rotating electrodes and the gap between the disk and ring in relation to product detection as well as rotation rate, are factors that can affect how the product derived from CO_2 reduction is formed and subsequently oxidised. The general trend was in accordance with the charge passed for the electrochemical reduction of CO_2 to formic acid in Chapter 4, where at –1.2 V, the charge passed for formic acid formation was lower than the charge passed for –1.4 V, indicating and further confirming herein, that more formic acid is formed when the disk is held at –1.4 V.

6.3.4.4 Comparison of product formation between CuO and Ni-doped CuO using RRDE

Ni doped CuO was tested on the RRDE and compared to the optimal CuO catalyst (Chapter 4). The Pt ring CV, in the range 0.55 to –0.6 V, was collected for when the disk was held at different reduction potentials (Figure 6-16). A reference for CuO is also shown. Herein, the comparison is only made for the sample that achieved the highest Faradaic efficiency for Ni-modified CuO catalyst (CuO-Ni[9]/SM) at –1.2 V vs. Ag/AgCl.

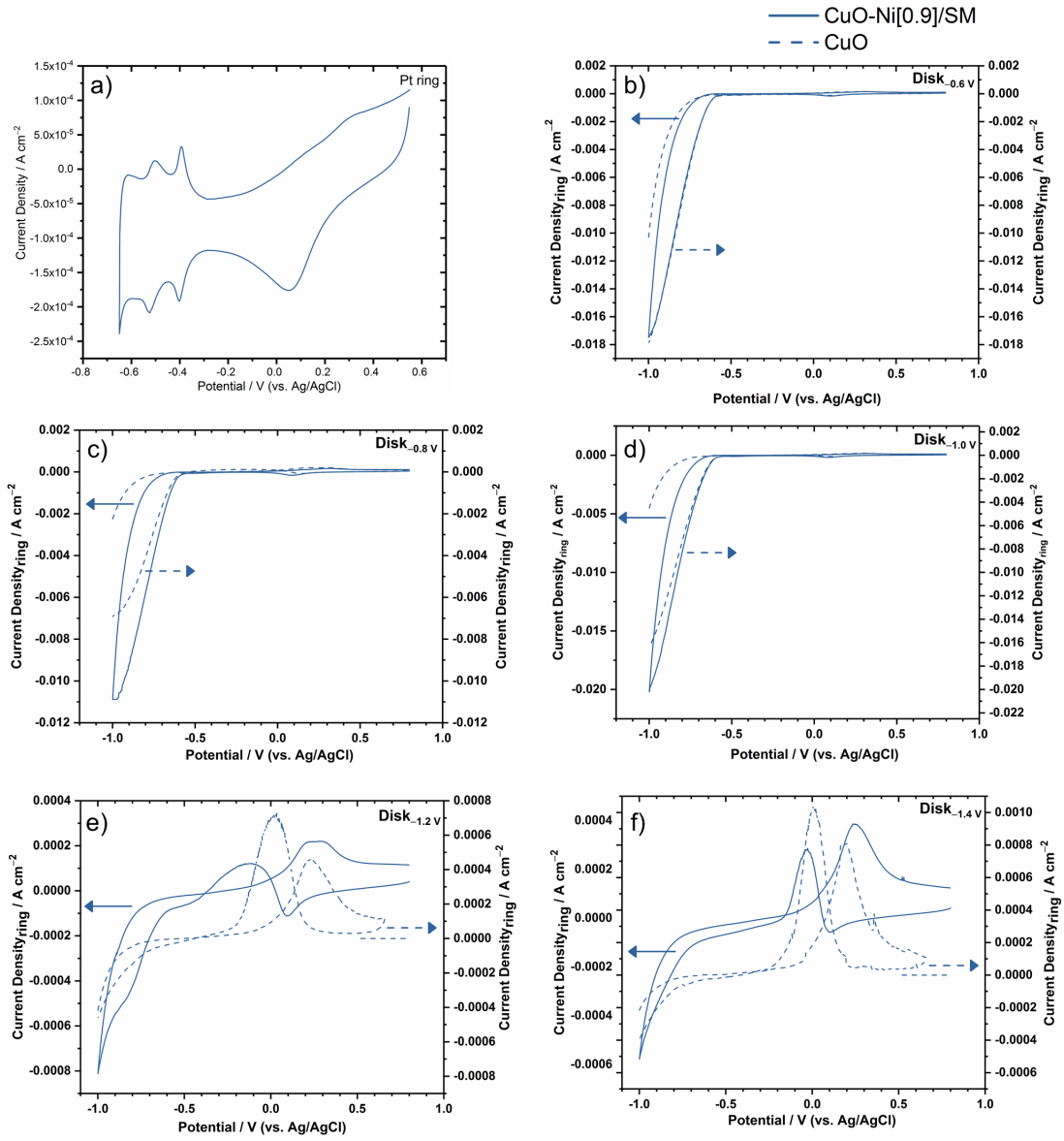

Figure 6-16 - Cyclic voltammetry scans of the Pt ring electrode as it was scanned in the range –0.6 to –1.4 V vs. Ag/AgCl and the CuO-Ni[9]/SM coated disk electrode was held at various potentials (–0.6 to –1.4 V) to evaluate the potential dependency at a rotation rate of 2500 rpm.

As observed in the case of CuO, sample CuO-Ni[9]/SM did not present any product peaks, when the disk was held at potentials lower than –1.2 V. Features from the oxidation of the Pt and the subsequent oxide stripping peaks were observable at lower overpotentials (Figure 6-16 b-d). This may also be applicable for Figure 6-16e, where broad features in the positive going scan are observed for the Ni doped sample in the Pt oxidation region. The CV scans for when the disk is held at –1.2 and –1.4 V (Figure 6-16 e and f) showed the presence of formic acid as the peak shape and positions

matched well with the calibration conducted in Section 6.3.3. On the negative going scan, similar broader features were observed in the formic acid oxidation. This was not observed in the disk held at –1.4V. In comparison to the CuO sample, the formic acid oxidation peaks did not show this behaviour at –1.2 V.

From the NMR data and the Faradaic efficiency results as discussed in Chapter 5, at a potential of –1.2 V, the formic acid production was significantly higher for this sample compared to the same sample at other potentials. Integration of the formic acid peak area on the negative going scan provided the charge passed to oxidise formic acid on the Pt ring electrode, which could be related to how much formic acid was produced at the disk electrode. This was only done for the scans at –1.2 and –1.4 V. The charge passed for –1.2 V was 3 C and at –1.4 V, the value was calculated to be 517 mC. It should be noted that the broadness of the formic acid oxidation peak for the scan at –1.2 V, would contribute to the higher charge passed. It is speculated that in combination with formic acid, there is contribution from other species in solution, which have not been identified or it is due to pH effects at lower disk overpotentials. The charge passed at –1.2 V is significantly higher than at -1.4 V but the formic acid contribution cannot be easily deconvoluted from other contributions.

The charge passed for formic acid oxidation on the Pt ring electrode was higher for the nickel doped CuO samples than CuO when the disk potential was held at –1.2 and –1.4 V. Tafel analysis conducted for samples investigated in Chapter 6, indicated a decrease of the Tafel slope when Ni doped CuO were compared to the optimal CuO catalyst, suggesting that the electrochemical reduction of CO_2 on Ni doped catalysts occurred faster than with CuO, further corroborated with electrochemical impedance spectroscopy. This was in good agreement with the data presented from the RRDE. It should also be noted that whilst initial results suggest that data

presented agrees between the RRDE and bulk electrolysis, the timescales for product detection on the ring are on the order of milliseconds. The data obtained from bulk electrolysis is related to the total time the reaction was conducted for, so the charge passed, concentration of product generated and the Faradaic efficiency is related to the total time. It is possible over time the amount of product generated varies, as the catalyst degrades or the electrode surface is saturated with the product.

Based on the Faradaic efficiency data collected for CuO (Chapter 4), it was expected that the current achieved for formic acid oxidation on the Pt ring electrode corresponding to the high production of formic acid on CuO would be high but this was not the case here. Interestingly, for the optimal Ni doped CuO sample (CuO-Ni[9]/SM, with the highest Faradaic efficiency at –1.2 V) presented with higher charge passed for the electrochemical oxidation of HCOOH on Pt. This corresponded to the higher amounts of formic acid formed on the disk electrode.

Tafel analysis and EIS indicated that the Ni doped CuO presented with faster kinetics than undoped CuO, however, the overall Faradaic efficiency was significantly lower for the same period compared to the undoped CuO sample. It is possible that the Ni doped CuO sample was more prone to degradation compared to CuO, so it would be crucial to understand the catalytic stability over time.

6.3.4.5 Kinetic analysis of the electrocatalysts using RRDE

The rotational dependence of the current density of the CO_2 reduction current was also investigated. LSVs were obtained for all catalysts at rotation rates in the range 0 and 2500 rpm. The current density obtained at –1.4 V (from the LSVs) was plotted as reciprocal current density vs. reciprocal rotation rate to obtain a Koutcký-Levich plot (Figure 6-17). As mentioned in Section 6.1, a linear dependence of current density with increasing rotation rate indicated that the reaction was mass transport limited. However, herein,

the reduction current was not dependent on the rotation rate and thus the reaction was not limited by mass transport. This is consistent with observations in literature where RDE studies have been conducted with a range of catalyst for CO_2 electro-reduction.[235,236,258] This further confirmed that the reaction on copper oxide derived catalyst was due to surface species (non-diffusing). Not all samples tested are shown as generally the same trend was observed for the remaining samples.

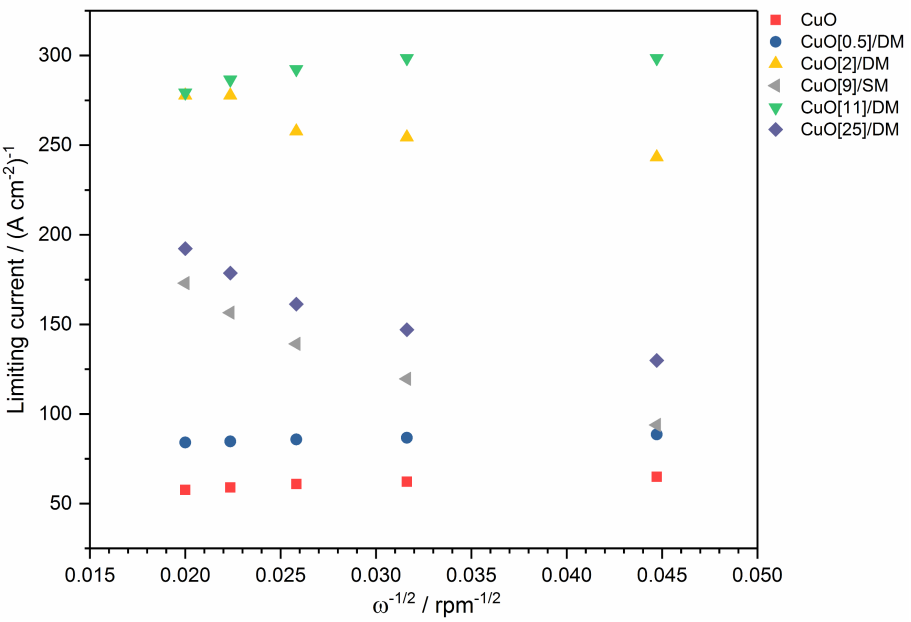

Figure 6-17 – Koutcekỳ-Levich plot - reciprocal current density vs. reciprocal rotation rate for catalysts tested. Current density taken from –1.4 V vs. Ag/AgCl from LSVs, in 0.5 M $KHCO_3$, saturated with CO_2, RRDE rotated in the range 0 – 2500 rpm.

6.4 Conclusions and future work

In conclusion, the RRDE set-up was designed and tested for successful use with the electrochemical reduction of CO_2. It was shown that formic acid generated at the disk could be detected at the ring electrode. The set up was validated with a well-known one-electron ferro/ferricyanide redox couple, which also confirmed that no electrical cross-talk occurred between the disk and ring electrode. The electrochemistry of the Pt ring electrode was also studied in H_2SO_4, $KHCO_3$ and K_2HPO4 to understand its behaviour in these electrolytes prior to product calibration. A product calibration was conducted

for the most common products derived from the electrochemical reduction of CO_2, namely methanol and formic acid. The electro-oxidation of the products on the Pt ring electrode was studied in $KHCO_3$ and KH_2PO_4, where it was shown that the electrolyte environment made a significant difference to the current density achieved for the oxidation of formic acid and methanol. Methanol oxidation was favoured in K_2HPO_4 and significantly suppressed in $KHCO_3$, whereas the reverse trend was observed for formic acid oxidation. $KHCO_3$ was chosen as the electrolyte as electroreduction of CO_2 was favourable in this electrolyte.

The CuO based catalysts were tested using the RRDE set up (as used previously in this thesis in Chapter 4 and 5), where the effect of rotation rate and disk potential on the product detection on the Pt ring electrode was investigated. It was observed that 2500 rpm was the optimum rotation rate for HCOOH detection (in the range 0 to 2500 rpm), as shown by the highest current density achieved. No other products apart from formic acid were observed on the Pt ring electrode.

When the disk was held at different reducing potentials (in the range –0.6 to –1.4 V) and the Pt ring electrode cycled (in the range 0.6 to –1.0 V), formic acid and the hydrogen evolution reaction was observed on the Pt ring. No products were detected below –1.2 V, where the features from the Pt ring were observed in the CV. The CuO catalyst was compared with the Ni-doped CuO catalyst and showed that the formic acid detected at the ring electrode when the Ni doped CuO catalyst was used was higher compared to the CuO catalyst. This was determined from the charge passed for formic acid oxidation. This was in agreement with Tafel and EIS analysis, however, the total Faradaic efficiency was lower for the Ni doped CuO samples (Chapter 6).

Kinetic analysis was also considered where the rotation dependency on the CO_2 reduction current was studied. No meaningful link was observed

between the rotation rate and the current for CO_2 reduction, confirming that this was not mass transport limited.

Future work may consider studying the degradation of the catalysts tested to study how the product formation varies over time and investigate the ability of the RRDE to detect products over time. The ring could be polarised at the correct oxidation potentials at certain periods during long-term bulk electrolysis at the disk electrode to understand how the formic acid oxidation varies over time. This would provide a better insight into whether there is catalyst degradation and if there is a time induction present in product formation (particularly at lower overpotentials). This chapter has also shown that the RRDE set up may be used for high-throughput screening of catalysts by in-situ detection of products derived from CO_2 reduction. Other catalysts may also be used in the future, which have been shown to form other products, such as CO, methane, methanol and ethanol. The RRDE's effectiveness for such product detection would also need to be confirmed.

Other future work could also probe the effect of the product concentration in the calibration stage. Constructing a calibration curve would also allow to detect the amount of product formed in-situ and compare with NMR and GC data at the bulk electrolysis stage. Similarly, the effect of product concentration would also shed an insight into the cyclic voltammetry behaviour with varying concentration.

Chapter 7. Conclusions and Future Work

7.1 Summary of conclusions

The work presented in this thesis considered the synthesis of copper-based nanocatalysts via continuous hydrothermal flow synthesis for the electroreduction of CO_2 to fuels (formic acid, methanol, CO and CH_4). The aim of this thesis was to investigate the effect of nanomaterials and their catalytic properties modulated by tailoring experimental parameters during the CHFS process.

The synthesis of CuO nanoparticles was explored via CHFS, where single and dual mixers were investigated with three different copper salt precursors (sulfate, nitrate and acetate). No significant differences were observed in particle size or morphology with the three precursors. However, the particle size significantly reduced with the use of a quench feed, from 16.6 to 10.5 nm, in the case of CuO-acetate. In the absence of a quench feed, CuO particles grew through coalescence; and particle size was significantly hindered through the use of a quench. The mixing temperature and pH were found to affect the crystallite size of CuO (from copper sulfate) and at low mixing temperatures and pH, brochantite ($Cu(SO_4)OH_6$) was favourably formed which converted to CuO with increasing mixing temperatures. The effect of concentration was investigated with copper acetate, in the absence of base. It was found that the particle size decreased with increasing concentration, due to increased supersaturation and enhanced nucleation rate. H_2O_2 was introduced in the metal feed in varying concentrations and it was found that H_2O_2 greatly reduced the particle size by increasing the nucleation rate or by hindering particle growth.

The synthesis of Cu_2O and Cu was attempted by altering mixer set ups such as pre-mixer and dual mixers and by using reducing agents (formic acid and fructose). A pre-mixer was used to decompose the formic acid with supercritical water. This was compared to a dual mixer, and it was possible to synthesise Cu_2O and Cu without decomposing the formic acid prior to meeting the precursor feed. However, the oxidation of Cu_2O and Cu was facile and the use of PVP as a capping agent did not prevent oxidation of Cu_2O and Cu. Fructose was also explored as a reducing agent and offered better protection than PVP in preventing further oxidation of Cu_2O and Cu. CHFS was shown to be to suitable technique for the controlled synthesis of copper-based nanoparticles, whereby the properties, particularly size could be modulated by altering the mixing regime within the reactor.

Ultra-fine CuO was formulated into homogeneous Nafion based inks that were employed to prepare stable catalyst layers on glassy carbon electrodes. The ink formulation was systematically evaluated by assessing the effect of the preparation method, solvent system and drying methods by DLS and SEM. The ink composition was also optimised with varying Nafion fractions to maximise the performance for the electrocatalytic reduction of CO_2 to formic acid on copper surfaces, derived from the CuO nanoparticles. The highest measured Faradaic efficiency for HCOOH was observed (>60%) with 25 wt% Nafion fraction (vs. solid state fraction). This was considerably higher than previously reported Faradaic efficiency with copper-based systems. This was explained by conducting electrochemical impedance spectroscopy, which showed that the charge and mass transfer resistance was lowest for the sample with the optimised Nafion fraction. The selective product formation was explained by post structural characterisation by TEM, which showed the presence of Cu(111) plane, which favoured HCOOH formation as well as the small size of CuO synthesised.

Ni doped CuO catalysts were developed by co-precipitation and compared to CHFS. A limit of 5 at% Ni was observed through co-precipitation and >5 at%, NiO formation was observed with CuO. Ni doped CuO (1 to 50 at% Ni) were successfully synthesised via CHFS (dual mixer) and characterised by PXRD, TEM, EDS, ICP-AES and XPS. Considerably higher amounts of Ni could be included (30 at%) in the CuO host structure compared to conventional routes, before phase segregation may be observed. ICP-AES analysis verified the Ni content, within the samples and a significant discrepancy was observed between the nominal and actual Ni at% when the Ni doped CuO was synthesised via the dual mixer. This may be due to the dissolution of Ni in the quench feed or through sample processing. The catalysts were formulated into inks with the optimised Nafion fraction and tested for CO_2 electroreduction. The Faradaic efficiency (sub-25 %) was unremarkable in general. Significant morphology change was observed between the samples before and after electrolysis; where copper nickel dendrites were formed. This was linked to the interaction of carbonate anion (from the electrolyte) and the Ni. This was verified by conducting experiments in a phosphate based electrolyte, where dendritic formation was not observed. The interaction of Ni in driving the dendritic growth was explored further by synthesising Ni doped CuO via a single mixer set up, where Ni rich surface was formed, characterised by XPS depth profiling. The catalysts were subsequently tested and showed unremarkable selectivity but significant dendritic growth was not observed within the conditions tested. Although the synthesis of ultra-fine Ni doped CuO was possible through CHFS, the catalysts exhibited unremarkable catalytic activity and selectivity for CO_2 conversion.

Rotating Ring Disk Electrode (RRDE) could be successfully employed as an electrochemical screening tool for catalysts for CO_2 electroreduction. It could be used for high-throughput electrochemical testing as predicted in the hypothesis in Chapter 1. This is particularly important as compared to current

three electrode systems that are typically used for CO_2 electroreduction where the catalyst testing is significantly limited. A product calibration was carried out, where known concentrations of formic acid (125 mM) and methanol (12 mM) were added to the electrolytes ($KHCO_3$ and K_2HPO_4) and their electrochemical response was studied. The oxidation peak for formic acid was observed at 0.14 V and methanol at 0.19 V. It was observed that the electrolyte made a significant difference to the current density during the product oxidation; methanol oxidation was favourable in phosphate based electrolyte compared to formic acid oxidation, which was favourable in $KHCO_3$. This was due to the preferential binding of carbonate on Pt, which suppressed methanol oxidation.

CuO based catalysts were tested using the RRDE for CO_2 electroreduction where the effect of the disk potential on the Pt ring and product oxidation was investigated. The disk was held in the range –0.6 to –1.4 V vs Ag/AgCl and HCOOH was detected on the Pt ring above –1.2 V. The rotation rate was altered, from 0 to 2500 rpm, and 2500 rpm was found to the optimum rotation rate as the highest current density was achieved for formic acid oxidation.

7.2 Future Work

The work conducted in this thesis presents with scope for future work. The insight gained from the synthesis of CuO, Cu_2O and Cu can be applied to other potential nanocatalysts for electroreduction of CO_2, such as SnO_2, ZnO and NiO. Further study with a wider range of parameter may be explored, such as combining KOH and H_2O_2 to maximise supersaturation and increase the nucleation rate even further, and could allow for the synthesis of even smaller CuO nanoparticles. For the synthesis of Cu_2O and Cu, mixer designs can be altered, by use of a laminar mixer, to limit particle growth or to control morphology and size through changing surface functionalisation groups (from PVP to triethanolamine).

Through the optimisation of the catalyst layer and Nafion fraction, high Faradaic efficiency for HCOOH could be obtained. The inks can be tested in an electrolyser type device for the scale up conversion of CO_2 to HCOOH. Preliminary studies show contamination issue, which need to be resolved and the testing conditions need to be optimised. For CO_2 utilisation is concerned, as mentioned in Chapter 1, scale up devices are required to move it further up in terms of technology readiness levels. Currently, the optimised catalyst has been tested for 24 hours and longer stability tests in a device set up are required to further optimise the structure property relationship, and synthesise further optimised catalysts. Other optimisation routes include exploring different ionomers including modified Nafion ionomers with improved proton conductivity or exploring binders such as PVDF or PTFE.

Doping CuO via CHFS can allow the overpotential to be lowered and the Faradaic efficiency to be increased in the electroreduction of CO_2. Other metal dopants, apart from Ni, may be explored (Zn, Fe, Mn, Co), which may enhance the electroreduction of CO_2. Further structural characterisation is required to understand the interaction of Ni within the CuO host structure, through synchrotron XAS and XRD studies. Moreover, in operando studies are required to understand how the morphology changes in situ to relate this to structure property relationship and better control the morphology change in electrocatalysis to favourably hinder or enhance certain products.

Future work may involve studying the degradation of the catalysts tested to study how the product formation would vary over time. This would provide an insight into whether there is catalyst degradation and if there is a time induction present in product formation, particularly at lower overpotentials. This has not been previously considered in the literature for CO_2 catalysis and would further exploit the RRDE system for in-situ product detection. The RRDE could also probe the effect of the product concentration in the

calibration stage. Constructing a calibration curve could allow detection of the amount of product formed in-situ and compare with NMR and GC data at the bulk electrolysis stage.

Chapter 8. References

1 Q. Ma, Greenhouse Gases: Refining the Role of Carbon Dioxide, https://www.giss.nasa.gov/research/briefs/ma_01/, (accessed 18 February 2018).

2 2013 IPCC, *Climate Change 2013: The Physical Science Basis. Contribution of Working Group I to the Fifth Assessment Report of the Intergovern- mental Panel on Climate Change*, Cambridge University Press, Cambridge, United Kingdom, 2013.

3 2014 IPCC, *Climate Change 2014: Mitigation of Climate Change. Contribution of Working Group III to the Fifth Assessment Report of the Intergovernmental Panel on Climate Change*, Cambridge University Press, Cambridge, United Kingdom, 2014.

4 C. Song, *Catal. Today*, 2006, **115**, 2–32.

5 BP, BP Energy Outlook 2030, http://www.bp.com/content/dam/bp/pdf/energy-economics/energy-outlook-2015/bp-energy-outlook-booklet_2013.pdf, (accessed 25 August 2017).

6 E. V. Kondratenko, G. Mul, J. Baltrusaitis, G. O. Larrazabal, J. Perez-Ramirez, G. O. Larrazábal and J. Pérez-Ramírez, *Energy Environ. Sci.*, 2013, **6**, 3112.

7 J. N. Armor, *Catal. Today*, 2014, **236**, 171–181.

8 2005 IPCC, *IPCC Special Report on Carbon Dioxide Capture and Storage. Prepared by Working Group III of the Intergovernmental Panel on Climate Change*, Cambridge University Press for the Intergovernmental Panel on Climate Change, Cambridge, United Kingdom, 2005.

9 UNFCCC, The Paris Agreement, http://unfccc.int/paris_agreement/items/9485.php, (accessed 22 August 2017).

10 P. Styring, D. Jansen, H. de Coninck, H. Reith and K. Armstrong, *Carbon Capture and Utilisation in the green economy*, The Centre for

Low Carbon Futures 2011 and CO2Chem Publishing 2012, 2011.

11 P. Freund, *Anthropogenic climate change and the role of CO2 capture and storage (CCS)*, Woodhead Publishing Limited, 2013.

12 S. L. Suib, *New and future developments in catalysis activation of carbon dioxide*, Elsevier Science & Technology, 2013.

13 M. A. Scibioh and B. Viswanathan, *Proc. Indian Natl. Sci. Acad. Part A Phys. Sci.*, 2004, **70**, 407–462.

14 D. Keith and M. Mahmoudkhani, *Carbon dioxide capture and storage*, Cambridge University Press, 2012.

15 M. Mikkelsen, M. Jørgensen and F. C. Krebs, *Energy Environ. Sci.*, 2010, **3**, 43–81.

16 J. Wu and X.-D. Zhou, *Chinese J. Catal.*, 2016, **37**, 999–1015.

17 I. Ganesh, *Renew. Sustain. Energy Rev.*, 2014, **31**, 221–257.

18 S. Enthaler, J. von Langermann and T. Schmidt, *Energy Environ. Sci.*, 2010, **3**, 1207–1217.

19 G. A. Olah, A. Goeppert and G. K. S. Prakash, *Beyond Oil and Gas: The Methanol Economy*, Wiley-VCH Verlag GmbH & Co. KGaA, 2nd edn., 2011.

20 I. Ganesh, *Mater. Sci. Forum*, 2013, **764**, 1–82.

21 S. Mukhopadhyay and A. T. Bell, *Adv. Synth. Catal.*, 2004, **346**, 913–916.

22 C. D. Windle and R. N. Perutz, *Coord. Chem. Rev.*, 2012, **256**, 2562–2570.

23 N. A. M. Razali, K. T. Lee, S. Bhatia and A. R. Mohamed, *Renew. Sustain. Energy Rev.*, 2012, **16**, 4951–4964.

24 S. Das and W. M. a. Wan Daud, *RSC Adv.*, 2014, **4**, 20856–20893.

25 W. Wang, S. Wang, X. Ma and J. Gong, *Chem. Soc. Rev.*, 2011, **40**, 3703–3727.

26 E. E. Benson, C. P. Kubiak, A. J. Sathrum and J. M. Smieja, *Chem. Soc. Rev.*, 2009, **38**, 89–99.

27 M. Michman, L. Appelbaum, J. Gun, A. D. Modestov and O. Lev, *Organometallics*, 2014, **33**, 4729–4737.

28 V. Jeyalakshmi, K. Rajalakshmi, R. Mahalakshmy, K. R. Krishnamurthy and B. Viswanathan, *Res. Chem. Intermed.*, 2013, **39**, 2565–2602.

29 X. Lu, D. Y. C. Leung, H. Wang, M. K. H. Leung and J. Xuan, *ChemElectroChem*, 2014, **1**, 836–849.

30 M. Gattrell, N. Gupta and A. Co, *J. Electroanal. Chem.*, 2006, **594**, 1–19.

31 J. P. Jones, G. K. Prakash and G. A. Olah, *Isr. J. Chem.*, 2014, **54**, 1451–1466.

32 B. Viswanathan, in *New and Future Developments in Catalysis: Activation of carbon dioxide*, ed. S. L. Suib, Elsevier B.V, 2013, pp. 275–295.

33 M. Alvarez-Guerra, J. Albo, E. Alvarez-Guerra, A. Irabien, W. Zhu, A. Salehi-Khojin, D. D. Dlott, R. I. Masel, W. Zhu, R. Haasch, R. F. Klie, P. Král, J. Abiade, A. Salehi-Khojin, D. H. Gibson, W. A. Goddard, D. W. Goodman, J. Keller, G. J. Kubas, H. H. Kung, J. E. Lyons, L. E. Manzer, T. J. Marks, K. Morokuma, K. M. Nicholas, R. Periana, L. Que, J. Rostrup-Nielson, W. M. H. Sachtler, L. D. Schmidt, A. Sen, G. A. Somorjai, P. C. Stair, B. R. Stults and W. Tumas, *Energy Environ. Sci.*, 2015, **8**, 2574–2599.

34 M. Bersani, K. Gupta, A. K. Mishra, R. Lanza, S. F. R. Taylor, H. U. Islam, N. Hollingsworth, C. Hardacre, N. H. De Leeuw and J. A. Darr, *ACS Catal.*, 2016, **6**, 5823–5833.

35 A. J. Bard and L. R. Faulkner, *Electrochemical Methods: Fundamentals and Applications*, Wiley-VCH Verlag GmbH & Co. KGaA, 2nd edn.

36 Y. Hori, K. Kikuchi and S. Suzuki, *Chem. Lett.*, 1985, **14**, 1695–1698.

37 D. Pletcher, *Electrochem. commun.*, 2015, **61**, 97–101.

38 L. Carrette, K. A. Friedrich and U. Stimming, *Chem. Phys. Chem*,

2000, **1**, 162–193.

39 H. Yoshio, K. Katsuhei, M. Akira and S. Shin, *Chem. Lett.*, 1986, **15**, 897–898.

40 Y. Hori, in *Solar to Chemical Energy Conversion*, Springer International Publishing, 2016, vol. 32, pp. 191–211.

41 R. Kortlever, J. Shen, K. J. P. Schouten, F. Calle-Vallejo and M. T. M. Koper, *J. Phys. Chem. Lett.*, 2015, **6**, 4073–4082.

42 W. Sheng, S. Kattel, S. Yao, B. Yan, Z. Liang, C. J. Hawxhurst, Q. Wu, J. G. Chen, S. H. Sun, R. E. Winans and A. K. Datye, *Energy Environ. Sci.*, 2017, **10**, 1180–1185.

43 K. J. P. Schouten, Z. Qin, E. P. Gallent and M. T. M. Koper, *J. Am. Chem. Soc.*, 2012, **134**, 9864–9867.

44 Y. Hori, R. Takahashi, Y. Yoshinami and A. Murata, *J. Phys. Chem. B*, 1997, **101**, 7075–7081.

45 D. Kim, J. Resasco, Y. Yu, A. M. Asiri and P. Yang, *Nat. Commun.*, 2014, **5**, 4948.

46 A. Murata and Y. Hori, *Chem. Soc. Japan*, 1991, **64**, 123–127.

47 I. Takahashi, O. Koga, N. Hoshi and Y. Hori, *J. Electroanal. Chem.*, 2002, **533**, 135–143.

48 D. D. Zhu, J. L. Liu and S. Z. Qiao, *Adv. Mater.*, 2016, **28**, 3423–3452.

49 M. Le, M. Ren, Z. Zhang, P. T. Sprunger, R. L. Kurtz and J. C. Flake, *J. Electrochem. Soc.*, 2011, **158**, E45–E49.

50 J. J. Kim, D. P. Summers and K. W. Frese, *J. Electroanal. Chem. Interfacial Electrochem.*, 1988, **245**, 223–244.

51 K. W. Frese, *J. Electrochem. Soc.*, 1991, **138**, 3338.

52 Y.-J. Zhang and A. a Peterson, *Phys. Chem. Chem. Phys.*, 2015, **17**, 4505–15.

53 R. Reske, M. Duca, M. Oezaslan, K. J. P. Schouten, M. T. M. Koper

and P. Strasser, *J. Phys. Chem. Lett.*, 2013, **4**, 2410–2413.

54 A. Dutta, M. Rahaman, N. C. Luedi, M. Mohos and P. Broekmann, *ACS Catal.*, 2016, **6**, 3804–3814.

55 Z.-L. Wang, C. Li and Y. Yamauchi, *Nano Today*, 2016, **11**, 373–391.

56 R. Reske, H. Mistry, F. Behafarid, B. R. Cuenya and P. Strasser, *J. Am. Chem. Soc.*, 2014, **136**, 6978–6986.

57 K. Manthiram, B. J. Beberwyck and A. P. Alivisatos, *J. Am. Chem. Soc.*, 2014, **136**, 13319–13325.

58 W. Tang, A. A. Peterson, A. S. Varela, Z. P. Jovanov, L. Bech, W. J. Durand, S. Dahl, J. K. Norskov and I. Chorkendorff, *Phys. Chem. Chem. Phys.*, 2012, **14**, 76–81.

59 S. Sen, D. Liu and G. T. R. Palmore, *ACS Catal.*, 2014, **4**, 3091–3095.

60 T. Y. Chang, R. M. Liang, P. W. Wu, J. Y. Chen and Y. C. Hsieh, *Mater. Lett.*, 2009, **63**, 1001–1003.

61 S. Ohya, S. Kaneco, H. Katsumata, T. Suzuki and K. Ohta, *Catal. Today*, 2009, **148**, 329–334.

62 C. W. Li and M. W. Kanan, *J. Am. Chem. Soc.*, 2012, **134**, 7231–7234.

63 J. F. Xie, Y. X. Huang, W. W. Li, X. N. Song, L. Xiong and H. Q. Yu, *Electrochim. Acta*, 2014, **139**, 137–144.

64 A. J. Martín, G. O. Larrazábal and J. Pérez-Ramírez, *Green Chem.*, 2015, **17**, 5114–5130.

65 K. Philippot and P. Serp, in *Nanomaterials in Catalysis*, Wiley-VCH Verlag GmbH & Co. KGaA, Weinheim, Germany, 2012, pp. 1–54.

66 M. H. Van de Voorde and H. Dosch, *Grand European initiative on nanoscience and nanotechnology using neutron and synchrotron radiation sources*, Max-Planck-Institut Fur Metallforschung, Stuttgart, 2009.

67 T. Prasad Yadav, R. Manohar Yadav and D. Pratap Singh, *Nanosci. Nanotechnol.*, 2012, **2**, 22–48.

68 V. Sebastian, M. Arruebo and J. Santamaria, *Small*, 2014, **10**, 835–853.

69 S. Barth, F. Hernandez-Ramirez, J. D. Holmes and A. Romano-Rodriguez, *Prog. Mater. Sci.*, 2010, **55**, 563–627.

70 E. C. Vreeland, J. Watt, G. B. Schober, B. G. Hance, M. J. Austin, A. D. Price, B. D. Fellows, T. C. Monson, N. S. Hudak, L. Maldonado-Camargo, A. C. Bohorquez, C. Rinaldi and D. L. Huber, *Chem. Mater.*, 2015, **27**, 6059–6066.

71 G. Oskam and F. de J. P. Poot, *J. Sol-Gel Sci. Technol.*, 2006, **37**, 157–160.

72 G. Coquerel, *Chem. Soc. Rev.*, 2014, **43**, 2286.

73 N. T. K. Thanh, N. Maclean and S. Mahiddine, *Chem. Rev.*, 2014, **114**, 7610–7630.

74 M. B. Gawande, A. Goswami, F.-X. Felpin, T. Asefa, X. Huang, R. Silva, X. Zou, R. Zboril and R. S. Varma, *Chem. Rev.*, 2016, **116**, 3722–3811.

75 C. Wang, Q. Li, F. Wang, G. Xia, R. Liu, D. Li, N. Li, J. S. Spendelow and G. Wu, *ACS Appl. Mater. Interfaces*, 2014, **6**, 1243–1250.

76 Z. Zhang and P. Wang, *J. Mater. Chem.*, 2012, **22**, 2456–2464.

77 K. J. Choi and H. W. Jang, *Sensors*, 2010, **10**, 4083–4099.

78 X. Zhang, W. Shi, J. Zhu, D. J. Kharistal, W. Zhao, B. S. Lalia, H. H. Hng and Q. Yan, *ACS Nano*, 2011, **5**, 2013–2019.

79 C. C. Vidyasagar, Y. A. Naik, T. G. Venkatesh and R. Viswanatha, *Powder Technol.*, 2011, **214**, 337–343.

80 B. Rohe, R. Weiss, S. Vukojević, C. Baltes, M. Muhler, M. Tausch and M. Epple, *Eur. J. Inorg. Chem.*, 2007, **2007**, 1723–1727.

81 J. Zhu, H. Bi, Y. Wang, X. Wang, X. Yang and L. Lu, *Mater. Chem. Phys.*, 2008, **109**, 34–38.

82 X. Zhang, D. Zhang, X. Ni, J. Song and H. Zheng, *J. Nanoparticle*

Res., 2008, **10**, 839–844.

83 M. P. Neupane, Y. K. Kim, S. Park, K. A. Kim, M. H. Lee and T. S. Bae, *Surf. Interface Anal.*, 2009, **41**, 259–263.

84 S. Chakraborty, A. Das, M. R. Begum, S. Dhara and A. K. Tyagi, *AIP Conf. Proc.*, 2011, **1349**, 841–842.

85 A. S. Ethiraj and D. J. Kang, *Nanoscale Res. Lett.*, 2012, **7**, 70.

86 A. Nowak, J. Szade, E. Talik, A. Ratuszna, M. Ostafin and J. Peszke, *Mater. Chem. Phys.*, 2014, **145**, 465–470.

87 C. H. Kuo and M. H. Huang, *Nano Today*, 2010, **5**, 106–116.

88 Y. Cao, Y. Xu, H. Hao and G. Zhang, *Mater. Lett.*, 2014, **114**, 88–91.

89 D. Dodoo-Arhin, M. Leoni, P. Scardi, E. Garnier and A. Mittiga, *Mater. Chem. Phys.*, 2010, **122**, 602–608.

90 Y. Qu, X. Li, G. Chen, H. Zhang and Y. Chen, *Mater. Lett.*, 2008, **62**, 886–888.

91 P. Dunn, in *Handbook of Green Chemistry, Green Solvents, Reactions in Water*, eds. P. Anastas and C. Jun-Li, Wiley-VCH Verlag GmbH & Co. KGaA, 2010.

92 C. Aymonier, A. Loppinet-Serani, H. Reverón, Y. Garrabos and F. Cansell, *J. Supercrit. Fluids*, 2006, **38**, 242–251.

93 M. Boero, K. Terakura, T. Ikeshoji, C. C. Liew and M. Parrinello, *J. Chem. Phys.*, 2001, **115**, 2219–2227.

94 D. Larsen, 'Phase Diagrams' Chem Wiki: The Dynamic Chemistry Textbook, https://chem.libretexts.org/LibreTexts/University_of_Arkansas_Little_Rock/Chem_1403%3A_General_Chemistry_2/Chapters/12%3A_Solids/12.7_Phase_Diagrams, (accessed 25 July 2017).

95 H. Weingärtner and E. U. Franck, *Angew. Chemie - Int. Ed.*, 2005, **44**, 2672–2692.

96 D. P. Fernández, Y. Mulev, A. R. H. Goodwin and J. M. H. L. Sengers,

J. Phys. Chem. Ref. Data, 1995, **24**, 33–70.

97 G. Brunner, *Annu. Rev. Chem. Biomol. Eng.*, 2010, **1**, 321–342.

98 J. W. Tester and J. Cline, *Corrosion*, 1999, **55**, 1088–1100.

99 M. M. Hoffmann, J. G. Darab, B. J. Palmer and J. L. Fulton, *J. Phys. Chem. A*, 1999, **103**, 8471–8482.

100 K. Byrappa and T. Adschiri, *Prog. Cryst. Growth Charact. Mater.*, 2007, **53**, 117–166.

101 T. Adschiri, K. Kanazawa and K. Arai, *J. Am. Ceram. Soc.*, 1992, **75**, 1019–1022.

102 Y. Hakuta, T. Adschiri, T. Suzuki, T. Chida, K. Seino and K. Arai, *J. Am. Ceram. Soc.*, 2005, **81**, 2461–2464.

103 E. Lester, P. Blood, J. Denyer, D. Giddings, B. Azzopardi and M. Poliakoff, *J. Supercrit. Fluids*, 2006, **37**, 209–214.

104 S.-I. Kawasaki, K. Sue, R. Ookawara, Y. Wakashima, A. Suzuki, Y. Hakuta and K. Arai, *J. Supercrit. Fluids*, 2010, **54**, 96–102.

105 S. ichiro Kawasaki, K. Sue, R. Ookawara, Y. Wakashima and A. Suzuki, *J. Oleo Sci.*, 2010, **59**, 557–562.

106 K. Sue, T. Sato, S. Kawasaki, Y. Takebayashi, S. Yoda, T. Furuya and T. Hiaki, *Ind. Eng. Chem. Res.*, 2010, **49**, 8841–8846.

107 C. J. Tighe, R. I. Gruar, C. Y. Ma, T. Mahmud, X. Z. Wang and J. A. Darr, *J. Supercrit. Fluids*, 2012, **62**, 165–172.

108 C. J. Tighe, R. Q. Cabrera, R. I. Gruar and J. A. Darr, *Ind. Eng. Chem. Res.*, 2013, **52**, 5522–5528.

109 R. I. Gruar, C. J. Tighe and J. A. Darr, *Ind. Eng. Chem. Res.*, 2013, **52**, 5270–5281.

110 Darr, J.A., Tighe, C., Gruar, R., US Patent Office, 9,192,901, 2015.

111 R. I. Gruar, C. J. Tighe, P. Southern, Q. a. Pankhurst and J. a. Darr, *Ind. Eng. Chem. Res.*, 2015, **54**, 7436–7451.

112 P. Boldrin, PhD Thesis, Queen Mary, University of London, 2008.

113 C. J. Denis, C. J. Tighe, R. I. Gruar, N. M. Makwana and J. A. Darr, *Cryst. Growth Des.*, 2015, **15**, 4256–4265.

114 N. M. Makwana, PhD Thesis, University College London (UCL), 2015.

115 C. J. Denis, PhD Thesis, University College London (UCL), 2016.

116 S. Schimpf, A. Rittermeier, X. Zhang, Z. A. Li, M. Spasova, M. W. E. van den Berg, M. Farle, Y. Wang, R. A. Fischer and M. Muhler, *ChemCatChem*, 2010, **2**, 214–222.

117 J. B. Park, J. Graciani, J. Evans, D. Stacchiola, S. D. Senanayake, L. Barrio, P. Liu, J. F. Sanz, J. Hrbek and J. A. Rodriguez, *J. Am. Chem. Soc.*, 2010, **132**, 356–363.

118 Q. Zhang, K. Zhang, D. Xu, G. Yang, H. Huang, F. Nie, C. Liu and S. Yang, *Prog. Mater. Sci.*, 2014, **60**, 208–237.

119 K. Sue, M. Suzuki, K. Arai, T. Ohashi, H. Ura, K. MATSUI, Y. Hakuta, H. Hayashi, M. Watanabe and T. Hiaki, *Green Chem.*, 2006, **8**, 634–638.

120 K. Sue, S. I. Kawasaki, M. Suzuki, Y. Hakuta, H. Hayashi, K. Arai, Y. Takebayashi, S. Yoda and T. Furuya, *Chem. Eng. J.*, 2011, **166**, 947–953.

121 L. Zhou, S. Wang, D. Xu and Y. Guo, *Ind. Eng. Chem. Res.*, 2014, **53**, 481–493.

122 P. Boldrin, A. K. Hebb, A. A. Chaudhry, L. Otley, B. Thiebaut, P. Bishop and J. A. Darr, *Ind. Eng. Chem. Res.*, 2007, **46**, 4830–4838.

123 L. Shi, A. J. T. Naik, J. B. M. Goodall, C. Tighe, R. Gruar, R. Binions, I. Parkin and J. Darr, *Langmuir*, 2013, **29**, 10603–10609.

124 E. Lester, G. Aksomaityte, J. Li, S. Gomez, J. Gonzalez-Gonzalez and M. Poliakoff, *Prog. Cryst. Growth Charact. Mater.*, 2012, **58**, 3–13.

125 K. J. Ziegler, R. C. Doty, K. P. Johnston and B. A. Korgel, *J. Am. Chem. Soc.*, 2001, **123**, 7797–7803.

126 S. Kubota, T. Morioka, M. Takesue, H. Hayashi, M. Watanabe and R. L. Smith, *J. Supercrit. Fluids*, 2014, **86**, 33–40.

127 L. Zhou, S. Wang, H. Ma, S. Ma, D. Xu and Y. Guo, *Chem. Eng. Res. Des.*, 2015, **98**, 36–43.

128 S. W. Young and A. E. Stearn, *J. Am. Chem. Soc.*, 1916, **38**, 1947–1953.

129 A. H. Zittlau, Q. Shi, J. Boerio-Goates, B. F. Woodfield and J. Majzlan, *Chemie der Erde - Geochemistry*, 2013, **73**, 39–50.

130 J. Stodola, P. Tremaine, V. Binette and L. Trevani, *Powerpl. Chem.*, 2000, **2**, 9–13.

131 D. A. Palmer, J. M. Simonson and D. B. Joyce, in *Conference on Interaction of Non Iron-Based Material with Water and Steam*, Piacenza, Italy, 1996, pp. 7-1-7–17.

132 Z. Xiao, C. H. Gammons and A. E. Williams-Jones, *Geochim. Cosmochim. Acta*, 1998, **62**, 2949–2964.

133 J. Brugger, D. C. McPhail, J. Black and L. Spiccia, *Geochim. Cosmochim. Acta*, 2001, **65**, 2691–2708.

134 T. Jiang, M. Bujoli-Doeuff, Y. Farré, Y. Pellegrin, E. Gautron, M. Boujtita, L. Cario, S. Jobic, F. Odobel, F. Odobel and W. J. Youngblood, *RSC Adv.*, 2016, **6**, 112765–112770.

135 A. V. Nikam, A. Arulkashmir, K. Krishnamoorthy, A. A. Kulkarni and B. L. V Prasad, *Cryst. Growth Des.*, 2014, **14**, 4329–4334.

136 X. Liu, J. Zhang, Y. Kang, S. Wu and S. Wang, *CrystEngComm*, 2012, **14**, 620–625.

137 A. A. Novikova, D. Y. Moiseeva, E. V. Karyukov and A. A. Kalinichenko, *Mater. Lett.*, 2016, **167**, 165–169.

138 D. Palmer and P. Bénézeth, in *14th International Conference on the Properties of Water and Steam in Kyoto*, 2004, pp. 491–496.

139 K. Sue, Y. Hakuta, R. L. Smith, T. Adschiri and K. Arai, *J. Chem. Eng. Data*, 1999, **44**, 1422–1426.

140 L. J. Cote, A. S. Teja, A. P. Wilkinson and Z. J. Zhang, *J. Mater. Res.*, 2002, **17**, 2410–2416.

141 A. Cabañas and M. Poliakoff, *J. Mater. Chem.*, 2001, **11**, 1408–1416.

142 P. E. Savage, *Chem. Rev.*, 1999, **99**, 603–622.

143 N. Takeno, *Atlas of Eh-pH diagrams*, Japan, 2005.

144 B. Beverskog and I. Puigdomenech, *J. Electrochem. Soc.*, 1997, **144**, 3476.

145 A. Sleigh and C. Noakes, *An Introduction To Fluid Mechanics*, 2009.

146 W. Wagner and A. Pruß, *J. Phys. Chem. Ref. Data*, 2002, **31**, 387–535.

147 T. Morioka, M. Takesue, H. Hayashi, M. Watanabe and R. L. Smith, *ACS Appl. Mater. Interfaces*, 2016, **8**, 1627–1634.

148 J. L. Yu and P. E. Savage, *Ind. Eng. Chem. Res.*, 1998, **37**, 2–10.

149 Y. Zhang, J. Zhang, L. Zhao and C. Sheng, *Energy and Fuels*, 2010, **24**, 95–99.

150 G. Aksomaityte, M. Poliakoff and E. Lester, *Chem. Eng. Sci.*, 2013, **85**, 2–10.

151 C. Peniche, D. Zaldívar, M. Pazos, S. Páz, A. Bulay and J. S. Román, *J. Appl. Polym. Sci.*, 1993, **50**, 485–493.

152 Y. Yasaka, K. Yoshida, C. Wakai, N. Matubayasi and M. Nakahara, *J. Phys. Chem. A*, 2006, **110**, 11082–11090.

153 S. Poulston, P. M. Parlett, P. Stone and M. Bowker, *Surf. Interface Anal.*, 1996, **24**, 811–820.

154 S. Komarneni, Y. Noh, J. Kim, S. Kim and H. Katsuki, *Z. Naturforsch*, 2010, **65b**, 1033–1037.

155 S. Magdassi, *The Chemistry of Inkjet Inks*, World Scientific Publishing Co. Pte. Ltd., 2010.

156 J. Qiao, M. Fan, Y. Fu, Z. Bai, C. Ma, Y. Liu and X. D. Zhou, *Electrochim. Acta*, 2015, **153**, 559–565.

157 J. Albo, M. Alvarez-Guerra, P. Castaño and A. Irabien, *Green Chem.*, 2015, **17**, 2304–2324.

158 H. Mistry, F. Behafarid, R. Reske, A. S. Varela, P. Strasser and B. Roldan Cuenya, *ACS Catal.*, 2016, **6**, 1075–1080.

159 W. Grot, *Fluorinated Ionomers*, Elsevier, 2nd edn., 2011.

160 PermaPure, All about Nafion, http://www.permapure.com/resources/all-about-nafion-and-faq/, (accessed 25 June 2017).

161 D. Dunwoody and J. Leddy, *Electrochem. Soc. Interface*, 2005, **14**, 37–39.

162 J. Wu, F. G. Risalvato, P. P. Sharma, P. J. Pellechia, F.-S. Ke and X.-D. Zhou, *J. Electrochem. Soc.*, 2013, **160**, 953–957.

163 T. T. Ngo, T. L. Yu and H. L. Lin, *J. Power Sources*, 2013, **225**, 293–303.

164 S. M. Andersen and L. Grahl-Madsen, *Int. J. Hydrogen Energy*, 2016, **41**, 1892–1901.

165 Q. Wang, H. Dong and H. Yu, *RSC Adv.*, 2014, **4**, 59970–59976.

166 J. Wu, P. P. Sharma, B. H. Harris and X. Zhou, *J. Power Sources*, 2014, **258**, 189–194.

167 S.-J. Shin, J.-K. Lee, H.-Y. Ha, S. -a. Hong, H.-S. Chun and I.-H. Oh, *J. Power Sources*, 2002, **106**, 146–152.

168 B. G. Pollet and J. T. E. Goh, *Electrochim. Acta*, 2014, **128**, 292–303.

169 A. Suzuki, U. Sen, T. Hattori, R. Miura, R. Nagumo, H. Tsuboi, N. Hatakeyama, A. Endou, H. Takaba, M. C. Williams and A. Miyamoto, *Int. J. Hydrogen Energy*, 2011, **36**, 2221–2229.

170 C. J. Jacobs, Master's Thesis, University of Cape Town, 2016.

171 B. Cullity, *Elements of X-Ray Diffraction*, Pearson, 3rd edn., 2001.

172 J. A. Darr and M. Poliakoff, *Chem. Rev.*, 1999, **99**, 495–541.

173 K. Byrappa, S. Ohara and T. Adschiri, *Adv. Drug Deliv. Rev.*, 2008, **60**, 299–327.

174 K. Byrappa and T. Adschiri, *Prog. Cryst. Growth Charact. Mater.*, 2007, **53**, 117–166.

175 L. Serguei, B. Justin and M. LaBarbera, in *Carbon-Neutral Fuels and Energy Carriers*, eds. N. Z. Muradov and T. N. Veziroglu, CRC Press, 2011, pp. 363–400.

176 H. Momand, Master's Thesis, University of Birmingham, 2013.

177 B. G. Pollet, *Electrocatalysis*, 2014, **5**, 330–343.

178 S. S. Kocha, J. W. Zack, S. M. Alia, K. C. Neyerlin and B. S. Pivovar, *ECS Trans.*, 2013, **50**, 1475–1485.

179 C.-H. Ma, T. L. Yu, H.-L. Lin, Y.-T. Huang, Y.-L. Chen, U.-S. Jeng, Y.-H. Lai and Y.-S. Sun, *Polymer (Guildf).*, 2009, **50**, 1764–1777.

180 T. T. Ngo, T. L. Yu and H. L. Lin, *J. Power Sources*, 2013, **238**, 1–10.

181 M. K. Sharma, *Surface Phenomena in Coatings and Printing Technology*, Plenum Press, 1991.

182 Y. Lan, C. Gai, P. J. A. Kenis and J. Lu, *Chemelectrochem*, 2014, **1**, 1577–1582.

183 W. Yi, J. Liu, H. Chen, Y. Gao and H. Li, *J. Solid State Electrochem.*, 2015, **19**, 1511–1521.

184 A. A. Peterson, F. Abild-Pedersen, F. Studt, J. Rossmeisl and J. K. Norskov, *Energy Environ. Sci.*, 2010, **3**, 1311–1315.

185 W. J. Durand, A. A. Peterson, F. Studt, F. Abild-Pedersen and J. K. Nørskov, *Surf. Sci.*, 2011, **605**, 1354–1359.

186 X. Su, J. Zhao, H. Bala, Y. Zhu, Y. Gao, S. Ma and Z. Wang, *J. Phys. Chem. C*, 2007, **111**, 14689–14693.

187 Y. Hori, H. Konishi, T. Futamura, A. Murata, O. Koga, H. Sakurai and

K. Oguma, *Electrochim. Acta*, 2005, **50**, 5354–5369.

188 A. Taheri Najafabadi, *Int. J. Energy Res.*, 2013, **37**, 485–499.

189 J. W. Vickers, D. Alfonso and D. R. Kauffman, *Energy Technol.*, 2017, **5**, 775–795.

190 F. Jia, X. Yu and L. Zhang, *J. Power Sources*, 2014, **252**, 85–89.

191 M. Watanabe, M. Shibata and A. Kato, *J. Electrochem. Soc.*, 1991, **138**, 3382–3389.

192 N. Todoroki, N. Yokota, S. Nakahata, H. Nakamura and T. Wadayama, *Electrocatalysis*, 2016, **7**, 97–103.

193 L. Ou, W. Long, J. Huang, Y. Chen and J. Jin, *RSC Adv.*, 2017, **7**, 11938–11950.

194 P. Hirunsit, *J. Phys. Chem. C*, 2013, **117**, 8262–8268.

195 P. Hirunsit, W. Soodsawang and J. Limtrakul, *J. Phys. Chem. C*, 2015, **119**, 8238–8249.

196 J. A. Schwarz, C. Contescu and A. Contescu, *Chem. Rev.*, 1995, **95**, 477–510.

197 N. Mohamed Basith, J. Judith Vijaya, L. John Kennedy and M. Bououdina, *Phys. E Low-Dimensional Syst. Nanostructures*, 2013, **53**, 193–199.

198 J. B. Amaral, R. M. Araujo, P. P. Pedra, C. T. Meneses, J. G. S. Duque and M. V. D. Rezende, *J. Solid State Chem.*, 2016, **241**, 26–29.

199 S. Ramya, G. Viruthagiri, R. Gobi, N. Shanmugam and N. Kannadasan, *J. Mater. Sci. Mater. Electron.*, 2016, **27**, 2701–2711.

200 C. T. Meneses, J. G. S. Duque, L. G. Vivas and M. Knobel, *J. Non. Cryst. Solids*, 2008, **354**, 4830–4832.

201 D. P. Howard, P. Marchand, L. McCafferty, C. J. Carmalt, I. P. Parkin and J. A. Darr, *ACS Comb. Sci.*, 2017, **19**, 239–245.

202 I. D. Johnson, M. Lübke, O. Y. Wu, N. M. Makwana, G. J. Smales, H.

U. Islam, R. Y. Dedigama, R. I. Gruar, C. J. Tighe, D. O. Scanlon, F. Corà, D. J. L. Brett, P. R. Shearing and J. A. Darr, *J. Power Sources*, 2016, **302**, 410–418.

203 M. Lübke, I. Johnson, N. M. Makwana, D. Brett, P. Shearing, Z. Liu and J. A. Darr, *J. Power Sources*, 2015, **294**, 94–102.

204 W. L. Suchanek, *J. Cryst. Growth*, 2009, **312**, 100–108.

205 J. B. M. Goodall, PhD Thesis, University College London (UCL), 2009.

206 J. Matienzo, L. I. Yin, S. O. Grim and W. E. Swartz, *Inorg. Chem.*, 1973, **12**, 2762–2769.

207 D. Rangappa, S. Ohara, M. Umetsu, T. Naka and T. Adschiri, *J. Supercrit. Fluids*, 2008, **44**, 441–445.

208 L. Vegard, *Zeitschrift für Phys.*, 1921, **5**, 17–26.

209 J. D. Bryan and D. R. Gamelin, John Wiley & Sons, Inc., 2005, pp. 47–126.

210 S. Al-Amri, M. Ansari, S. Rafique, M. Aldhahri, S. Rahimuddin, A. Azam and A. Memic, *Curr. Nanosci.*, 2015, **11**, 191–197.

211 P. M. Diehm, P. Ágoston and K. Albe, *ChemPhysChem*, 2012, **13**, 2443–2454.

212 W. Qin, T. Nagase, Y. Umakoshi and J. A. Szpunar, *Philos. Mag. Lett.*, 2008, **88**, 169–179.

213 W. H. Qi, M. P. Wang and Y. C. Su, *J. Mater. Sci. Lett.*, 2002, **21**, 877–878.

214 F. Zhang, S.-W. Chan, J. E. Spanier, E. Apak, Q. Jin, R. D. Robinson and I. P. Herman, *Appl. Phys. Lett.*, 2002, **80**, 127–129.

215 F. Zhang, Q. Jin and S.-W. Chan, *J. Appl. Phys.*, 2004, **95**, 4319–4326.

216 J. Song, P. P. Rodenbough, L. Zhang and S.-W. Chan, *Int. J. Appl. Ceram. Technol.*, 2016, **13**, 389–394.

217 V. Perebeinos, S.-W. Chan and F. Zhang, *Solid State Commun.*, 2002,

123, 295–297.

218 P. P. Rodenbough, C. Zheng, Y. Liu, C. Hui, Y. Xia, Z. Ran, Y. Hu and S.-W. Chan, *J. Am. Ceram. Soc.*, 2017, **100**, 384–392.

219 D. S. Hall, D. J. Lockwood, C. Bock and B. R. MacDougall, *Proceedings. Math. Phys. Eng. Sci.*, 2015, **471**, 20140792.

220 J. Crousier and I. Bimaghra, *J. Appl. Electrochem.*, 1993, **23**, 775–780.

221 J. K. Nørskov, J. Rossmeisl, A. Logadottir, L. Lindqvist, J. R. Kitchin, T. Bligaard and H. Jónsson, *J. Phys. Chem. B*, 2004, **108**, 17886–17892.

222 M. Gong, D.-Y. Wang, C.-C. Chen, B.-J. Hwang and H. Dai, *Nano Res.*, 2016, **9**, 28–46.

223 K. I. Popov, S. Djokic, Stojan and B. N. Grgur, *Fundamental Aspects of Electrometallurgy*, Kluwer Academic Publishers, 2002.

224 G. O. Larrazábal, A. J. Martín, F. Krumeich, R. Hauert and J. Pérez-Ramírez, *ChemSusChem*, 2017, **10**, 1255–1265.

225 W. Shao and G. Zangari, *J. Phys. Chem. C*, 2009, **113**, 10097–10102.

226 J. Wu, F. G. Risalvato, F.-S. Ke, P. J. Pellechia and X.-D. Zhou, *J. Electrochem. Soc.*, 2012, **159**, F353–F359.

227 G. Carneval and J. B. de Cusminsky, *J. Electrochem. Soc.*, 1981, **128**, 1215.

228 D. Ren, Y. Deng, A. D. Handoko, C. S. Chen, S. Malkhandi and B. S. Yeo, *ACS Catal.*, 2015, **5**, 2814–2821.

229 A. Damjanovic, M. Paunovic and J. O. Bockris, *J. Electroanal. Chem.*, 1965, **9**, 93–111.

230 A. S. Varela, W. Ju, T. Reier and P. Strasser, *ACS Catal.*, 2016, **6**, 2136–2144.

231 V. Lates, A. Falch, A. Jordaan, R. Peach and R. J. Kriek, *Electrochim. Acta*, 2014, **128**, 75–84.

232 N. D. Nikolić, G. Branković, M. G. Pavlović and K. I. Popov, *J.*

Electroanal. Chem., 2008, **621**, 13–21.

233 N. Sreekanth and K. L. Phani, *Chem. Commun.*, 2014, **50**, 11143.

234 J. Tang, X. Zou and F. Hong, in *Electrochemical Reduction of Carbon Dioxide: Fundamentals and Technologies*, eds. J. Qiao, Y. Liu and J. Zhang, CRC Press, Canada, 2016, pp. 293–310.

235 J. Zhang, W. J. Pietro and a. B. P. Lever, *J. Electroanal. Chem.*, 1996, **403**, 93–100.

236 A. Aoki and G. Nogami, *J. Electrochem. Soc.*, 1995, **142**, 423–427.

237 O. A. Baturina, Q. Lu, M. A. Padilla, L. Xin, W. Li, A. Serov, K. Artyushkova, P. Atanassov, F. Xu, A. Epshteyn, T. Brintlinger, M. Schuette and G. E. Collins, *ACS Catal.*, 2014, **4**, 3682–3695.

238 P. Sun, F. O. Laforge, M. V. Mirkin, P. de Oliveira, M. Erard, M. Vuillaume and D. O. Wipf, *Phys. Chem. Chem. Phys.*, 2007, **9**, 802–823.

239 L. Wang, K. Gupta, J. B. M. Goodall, J. A. Darr and K. B. Holt, *Faraday Discuss.*, 2017, **197**, 517–532.

240 H. Li, X.-Z. Yuan and H. Wang, Eds., *PEM Fuel Cell Diagnostic Tools*, CRC Press, 2011.

241 D. Pletcher, *A First Course in Electrode Process*, Royal Society of Chemistry, Cambridge, UK, 2nd edn., 2009.

242 S. Vesztergom, M. Ujvári and G. G. Láng, *Electrochem. commun.*, 2012, **19**, 1–4.

243 S. Vesztergom, M. Ujvári and G. Győző, *Electrochim. Acta*, 2013, **110**, 49–55.

244 N. P. C. Stevens, M. B. Rooney, a. M. Bond and S. W. Feldberg, *J. Phys. Chem. A*, 2001, **105**, 9085–9093.

245 PINE Research Instruments, Collection Efficiency, https://www.pineresearch.com/shop/products/electrodes/rrde/classic-ptfe-rrde/e7r9/, (accessed 22 May 2017).

246 S. Vesztergom, N. Barankai, N. Kovács, M. Ujvári, P. Broekmann, H. Siegenthaler and G. Láng, *Electrochem. commun.*, 2016, **68**, 54–58.

247 P. Daubinger, J. Kieninger, T. Unmüssig and G. a Urban, *Phys. Chem. Chem. Phys.*, 2014, **16**, 8392–9.

248 E. H. Yu, K. Scott and R. W. Reeve, *J. Electroanal. Chem.*, 2003, **547**, 17–24.

249 I. T. McCrum and M. J. Janik, *J. Phys. Chem. C*, 2016, **120**, 457–471.

250 J. Joo, T. Uchida, A. Cuesta, M. T. M. Koper and M. Osawa, *J. Am. Chem. Soc.*, 2013, **135**, 9991–9994.

251 R. Mancharan and J. B. Goodenough, *J. Mater. Chem.*, 1992, **2**, 875–887.

252 A. M. Hofstead-Duffy, D.-J. Chen, S.-G. Sun, Y. J. Tong, T. Iwasita, W. Vielstich and Y. Y. J. Tong, *J. Mater. Chem.*, 2012, **22**, 5205.

253 D. Y. Chung, K.-J. Lee and Y.-E. Sung, *J. Phys. Chem. C*, 2016, **120**, 9028–9035.

254 J. Raoof, R. Ojani and S. Hosseini, *S. Afr. J. Chem.*, 2013, **66**, 47–53.

255 A. V. Tripkovic, S. L. Gojkovic, K. D. Popovic and J. D. Lovic, *J. Serbian Chem. Soc.*, 2006, **71**, 1333–1343.

256 J. V. Perales-Rondón, S. Brimaud, J. Solla-Gullón, E. Herrero, R. Jürgen Behm and J. M. Feliu, *Electrochim. Acta*, 2015, **180**, 479–485.

257 C. F. C. Lim, D. A. Harrington and A. T. Marshall, *Electrochim. Acta*, 2017, **238**, 56–63.

258 A. Bandi and H. -M. Kühne, *J. Electrochem. Soc.*, 1992, **139**, 1605.